

THESIS

CHARACTERIZATION OF HOLLOW CATHODES USING A FAST ACTUATING  
ELECTROSTATIC PROBE

Submitted by

Russell Hamilton Martin

Mechanical Engineering

In partial fulfillment of the requirements

For the Degree of Masters of Science

Colorado State University

Fort Collins, Colorado

Spring 2009

COLORADO STATE UNIVERSITY

March 9, 2009

WE HEREBY RECOMMEND THAT THE THESIS PREPARED UNDER OUR SUPERVISION BY RUSSELL H. MARTIN ENTITLED CHARACTERIZATION OF HOLLOW CATHODES USING A FAST ACTUATING ELECTROSTATIC PROBE BE ACCEPTED AS FULFILLING IN PART REQUIREMENTS FOR THE DEGREE OF MASTER OF SCIENCE.

Committee on Graduate Work

---

Dr. Azer P. Yalin

---

Dr. Raymond S. Robinson

---

Dr. John D. Williams, Advisor

---

Dr. Allan T. Kirkpatrick, Department Head

## ABSTRACT OF THESIS

### CHARACTERIZATION OF HOLLOW CATHODES USING A FAST ACTUATING ELECTROSTATIC PROBE

Despite their great advantages, electric propulsive devices have seen limited use by NASA and other space agencies over the past 50 years. While this stems from several different issues, the long operation characteristics of most electric propulsive devices make reliability/lifetime one of the driving factors in their selection. Data from JPL's Extended Life Test of the Deep Space 1 flight spare ion thruster (NSTAR thruster design) revealed several important life limiting issues, one of which being hollow cathode erosion. To better understand this erosion and physical processes taking place, characterizations of the cathode plasma region must be made.

The work herein describes a method for mapping plasma parameters nearby a hollow cathode using a high speed positioning system and a segment-shielded electrostatic probe. Contour maps of plasma density, plasma potential, and electron temperature are presented for wide ranges of discharge current (2-20 A) and xenon flow rate (1.5-6 sccm). These contour maps are constructed over an axial and radial region 2.5-mm to 32.5-mm and 0-mm to 20-mm, respectively, relative to the orifice of the hollow cathode. A comparison of plasma properties is presented for different cathode configurations including (1) a keeper-free cathode, (2) three enclosed-keeper configurations, (3) three anode configurations, and (4) an enclosed-keeper configuration with an applied magnetic field meant to simulate the NSTAR thruster discharge cathode. Electron number densities

measured range from  $1 \times 10^9$  to  $1 \times 10^{13} \text{ cm}^{-3}$ , with plasma potentials and electron temperatures ranging from 9 to 30V and 1.5 to 3eV, respectively. Several different expansion behaviors were observed corresponding to different discharge conditions and configurations. Finally, these expansion behaviors and other measurements made during the study are summarized and briefly used to compare with erosion models and others work as well to make suggestions for future areas of study.

Russell Hamilton Martin  
Mechanical Engineering  
Colorado State University  
Fort Collins, CO 80523  
Spring 2009

## **ACKNOWLEDGEMENTS**

The author would like to thank John D. Williams, Desiree D. Williams, Paul J. Wilbur, Mark S. Buttweiler, and the 2004-05 ME486 senior design team (Seth Bell, Markus Jones, James Perkins, Brad Maraccini, and Dennis Schmitt) for their assistance and support throughout this project. Financial support from the Jet Propulsion Laboratory/Caltech and the Air Force Research Laboratory, Edwards Air Force Base is also gratefully acknowledged. Furthermore, none of this research would be as entertaining and interesting without the intellectual and fun atmosphere currently present at CSU's Plasma Research Lab. While this thesis is mainly the result of the author's work, all who have taken part in this study and all who helped with numerous small details made this work more valuable in both technical and sentimental ways (Kirk, Casey, and Cody don't think you slipped through the cracks). No animals were harmed in the making of this document.

# TABLE OF CONTENTS

Abstract Of Thesis .....	ii
Acknowledgements .....	v
Table of Contents.....	vi
List of Figures .....	viii
Nomenclature.....	xvi
Chapter 1: Introduction .....	18
1.1 The Hollow Cathode Assembly within Ion and Hall Thrusters .....	21
Chapter 2: Experimental Apparatus .....	29
2.1 Rapidly Actuating Probe for Ion Diagnostics System (RAPID) .....	30
2.1.1 Natural Frequency and Vibration of the Langmuir Probe .....	31
2.2 Langmuir Probe Design .....	34
2.2.1 Segmented Langmuir Probe Design and Construction .....	35
2.2.1.1 Probe Assembly.....	38
2.2.2 Probe Thermal Analysis .....	40
2.2.2.1 Probe Heating Model.....	41
Chapter 3: Probe Theory and Analysis .....	51
3.1 Single Langmuir Probe .....	51
3.1.1 Langmuir Probe Circuitry and Measurement Technique .....	55
3.1.2 Software Calculations .....	59
Chapter 4: Hollow Cathode Measurement Setup .....	62
4.1 General Setup and Motion .....	63
4.2 Cathode Configurations.....	65

4.3	Vacuum Chamber .....	71
Chapter 5:	Results .....	73
5.1	Simple Cathode (SC) .....	78
5.2	Simple Cathode with Near Plate Anode (SCP).....	90
5.3	Keeper Orifice Diameter = 2.7 mm (SK) .....	96
5.4	Keeper Orifice Diameter = 3.8 mm (MK) .....	103
5.5	Keeper Orifice Diameter = 4.75mm (LK) .....	111
5.6	Cathode in a Magnetic Field with a Plate Anode (MP) .....	117
5.7	Cathode in a Magnetic Field with a Ring Anode (MR) .....	125
5.8	Cathode in a Magnetic Field with a Ring Anode at High Discharge Currents (MRH) .....	131
5.9	FFT Analysis .....	137
5.10	Knee Analysis .....	140
5.11	Discharge Characteristics .....	145
Chapter 6:	Conclusions .....	148
6.1	Simple Cathode Plasma Parameters .....	149
6.2	Enclosed Keeper Effects.....	150
6.3	Magnetic Field Effects .....	153
6.4	Plasma Oscillations .....	155
6.5	Final Statements .....	156
Appendix A	.....	158
References	.....	204

## LIST OF FIGURES

Figure 1: Hollow cathode schematic.....	22
Figure 2: NSTAR ELT discharge cathode at beginning of life (a). NSTAR ELT discharge cathode after 30,000 hrs. Note large keeper erosion and moderate cathode orifice erosion (b).....	25
Figure 3: Generalized schematic of hollow cathode and Langmuir probe, showing probe motion and encompassing probe measurement field. ....	29
Figure 4: RAPID system shown without the stainless shroud installed. ....	30
Figure 5: Positional resolution showing unknown vertical vibration of Langmuir probe tip.....	31
Figure 6: Displacement vs. time at 0.5 and 1.0 m/s.....	32
Figure 7: Tungsten segmented Langmuir probe immersed in plasma of varying plasma potentials as it travels through hollow cathode plume. ....	34
Figure 8: Setup for segmentation of Langmuir probes .....	36
Figure 9: Masking plate assembly assembled (a), disassembled (b), plate design (c), mounted to motor assembly (d).....	37
Figure 10: Results between different masking plates .....	37
Figure 11: Final Langmuir probe assembly .....	38
Figure 12: Completed Langmuir probes of different types: A segmented Langmuir probe (Top), a standard Langmuir probe (Mid), and a double Langmuir probe (Bottom). ....	39
Figure 13: Thermal analysis of diagnostic probe and resistive thermal network representation .....	42
Figure 14: Power input to the probe as a function of time due to electron collection .....	44

Figure 15: Combined probe thermal network.....	49
Figure 16: Probe temperature versus time for a Gaussian density distribution .....	50
Figure 17: Idealized I-V curve showing important parameters and regions.....	51
Figure 18: Waveform biasing scheme and resulting collected current as a function of time / position.....	57
Figure 19: Langmuir probe circuit schematic including PXI and ELMO drive systems	58
Figure 20: Analysis of actual Langmuir trace taken at listed conditions with the simple cathode configuration.....	60
Figure 21: Cathode assembly mounted to THK placed ~10 cm perpendicularly in front of the RAPID system.....	63
Figure 22: Hollow cathode investigation setup showing Langmuir sweep path lines and distant ring anode .....	64
Figure 23: Simple cathode and distant ring anode with probe at 0.25 cm axial distance.....	65
Figure 24: Schematic diagram of enclosed keeper and hollow cathode (a) and photo of small holed keeper and near plate anode (b).....	66
Figure 25: Schematic diagram of simple cathode with ring anode system. Shown also is the measurement field directly in front of the cathode (explained in section 4.1).....	67
Figure 26: Schematic diagram of near plate anode.....	68
Figure 27: Schematic diagram of near ring anode.....	68
Figure 28: Photo of enclosed keeper cathode with axial magnetic field and near field ring anode.....	69

Figure 29: Magnetic field strength through cathode centerline .....	70
Figure 30: Magnetic field strength contours versus radial and axial position .....	71
Figure 31: Varian 0.76m x 1.0m vacuum chamber .....	72
Figure 32: Common Langmuir trace for SC6. 1000 $\Omega$ resistor, -32V to +37V waveform.....	73
Figure 33: Common Langmuir trace for SC10. 100 $\Omega$ resistor, -20V to +25V waveform.....	73
Figure 34: Common Langmuir trace from SC12. 33 $\Omega$ resistor, -20V to +25V waveform.....	74
Figure 35: Combined Langmuir traces for flow condition SC3 at 0.25 cm axial position. Representative of common radial sweep at small axial positions. ....	75
Figure 36: Combined Langmuir traces for flow condition SC10 at 1.0 cm axial position. Representative of common radial sweep at medium axial positions. ...	76
Figure 37: Cathode orientation with respect to RAPID system measurement field. ....	77
Figure 38: $n_e$ contour plot for SC1 ( $\times 10^9$ cm <sup>-3</sup> ).....	79
Figure 39: $n_e$ contour plot for SC2 ( $\times 10^9$ cm <sup>-3</sup> ).....	79
Figure 40: $n_e$ contour plot for SC3 ( $\times 10^9$ cm <sup>-3</sup> ).....	80
Figure 41: $n_e$ contour plot for SC4 ( $\times 10^9$ cm <sup>-3</sup> ).....	80
Figure 42: Overlay of plasmoid contour structure measured on photo of plasmoid. ....	80
Figure 43: $V_p$ contour plot for SC3 (V). ....	82
Figure 44: $V_p$ contour plot for SC4 (V). ....	82
Figure 45: $T_e$ contour plot for SC3 (eV).....	84
Figure 46: $T_e$ contour plot for SC4 (eV).....	84

Figure 47: $n_e$ contour plot for SC7 ( $\times 10^9 \text{ cm}^{-3}$ ).....	84
Figure 48: $n_e$ contour plot for SC8 ( $\times 10^9 \text{ cm}^{-3}$ ).....	84
Figure 49: $V_p$ contour plot for SC7 (V). ....	85
Figure 50: $V_p$ contour plot for SC8 (V). ....	85
Figure 51: $T_e$ contour plot for SC7 (eV).....	86
Figure 52: $T_e$ contour plot for SC8 (eV).....	86
Figure 53: $n_e$ contour plot for SC10 ( $\times 10^9 \text{ cm}^{-3}$ ).....	87
Figure 54: $n_e$ contour plot for SC11 ( $\times 10^9 \text{ cm}^{-3}$ ).....	87
Figure 55: $V_p$ contour plot for SC10 (V). ....	88
Figure 56: $n_e$ contour plot for SCP2 ( $\times 10^9 \text{ cm}^{-3}$ ). ....	91
Figure 57: $n_e$ contour plot for SCP3 ( $\times 10^9 \text{ cm}^{-3}$ ). ....	91
Figure 58: $V_p$ plot for Condition # SCP3 (V). ....	92
Figure 59: $T_e$ contour plot for SCP3 (eV).....	92
Figure 60: $n_e$ contour plot for SCP4 ( $\times 10^9 \text{ cm}^{-3}$ ). ....	93
Figure 61: $n_e$ contour plot for SCP5 ( $\times 10^9 \text{ cm}^{-3}$ ). ....	93
Figure 62: $n_e$ contour plot for SCP6 ( $\times 10^9 \text{ cm}^{-3}$ ). ....	93
Figure 63: $V_p$ contour plot for SCP6 (V).....	94
Figure 64: $T_e$ contour plot for SCP6 (eV).....	94
Figure 65: $n_e$ contour plot for SCP9 ( $\times 10^9 \text{ cm}^{-3}$ ). ....	95
Figure 66: $V_p$ contour plot for SCP9 (V).....	95
Figure 67: $T_e$ contour plot for SCP9 (eV).....	95
Figure 68: $n_e$ contour plot for SK1 ( $\times 10^9 \text{ cm}^{-3}$ ). ....	97
Figure 69: $V_p$ contour plot for SK1 (V).....	97

Figure 70: $T_e$ contour plot for SK1 (eV).....	98
Figure 71: $n_e$ contour plot for SK2 ( $\times 10^9 \text{ cm}^{-3}$ ). .....	99
Figure 72: $n_e$ contour plot for SK3 ( $\times 10^9 \text{ cm}^{-3}$ ). .....	99
Figure 73: $n_e$ contour plot for SK4 ( $\times 10^9 \text{ cm}^{-3}$ ). .....	99
Figure 74: $V_p$ contour plot for SK2 (V).....	100
Figure 75: $V_p$ contour plot for SK4 (V).....	100
Figure 76: $T_e$ contour plot for SK2 (eV).....	101
Figure 77: $T_e$ contour plot for SK4 (eV).....	101
Figure 78: $n_e$ contour plot for SK8 ( $\times 10^9 \text{ cm}^{-3}$ ). .....	102
Figure 79: $V_p$ contour plot for SK8 (V).....	102
Figure 80: $T_e$ contour plot for SK8 (eV).....	102
Figure 81: $n_e$ contour plot for MK1 ( $\times 10^9 \text{ cm}^{-3}$ ). .....	104
Figure 82: $n_e$ contour plot for MK4 ( $\times 10^9 \text{ cm}^{-3}$ ). .....	104
Figure 83: $V_p$ contour plot for MK1 ( $\times 10^9 \text{ cm}^{-3}$ ). .....	105
Figure 84: $V_p$ contour plot for MK4 ( $\times 10^9 \text{ cm}^{-3}$ ). .....	105
Figure 85: $T_e$ contour plot for MK1 ( $\times 10^9 \text{ cm}^{-3}$ ). .....	106
Figure 86: $T_e$ contour plot for MK4 ( $\times 10^9 \text{ cm}^{-3}$ ). .....	106
Figure 87: $n_e$ contour plot for MK5 ( $\times 10^9 \text{ cm}^{-3}$ ). .....	107
Figure 88: $n_e$ contour plot for MK6 ( $\times 10^9 \text{ cm}^{-3}$ ). .....	107
Figure 89: $V_p$ contour plot for MK5 (V).....	108
Figure 90: $V_p$ contour plot for MK6 (V).....	108
Figure 91: $n_e$ contour plot for MK12 ( $\times 10^9 \text{ cm}^{-3}$ ). .....	109
Figure 92: $V_p$ contour plot for MK12 (V).....	109

Figure 93: Single radial sweep at 0.25 cm axial position for MK12. Showing three orders of magnitude increase in density close to the cathode. Also displayed are the plasma potential and electron temperature profiles.....	109
Figure 94: $n_e$ contour plot for LK1 ( $\times 10^9 \text{ cm}^{-3}$ ).....	111
Figure 95: $V_p$ contour plot for LK1 (V).....	111
Figure 96: $T_e$ contour plot for LK1 (eV).....	112
Figure 97: $n_e$ contour plot for LK4 ( $\times 10^9 \text{ cm}^{-3}$ ).....	112
Figure 98: $V_p$ contour plot for LK4 (V).....	112
Figure 99: $T_e$ contour plot for LK4 (eV).....	113
Figure 100: $n_e$ contour plot for LK5 ( $\times 10^9 \text{ cm}^{-3}$ ).....	114
Figure 101: $V_p$ contour plot for LK5 (V).....	114
Figure 102: $T_e$ contour plot for LK5 (eV).....	114
Figure 103: $n_e$ contour plot for LK12 ( $\times 10^9 \text{ cm}^{-3}$ ).....	115
Figure 104: $V_p$ contour plot for LK12 (V).....	115
Figure 105: $T_e$ contour plot for LK12 (eV).....	116
Figure 106: $n_e$ contour plot for MP1 ( $\times 10^9 \text{ cm}^{-3}$ ).....	117
Figure 107: $V_p$ contour plot for MP1 (V).....	117
Figure 108: $T_e$ contour plot for MP1 (eV).....	118
Figure 109: Azimuthal Current Density for MP1 ( $J_D = 2\text{A}$ , $m = 1.5\text{sccm}$ ).....	122
Figure 110: $n_e$ contour plot for MP2 ( $\times 10^9 \text{ cm}^{-3}$ ).....	123
Figure 111: $V_p$ contour plot for MP2 (V).....	123
Figure 112: $T_e$ contour plot for MP2 (eV).....	123
Figure 113: Azimuthal Current Density for MP2 ( $J_D = 4\text{A}$ , $m = 1.5\text{sccm}$ ).....	124

Figure 114: $n_e$ contour plot for MR1 ( $\times 10^9 \text{ cm}^{-3}$ ).	126
Figure 115: $V_p$ contour plot for MR1 (V).	126
Figure 116: $T_e$ contour plot for MR1 (eV).	127
Figure 117: $n_e$ contour plot for MR4 ( $\times 10^9 \text{ cm}^{-3}$ ).	128
Figure 118: $V_p$ contour plot for MR4 (V).	128
Figure 119: $T_e$ contour plot for MR4 (eV).	128
Figure 120: $T_e$ contour plot for MR7 (eV).	128
Figure 121: $n_e$ contour plot for MR11 ( $\times 10^9 \text{ cm}^{-3}$ ).	129
Figure 122: $n_e$ contour plot for MR12 (V).	129
Figure 123: $V_p$ contour plot for MR12 (V).	129
Figure 124: $T_e$ contour plot for MR12 (eV).	129
Figure 125: Azimuthal Current Density for MR11 ( $J_D = 6\text{A}$ , $m = 4.5\text{sccm}$ ).	130
Figure 126: $n_e$ contour plot for MRH1 ( $\times 10^9 \text{ cm}^{-3}$ ).	132
Figure 127: $V_p$ contour plot for MRH1 (V).	132
Figure 128: $T_e$ contour plot for MRH1 (eV).	132
Figure 129: $n_e$ contour plot for MRH2 ( $\times 10^9 \text{ cm}^{-3}$ ).	133
Figure 130: $n_e$ contour plot for MRH3 ( $\times 10^9 \text{ cm}^{-3}$ ).	133
Figure 131: $n_e$ contour plot for MRH4 ( $\times 10^9 \text{ cm}^{-3}$ ).	134
Figure 132: $T_e$ contour plot for MRH4 (eV).	134
Figure 133: $n_e$ contour plot for MRH7 ( $\times 10^9 \text{ cm}^{-3}$ ).	135
Figure 134: $V_p$ contour plot for MRH7 (V).	135
Figure 135: $T_e$ contour plot for MRH7 (eV).	135
Figure 136: Azimuthal Current Density for MRH7 ( $J_D = 20\text{A}$ , $m = 4.5\text{sccm}$ ).	136

Figure 137: Periodic oscillation seen in Langmuir trace at conditions listed. ....	138
Figure 138: FFT analysis for MRH7. ....	139
Figure 139: Knee region of two different Langmuir traces showing a small and large voltage range. ....	140
Figure 140: EEDF plots for traces possessing a 2.3 V and 9.6V knee. ....	142
Figure 141: Sample modified trace for the SC3 condition possessing a knee voltage of 2.3V. ....	142
Figure 142: Knee contour plot for Condition # SC3. ....	144
Figure 143: $n_e$ contour plot for MRH7 ( $\times 10^9 \text{ cm}^{-3}$ ). ....	144
Figure 144 $V_p$ contour plot for MRH7 (V). ....	144
Figure 145: Discharge fluctuations due to probe sweep through cathode plume. ....	145
Figure 146: FFT analysis of anode voltage, revealing three harmonics of the anode oscillation. ....	146

# NOMENCLATURE

## Variables

<p><math>A</math> = cross-sectional area of probe shaft (cm<sup>2</sup>) or general area (m<sup>2</sup>)</p> <p><math>A_{RD}</math> = Richardson-Dushman constant (<math>4\pi m_e q k^2/h^3</math>) (120 A/cm<sup>2</sup>K<sup>2</sup>)</p> <p><math>A_{probe}</math> = probe surface area (cm<sup>2</sup>)</p> <p><math>B</math> = magnetic field (Gauss)</p> <p><math>c_p</math> = tungsten probe specific heat (J/kgK)</p> <p><math>d_{a,b}</math> = probe shaft outer and inner diameters (m)</p> <p><math>d_{eff}</math> = effective separation (m)</p> <p><math>\delta</math> = probe deflection (m)</p> <p><math>E</math> = electron energy (eV)</p> <p><math>E_{x,y,z}</math> = electric field (V/m)</p> <p><math>E_{rod}</math> = modulus of elasticity (Pa)</p> <p><math>\dot{E}</math> = thermal energy (J)</p> <p><math>E_s</math> = local electric field (V/m)</p> <p><math>\epsilon</math> = emissivity of a material</p> <p><math>\epsilon_o</math> = permittivity of free space (<math>8.85 \times 10^{-12}</math> F/m)</p> <p><math>F</math> = Lorentz force (N)</p> <p><math>F_j</math> = view factor</p> <p><math>g_o</math> = gravitational force at the surface of the earth (N)</p> <p><math>h</math> = Plancks constant (<math>6.626 \times 10^{-34}</math> Js)</p> <p><math>I</math> = moment of inertia (m<sup>4</sup>)</p>	<p><math>I_{sp}</math> = specific impulse (s)</p> <p><math>I_e</math> = electron collection current (A)</p> <p><math>I_{sat e}</math> = electron saturation current (A)</p> <p><math>j_{r,\theta,z}</math> = current density (A/m<sup>2</sup>)</p> <p><math>J</math> = radiosity (W/m<sup>2</sup>)</p> <p><math>k</math> = Boltzmann constant (J/K)</p> <p><math>k_{rod}</math> = probe spring stiffness (kg/s<sup>2</sup>)</p> <p><math>L</math> = probe shaft length (m)</p> <p><math>m</math> = probe mass (kg)</p> <p><math>M_f</math> = spacecraft final mass (kg)</p> <p><math>M_i</math> = spacecraft initial mass (kg)</p> <p><math>m_{rod}</math> = probe shaft mass (kg)</p> <p><math>\dot{m}</math> = mass flow rate (kg/s)</p> <p><math>m_{e,i}</math> = electron or ion mass (kg)</p> <p><math>n_e</math> = electron number density (cm<sup>-3</sup>)</p> <p><math>n_o</math> = neutral density (cm<sup>-3</sup>)</p> <p><math>\dot{n}</math> = neutral density flow rate (cm<sup>-3</sup>s<sup>-1</sup>)</p> <p><math>\eta_{t,c}</math> = thruster and power conversion efficiency</p> <p><math>\sigma</math> = Stefan-Boltzmann constant (<math>5.67 \times 10^{-8}</math> W/m<sup>2</sup>K<sup>4</sup>)</p> <p><math>\sigma_c</math> = plasma conductivity (W/m<sup>2</sup>K<sup>4</sup>)</p> <p><math>\Sigma</math> = error in EEDF second derivative</p> <p><math>\dot{P}_{probe}</math> = heating due to electron collection (J/s)</p>
--	---

$q$  = elementary charge (C)  
 $\dot{Q}_{cond}$  = cooling effect due to conduction (J/s)  
 $\dot{Q}_{rad}$  = radiation heating component (J/s)  
 $\dot{Q}_{re-rad}$  = cooling effect due to re-radiating the heat to the surroundings (J/s)  
 $\Phi_w$  = temperature independent work function (eV)  
 $\rho$  = probe shaft density (kg/m<sup>3</sup>)  
 $T$  = thrust (N)  
 $\Delta t$  = incremental time step (s)  
 $T_{e,i}$  = electron or ion temperature (eV)  
 $T_\infty$  = temperature of the surroundings (K)  
 $T_{p,i}$  = probe temperature at the current time step (K)  
 $T_{p,i-1}$  = probe temperature from the previous step (K)  
 $r$  = probe shaft radius (kg)  
 $r_{e,i}$  = electron or ion gyro radius (m)  
 $R_p$  = probe radius (m)  
 $R_{tot}$  = thermal network resistance  
 $V_B$  = probe bias potential (V)  
 $V_p$  = plasma potential (V)  
 $V_{p-p}$  = peak to peak voltage of biasing waveform (V)  
 $\Delta V$  = incremental voltage step used in EEDF calculation (V)

$\dot{W}$  = Ohmic heating effect (J/s)  
 $\omega_n$  = probe shaft natural frequency (rad/sec)  
 $v_{e,i}$  = particle velocity (electron or ion in m/s)  
 $v_{ex}$  = rocket exhaust velocity (m/s)  
 $v_o$  = neutral thermal velocity (m/s)  
 $\Delta v$  = characteristic mission change in velocity (electron or ion in m/s)  
 $\nu_e$  = collision frequency (s<sup>-1</sup>)

### Acronyms

NSTAR = NASA Solar electric propulsion Technology Applications Readiness  
 GRC = Glenn Research Center  
 JPL = Jet Propulsion Laboratory  
 CSU = Colorado State University  
 DAQ = Data Acquisition System  
 NASA = National Aeronautics and Space Administration  
 PXI = PCI eXtensions for Instrumentation (the type of computer system used to record data)  
 RAPID = Rapidly Actuating Probe for Ion Diagnostics  
 EEDF = Electron Energy Distribution Function  
 FFT = Fast Fourier Transform

# CHAPTER 1: INTRODUCTION

Modern electric propulsion can trace its roots back some hundred years to Robert Goddard and his early experiments with discharge tubes<sup>1,2</sup>. Goddard proposed that charged particles could be accelerated to great velocities by an electric field without excessive heating of the propellant. In contrast, no known material at that time or presently can withstand the heat load required to accelerate gas particles to similar speeds through chemical means (e.g., via a chemical rocket). Over the next fifteen years Goddard again and again came back to his ideas on electric propulsion, where he eventually performed some of the first experiments in electric propulsion. Goddard and others at this early time concluded that a stream of positive and negative particles could be the basis for a high exhaust velocity propulsion system of the future.

A few years before Goddard began his inquiries into electric propulsion another man, Konstantin Tsiolkovsk, in 1903 first published the derivation of what is now known as the rocket equation<sup>3,4</sup>, which relates the ratio of the final-to-initial mass of a spacecraft,  $M_f/M_i$ , to the negative exponential of the ratio of the characteristic velocity change,  $\Delta v$ , and the propulsion system effective exhaust velocity,  $v_{ex}$ . The characteristic velocity change represents the requirement of a given mission, and, along with the effective exhaust velocity, fixes the amount of propellant mass needed to accomplish the mission (i.e.,  $M_i - M_f$ ).

$$\frac{M_f}{M_i} = e^{\frac{-\Delta v}{v_{ex}}} = e^{\frac{-\Delta v}{g_o I_{sp}}} \quad 1.1$$

This equation is further defined by the right side of equation 1.2 where:

$$I_{sp} = \frac{T}{\dot{m}g_o} = \frac{v_{ex}}{g_o} \quad 1.2$$

The specific impulse,  $I_{sp}$ , of a rocket is commonly used as a quality parameter that is proportional to the exhaust velocity. It is a measure of how much thrust is generated per unit flow rate of propellant. Modern chemical rockets achieve specific impulses in the range of a few hundred seconds. Electric propulsion devices such as Hall and Ion thrusters are capable of operating at specific impulses of several thousands of seconds<sup>5</sup>, an order of magnitude higher than chemical rockets. Thus for the same mission  $\Delta v$  and initial mass,  $M_i$ , the use of an electric rocket would allow a far greater final useable payload when compared to a chemical rocket. This is especially true when the power source required to drive an electric propulsion system is needed by the payload at the final destination.

Despite this great advantage, electric propulsion devices have seen limited use by NASA and other space agencies over the past 50 years. This is due in part to (1) marginal electrical efficiency in the early years, (2) high fabrication and test costs, and (3) reliability/lifetime issues related to the complexity of these systems relative to chemical rocket technology<sup>6</sup>. Continuous improvements have been made in all three areas, but an improvement in the last item (and especially in regard to lifetime) is essential to see the use of electric propulsion become common place in future space missions. This is because thrust in an electric propulsion system is limited by the total available power generation capability of a spacecraft. When thrust is low, thrust times (and thruster lifetimes) must be large to deliver the required impulse to a spacecraft. Equation 1.3 demonstrates this limitation:

$$\eta_c \eta_t P = \frac{1}{2} \dot{m} g_o^2 I_{sp}^2 = \frac{1}{2} g_o I_{sp} T \quad 1.3$$

This equation equates the electrical power deposited into a beam of accelerated propellant to the rate of kinetic energy change in the beam. The product of the thruster efficiency,  $\eta_t$ , and the power conversion efficiency,  $\eta_c$ , decreases the amount of available spacecraft power delivered into the beam, and, consequently, reduces the thrust that can be produced by an electric propulsion system. This efficiency product is typically in the 0.5 to 0.7 range for modern electric propulsion systems. One can rearrange Eq. (1.3) into a more common form where the fundamental limitation of an electric propulsion system on available system power is even more evident:

$$\frac{T}{P} = \frac{2\eta_t \eta_c}{g_o I_{sp}} \quad 1.4$$

Currently available solar electric power systems for satellites and spacecraft are in the 10 kW range, and, for a typical electrical thruster system efficiency product of 0.6 and a specific impulse of 3000 sec, the thrust-to-power ratio is only 40.8 mN/kW. At 10 kW of solar array output power and a specific impulse of 3000 sec, the thrust is only 0.4 N. To affect a velocity change of 5000 m/s to a 1000 kg spacecraft, the thruster must fire for ~3500 hrs. More clearly stated, one must design electric propulsion systems for long life times to take advantage of their efficient use of propellant under conditions of limited power generation capability. Furthermore, slow erosion processes occurring on various components of electric propulsion systems need to be carefully evaluated because they can limit the life time of the propulsion system and endanger the accomplishment of a given mission.

## 1.1 The Hollow Cathode Assembly within Ion and Hall Thrusters

While there are numerous types of electric propulsive devices and many more components of these devices that can wear out over time, throughout the entirety of this thesis, focus will remain on only one component, the hollow cathode assembly.

Specially designed, orificed hollow cathodes have been developed for a wide variety of applications including plasma generation for spacecraft charging control,<sup>7,8,9,10</sup> plasma contactors for electro-dynamic tether-based propulsion systems,<sup>11,12,13</sup> and as the plasma electron source for ion and Hall thrusters.<sup>14,15,16,17</sup> The most notable differences between these cathodes and the original, open-ended hollow cathodes<sup>18</sup> are the addition of (1) an orifice plate to the downstream end of the hollow cathode tube and (2) a porous tungsten insert impregnated with low-work-function material placed within the tube near the orifice plate as shown in Figure 1. The orifice plate increases the pressure within the hollow cathode at any given flow rate and enables the hollow cathode to operate at lower flows compared to open-ended hollow cathode geometries. The low-work-function insert reduces the operating temperature of the cathode, which in turn reduces the power required to maintain temperature of the cathode as compared to thermionic cathodes not equipped with a low work function insert.

The low-work-function insert can be fabricated from solid materials like lanthanum hexaboride or porous materials (e.g., sintered tungsten) impregnated with oxides of alkali Earth metals. Inserts have also been fabricated from rolled refractory metal foils that are coated with low work function material<sup>19</sup>.

To a large part, development efforts in electric propulsion systems have driven the evolution of the orificed hollow cathode to a high level of refinement. Hollow cathodes

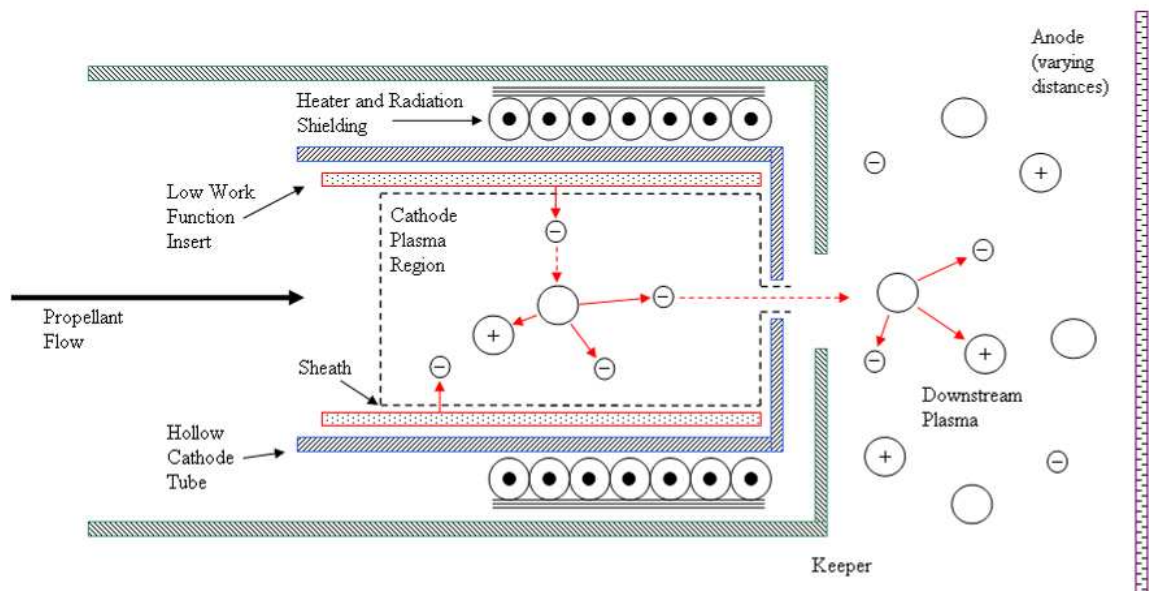


**Figure 1: Hollow cathode schematic**

are lightweight, relatively simple to build, require very little gas flow, and can survive the severe vibration and shock requirements placed on space flight hardware. Experiments have also been performed that demonstrate very long life times (30,000 hr) that are in excess of the required operational period for some space and ground-based applications<sup>20,21</sup>.

Although highly advanced, hollow cathodes still display some troubling features. For example, hollow cathodes can be (1) difficult to start, (2) need protection against exposure to laboratory or launch environment atmosphere, (3) demand sophisticated high temperature heaters, and (4) require high heater power / long conditioning and starting times. Operationally, hollow cathodes require gas flow control as well as a specialized keeper and discharge power supply. In some applications, the hollow cathode discharge can be quite noisy, and, although hollow cathodes are already fairly power and flow efficient, lower power and flow operation is desired. Often times a particular hollow cathode design is so specialized that the design can not be used for a slightly different application or significantly longer mission without being modified considerably.

Developmental efforts in ground-based plasma processing have been successful in developing hollow cathodes that are extremely tolerant of the effects of (1) fast batch turnaround times, (2) multiple atmospheric exposures, and (3) the presence of insert poisoning environments<sup>22</sup>. Lifetimes of several hundred hours are the norm for these industrial cathodes. The improvements to industrial cathodes have been accomplished to a large part by increasing the power, voltage, and gas flow available to the cathode and by shielding the environment around the cathode with added structure and through high volume gas purging, all of which are not desirable options for aerospace applications with limited power or volume/weight constraints.

Although inserts fabricated from many materials are available, the work described herein utilized porous tungsten inserts that were impregnated with barium-calcium aluminate where the molar ratios of barium oxide, calcium oxide, and alumina were 4, 1, 1, respectively. As shown in Figure 1, a heater is required to increase the temperature of

the insert to a point where barium and barium oxide is produced at a sufficient rate to coat the interior surface of the hollow cathode and the interior and exterior of the orifice plate (typically ~1000-1250 °C). Applying voltage to an electrode downstream of the orifice plate and introducing gas flow into the hollow cathode tube is required to initiate a plasma discharge and start the hollow cathode. Typically, the xenon neutral pressure within the hollow cathode can range from 1 to many torr depending to first order on the flow rate and the electron emission current extracted from the hollow cathode. Any inert gas, nitrogen, hydrogen, or a mixture of these gases can be used to operate a hollow cathode discharge. Work herein focuses on xenon cathode operation. The plasma density within the hollow cathode can be as high as  $10^{14} \text{ cm}^{-3}$ ,<sup>23,24</sup> with electron temperatures typically between 0.5 and 1 eV, but higher temperatures are possible in larger cathodes. The plasma potential within a typical hollow cathode is about 5 V to 15 V positive of the hollow cathode tube, but can be higher in larger cathodes as well. Ions produced within this plasma are accelerated into the insert and orifice plate surfaces, and this ion bombardment (and subsequent release of ionization energy when the ion becomes neutralized on the cathode surface) heats the cathode. In most space applications, the heating action provided by the interior plasma is sufficient to maintain the temperature of the insert, and the heater power can be reduced or shut off. Although a wide range of operational conditions is presented, it is important to note that hollow cathodes display an ability to adjust the properties of the internal and external plasmas that enable them to attain the necessary temperatures to supply the emission current that is demanded from them. For instance, a hollow cathode operated at too low of a discharge current or possessing insufficient radiation shielding will operate at higher internal plasma

potentials and electron temperatures, which will cause higher rates of heating via ion bombardment. Another inter-related problem is how the plasma properties downstream of the hollow cathode establish and what geometrical and operational parameters affect them. This second problem is the focus of the work described herein.

Life tests performed on both an engineering model NSTAR thruster and an NSTAR flight spare thruster conducted at the NASA Glenn Research Center (GRC) and the Jet Propulsion Laboratory (JPL) have revealed extensive erosion on both the discharge

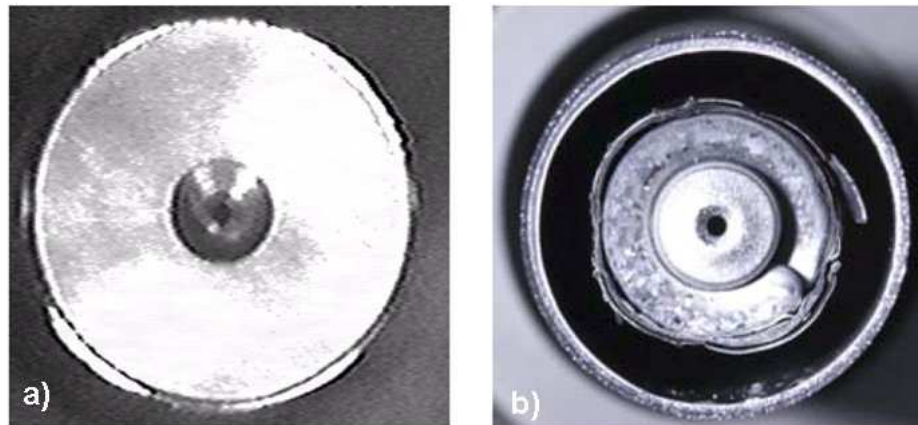


**Figure 2: NSTAR ELT discharge cathode at beginning of life (a). NSTAR ELT discharge cathode after 30,000 hrs. Note large keeper erosion and moderate cathode orifice erosion (b).**

keeper and hollow cathode electrodes.<sup>20,21,25</sup> (as demonstrated in Figure 2 courtesy of Sengupta, Deep Space 1 flight spare extended life test (ELT)<sup>21</sup>). The reason for this erosion has not been fully explained, although several theories have been presented. The most likely cause of keeper and cathode erosion is bombardment by energetic or multi-charged ions, causing atoms to be sputtered from the keeper and cathode surfaces. Energetic ions are inferred to be ions produced in the discharge plasma with energies exceeding the cathode-to-anode potential difference. Multi-charged ions produced near the keeper and cathode can also cause sputter erosion, because the energy they obtain

when striking a surface is a multiple of their charge state and the potential difference they fall through. Both high-energy singly and multiply charged ions have been detected using remotely located probes.<sup>26</sup> One theory proposed for how singly and multiply charged ions gain the required energy to cause cathode/keeper erosion is the potential hill model, described in different ways by Boyd and Crofton<sup>27</sup>, Williams and Wilbur<sup>28</sup>, and Kameyama and Wilbur<sup>29</sup>. In this theory, a standing DC potential hill is assumed to be formed by a region of net positive space charge that is created nearby the cathode orifice. Ions created throughout the potential hill are accelerated from their point of origin both toward and away from the cathode (depending upon which side of the hill they are created on). In contrast to the remotely located probes, direct measurements, like the work described herein and in Ref. 26 and references contained therein, of the DC plasma potential do not point to the presence of DC potential hill structures.

A second theory proposed by Rovey, Herman, and Gallimore<sup>30</sup> assumes the presence of multi-charged ions and their motion calculated from experimentally measured DC plasma potential flow fields to explain the erosion of cathode and keeper structures. Yet another theory, presented by Goebel et al.,<sup>31</sup> imposes a strongly oscillating plasma potential where high energy ions are formed and directed away from regions surrounding intense plasma ball structures, which form immediately in front of hollow cathodes at some operating conditions. This theory is based on direct temporal measurements of plasma potential in the region in front of hollow cathode discharges where oscillations of several tens of volts have been observed in the 50 kHz to 500 kHz range. Cathode and keeper erosion in all theories is greatly affected by plasma density and potential (both temporal and spatial), and it is pointed out that a combination of all three mechanisms

might be present at any given time (i.e., temporally and spatially varying potential hill structures, multi-charged ions, and intense plasma potential oscillation may all play some role in high energy ion production and subsequent sputter erosion of cathode and keeper structures).

It is believed that mapping of average plasma flow field properties directly downstream of a cathode assembly may assist in developing a better understanding of the erosion processes, and several research groups have successfully mapped the internal plasma of an ion engine nearby<sup>32,33,34</sup> and within<sup>35,36,37</sup> the hollow cathode and keeper structures. However, few have systematically tested the effect of different cathode assembly configurations on the plasma flow field. This work is the focus of the present study. Specifically, we present a systematic study of a hollow cathode operated in various configurations, from keeper-free without an applied magnetic field to an enclosed keeper of NSTAR dimensions with an applied magnetic field. Of the many possible components that could be changed in the cathode assembly, four were selected. The first was the addition of an enclosed keeper to the hollow cathode, and comparisons between this and a cathode operated without a keeper are presented. The orifice diameter of this keeper was then increased in even orifice area increments to determine the effect this dimension has on the plasma flow field. To quantify the effects that plasma expansion (and the resulting plasma conductivity pathway) had on the cathode near-field plume, several different discharge anodes (flat plate, distant ring, near ring) were studied and results of these tests are compared and contrasted. Lastly, an axial magnetic field closely matching that of the NSTAR thruster was introduced. This configuration provides a measurement environment that most closely matches that of the above mentioned life

tests, where cathode and keeper erosion was observed after long operational periods. Combined, this work provides plasma flow field data at various cathode assembly complexities for model application and validation that may be useful for finding and avoiding certain plasma conditions detrimental to cathode life.

In regard to flow field measurement, a method developed during the course of this work for obtaining high spatial resolution maps of plasma parameters near the hollow cathode is described in Chapter 2. This method is based on a fast actuating motion apparatus that is integrated with a high speed data acquisition system. Chapter 3 follows with a presentation of (a) the physics behind probe measurements and data analyses and (b) explanation of the data reduction and interpolation/extrapolation process. Chapters 4 and 5 present plasma property contour maps constructed under different conditions, along with some comparisons of results at selected conditions to results in the literature. Finally, conclusions are drawn and recommendations for future work are made in Chapter 6.

## CHAPTER 2: EXPERIMENTAL APPARATUS

In order to measure plasma properties such as electron number density, electron temperature, and plasma potential in the discharge plume of a hollow cathode; a device called a Langmuir probe is utilized. A two-dimensional map of these properties is

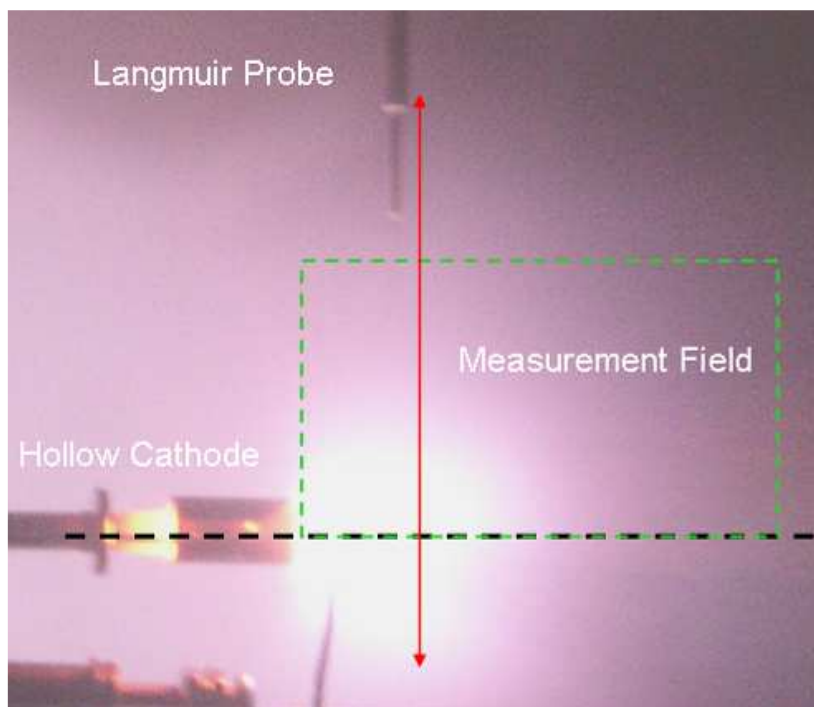


**Figure 3: Generalized schematic of hollow cathode and Langmuir probe, showing probe motion and encompassing probe measurement field.**

created by placing this probe atop a multi-axis motion system, while placing the hollow cathode in the region traversed by the motion system. This idea is illustrated in Figure 3. A description of the electrostatic probe positioning apparatus and related details is contained in Sections 2.1 and 2.2 below, followed by a description of cathode assemblies in Chapter 4. Lastly, a brief description of the vacuum test facilities is provided in Section 4.3.

## 2.1 Rapidly Actuating Probe for Ion Diagnostics System (RAPID)

The key component for this study was the use of a fast positioning system for electrostatic probe placement. Aptly named RAPID (Rapidly Actuating Probe for Ion Diagnostics), this system was designed and constructed by a team of undergraduates, under the authors supervision, at Colorado State University during the 2004-2005

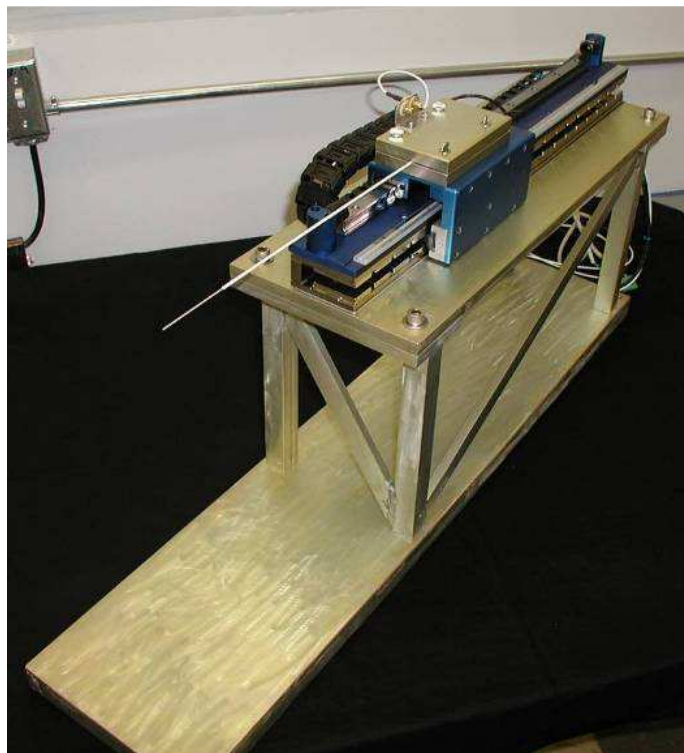


**Figure 4: RAPID system shown without the stainless shroud installed.**

academic year<sup>38</sup>. The system uses an H2W SR linear motor consisting of a “U” shaped magnetic track and a “T” shaped coil. The coil was mounted beneath a platform/stage riding on a ball-bearing supported rail. The H2W motor has a position range of 36 cm and includes an optical encoder with a resolution of 5  $\mu\text{m}$ . The motor stage is capable of moving at velocities up to 6 m/s with a maximum acceleration of 12 g.

The H2W motor was mounted to an aluminum table, and the entire system was surrounded by a stainless steel shroud. A small hole placed at one end of the shroud (1 cm diameter) was used to allow probe passage during testing. The system is shown in Figure 4 without the stainless steel shroud installed. The linear motor was driven by an ELMO Harmonica digital servo drive controller, that was custom programmed through the use of ELMO-Basic. An interface between the driver and a computer-based data acquisition and control system was achieved via RS-232 and LabVIEW.

Since the system experiences large accelerations and high speeds of travel, it was important to ensure the Langmuir probe did not exhibit large vibrations, specifically perpendicular to its travel, which would decrease positional accuracy. Both model and experimental vibration results were obtained revealing the vibration magnitude at the tip of the probe during measurement to be  $<10^{-3}$  mm; small enough to be ignored. A brief description of the vibration analysis used to determine this number is described next.

### ***2.1.1 Natural Frequency and Vibration of the Langmuir Probe***

As stated before, the RAPID system features an optical encoder with a resolution within 5  $\mu$ m. This resolution is quite impressive and far better than what is required for quality Langmuir traces. However, vibrations of the probe tip induced perpendicular to

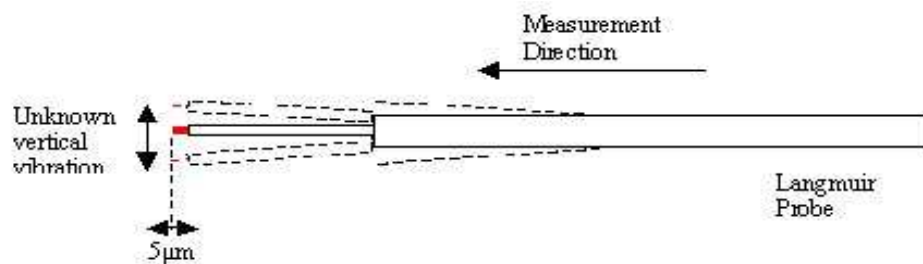


**Figure 5: Positional resolution showing unknown vertical vibration of Langmuir probe tip**

probe travel during a sweep can affect measurements. This is diagramed in Figure 5. If the vibration amplitude were large, probe measurements could become inaccurate and, as a worse case scenario, the probe could whip into the cathode or the stainless steel shroud during a sweep, which would result in the destruction of the probe. To determine the magnitude of probe perpendicular vibration a series of tests and calculations were conducted<sup>39, 40, 41, 42</sup>.

During the time of this vibration analysis, the linear motor used on the final RAPID system was not yet available. Instead a prototype lead-screw stage was used. It is noted that this will not exactly model the linear stage. However, lead-screw systems in general are far less smooth than linear motors, and a worst-case result is expected. Also, when the linear motor did become available, tests were conducted to verify that vibration amplitudes were still small. Accelerometers were placed at key locations on the both the stage, a mock probe shaft, and a reference point. An infrared ranger was also used to measure position during travel. Probe traveling velocities of 0.1 m/s, 0.5 m/s, and 1 m/s were tested with varying acceleration profiles. Also, “bump” tests confirmed that

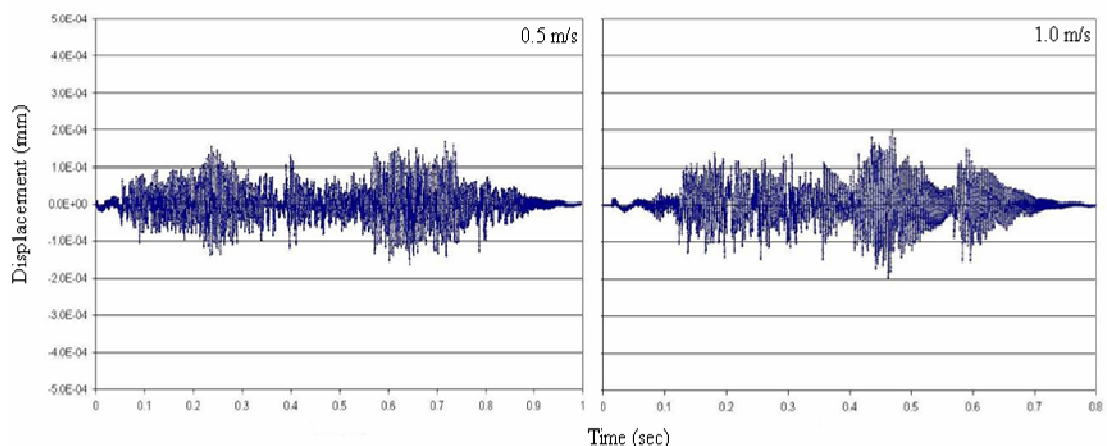


**Figure 6: Displacement vs. time at 0.5 and 1.0 m/s.**

calculated natural frequencies were within 10% of measured natural frequencies. Data revealed that the probe shaft vibrated at a frequency of 250 Hz throughout its travel. The natural frequency of the mock probe shaft was measured to be 20 Hz, based on a bump test, leaving an order of magnitude between the traveling frequency and the natural frequency. The large difference in natural and forced frequencies ensures that excessive amplification of the traveling frequency driven oscillations will not occur. Accelerometer results at 0.5 m/s and 1.0 m/s are shown in Figure 6. It was observed that little variation in traveling frequency or vibration amplitude was observed at different speeds.

It is important to note that the above presented data was constructed using a mock probe shaft of steel. This was an unavoidable requirement of the accelerometer measurement system. However, as measured values of amplitude and frequency matched those predicted in calculation for the steel rod, it is believed that calculated values for the ceramic shaft of the actual Langmuir probe will at least be in range of actual ones. These calculations suggest that the perpendicular vibration of Langmuir probes during travel will be much less than 0.1 mm in amplitude and error in position in the perpendicular direction will be assumed to be no greater than 0.25 mm (i.e., the maximum shaft deflection due to weight of the ceramic rod).

## 2.2 Langmuir Probe Design

Simply the presence of an object, say the Langmuir probe, within a plasma has a perturbing effect on the plasma. This is especially true if the object is within a region of plasma that possesses large property gradients. A secondary but equally important perturbation effect specific to Langmuir probes is the probe electrical biasing scheme. To acquire what is called an I-V characteristic curve, explained in section 3.1, the potential of the probe must be changed through a range of about  $\pm 30\text{V}$  for a typical plasma. The plasma in the close vicinity of the probe is affected throughout this range, especially when excessively positive voltage biases cause large electron currents to flow to the probe. The plasma perturbations caused by excessive positive biases, for example, are both expected and more or less unavoidable. However, Staack et al. have found that secondary electron emission from the insulated ceramic tubes surrounding and supporting most Langmuir probes can also induce significant plasma perturbations<sup>43</sup>. These

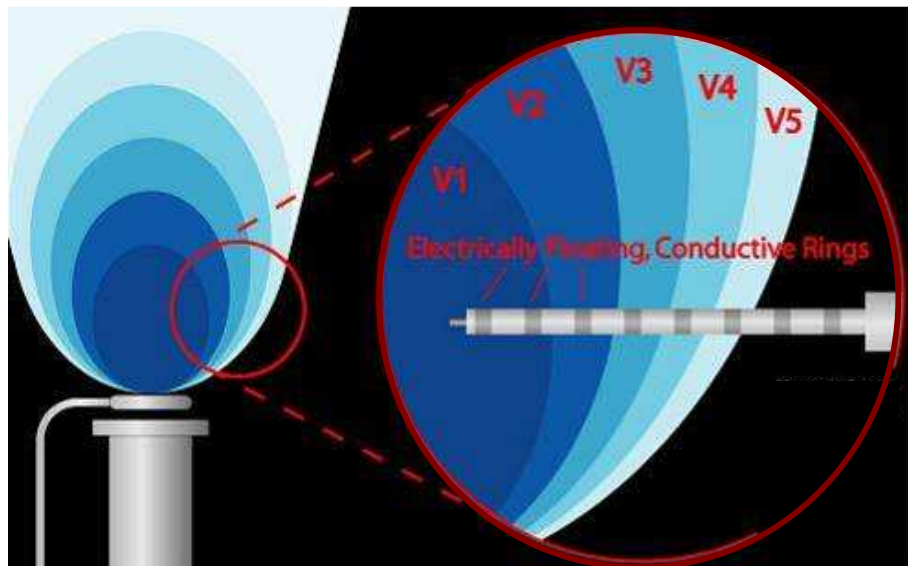


**Figure 7: Tungsten segmented Langmuir probe immersed in plasma of varying plasma potentials as it travels through hollow cathode plume.**

perturbations were noted to be large enough to change plasma parameters by the order of their steady state values. In order to find a solution to this problem, Staack et al. researched several low secondary electron emissive materials to shield the ceramic tubing from the plasma. Their research showed that a ceramic tube coated with a low secondary electron emission material (tungsten) did indeed reduce perturbations. As a further step, to eliminate shorting of the plasma through this new conductive shielding, the coating was segmented in small sections. If a plasma contains large potential gradients, this segmenting is believed to allow each section to acquire a potential different than those around it. Thus isolating each section, grading the potential, and lowering the perturbation of the local plasma potential that would be caused by an un-segmented probe shaft. Figure 7 contains an illustration of this idea.

Several different techniques were evaluated to add segmented rings to a Langmuir probe support shaft,<sup>44,45, 46</sup>. The techniques utilized herein are explained in section 2.2.1.

### ***2.2.1 Segmented Langmuir Probe Design and Construction***

Mastering a process in which Langmuir probes can be segmented properly took several iterations. The general setup for segmenting is shown in Figure 8. Originally a 1.27 mm diameter ceramic tube was rotated about its axis while being placed in the path of a vapor stream of stainless steel created by ion bombardment (sputtering). The deposited material created an even coating over the surface of the ceramic. The tubes were then taken out of vacuum and placed on a lathe in an attempt to remove the coating in desired locations. This attempt to segment the probes proved ineffective and several ceramic probe shafts were broken.

A second process was devised in which the segments were coated onto the ceramic directly. This was done using a mask with a series of holes cut through it (0.6-mm in diameter, 1.2-mm apart), which was placed in the path of the sputtered particles, only allowing particles to pass to the spinning ceramic through the holes. The mask assembly is shown in Figure 9.

Two different masking plates were tested. Figure 10 shows both the differences between each plate and the resulting segmented probes. It was found that mask A resulted in too small of separation between segments, allowing some conduction between each. The thicker mask B let fewer particles reach the probe and resulted in completely isolated segments. Resistance measured on each segment was under  $10 \Omega$ . This was felt to be adequate and several probes were made using mask B.

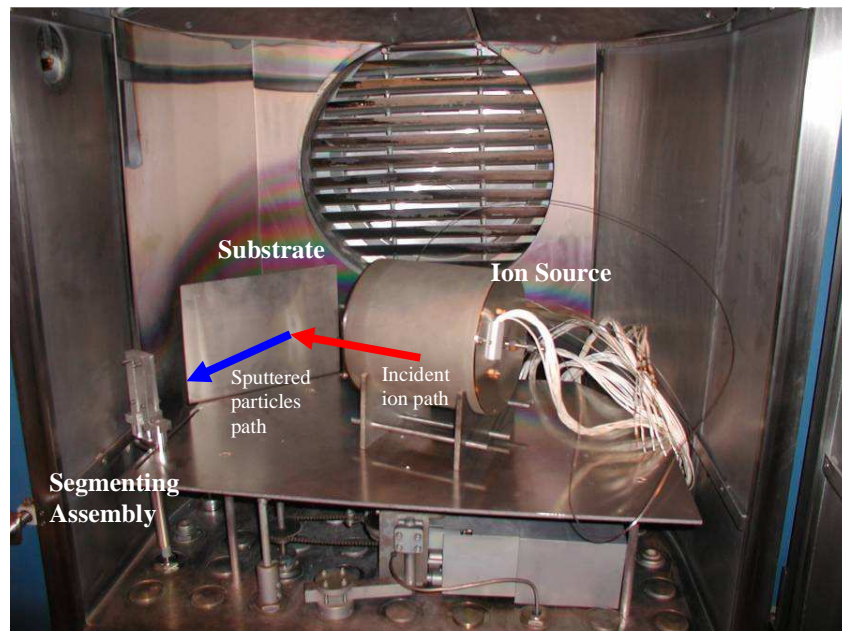


**Figure 8: Setup for segmentation of Langmuir probes**

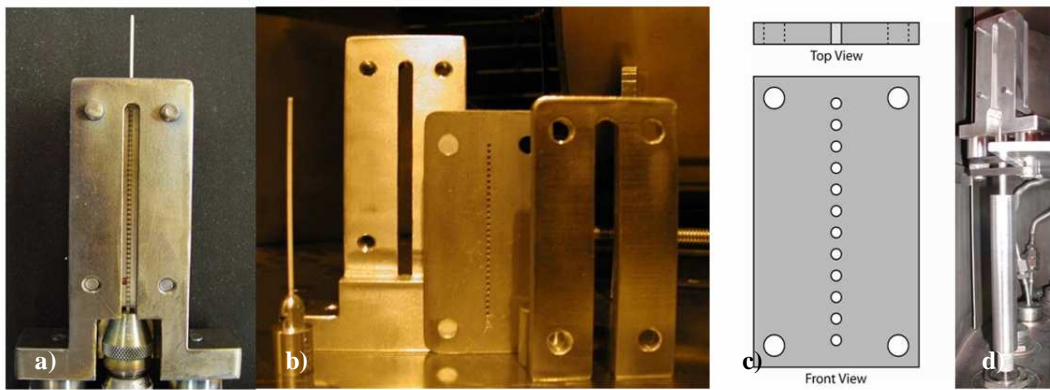


**Figure 9: Masking plate assembly assembled (a), disassembled (b), plate design (c), mounted to motor assembly (d)**

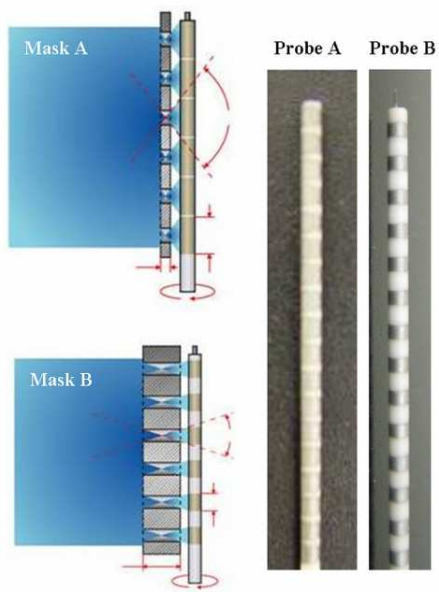


**Figure 10: Results between different masking plates**

### 2.2.1.1 Probe Assembly

A diagram of the final assembly of the Langmuir probe is shown in Figure 11.

Dimensions and materials of the components used in the final assembly are listed below:

- approximately 10 cm long, 0.127 mm diameter tungsten wire
- approximately 7 cm section of stainless-segmented 1.27 mm O.D. x 0.51 mm I.D. 99.8% alumina-oxide tubing
- 40 cm section of 2.39 mm O.D. x 1.60 mm I.D. 99.8% alumina-oxide tubing
- approximately 40 cm of 0.81 mm O.D. x 0.51 mm I.D. Nickel capillary tubing
- ceramic paste
- 25 cm of Teflon coated coax cable
- RF coaxial connector
- Vacuum rated heat shrink tubing

All of the components were cut to size and the ends of the alumina tubing were sanded such that any sharp edges were removed. About 2.5 cm of tungsten probe material was inserted into the nickel capillary tubing and the tubing was crimped around the tungsten

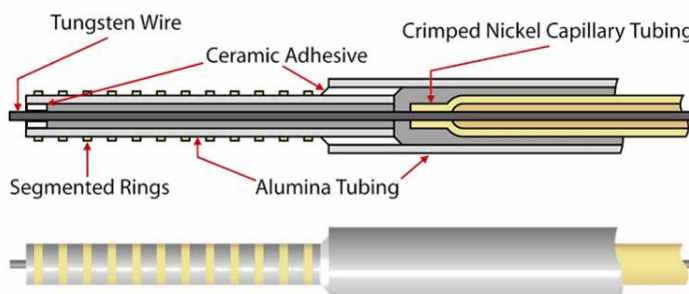


**Figure 11: Final Langmuir probe assembly**



**Figure 12: Completed Langmuir probes of different types: A segmented Langmuir probe (Top), a standard Langmuir probe (Mid), and a double Langmuir probe (Bottom).**

wire. The tungsten wire was then inserted into the 1.27 mm alumina tubing. Ceramic paste was applied to the last 3 cm of the 1.27 mm alumina tubing and then the sub-assembly (small alumina tubing, tungsten wire, and nickel capillary tubing) was inserted into the larger 2.39 mm diameter alumina tubing. After inserting the small alumina tubing 2.5 cm into the larger alumina tubing, the excess ceramic paste was wiped off and the assembly was allowed to cure in air overnight, or if it was needed sooner than that, it was cured in an oven at 200° C for about an hour. After curing the ceramic paste, the electrical connections to the nickel capillary tubing were completed. A small length (~3 cm) of the coax cable was stripped and the conductor was crimped to the nickel capillary tubing with a nickel crimp ring. The wire assembly was adjusted in or out of the alumina tubing until a 1.27 mm long section of the tungsten wire protruded from the tip of the small alumina tubing, resulting in a 0.127 mm diameter x 1.27 mm long cylindrical Langmuir probe. An RF coax connector was attached to the free end of the shielded coax cable. A photo of several finished probes is shown in Figure 12.

## 2.2.2 Probe Thermal Analysis

The electrostatic probes utilized in this study are comprised of small-diameter, short tungsten wires as described above. This probe collects current from a plasma as a function of the voltage applied to it (as explained further in section 3.1.1). With the small dimensions of the probe, current and heating effects must be controlled to prevent probe destruction and data corruption. For tungsten, the melting temperature is about 3300K<sup>47</sup>. To avoid destruction of the probe, one must assure that the probe not exceed this temperature, however, as the temperature of the probe increases, the probe will begin to thermionically emit electrons under some bias conditions. Thermionic emission is described according to the modified Richardson-Dushman equation for field-enhanced (Schottky effect) thermionic emission<sup>19,48,49,50,51</sup>:

$$J = A_{RD} T^2 e^{\frac{-q(\phi_w)}{kT}} e^{\frac{4.4}{T} \sqrt{\frac{E_s}{d_{eff}}}}$$

2.1

Here  $E_s$  is the electric field strength surrounding of the probe and  $\phi_w$  is the work function of the probe material. At high probe temperatures and negative probe biases, the thermionic electron emission current can be large and will perturb the Langmuir probe data. For this reason it is important to assure the tungsten probe stay as cool as possible. One method of controlling the probe temperatures, and the one utilized by the RAPID system, is to move the probe through the most intense plasma regions very quickly. This will minimize the time the probe tip is exposed to large heating loads. In addition, a specific biasing scheme has been adopted that reduces the time the probe is in the electron saturation region (positive probe biases) where the probe current is relatively

large (see section 3.1.1). The rest of section 2.2.2 is dedicated to determining the allowable speed and voltage limits on the probe so that the probe temperature does not exceed a given temperature limit.

### 2.2.2.1 Probe Heating Model

A one-dimensional thermal model was used to determine temperature and time constraints for the heating and cooling of the Langmuir probe subjected to immersion within intense plasma<sup>52,53,54,55,56,57,58</sup>. Factors included in the heating effects are absorption of radiation, electron collection, and ohmic heating. Cooling effects included conduction and emission of radiant energy.

Assumptions and known parameters include the chamber wall temperature, initial probe temperature, chamber wall emissivity, plasma plume specific geometry, probe distance from the hollow cathode, constant specific heat, and constant probe velocity. Additional assumptions made to allow for model simplification are utilizing a lumped capacitance approach for the exposed probe tip and by assuming that heating effects are distributed evenly across the entire exposed surface area of the probe.

#### Radiation Heating

One source of radiation heat transfer to the probe is from the hollow cathode itself. From experiment, the hollow cathode temperature can be as high as 1300°C<sup>59</sup>. A first law analysis of energy entering and leaving the probe yields the following relationship, (see Figure 13):

$$\dot{E}_{in} + \dot{E}_g - \dot{E}_{out} = \dot{E}_{st}$$

In Eq. 2.2,  $\dot{E}_{in}$  and  $\dot{E}_{out}$  are the rates of thermal energy that enter and leave the probe surface, respectively. The term,  $\dot{E}_g$ , in Eq. 2.2 is the rate of thermal energy that is generated within the probe and  $\dot{E}_{st}$  is the rate at which stored thermal energy increases within the probe. Also shown in Figure 13 is a resistive thermal network developed to represent the problem setup. View factors from the probe to the vacuum chamber walls and the hollow cathode to the vacuum chamber walls are assumed to be unity. The view

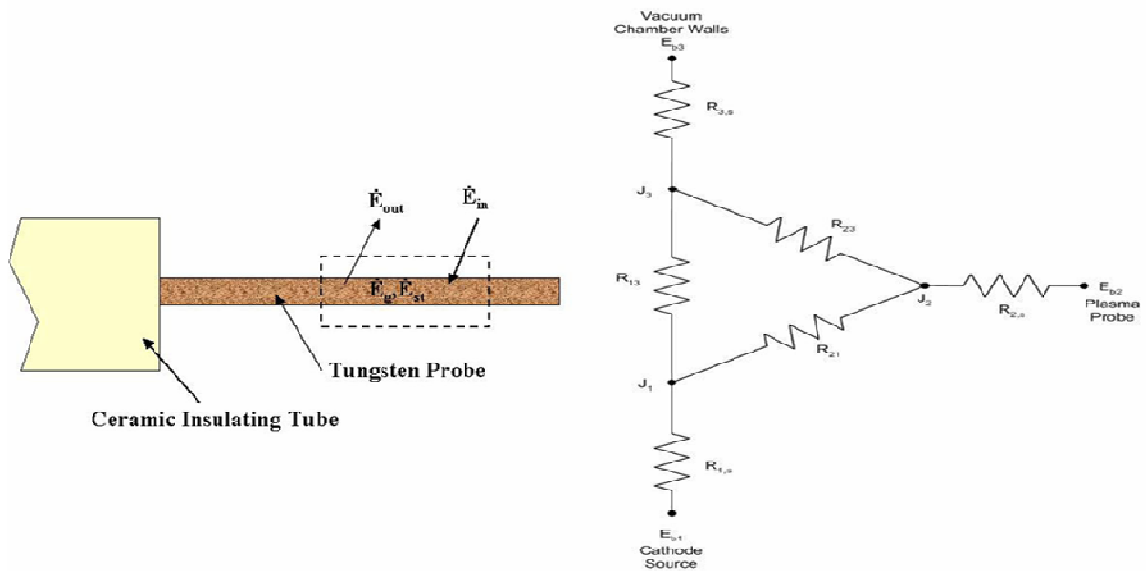


**Figure 13: Thermal analysis of diagnostic probe and resistive thermal network representation**

factor from the hollow cathode to the probe was modeled after a differential planar element (section on the surface of the probe), 0.5 cm away from and perpendicular to a circular disk (the hollow cathode tip)<sup>60</sup>. The distance of the probe from the axial location of the hollow cathode is a function of time since the probe is moving.

After determining the view factors; the thermal network resistances, emissive power, and radiosities were calculated next:

$$R_j = \frac{1 - \varepsilon_j}{\varepsilon_j A_j}$$

2.3

$$R_{ab} = \frac{1}{F_{ab} A_j}$$

2.4

$$E_j = \sigma T_j^4$$

2.5

Where  $j$  indicates the representative location in the resistive thermal network (i.e. 1, 2, 3, etc.). In the resistance and emissive power equations,  $\varepsilon$  is the emissivity of a material,  $A$  and  $T$  are the surface area and temperature of the same material, respectively. The term  $\sigma$  in Eq. 2.5 is Stefan-Boltzmann's constant and  $F$  is the view factor between two components. The system of equations used to determine the radiosities are listed below:

$$\frac{E_{b3} - J_3}{R_3} = \frac{J_3 - J_2}{R_{23}} + \frac{J_3 - J_1}{R_{13}}$$

2.6

$$\frac{E_{b2} - J_2}{R_2} = \frac{J_2 - J_3}{R_{23}} + \frac{J_2 - J_1}{R_{21}}$$

2.7

$$\frac{E_{b1} - J_1}{R_1} = \frac{J_1 - J_2}{R_{21}} + \frac{J_1 - J_3}{R_{13}}$$

2.8

After solving for radiosity  $J_2$ , heat flow from the probe was determined using Equation 2.9.

$$\dot{Q}_{rad} = \frac{J_2 - E_{b2}}{R_2}$$

2.9

Using average plasma parameters during this study, the heat addition due to radiation was calculated to be essentially constant at approximately 98 mW over regions of interest nearby the hollow cathode.

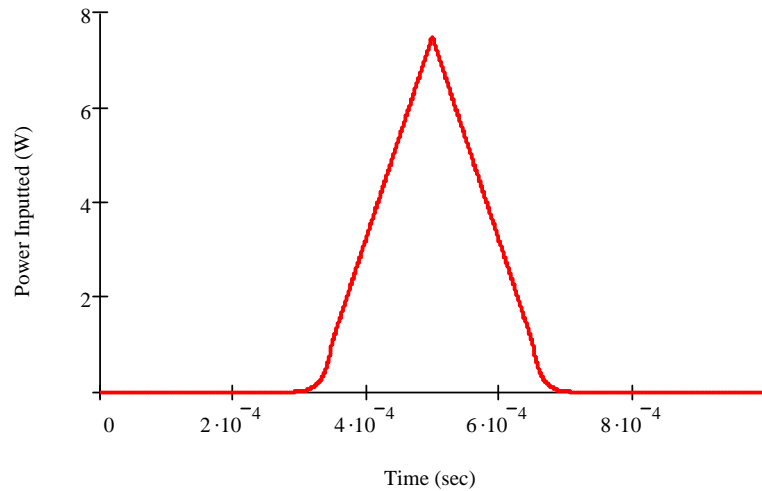


**Figure 14: Power input to the probe as a function of time due to electron collection**

### Electron Collection Heating

Due to the biasing scheme selected, the probe is periodically heated from plasma electrons collected during times when the probe is biased positive of the local plasma potential. Some heat is also provided by ions that flow to the probe, but this heat addition rate is small compared to the electron heating rate. Figure 14 is the assumed power input to the probe as a function of time due to electron collection.

For heating due to electron collection, the plasma potential was assumed to be 20 V, the electron temperature was 2.5 eV, and a peak electron density of  $10^{13} \text{ cm}^{-3}$ . With these parameters, the maximum plasma current is 214 mA, and plasma power is at a maximum of just over 7.506 W. The maximum plasma current and power to the probe changed linearly with density, which, in turn changes by orders of magnitude over regions nearby the cathode.

Collected electron current is calculated based upon the probe biasing voltage condition, which is a function of time. If the electrons are assumed to be Maxwellian and the biasing voltage is less than the plasma potential, equation 2.10 was used. Otherwise, when the probe biasing voltage is above the plasma potential, equation 2.11 was used.

For  $V_B(t) < V_p$ :

$$I_{probe}(t) = \frac{1}{4} q n_e v_e A_{probe} \exp\left(\frac{-(q \cdot |V_p - V_B(t)|)}{k \cdot T_e}\right)$$

2.10

For  $V_B(t) \geq V_p$ :

$$I_{probe} = \frac{1}{4} q n_e v_e A_{probe}$$

2.11

$V(t)$  is the probe biasing voltage,  $V_p$  is the plasma potential,  $A_{probe}$  is the exposed surface area of the probe, and  $n_e$  is the electron density. The electron velocity is defined as the average thermal velocity according to:

$$v_e = \sqrt{\frac{8kT_e}{\pi m_e}}$$

2.12

Where  $q$  is the electron charge and  $m_e$  is the mass of an electron.

Similar to the conditions for calculating current, equations for power deposition due to electron collection are also dependent upon the probe's biasing voltage<sup>61</sup>.

For  $V_B(t) < V_p$ :

$$\dot{P}_{probe}(t) = I_{probe}(t) \left( 2 \frac{kT_e}{q} \right)$$

2.13

For  $V_B(t) \geq V_p$ :

$$\dot{P}_{probe}(t) = I_{probe} \left[ 2 \frac{kT_e}{q} + (V_B(t) - V_p) \right]$$

2.14

Electron density, which was assumed to range between  $10^9$  to  $10^{13}$   $\text{cm}^{-3}$ , has a linear effect upon the current and hence the effective power. As mentioned above, the plasma density,  $n_e$ , changes several orders of magnitude through the plasma region nearby the cathode.

### Ohmic Heating

The probe is also affected by heating due to current flowing through the probe. The resistance of tungsten changes with temperature and was taken into account in the model. The equation for adding the effect of Ohmic heating to the probe is based upon Ohm's Law:

$$\dot{W}(t, T) = [I_{Probe}(t)]^2 \cdot R(T)$$

2.15

In Equation 2.15,  $I_{Probe}$  is the current due to the electron collection through the probe (as in Equations 2.10 and 2.11) and  $R(T)$  is the temperature dependent resistance of tungsten.

When evaluating the effects of different sources of heat addition, Ohmic heating was the least significant for our operating conditions. Comparing two heating models, one including this effect and another without, the temperature difference was only about 1 K, at the highest electron densities, and we can ignore this effect as a contributor to heat addition.

### **Re-radiation Cooling**

When the probe is removed from the dense plasma regions nearby the hollow cathode, it will cool down via radiation and conduction processes. These heat removal processes are also active when the probe is inserted into dense plasma. Radiative cooling can be modeled much like the previous radiative heating model. Following the same idea as Equation 2.2 another thermal network can be created. Using this network the cooling rate can be determined as:

$$\dot{Q} = \frac{\sigma \cdot (T_{p,i-1}^4 - T_{\infty}^4)}{R_{tot}}$$

2.16

Where  $R_{tot}$  is equal to:

$$R_{tot} = R_{Probe} + R_{ViewFactor} + R_{Walls}$$

2.17

It is noted again that this effect not only subtracts from the heat addition during probe travel, it also is the main contributor to probe cooling once a measurement has been taken and the probe returns to a position outside of an intense plasma region.

### **Conductive Cooling**

Along with re-radiation to its surroundings, the probe will experience a cooling effect due the conduction of heat through signal lines and the ceramic probe shaft. These

effects are believed to be small due to the small size of the conduction components, but nonetheless were incorporated into the final model to acquire a more accurate result. The cooling due to conduction can be defined as:

$$\dot{Q} = \frac{1}{R_{tot}} (T_{p,i} - T_{p,i-1})$$

**2.18**

In Equation 2.18,  $R_{tot}$  represents the sum of the conduction thermal resistive network.

Combining this with radiative cooling it was determined that 30 seconds was required before the probe was cool enough to begin another sweep. The motion control program was designed to assure dwell times between measurements greater than 30 seconds.

### **Combined Governing Equation**

By combining the equations for probe heating and cooling, our model includes the effects of radiation, re-radiation, electron collection, conduction, and ohmic heating. The final thermal network is illustrated in Figure 15.

Also, the complete governing equation (in discretized form) for calculating probe temperature as a function of time while immersed in plasma is:

$$T_{p,i}(t, T) = \frac{(\dot{Q}_{rad}(t) + \dot{P}_{probe}(t) + \dot{W}(t, T) - \dot{Q}_{re-rad}(t, T) - \dot{Q}_{cond}(T)) \cdot \Delta t}{m \cdot c_p} + T_{i-1}$$

**2.19**

for  $i = 1, 2, 3, \dots, n$

In Equation 2.19,  $m$  represents the probe mass,  $c_p$  is the specific heat of the probe material, and  $\Delta t$  is an incremental time step.  $T_{p,i}$  is the predicted probe temperature after  $n$  steps,  $T_{p,i-1}$  is the probe temperature at the previous step, and  $n$  is the step count integer.

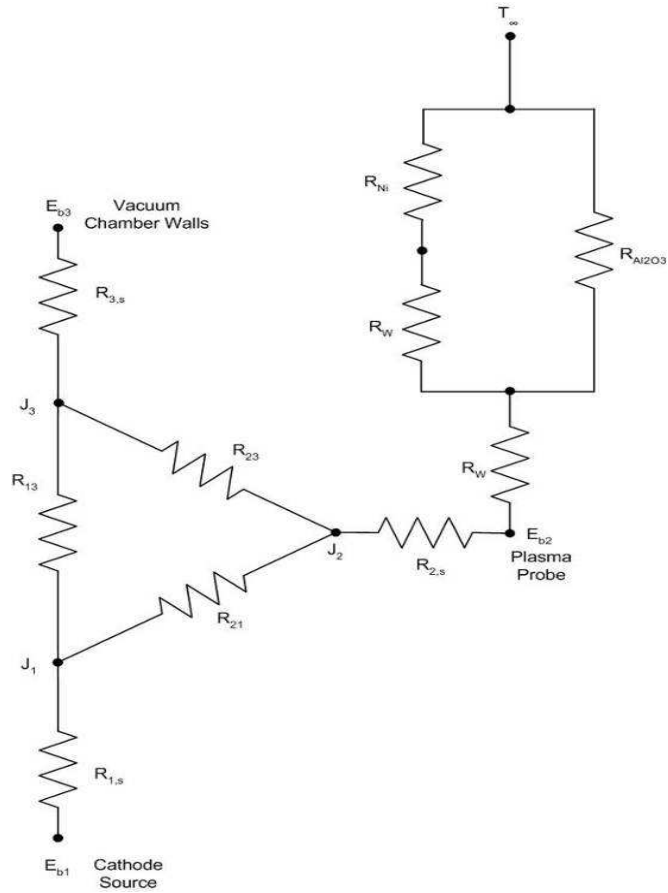


**Figure 15: Combined probe thermal network**

Results from the thermal model were encouraging. With the biasing waveform set to 1000 Hz at a duty cycle of 50%, the probe traveling through a 4 cm long plasma of  $T_e = 2.5$  eV,  $V_p = 20$  V, and  $n_e = 10^{12}$  cm<sup>-3</sup> at 0.5 m/s will reach a final predicted temperature of 489K. If, however, the plasma density rises to  $10^{13}$  cm<sup>-3</sup>, then the predicted probe temperature increases to 2034K, well into a region where thermionic emission becomes large. This prediction represents a worst case scenario by assuming a full 4 cm extent of the plasma column is at  $10^{13}$  cm<sup>-3</sup>, which is not the case. Generally, in plasmas measured with densities above  $10^{13}$  cm<sup>-3</sup>, the most intense region only exists for about 0.5 cm nearby the cathode orifice region. Assuming a Gaussian density distribution through a 4 cm distance, where plasma density ranges from  $10^9$  cm<sup>-3</sup> to  $10^{13}$  cm<sup>-3</sup>, the final predicted

temperature dropped to 832K. A plot of this temperature profile prediction is shown in Figure 16 where it is evident that the final temperature is not the maximum temperature. Instead, the maximum temperature of 874K occurs at a position just past the center line of the cathode (about 1 cm past centerline). This offset occurs because after the probe passes the centerline and the plasma density begins to drop rapidly, the rate of cooling, mainly radiation, eventually overcomes the rate of heating from electron collection.

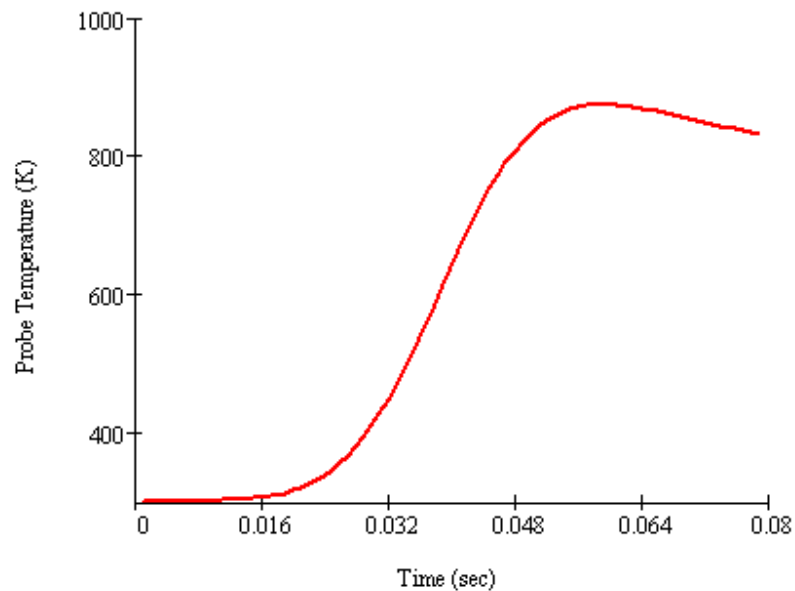


**Figure 16: Probe temperature versus time for a Gaussian density distribution**

Experiments using a type-K thermal couple as a Langmuir probe confirmed the above results to be correct.

## CHAPTER 3: PROBE THEORY AND ANALYSIS

### 3.1 Single Langmuir Probe

A Langmuir probe is a relatively simple device for use in determining plasma properties. At the most basic level, it consists of a small electrode immersed in plasma. Current collected by the electrode consists of ions and electrons that are attracted/repelled

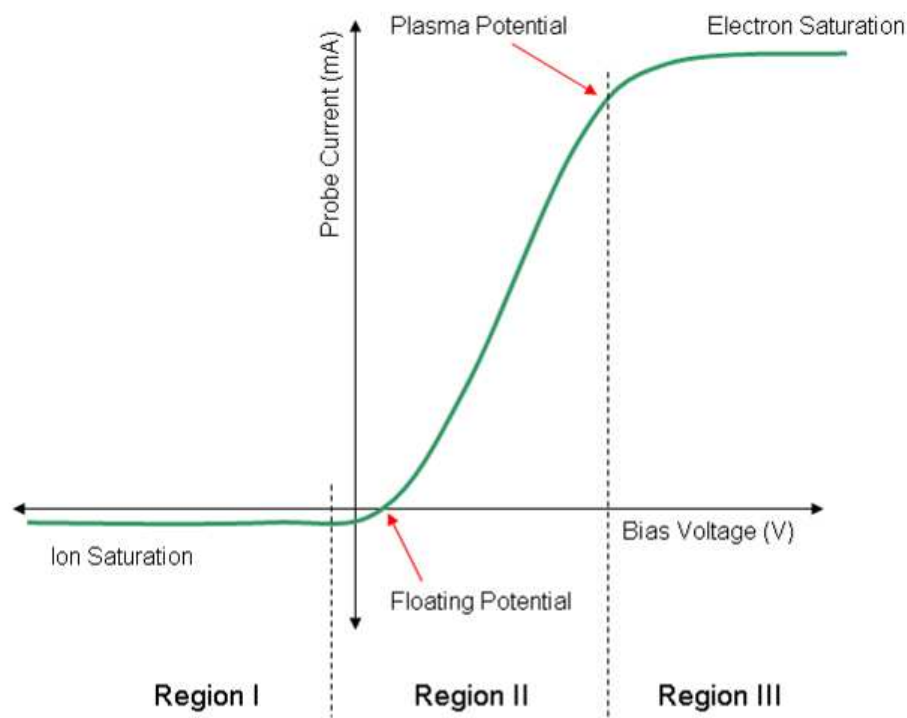


**Figure 17: Idealized I-V curve showing important parameters and regions.**

to/from it as a function of electrode potential. The plot of net current versus probe potential is often referred to as an I-V curve<sup>51, 62, 63</sup>. Figure 17 represents an idealized Langmuir I-V curve. Generally, I-V curves consist of three primary regions. The first of which, shown on the left of Figure 17, is the ion saturation region (greatly expanded in the y-axis scale to show more detail). In this region the probe potential is negative enough such that all electrons are repelled and only ions are collected according to the

Child-Langmuir law<sup>64, 65</sup>. The ion saturation current, which has been amplified in Figure 17 for illustration purposes, can be used to calculate ion density when the Bohm condition is applied to determine the ion arrival flux<sup>3, 5, 64, 65</sup>. As the probe potential is increased, one moves into Region II. This region, shown in the middle of Figure 17, is referred to as the electron retardation region and consists of the potential range where both electrons and ions are collected. In this region ions are attracted to the probe because it is still biased negative of plasma potential as it is in the ion saturation regions. Also, while electrons are being repelled, some high energy electrons can still make it to the probe. In the electron retardation region there are two points of notable significance, floating potential and plasma potential. The point where zero current is measured by the probe is called the floating potential. This is the voltage at which the ion current flowing to the probe exactly equals the electron current collected, and the net current to the probe is zero. To the right of the floating potential the curve tends to grow steeply for most plasmas. If the electron population can be described as Maxwellian, the current collected by the probe can be modeled by Equations 3.1 and 3.2.

$$I_e(V_B) = I_{sat,e} e^{\frac{-(V_p - V_B)}{T_e}}$$

3.1

$$I_{sat,e} = \frac{1}{4} q n_e v_e A_{probe} = q n_e A_{probe} \sqrt{\frac{q T_e}{2 \pi m_e}}$$

3.2

As the probe potential is increased, the I-V curve reaches a point referred to as plasma potential. This is the point where no further ions are collected and only electron current is

present. This is also the beginning point for region three. In region three, the probe potential is above plasma potential, and the electron current saturates at a current predicted by Equation 3.2. In the ideal case the transition is sharp between the electron retardation and electron saturation regions, thus making the determination of plasma potential straightforward. With cylindrical probes in actual plasma, the saturation current continues to grow slowly as the probe voltage is increased due to sheath growth effects. Other effects cause the electron retardation and saturation transition region (i.e., the I-V curve between region II and III) to be rounded. This area of an I-V curve is referred to as the knee. The presence of a highly rounded knee makes calculating plasma parameters increasingly difficult and suggests the possibility of plasma potential, plasma density, and/or electron temperature oscillations.

When using a Langmuir probe, it is important to ensure that the size of the probe is appropriate for the plasma being characterized. In general, one needs to be sure that the mean free path of both electrons and ions is far greater than the radius of the probe. This assures a collisionless sheath is present surrounding the probe<sup>3, 51, 62</sup>. The mean free path, given by Equation 3.3, for both electrons and ions is on the order of a meter or so for the plasmas studied herein. With a probe diameter of less than a millimeter,  $R_p \ll \lambda_{mp}$ , a collisionless sheath can be assumed.

$$\lambda_{mp} = \frac{1}{N\sigma}$$

### 3.3

Another factor that comes into play is the sheath thickness surrounding the probe<sup>62</sup>. As the probe is immersed in regions with different plasma density, the volume from which charged particles are collected will vary. If the charged particle collection sheath

is small relative to the probe radius ( $R_p$ ), the probe is said to be operated in the thin-sheath regime, and our above equations hold true. As the sheath size approaches the probe radius, probe geometry begins to affect the collected particles greatly and corrections must be made using either low temperature (Allen-Boyd-Reynolds) or finite temperature (orbital-limited motion (OLM)) assumptions. The thickness of the sheath around any conducting surface is assumed to be on the order of the Debye length ( $\lambda_D$ ), given by Equation 3.4. In general if the probe radius is greater than 10 times  $\lambda_D$ , a thin sheath can be assumed<sup>33</sup>.

$$\lambda_D = \sqrt{\frac{\epsilon_o k T_e}{n_e q^2}} = 7430 \sqrt{\frac{T_e (eV)}{n_e (m^{-3})}}$$

**3.4**

For typical plasmas measured in our study  $\lambda_D$  ranged from 0.01 mm to 0.0005 mm with rare excursions to 0.1 mm. A Debye length of 0.01 mm, is  $\sim 1/10^{\text{th}}$   $R_p$  ( $T_e = 2\text{eV}$ ,  $n_e = 10^{11}\text{cm}^{-3}$ ) and well within the thin-sheath regime. In fact all measurements taken on cathode centerline were well within the thin-sheath regime with only a few outside of this regime at low flow rates and low discharge current conditions. For this reason and the fact that our I-V curves did not exhibit a nature which would lead us to believe thick-sheath effects were present<sup>51</sup>, thin-sheath analysis was assumed throughout.

One last consideration that can have an affect, predominately in the electron collection region, is that of an applied magnetic field. This field will confine electrons to travel mostly in the direction of the magnetic field lines and suppress diffusion across them, creating electron flux tubes along the magnetic field that can be depleted faster (via parallel field transport) than they are re-supplied (via perpendicular field transport). This can cause errors in the calculation of both electron saturation current and electron

temperature (from the anisotropy induced in the EEDF<sup>66</sup>). The electron confinement to these flux tubes is associated with the electron gyro radius defined in Equation 3.5.

$$r_{i,e} = \frac{v_{i,e} m_{i,e}}{qB}$$

3.5

For cylindrical probes the influence of magnetic field is minimized when the probe axis is oriented perpendicular to the magnetic field, thus increasing the number of flux tubes that end on the probe surface. This is the situation present in our case. It has also been found that for probes of  $R_p / r_e < 2$  the reduction in electron saturation current due to an applied, perpendicular magnetic field is less than general errors assumed present in calculating  $I_e$ . Meaning, the smaller the probe is compared to the electron gyro radius, the closer calculated values for  $n_e$  will be to actual ones. Also, the ratio of magnetic field to chamber pressure,  $B/P_o$ , can be used as a quantitative measure for the EEDF anisotropy. For values of  $B/P_o \leq 3 \times 10^6$  G/Torr, EEDF anisotropy can be neglected<sup>33, 66</sup>. In our case the electron gyro radius is on the order of 10 times the probe radius and  $B/P_o$  is roughly  $1 \times 10^5$  to  $1 \times 10^6$  G/Torr, allowing us to neglect magnetic field effects. A very in-depth analysis of Langmuir probes of all different types and the effects of several different parameters can be found in references 51, 62, 63, and 66.

### ***3.1.1 Langmuir Probe Circuitry and Measurement Technique***

Throughout this study the Langmuir probe was traversed through plasmas with properties that varied as a function of position. In general, at the beginning of a measurement, the probe would be in a low density plasma region at large radial positions. As the probe was moved toward the cathode, it experienced an increase in plasma density

of several orders of magnitude until a maximum plasma density was reached on the cathode centerline. In order for the probe to be of use for measuring plasma parameters, a plot like that in Figure 17 must be constructed. To measure the change in properties through space, several of these curves must be constructed at small increments of distance. Traditional techniques used elsewhere apply a single voltage to the probe as it travels through the plasma. During this process, current collected by the probe is monitored as a function of position. And this process is repeated many times at different (fixed) probe biases. To obtain complete Langmuir probe traces the position sweeps performed at different probe voltages must be correlated back together by position (and probe current). Although relatively straightforward to implement, this technique can be very time consuming to acquire sufficient data. Furthermore, this technique assumes that plasma properties and positions are constant throughout the lengthy measurement period. Instead, the technique devised for the RAPID system is to directly acquire a complete set of many I-V traces during every motion sweep. Throughout the inward trajectory of the probe, a rapidly varying saw-tooth bias was applied to the probe and the resultant collected current was recorded along with the probe bias, which was then also correlated to position. One disadvantage of this technique is that I-V curves do not correspond to fixed positions, but are spread out over a small distance. For example, a 1-kHz waveform applied to a probe that is moving at 1 m/s, will have a full waveform period every 1 ms, corresponding to a distance traveled of 1 mm per waveform period. However, a Langmuir probe trace only requires the probe to have a voltage range of  $\sim 60\text{V}$ . By applying a saw-tooth waveform to the probe, this voltage range can be covered within the upswing of a single saw-tooth bias cycle. If the saw-tooth duty cycle is a small fraction

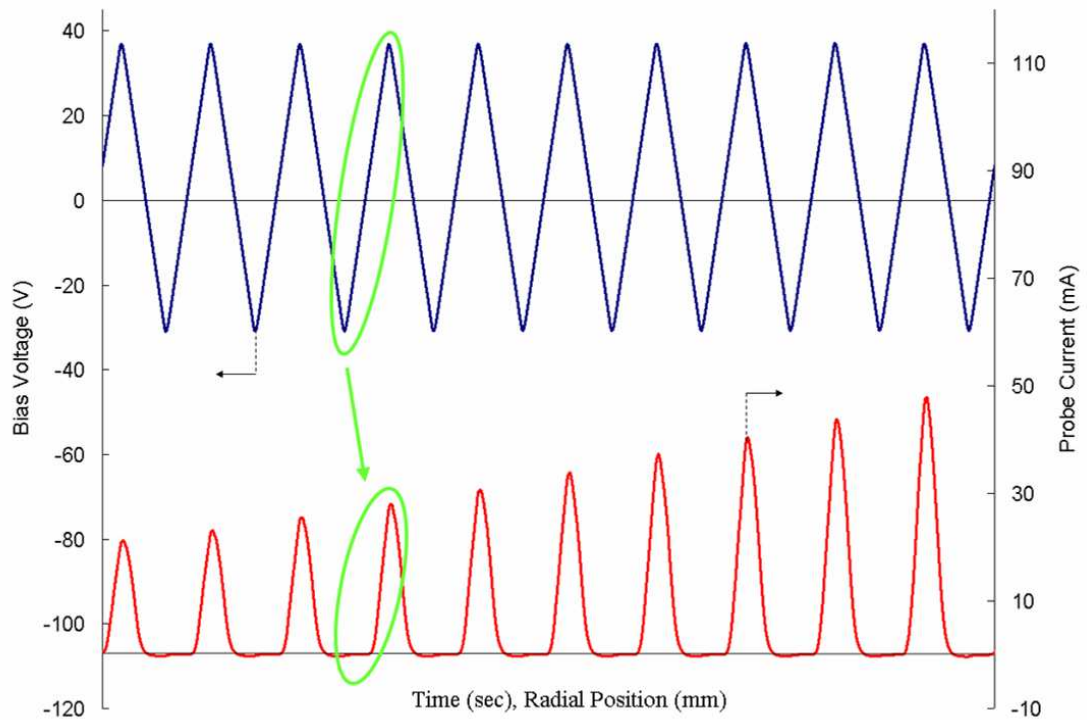


**Figure 18: Waveform biasing scheme and resulting collected current as a function of time / position** of the waveform period, sub-millimeter positional resolution is readily achievable. An actual waveform (in this case triangular) and the resulting current collected is plotted in Figure 18. Note as time / position increases the current collected also increases. This happens as the probe travels inward toward the cathode where the plasma density is highest.

Most of the results reported in this paper were acquired using a 60 V amplitude, 1-kHz triangular waveform applied to the probe, which was moved at a constant velocity of 0.5 m/s. Since the waveform is triangular, a full Langmuir sweep is present on either side of the triangle. In an attempt to limit disturbances from both capacitance, witnessed in measurement lines (which was subtracted out of final data), and the perturbation of the plasma at high positive biases, data were only taken on the upslope portion of each waveform well away from waveform slope transitions. These parameters resulted in

acquisition of an individual Langmuir trace over a spatial extent of 0.25 mm, and the distance between adjacent Langmuir probe traces was 0.5 mm. Notably, the data acquired from the optical encoder indicated that the Langmuir probe traces were being recorded over spatial distances of  $0.25 \text{ mm} \pm 0.01 \text{ mm}$ , providing positive evidence in the accuracy of the data collection scheme.

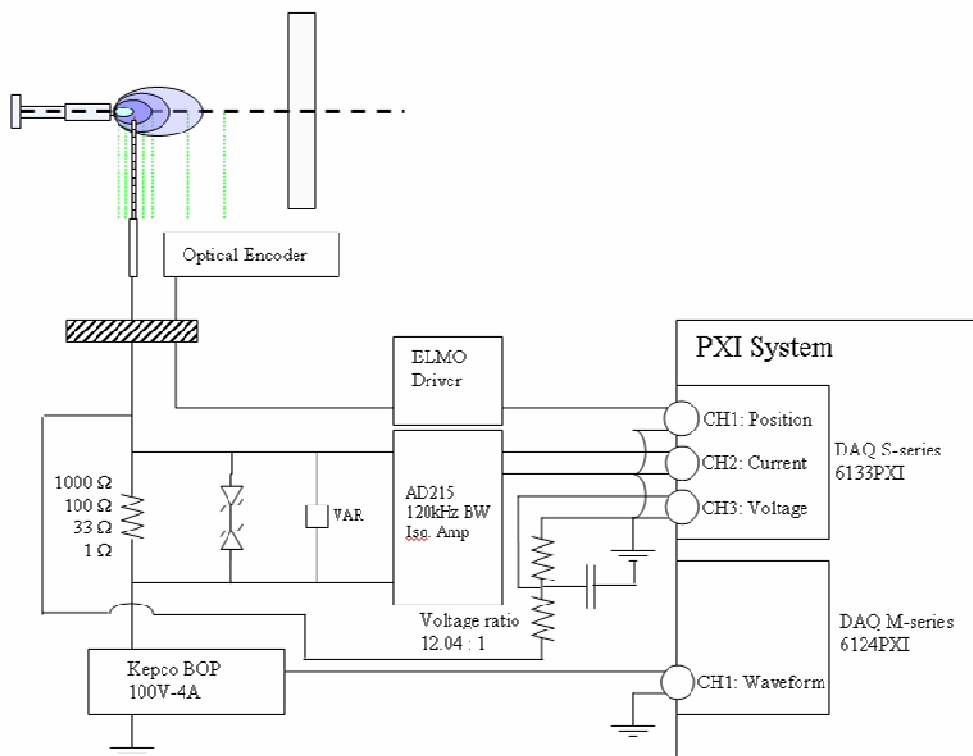


**Figure 19: Langmuir probe circuit schematic including PXI and ELMO drive systems**

As for the electrical circuitry of the RAPID system, the probe is biased by a bipolar power supply. This supply has an output range of  $\pm 100 \text{ V}$  at  $4 \text{ A}$  with a frequency response from DC to  $20 \text{ kHz}$ . The output of the supply is controlled by a signal waveform generated by the computer control system. Current to the probe is sensed by measuring the voltage across a resistor. This voltage (proportional to the probe current)

is fed through a wide-bandwidth isolation amplifier to a PXI-based data acquisition (DAQ) system, which was also used to simultaneously record the probe bias voltage and the stage position. The isolation amplifier has a unity gain bandwidth of 120 kHz. Probe bias voltage readings are first sent through a voltage divider to limit the maximum measured voltage to  $\pm 10$  V, as are readings of current output from the isolation amplifier. To avoid DAQ system damage, all signals are voltage limited by Zener diodes and varistors. An electrical schematic of the system is shown in Figure 19. Data collected by the computer system are acquired and stored through a National Instruments 6133PXI S-series DAQ card. The signal waveform used to control the power supply is produced on a National Instruments 6124PXI M-series DAQ card. The two cards have capabilities of 3 MS/s at 14-bits of resolution and 1 MS/s at 16 bits, respectively.

### ***3.1.2 Software Calculations***

In order to obtain plasma parameters such as  $n_e$ ,  $T_e$ , and  $V_p$ , it is necessary to analyze each I-V curve obtained with the Langmuir probe. On average, one single inward sweep contains roughly 175,000 data points for each position, voltage, and current. The LabView program written to control the acquisition of data divides these 175,000 points into seven separate files of 25,000 points each. This was done to optimize the speed of the analysis software, which was found to become poor at record lengths above  $\sim 25,000$  points. Position measurements are taken from the encoder and must be converted from their binary-encoded output to actual position. As mentioned above, voltage and current data are taken from one up slope region of the bias waveform, and approximately 1000 points are selected from the central region. In general, average up slope regions of the biasing waveform contain  $\sim 1300$  points.

Data are then separated into individual Langmuir traces. First the ion saturation current is subtracted out <sup>51</sup>. This is done to obtain a plot of electron current. The resulting data are then plotted on a semi-log plot,  $\ln I$  vs.  $V$ . From Equation 3.1, one can see that the slope of this curve is proportional to  $1/T_e$ . After calculating  $T_e$  from the slope of the electron retardation region, the next step is to determine the electron saturation current, which is the current where lines drawn through the electron retardation and

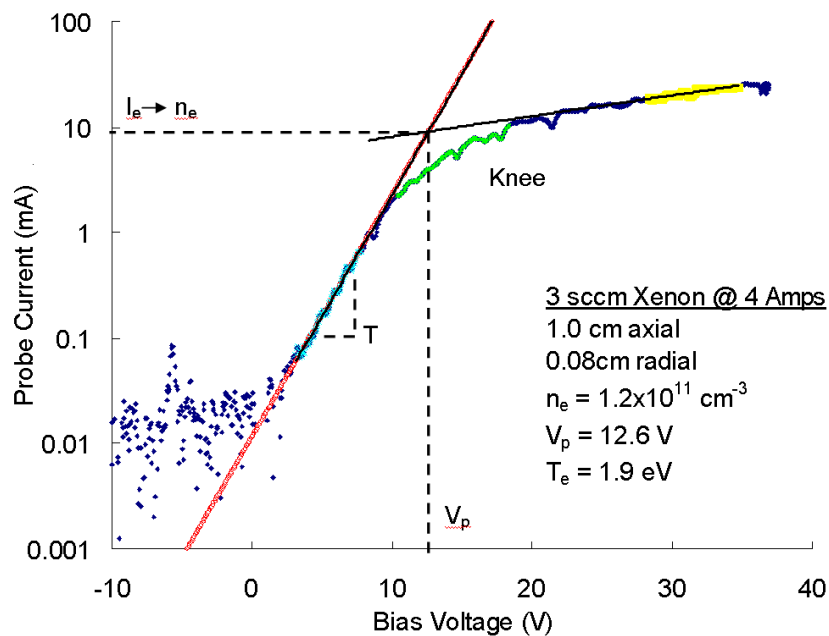


**Figure 20: Analysis of actual Langmuir trace taken at listed conditions with the simple cathode configuration**

electron saturation regions intersect. There are several more advanced methods for calculating this point as described by Chen <sup>62</sup> and many others, however, in our case adequate precision was obtained using the simple intersection method. The voltage at this intersection is defined as the plasma potential and the electron current at this intersection is used in Equation 3.2 to determine plasma density. A sample Langmuir

trace taken at a 3 sccm flow rate (Xe) and a 4 A discharge current in a position near the cathode centerline is presented in Figure 20.

Once each trace was analyzed, the program compiled all resulting data and created a summary file for each position sweep. Later, each position sweep dataset was fit to a 6<sup>th</sup> order polynomial and 2D contour plots were created.

The program written to analyze probe data was designed to be autonomous. This allowed for data analysis during periods when the hollow cathode was not being operated. A typical dataset consisting of several radial position sweeps took ~4 hours to acquire, and the analysis program took ~4 days to analyze.

## CHAPTER 4: HOLLOW CATHODE MEASUREMENT SETUP

Listed in Table 1 are the eight cathode configurations tested in this study and specifics for each condition. A distant plate anode was also tested on the simple cathode configuration but the resulting plasma was found to be too noisy to obtain meaningful data. All flow rates ranged between 1.5 and 4.5 sccm of xenon. The following sections describe the experimental apparatus for each condition along with the general setup for this study.

**Table 1: Cathode configurations studied**

<b>Configuration Name:</b>	<b>Acronym:</b>	<b>Keeper Style:</b>	<b>Anode Style:</b>	<b>Magnetic Field:</b>	<b>Current Range:</b>
Simple Cathode Ring Anode	SC	None (finger electrode used for starting)	Distant Ring	None	2A to 8A
Simple Cathode Plate Anode	SCP	None (finger electrode used for starting)	Near Plate	None	2A to 8A
Small Orifice Keeper	SK	Enclosed: 2.7mm Diameter, 1.27mm spacing	Near Plate	None	2A to 8A
Medium Orifice Keeper	MK	Enclosed: 3.8mm Diameter, 1.27mm spacing	Near Plate	None	2A to 8A
NSTAR Keeper	LK	Enclosed: 4.75mm Diameter, 1.27mm spacing	Near Plate	None	2A to 8A
NSTAR Keeper and Magnetic Field, Plate Anode	MP	Enclosed: 4.75mm Diameter, 1.27mm spacing	Near Plate	NSTAR-like Axial Magnetic Field	2A to 8A
NSTAR Keeper and Magnetic Field, Ring Anode	MR	Enclosed: 4.75mm Diameter, 1.27mm spacing	Near Ring	NSTAR-like Axial Magnetic Field	2A to 8A
NSTAR Keeper and Magnetic Field High Power	MRH	Enclosed: 4.75mm Diameter, 1.27mm spacing	Near Ring	NSTAR-like Axial Magnetic Field	10A to 20A

## 4.1 General Setup and Motion

A 6.4 mm diameter hollow cathode was utilized for all testing described in this study. The hollow cathode was equipped with an orifice plate that had a 0.64-mm diameter hole at its center. The hollow cathode was oriented 10-cm above a ball-screw stage and was mounted on an aluminum base plate. Each different anode configuration studied was also attached to this aluminum base plate. During operation and after starting, the keeper bias was set to 0 V relative to the cathode. The cathode assembly was oriented in such a way that the centerline of the cathode was in plane with and perpendicular to the center line of the RAPID system. A program was written allowing computer-monitored control of the ball screw stage over a 6.5 cm range from the RAPID system centerline. Figure 21 and

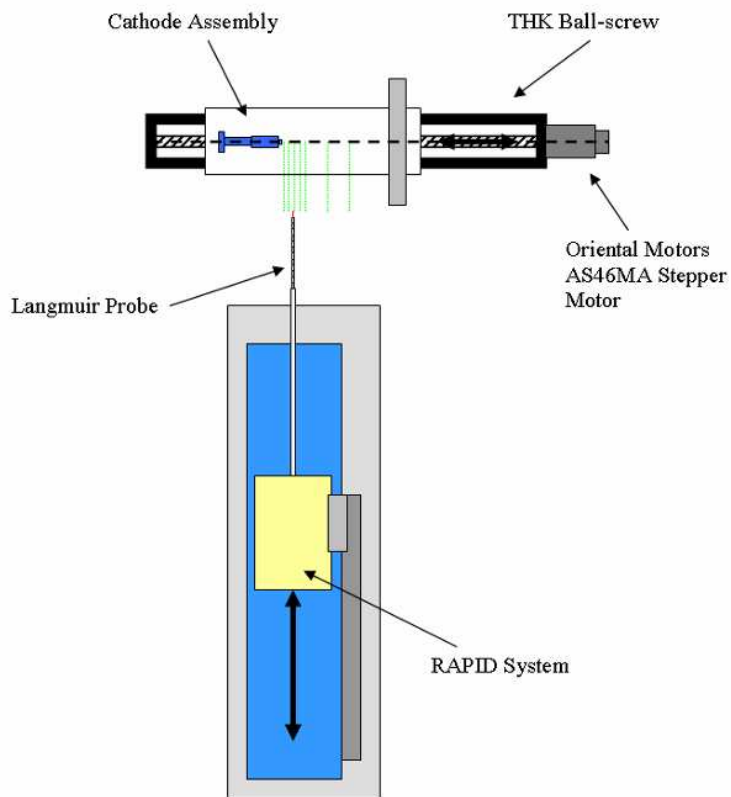


**Figure 21: Cathode assembly mounted to THK placed ~10 cm perpendicularly in front of the RAPID system**

Figure 22 show the setup and orientation of the cathode and RAPID system.

The dotted path lines drawn on these figures represent measurement lines used during testing. These lines began 0.25 cm axially downstream of the hollow cathode and continued in 0.25 cm steps to a position 1.75 cm axially downstream. At this point it was found that the plasma properties were not changing significantly, and, to save data acquisition and analysis time, only two final path lines at 2.25 cm and 3.25 cm were used.

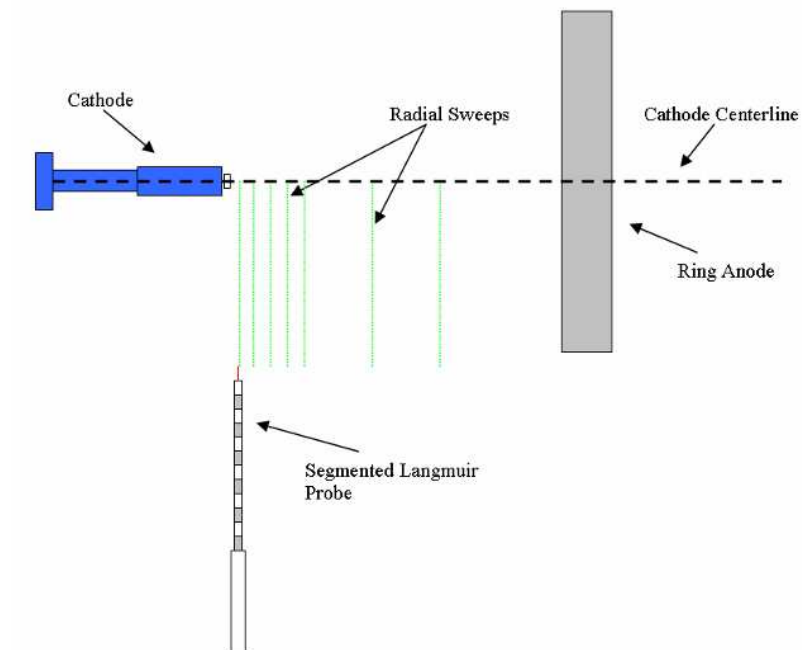


**Figure 22: Hollow cathode investigation setup showing Langmuir sweep path lines and distant ring anode**

All path lines began 2 cm radially away from the cathode centerline and sweep inward toward the cathode centerline.

## 4.2 Cathode Configurations

### Simple cathode

The first condition tested was that of a simple hollow cathode configuration without a magnetic field or enclosed keeper. A small electrode was located to one side of the hollow cathode to facilitate starting. The electrode was biased to high voltage to initiate an arc and allow the anode power supply to couple a discharge between the cathode and the anode. Once the discharge started, the small starting electrode was connected to cathode potential. Figure 23 shows the simple cathode and distant ring anode used in the first set of tests.

Throughout testing both the cathode and keeper structures were held at ground potential and the anode was biased using a DC power supply equipped with a large output capacitance and an inline ballast resistor (see Figure 25). The ballast resistor was

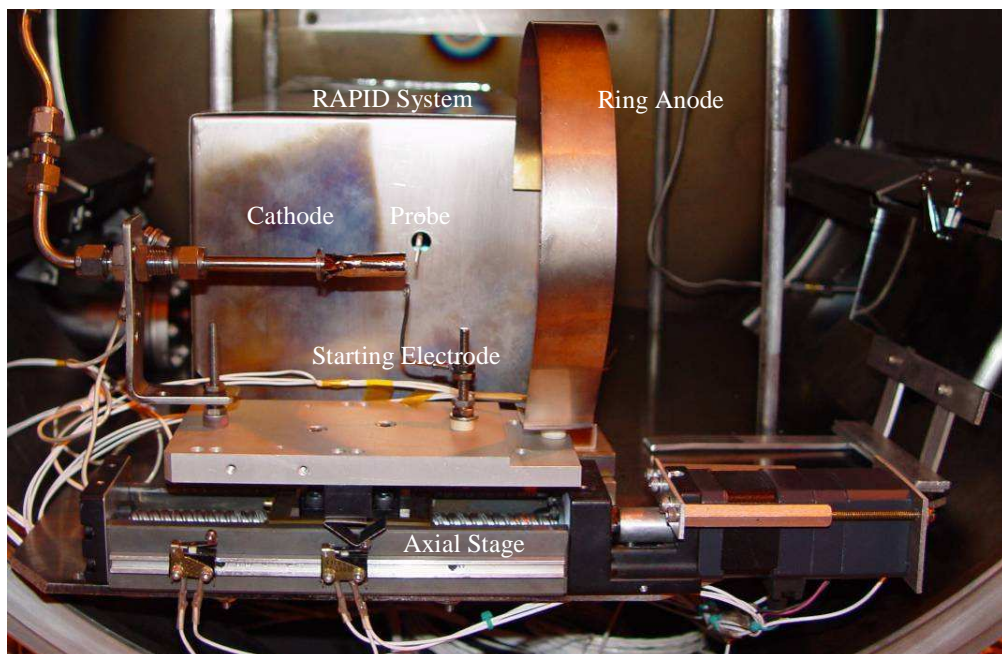


**Figure 23: Simple cathode and distant ring anode with probe at 0.25 cm axial distance.**

a 4.5  $\Omega$ , 250 W resistor for all cases except that of the high power NSTAR-like test conditions. This power supply provided a very stable power platform that reduced noise in the cathode discharge. In high power cases, the power supply was switched out to one with a lower output capacitance and the ballast resistor was dropped to 0.1 $\Omega$ . The drop in ballast resistance was required to avoid excessive ballast voltage drops at discharge currents above 20 A.

### Enclosed Keeper

The enclosed keeper added to the system was fabricated from a thin stainless steel tube equipped with a tantalum orifice plate. The tube had an inside diameter of 1.27 cm. Spacing between the keeper and cathode orifice plates was maintained at 1.27 mm  $\pm$  0.1 mm throughout testing. A small notch had to be cut in the side of the keeper tube for access to the cathode heater. A schematic diagram and a photograph are shown in Figure 24. The plate anode positioned in the “near” location is shown on the right side of the

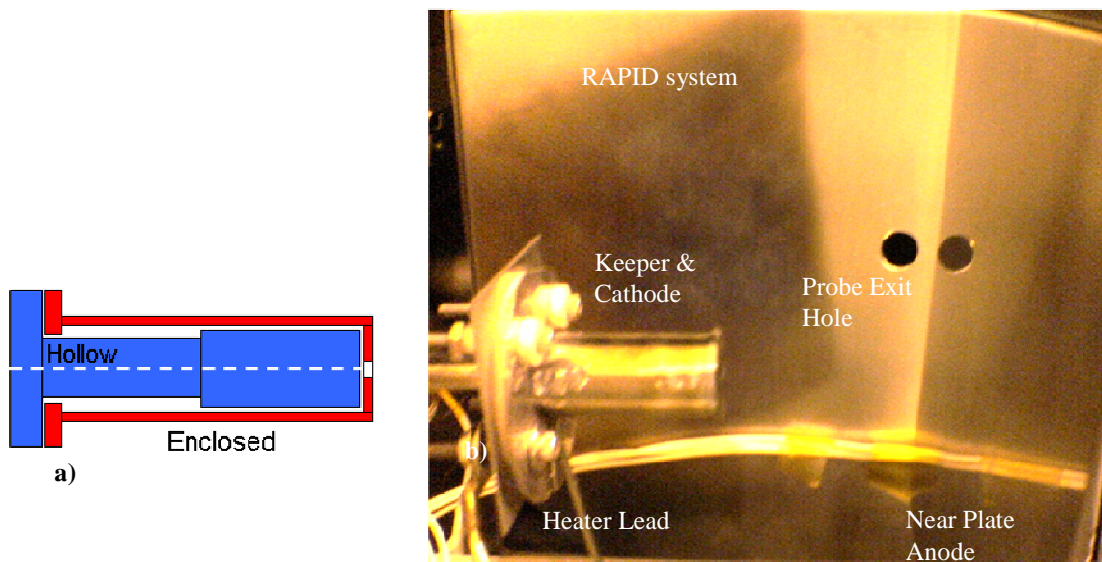
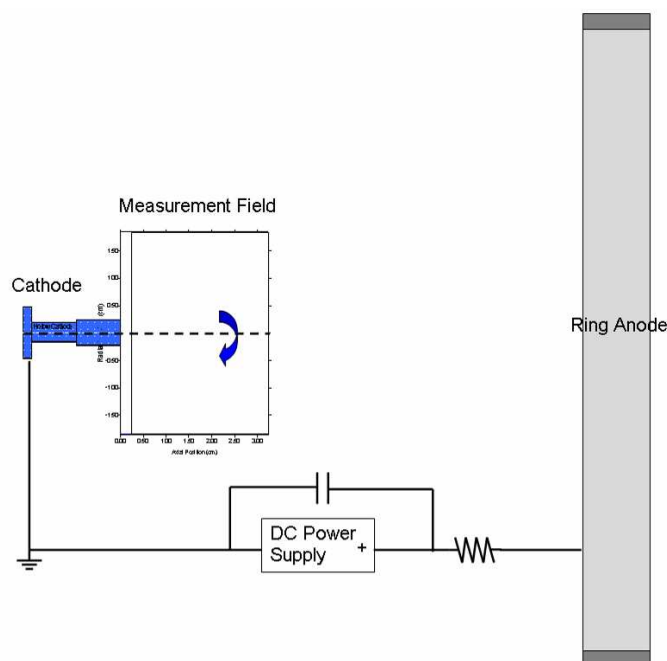


Figure 24: Schematic diagram of enclosed keeper and hollow cathode (a) and photo of small holed keeper and near plate anode (b)

photograph.

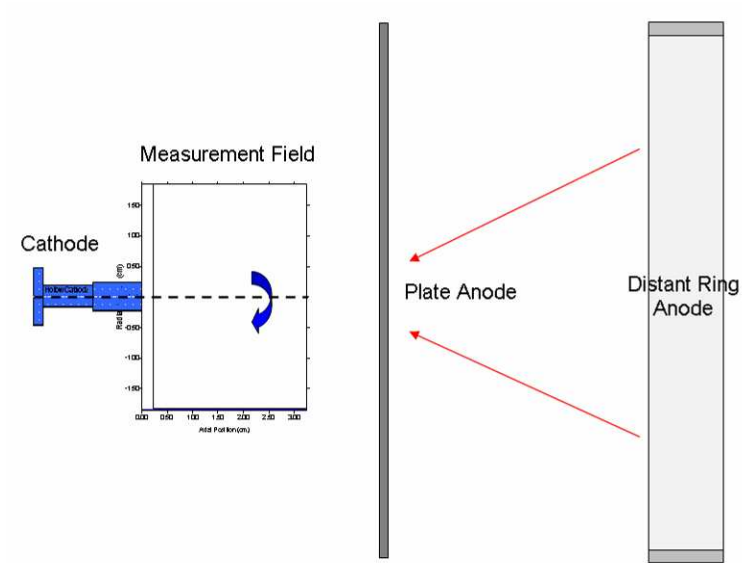
Three different keeper orifice hole diameters were tested. The first was 2.7 mm, followed by 3.8 mm, and ending with 4.75 mm. These diameters were chosen to have equal open area changes between the three holes. The final hole size is that of the NSTAR enclosed keeper.

## Anode



**Figure 25: Schematic diagram of simple cathode with ring anode system.** Shown also is the measurement field directly in front of the cathode (explained in section 4.1).

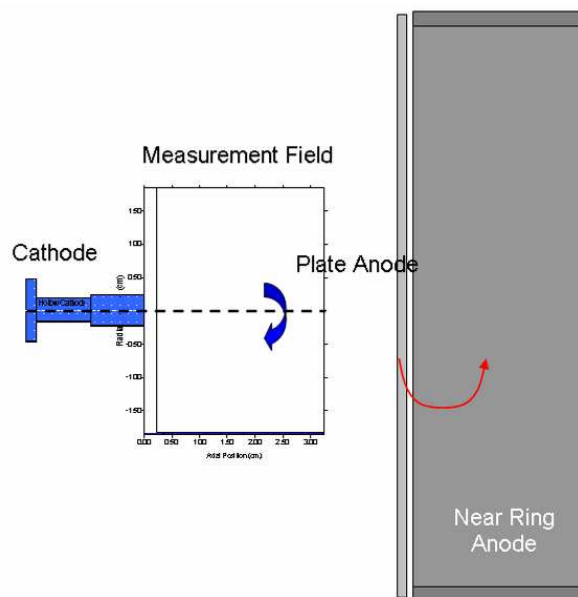
For the first test presented in this study, a relatively large ring anode was utilized. This anode consisted of a 3-cm wide, 15-cm diameter ring of thin, stainless steel sheet that was placed 13 cm downstream of the cathode (see Figure 23). A small section of the anode ring had to be cut to allow room for the RAPID system. A schematic view of this configuration and its relative size to the measurement field and cathode is shown in



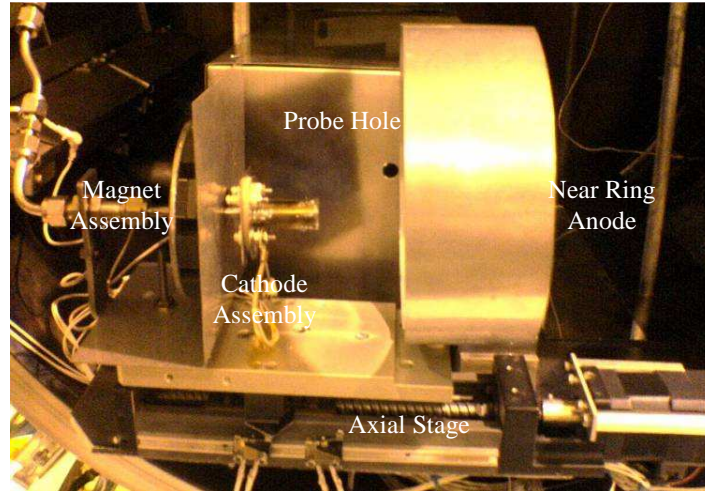
**Figure 26: Schematic diagram of near plate anode.**

Figure 25. Although this figure is not to scale, it provides a reasonably good approximation of the experimental layout.

The near plate anode configuration consisted of a square piece of stainless steel plate that was placed approximately 5 cm downstream of the cathode. This plate was 15 cm



**Figure 27: Schematic diagram of near ring anode.**



**Figure 28: Photo of enclosed keeper cathode with axial magnetic field and near field ring anode.**

wide and 15 cm tall, and is shown schematically in Figure 26.

The final anode configuration used in this study was a ring anode placed in the near field of the cathode. This anode was made of stainless steel sheet and was placed approximately 5 cm down stream of the cathode, similar to the axial location of the near plate anode. The dimensions of the near ring anode were 5 cm wide and 15 cm in diameter. Figure 27 shows a schematic of this anode, and Figure 28 shows a photograph of this anode configuration as it was used during tests conducted at high discharge powers.

### **NSTAR Magnetic field**

The final three test configurations evaluated during this study were performed with the inclusion of an applied axial magnetic field. To match conditions seen in other applications, the magnetic field was designed to be similar to that of the NSTAR thruster. A ferromagnetic ring was fabricated with an OD of 9.27 cm and a width just thick enough to completely cover a stack of SmCo magnets stacked three deep. These magnets are 1.27 cm wide by 1.7 cm long by 0.5 cm thick similar to the ones used within the end

wall structure of the NSTAR thruster. The total number of magnets used was 33. This magnetic ring was attached to a stainless steel cathode back plate (shown in Figure 28) by magnetic connection to a thin circle of ferrous sheet metal spot welded to the back plate. A photograph of this setup is shown in Figure 28.

The strength of the magnetic field along the centerline of the cathode is shown in Figure 29. These measurements were compared to NSTAR / DAWN ion thruster data presented in [67], and found to be very similar, with the magnetic field strength at the

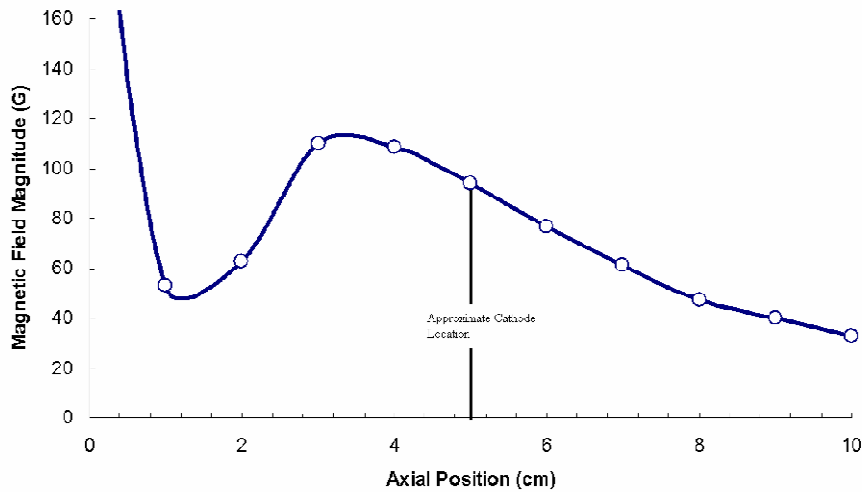


**Figure 29: Magnetic field strength through cathode centerline**

cathode orifice within 10% of the NSTAR thruster value. Figure 30 is a contour plot of magnetic field strength. Again, in comparison to the NSTAR magnetic field, the magnetic field in the cathode region was found to be very similar.

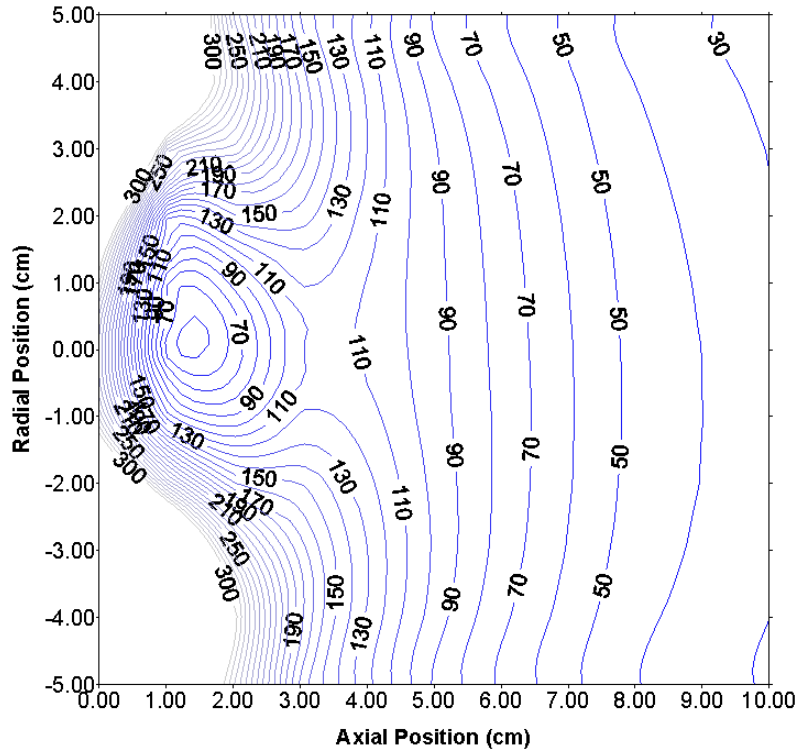


Figure 30: Magnetic field strength contours versus radial and axial position

### 4.3 Vacuum Chamber

Testing of the hollow cathode and RAPID system was conducted in a 1.0-m long by 0.76-m diameter, cylindrical vacuum chamber equipped with a CTI-8 Cryopump. The pumping speed for the cryopump is 1500 l/sec on air. Base pressures for this chamber are below  $2 \times 10^{-7}$  Torr and are obtained within four hrs from the start of rough-down. During operation of the cathode at Xe flow rates from 1.5 to 4.5 sccm, the chamber pressure rose to the mid to upper  $10^{-5}$  Torr range. The chamber pressure was sensed with a Granville-Philips ionization gauge and was corrected for xenon using a correction factor of 2.87.

Experiments carried out within the vacuum chamber were performed on a table bolted to four over-head mount points. The cathode was also mounted to the table to ensure that mechanical vibrations caused by the linear motor operation would be the same as the vibrations felt by the cathode. This orientation minimized to relative oscillatory motion between the cathode and linear motor and increased the reliability of probe positioning operations.



**Figure 31: Varian 0.76m x 1.0m vacuum chamber**

## CHAPTER 5: RESULTS

Three typical Langmuir probe traces are shown in Figure 32, Figure 33, and Figure 34. These correspond to operating at conditions SC6, SC10, and SC12, of the simple cathode configuration, respectively (see Table 2). Each I-V curve contains roughly 1,300 data points, which was standard during most testing. To obtain high quality traces in different plasma flow field conditions, adjustable amplification of the current signal was required. This was performed through selection of the current sense resistor shown in Figure 19. In addition, the amplitude of the saw-tooth biasing waveform was modified as needed to accommodate plasmas with different plasma potentials and densities. In general, a 100- $\Omega$  current sense resistor and a +50 V to -30 V (80 V<sub>p-p</sub>), 1-kHz triangular waveform was used. Modifications to these values were made when measured signals from the probe exceeded the  $\pm 10$  V limit of the DAQ system or when signal levels approached the noise floor of the 14-bit DAQ system.

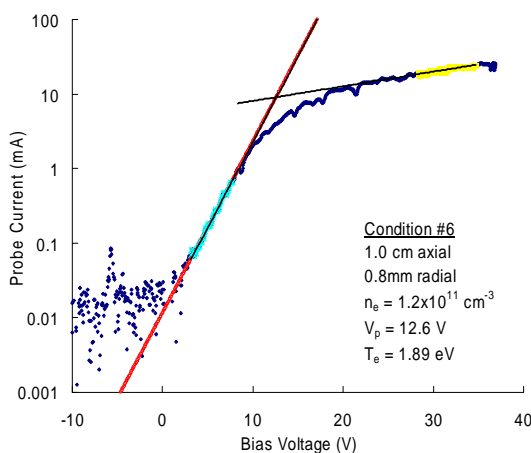


**Figure 32: Common Langmuir trace for SC6.  
1000  $\Omega$  resistor, -32V to +37V waveform**

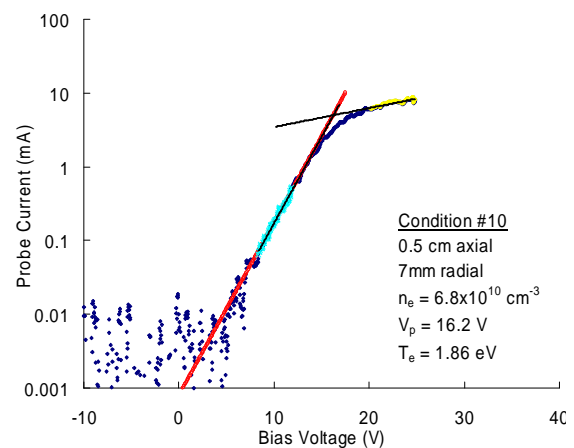


**Figure 33: Common Langmuir trace for SC10.  
100  $\Omega$  resistor, -20V to +25V waveform**

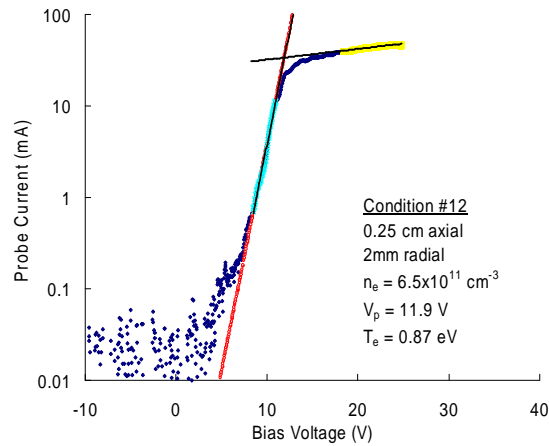


**Figure 34: Common Langmuir trace from SC12.  
33  $\Omega$  resistor, -20V to +25V waveform.**

From each trace, values for the plasma density, electron temperature, and plasma potential were calculated using procedures outlined in Chap. 3. Figure 33 and Figure 34 were both taken under modified waveform conditions where the waveform maximum voltage was decreased to prevent excessive electron current collection. In addition, Figure 34 was obtained by replacing the 100  $\Omega$  resistor with a 33  $\Omega$  resistor, which was done to avoid saturating the DAQ input limit of 10 V in this dense plasma. Because the maximum current in Figure 32 was low, it was possible to replace the 100  $\Omega$  resistor with a 1000  $\Omega$  one without exceeding the  $\pm 10$  V DAQ limit. With this modification, higher resolution results were possible in low density plasma, and, consequently, switching to a higher sense resistor was done whenever the plasma conditions granted. In general, linear behavior over two to three orders of magnitude on log-linear plots like the ones shown above were observed. The linear behavior suggests that the electron population is well thermalized. Although some evidence of primary or non-thermalized electrons was observed (e.g., see the region between 0 V and 6 V in Figure 34), their presence was neglected in analysis of the Langmuir probe data. Finally, it is noted that significant

rounding at the knee between the electron retardation and saturation regions was observed for some operating conditions. Excessive rounding can be indicative of noisy or turbulent plasma<sup>6869</sup> (see Section 5.10) and locations where excessive rounding exists might be indicative of concern due to possible formation of energetic ions during times when the (oscillatory) plasma potential increases to high positive values relative to the cathode.

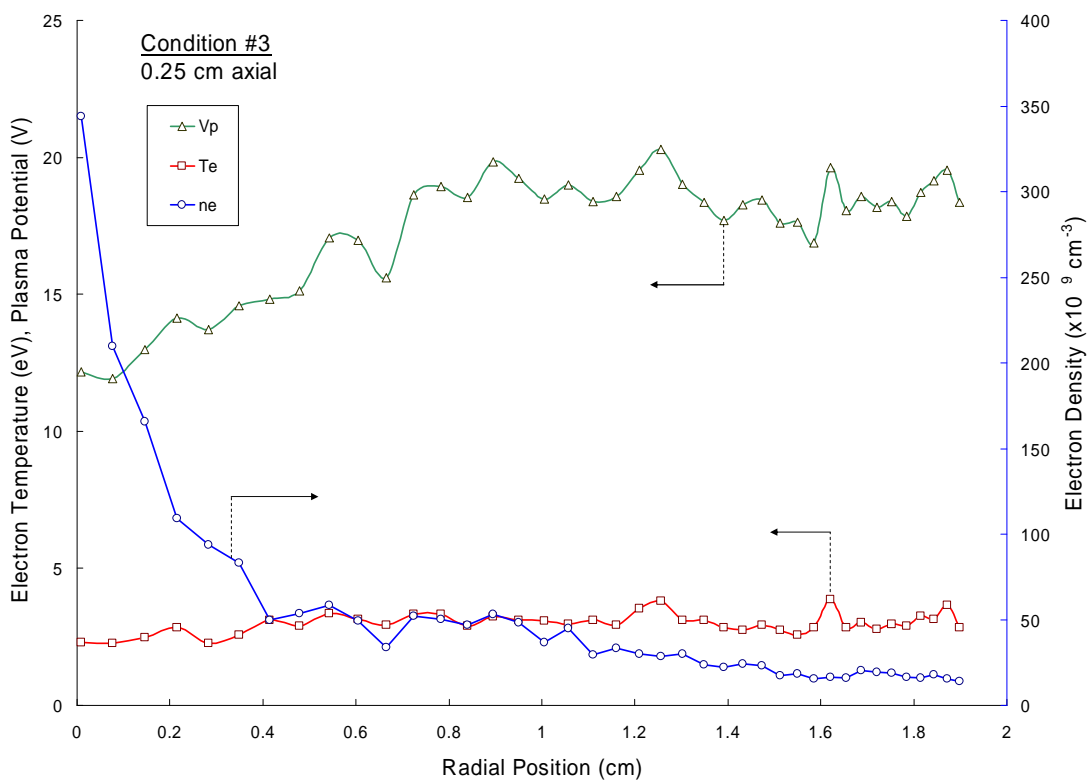
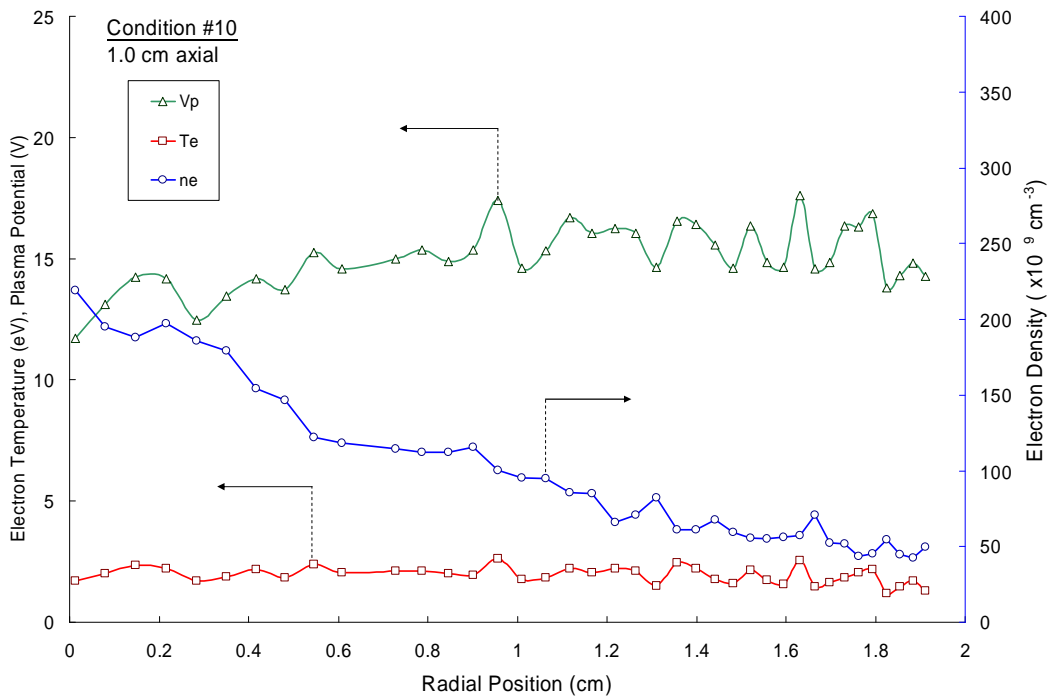


**Figure 35: Combined Langmuir traces for flow condition SC3 at 0.25 cm axial position. Representative of common radial sweep at small axial positions.**

Typically 40 Langmuir traces were taken over a ~2 cm radial scan at a given axial distance downstream of the hollow cathode orifice. Figure 35 contains plots of plasma density, electron temperature, and plasma potential obtained from the analysis of a typical radial scan. The data shown in Figure 35 correspond to an axial position of 0.25 cm with the hollow cathode operating at SC3 (see Table 2). Because of the close axial proximity

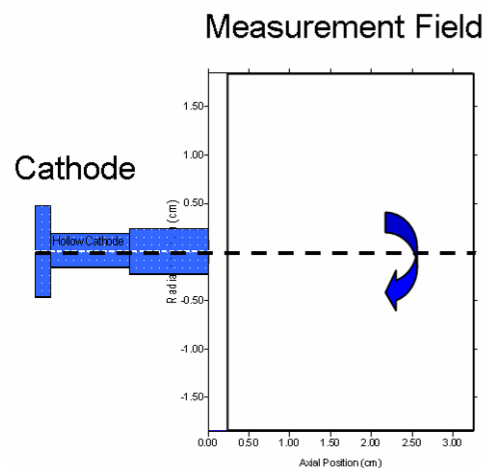
to the cathode, the plasma density is only observed to increase quickly near the center line of the cathode (i.e., near  $r = 0$  cm).

Figure 36 contains similar data collected at an axial position of 1 cm for simple cathode SC10. Here, the plasma density is shown to start increasing at a larger radial position, but in a much more gradual fashion. In general radial scans performed at larger axial positions ( $z = \sim 3$  to 4 cm) displayed nearly constant plasma density over the entire radial range investigated, except for high current operating conditions and when configurations using magnetic fields were tested. The radial profiles of electron temperature and plasma potential shown in Figure 35 and Figure 36 do not display as much variation when compared to the plasma density profiles (as was expected). This was true in general for all data collected during this study.



**Figure 36: Combined Langmuir traces for flow condition SC10 at 1.0 cm axial position. Representative of common radial sweep at medium axial positions.**

After a set of Langmuir probe traces for each radial position had been analyzed, the plasma property data were curve-fit to 6<sup>th</sup>-order polynomials and pooled together to create 2D contour plots. Three separate contours were formulated for each operating condition, one for each of the plasma parameters shown in Figure 35 and Figure 36. Contours are oriented such that the cathode tip is positioned at  $z=r=0$ -cm, as Figure 37 shows. As described above, Langmuir probe measurements were taken in the upper half of the measurement field (from  $r=2$ -cm to  $0$ -cm and from  $z=0.25$ -cm to  $3.25$ -cm) and then mirrored about the cathode axis to improve visualization of the plasma flow field. Also, no measurements were taken from  $z=0$ -cm to  $0.25$ -cm. This was done to ensure that the Langmuir probe did not accidentally come into contact with the cathode. This section will be boxed out in all contour plots, as the thin rectangular box in Figure 37 shows.



**Figure 37: Cathode orientation with respect to RAPID system measurement field.**

## 5.1 Simple Cathode (SC)

The first measurements to be presented were collected using a simple hollow cathode with no keeper and no magnetic field. Table 2 contains a list of operating conditions studied for the simple cathode configuration. Throughout this paper, labels listed in column 1 will be used to identify the test conditions referred to in the text.

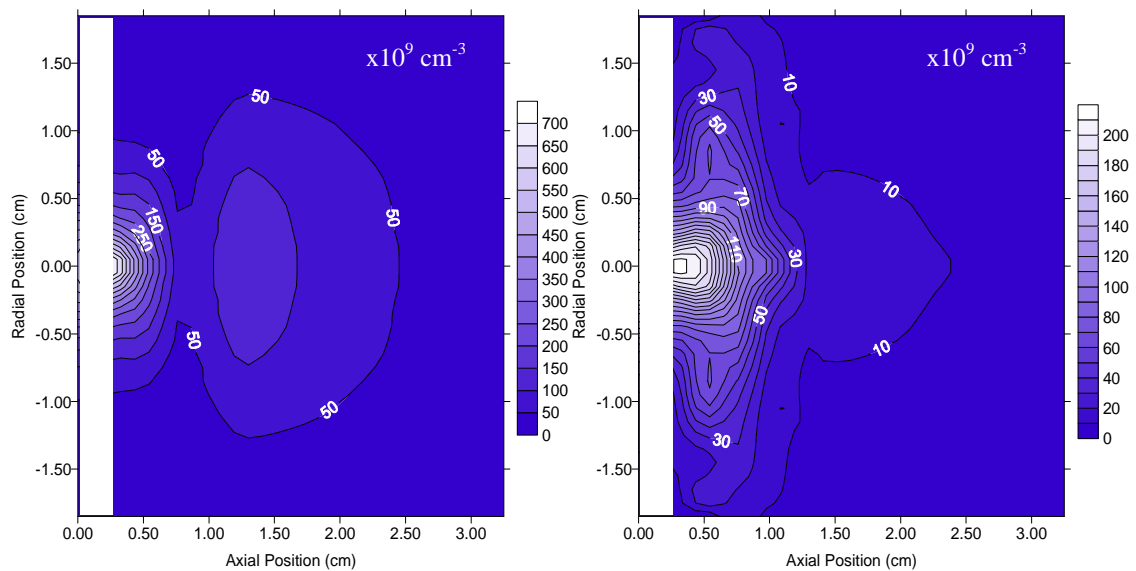
Table 2: Operating conditions for the simple hollow cathode configuration

Operating Condition	$J_d$ (A)	$V_d$ (V)	$\dot{m}$ (sccm)	Pressure ( $\times 10^{-5}$ Torr)
SC1	2	37.4	1.5	3.5
SC2	4	48.7	1.5	3.5
SC3	6	56.7	1.5	3.5
SC4	8	86.4	1.5	3.5
SC5	2	36.4	3	6.4
SC6	4	42.1	3	6.5
SC7	6	52.9	3	6.5
SC8	8	59.3	3	6.6
SC9	2	35.5	4.5	8.6
SC10	4	42.1	4.5	8.6
SC11	6	53.4	4.5	8.6
SC12	8	57.6	4.5	8.6

Figure 38 through Figure 55 show a variety of contour plots taken with the simple cathode configuration. Figure 38 through Figure 41 show plasma density plots for conditions SC1 to SC4. These figures, as with all other plasma density plots, are shown as lines of constant contour  $\times 10^9 \text{ cm}^{-3}$  versus axial and radial position. The cathode resides just to the left of each contour plot with the cathode tip centered at  $r=0$ -cm and the cathode axis oriented along the  $z$  direction. Again, the boxed off region between  $z=$

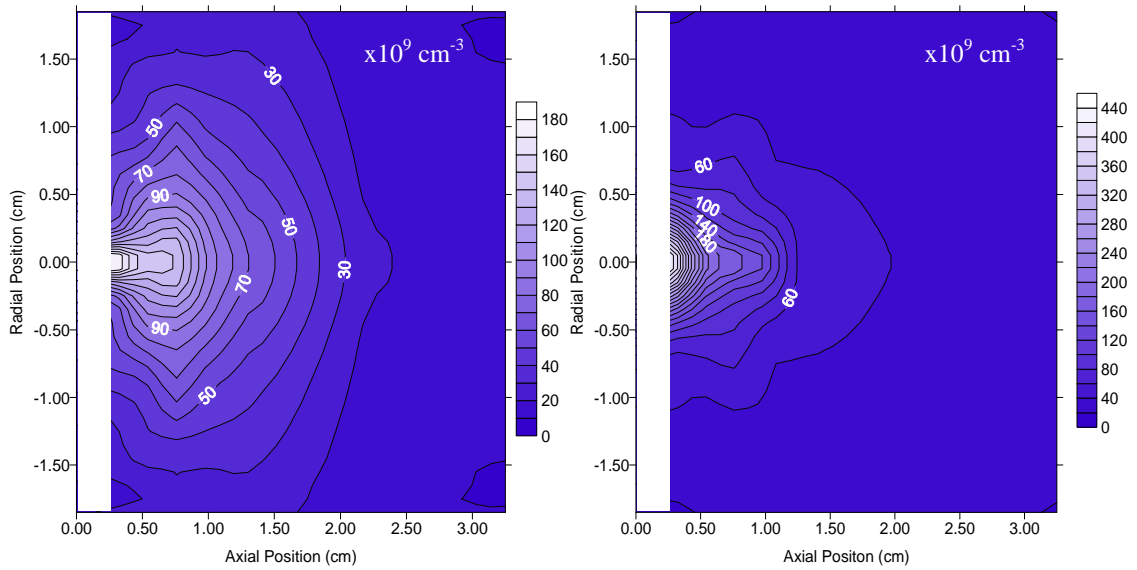
0-cm and  $z = 0.25$ -cm is where no data were taken. Due to drastic differences in densities between different operating conditions, each contour plot corresponds to a different scale.

Figure 38 displays a monotonic expansion in plasma density starting at the location  $r = 0$ -cm,  $z = 0.25$ -cm. The maximum plasma density recorded in Figure 38 is about  $7.5 \times 10^{11} \text{ cm}^{-3}$ . Density expansions such as this one represent approximately 70% of the plasma density contours observed during this study and are described as a “Standard” expansion process (i.e., expansion from a point source). One would think that this



**Figure 38:**  $n_e$  contour plot for SC1 ( $\times 10^9 \text{ cm}^{-3}$ ). **Figure 39:**  $n_e$  contour plot for SC2 ( $\times 10^9 \text{ cm}^{-3}$ ).

expansion process is related to spot mode operation, however, it was often difficult to distinguish between spot and plume mode<sup>70</sup> operation through inspection of plasma density contour plots alone, and our nomenclature for “Standard” expansion may define what might be visually observed as either spot or plume mode operation. For example, Figure 38 (2 A, 1.5 sccm) corresponded to a cathode operating in the spot mode (from visual observation) while Figure 41 (8 A, 1.5 sccm) was visually determined to be operating in the plume mode.



**Figure 40:  $n_e$  contour plot for SC3 ( $\times 10^9 \text{ cm}^{-3}$ ). Figure 41:  $n_e$  contour plot for SC4 ( $\times 10^9 \text{ cm}^{-3}$ ).**

As we follow the trends caused by increasing the electron emission current from 2 to 8 A (Figure 38 to Figure 41), we see the expansion change from a monotonic one in Figure 38 to what we have termed a “Plasmoid” expansion in Figure 39 (partially developed) and Figure 40 (fully developed). Our plasmoid expansions appear most similar to ball mode as described by other researchers, but herein this mode was defined only with

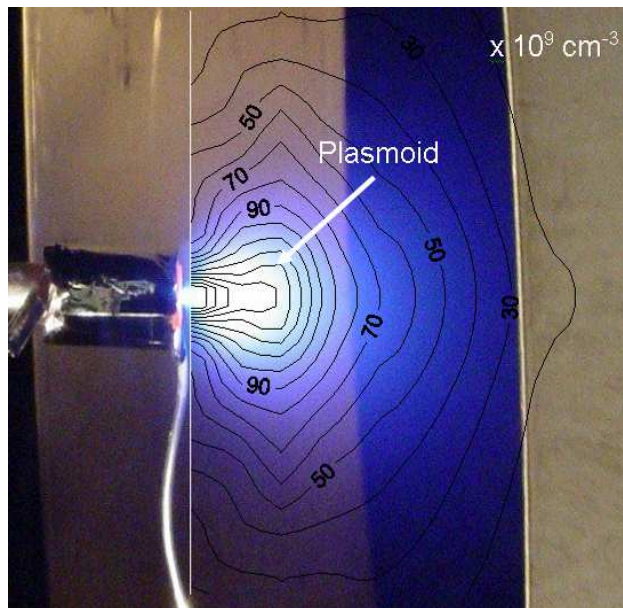


**Figure 42: Overlay of plasmoid contour structure measured on photo of plasmoid.**

regard to plasma density contours and not visually or through discharge voltage or current waveform monitoring. Therefore our plasmoid modes may not encompass all conventional ball modes or vice versa. In the simple cathode configuration, the plasmoid mode typically occurs between the spot and fully developed plume modes. In a large majority of cases, the existence of a plasmoid expansion feature corresponded to a ball-like structure (the plasmoid) seen to form some distance away from the cathode. As pointed out above, Figure 39 (condition SC2, 4 A, 1.5 sccm) seems to represent a transition from a monotonic expansion (SC1) to a plasmoidal expansion (SC3). If we take a photo of a plasmoid and overlay the plasmoid contour structure of SC3, we see that they match rather well (see Figure 42).

As we continue to follow the increase in current an interesting transition occurs. Figure 41 is a plasma density plot for condition SC4 (8 A, 1.5 sccm). Note that the anode voltage, shown in Table 2, for this condition is drastically higher than the previous, low-current cases (SC1, SC2, and SC3). What has happened, and what may not be so evident from the density contour, is that the cathode discharge has again transitioned into yet another operating mode. At condition SC4, the entire vacuum chamber was visually lit up with excitation. We have decided to term this mode the “Full-Plume” mode. The full-plume mode usually can not be detected by simply looking at density contours like Figure 41, which appears to be a standard monotonic expansion with about double the peak plasma density seen in SC2. However, when looking upon plots of both plasma potential and electron temperature (presented next), it becomes quite apparent that a very different mode is present. It is noted that at the low flow rate condition of 1.5 sccm (Xe), the cathode discharge was observed to transition between several different modes as the

current was increased from 2 A to 8 A. This suggests that a flow rate of 1.5 sccm may be too low for the cathode to couple easily to the smaller, distant anode used during these tests. Transitions between modes did not occur as much at higher flows used during the rest of the simple cathode configuration study.

Figure 43 is a plasma potential contour map corresponding to the plasma density map of Figure 40. Here we plot potential in volts versus axial and radial position. In this figure, a slight rise in plasma potential on centerline is observed near the cathode orifice, followed by a potential drop through a V-shaped valley structure that develops in the regions downstream of the cathode. In almost all SC to LK conditions, the plasma potential was noted to have a valley structure that would form some distance in front of the cathode on the centerline, many taking a similar V-shape to the one shown in Figure 43. Note the presence of the plasmoid observed during SC3 (6 A, 1.5 sccm) is not evident in the plasma contour plot shown in Figure 43. Also, from the structure of Figure 43, one can imagine the path of ions created within the span of this plot would tend to

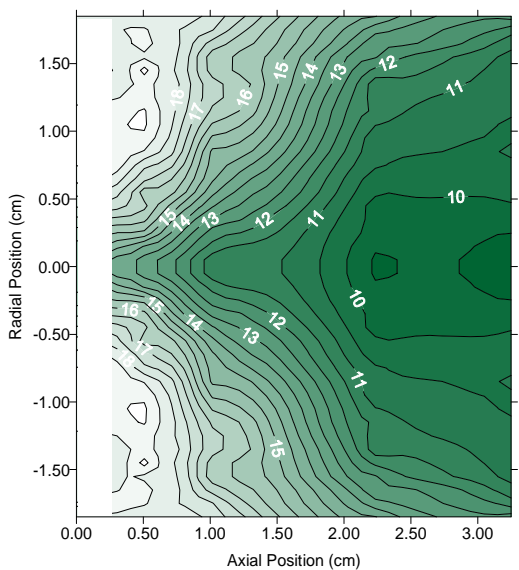


**Figure 43:  $V_p$  contour plot for SC3 (V).**

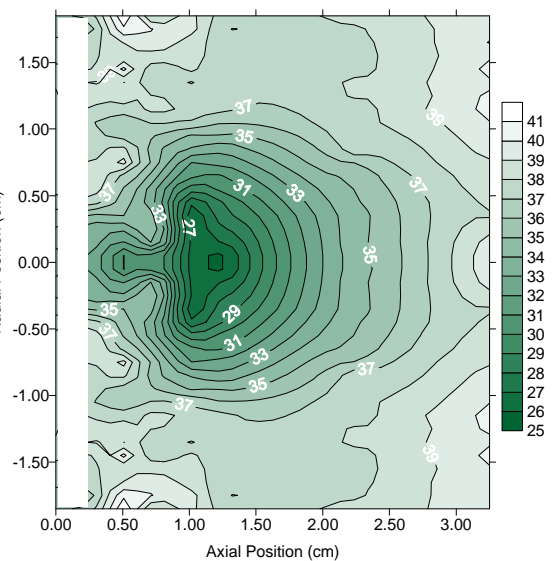


**Figure 44:  $V_p$  contour plot for SC4 (V).**

flow from the cathode ( $r,z = 0\text{-cm}$ ) toward regions further away from the cathode, following the gradient of the contour plot, with a maximum energy gain of 5 to 10-V for a singly charged ion.

Figure 44 shows the potential contour corresponding to SC4 (see Figure 41, 8 A, 1.5 sccm). Note several changes have occurred. The most apparent change is that the somewhat distant valley in Figure 43 has now become a deep hollow that sits directly in front of the cathode. Upon inspection, it can be seen that the potential has increased 20 V in the regions surrounding the hollow structure. The plasma potential contour plot shown in Figure 43 is very characteristic of a full-plume mode. Here again ions would tend to fall into the bowl from all other locations. It is noted that Langmuir probe traces contained features indicating that the plasma was quite noisy in the hollow region, and it is considered likely that the DC hollow structure is far from a hollow in an AC sense. Regardless of our speculation, the negative potential hill structure would tend to trap (or confine) low energy ions unless an ion heating mechanism was present to sweep them from the region either continuously or periodically. Neither Figure 43 nor Figure 44 present DC potential structures that exhibit strong evidence for ion bombardment of the cathode.

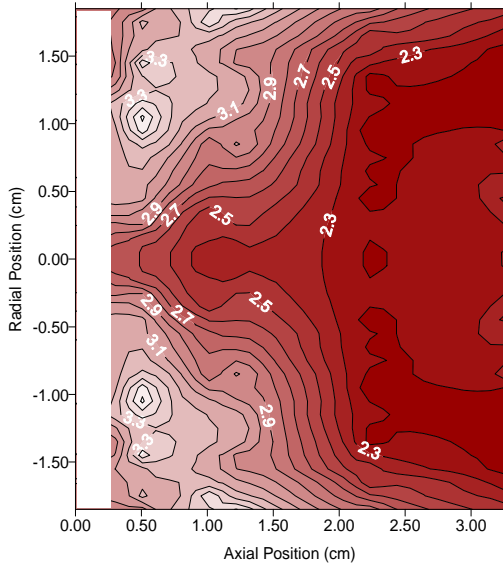


Figure 45:  $T_e$  contour plot for SC3 (eV).

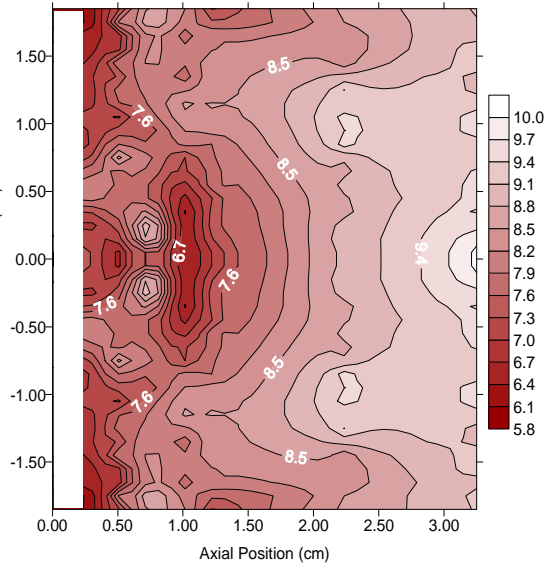


Figure 46:  $T_e$  contour plot for SC4 (eV).

Figure 45 and Figure 46 contain electron temperature contours for SC3 (6 A, 1.5 sccm) and SC4 (8 A, 1.5 sccm). Here we have plotted electron temperature in eV as a function of axial and radial position. It can be seen that each contour roughly follows the potential structures for these operating conditions. For example, Figure 45 displays a valley falling away from the cathode and Figure 46 displays a bowl or hollow just in front of the cathode. Electron temperature contours that follow their corresponding plasma

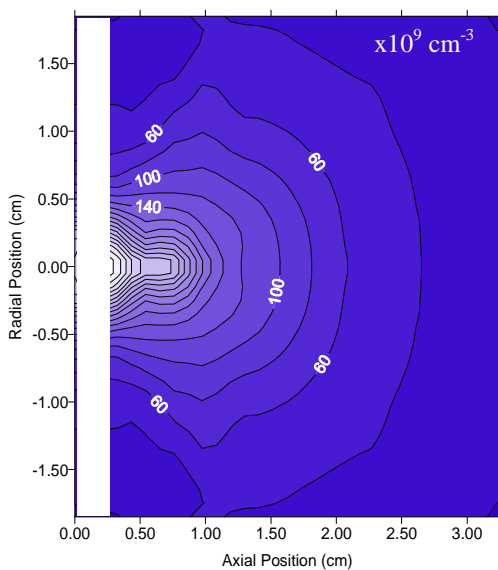


Figure 47:  $n_e$  contour plot for SC7 ( $\times 10^9 \text{ cm}^{-3}$ ).

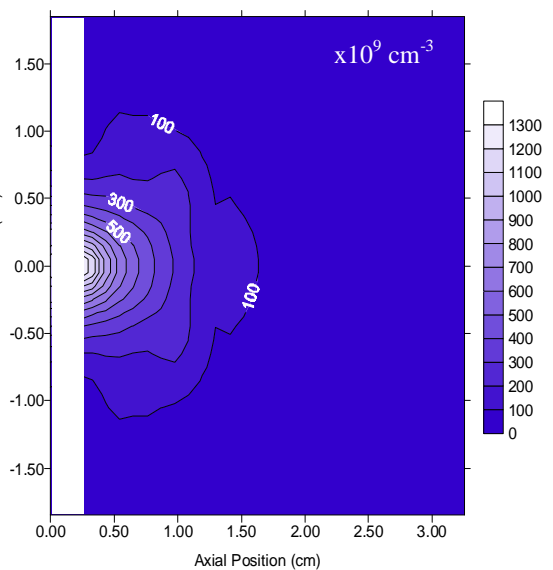
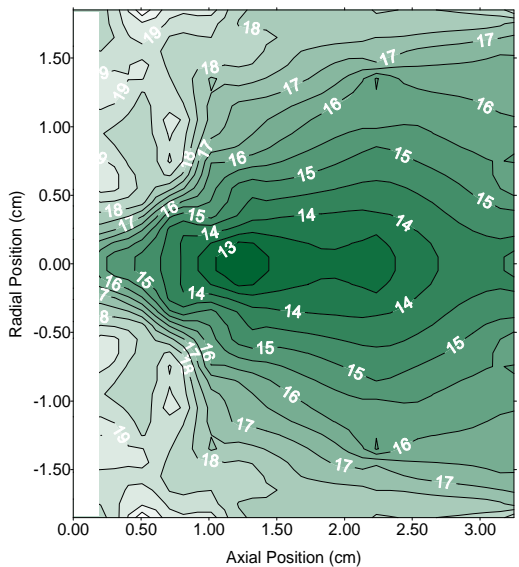
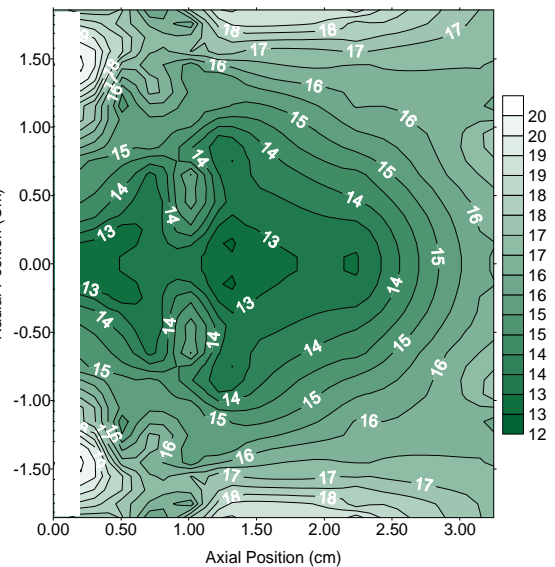


Figure 48:  $n_e$  contour plot for SC8 ( $\times 10^9 \text{ cm}^{-3}$ ).

potential contours were somewhat common, and (like plasma potential) electron temperature contour gradients were typically very small in comparison to plasma density gradients. There is one key point to notice in the electron temperature contour plot shown Figure 46 for the full plume mode; the average electron temperature was about 8 eV while Figure 45 displayed an average electron temperature of around 2.5 eV. This temperature is far greater than those displayed throughout the remainder of this paper, but was typical when the cathode operated in the full-plume mode.



**Figure 49:  $V_p$  contour plot for SC7 (V).**



**Figure 50:  $V_p$  contour plot for SC8 (V).**

At higher flow rate conditions of 3 and 4.5 sccm, we see some similar results to those presented above. Figure 47 and Figure 48 show plasma density contour plots for 6 and 8 A of electron emission at 3 sccm, conditions SC7 and SC8, respectively. At SC7 (6 A, 3 sccm) we begin to see the formation of a plasmoid, however it does not seem to form completely as it did in SC3 (6 A, 1.5 sccm) and the plasmoid appears to fall back to a monotonic expansion at 8 A. In addition, a full-plume mode was not observed to develop at SC8 (8 A, 3 sccm) in contrast to SC4 (8 A, 1.5 sccm), which is believed to be a result

of the higher flow rate. Note that peak plasma densities of  $10^{12} \text{ cm}^{-3}$  were measured just in front of the cathode for the SC8 condition. Plasma potential and electron temperature contours for SC7 and SC8 can be seen in Figure 49 through Figure 52. Comparing potential contours between SC7 and SC8, we see some resemblance to SC3 and SC4. Figure 49 shows a valley falling away from the cathode as in SC3, but the valley begins to close around  $z = 2.5 \text{ cm}$ , again suggesting that low energy ions produced in front of the cathode would be trapped (unless heated or periodically swept out due to potential

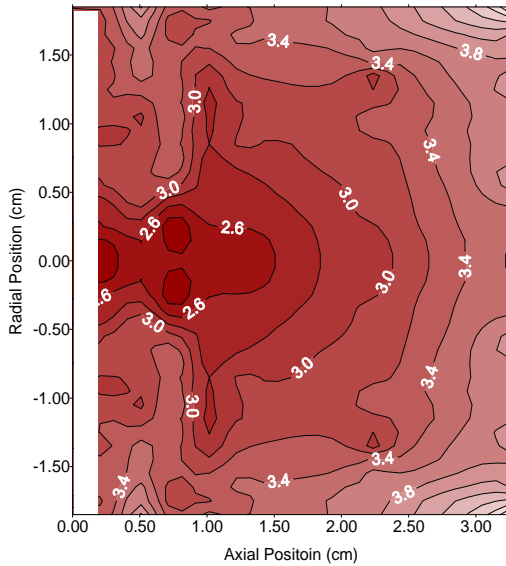


**Figure 51:  $T_e$  contour plot for SC7 (eV).**

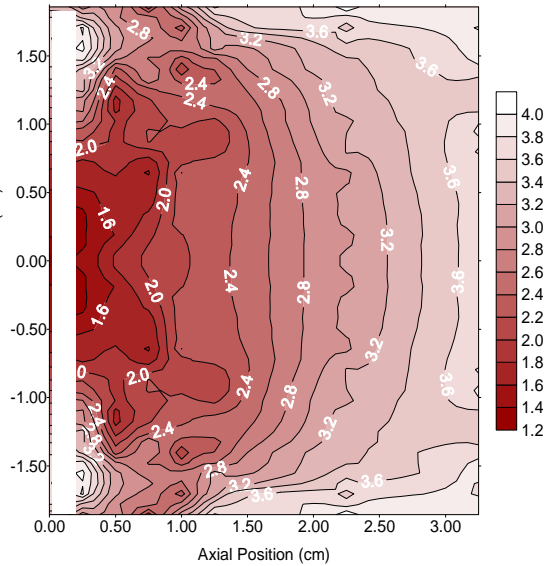


**Figure 52:  $T_e$  contour plot for SC8 (eV).**

fluctuations). Figure 50 resembles the potential bowl of SC4, however voltages throughout are much lower and comparable to that of Figure 49. It is interesting to note that Figure 28 shows evidence that ions formed at larger axial positions ( $z > 2.5 \text{ cm}$ ) could fall back into the cathode, although only with an energy gain of a few volts.

Figure 51 and Figure 52 are electron temperature contour plots for SC7 and SC8 respectively. The same sort of trends seen in Figure 45 (SC3, 6 A, 1.5 sccm) and Figure 46 (SC4, 8 A, 1.5 sccm) are exhibited here in that the electron temperature structure

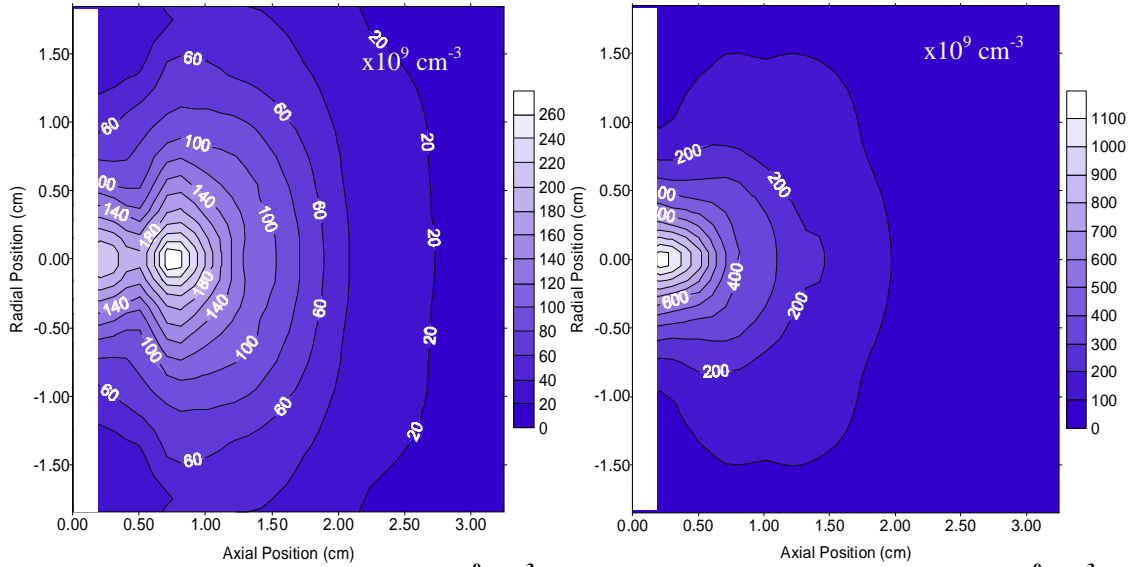


**Figure 53:  $n_e$  contour plot for SC10 ( $\times 10^9 \text{ cm}^{-3}$ ).** **Figure 54:  $n_e$  contour plot for SC11 ( $\times 10^9 \text{ cm}^{-3}$ ).**

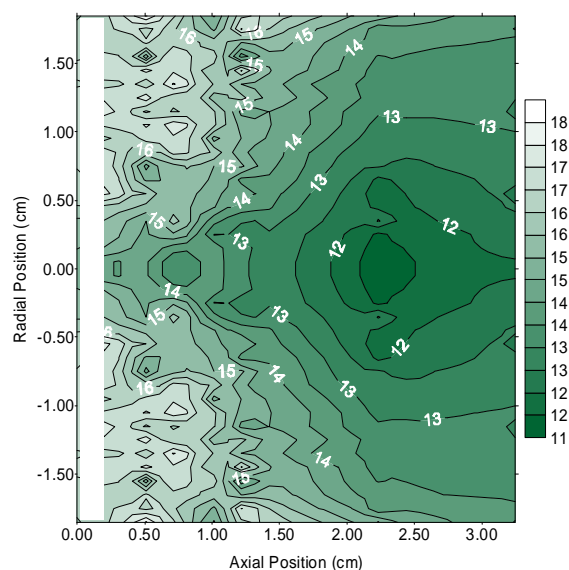
follows the potential structure. This time, however, both contours have an average electron temperature of around 2.5 to 3.0 eV.

Figure 53 and Figure 54 show plasma density plots for SC10 and SC11, 4 A and 6 A, respectively, for a flow rate of 4.5 sccm. Figure 53 shows the complete formation of a plasmoid, at a lower current than those seen before. Plasma densities for this condition are slightly higher than those for plasmoids shown previously as well. Also, the plasmoid seems to be larger and located further from the cathode than the lower flow plasmoids.

As we increase the current from 4 A to 6 A (Figure 53 to Figure 54), we again see the transition from a plasmoid back to a smaller plasmoid (or to a nearly monotonic expansion). As before, the peak density has increased drastically from about  $2.5 \times 10^{11} \text{cm}^{-3}$  to  $1.2 \times 10^{12} \text{cm}^{-3}$ . The increase in peak plasma density was observed whenever transitions occurred between a plasmoid and a higher current monotonic expansion.

As an interesting side note, if one takes the surface area and electron temperature of a given plasma density contour line that surrounds the cathode, the random thermal current on that surface is roughly equal to the current reported in Table 2. This situation suggests that in a DC sense, the plasma flow field downstream of a hollow cathode adjusts itself to just maintain the current being demanded of it. This observation was found to be nearly true throughout this study when no magnetic field was present.

A plot of the plasma potential from SC10 (4 A, 4.5 sccm) is shown in Figure 55. Again the standard v-shaped valley is observed to form downstream of the cathode, however the depth of the valley is not as deep as one measured at lower flow. At a flow



**Figure 55:  $V_p$  contour plot for SC10 (V).**

rate of 4.5 sccm, few potential plots exhibited large gradients. In fact, the plot shown in Figure 55 displayed the largest gradients observed in all potential contours measured with the simple cathode configuration at 4.5 sccm. In general, plasma potential was relatively constant at about 12.5 V throughout the measurement field for 4.5 sccm of flow. Table 3 contains a summary of contour structures observed in the simple cathode configuration.

Table 3: Contour plot structure for the simple cathode configuration..

Operating Condition	$J_d$ (A)	$V_d$ (V)	$\dot{m}$ (sccm)	Pressure ( $\times 10^{-5}$ Torr)	$n_e$ Shape	$T_e$ Shape	$V_p$ Shape
SC1	2	37.4	1.5	3.5	Standard Expansion	Depression at cathode	Fall From Cathode
SC2	4	48.7	1.5	3.5	Standard Exp. w/ Plasmoid	Constant	Valley from Cath
SC3	6	56.7	1.5	3.5	Plasmoid	V Shaped	V Shaped
SC4	8	86.4	1.5	3.5	Standard Expansion	Deep Depression near Cath.	Deep Depression near Cath.
SC5	2	36.4	3	6.4	Standard Expansion	Valley to Cathode	Central Valley
SC6	4	42.1	3	6.5	Standard Exp. w/ Plasmoid	Cathode Ridgeline	V Shaped
SC7	6	52.9	3	6.5	Standard Exp. w/ Plasmoid	Valley to Cathode	Central Valley
SC8	8	59.3	3	6.6	Standard Expansion	Valley to Cathode	Central Valley
SC9	2	35.5	4.5	8.6	Plasmoid	Constant	Small Valley
SC10	4	42.1	4.5	8.6	Plasmoid	Constant	Small Valley
SC11	6	53.4	4.5	8.6	Standard Exp. w/ Plasmoid	Valley to Cathode	Constant
SC12	8	57.6	4.5	8.6	Standard Exp. w/ Plasmoid	Cliff at Large Axial Locations	Constant

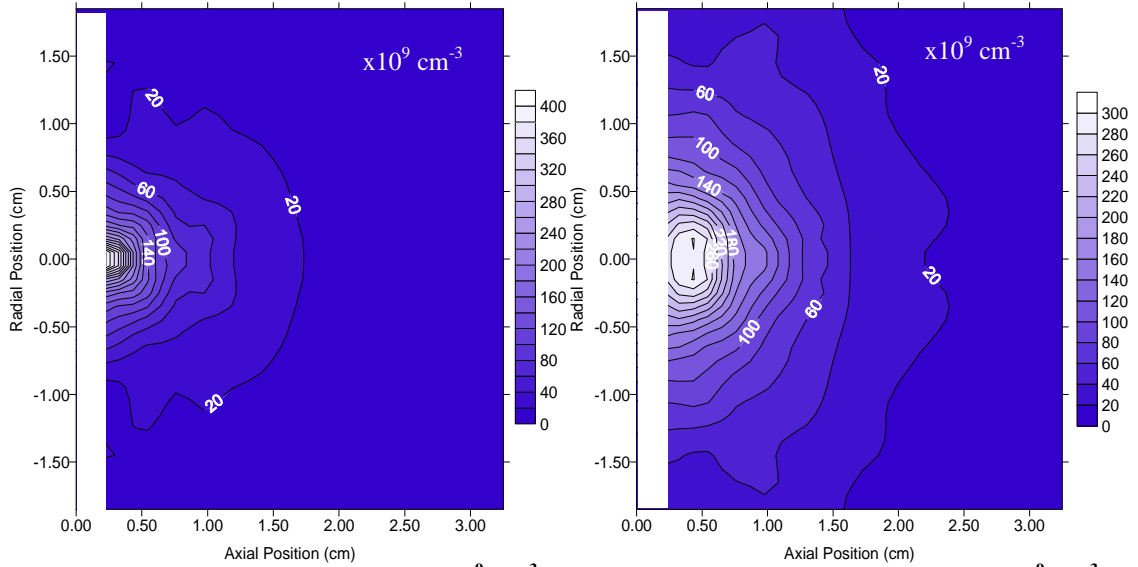
## 5.2 Simple Cathode with Near Plate Anode (SCP)

Table 4 displays operating conditions used for tests conducted with the near plate anode on the simple cathode configuration.

Table 4: Operating conditions for the simple hollow cathode configuration with a flat plate anode.

Operating Condition	$J_a$ (A)	$V_a$ (V)	$\dot{m}$ (sccm)	Pressure ( $\times 10^{-5}$ Torr)
SCP1	2	34.0	1.5	3.5
SCP2	4	41.7	1.5	3.5
SCP3	6	49.7	1.5	3.5
NA	8	75.6	1.5	3.5
SCP4	2	31.1	3	5.9
SCP5	4	40.8	3	5.9
SCP6	6	44.9	3	5.9
SCP7	8	55.1	3	5.9
SCP8	2	32.2	4.5	8.0
SCP9	4	34.0	4.5	8.0
NA	6	44.1	4.5	8.0
NA	8	56.7	4.5	8.0

Figure 56 and Figure 57 contain plasma density plots for 1.5 sccm at 4 and 6 A (SCP2 and SCP3). At 6 A, like the previous case at SC3, the cathode has transitioned into a plasmoid (e.g., see Figure 57 and compare to Figure 40). In this case, the plasmoid is compressed into a tighter ball that is located closer to the cathode. It is noted that the flat plate anode is much closer than the ring anode used in the SC case. This situation may be enhancing the neutral density nearby the cathode and increasing the ion production rates. Plasma density for SCP3 is about double that of the SC3 test case. At 4 A in the SC2 case, the beginning stages of a plasmoid were observed. Now, as shown in Figure 56 for 4 A, a standard expansion profile is observed. With the flat plate anode, plasmoid

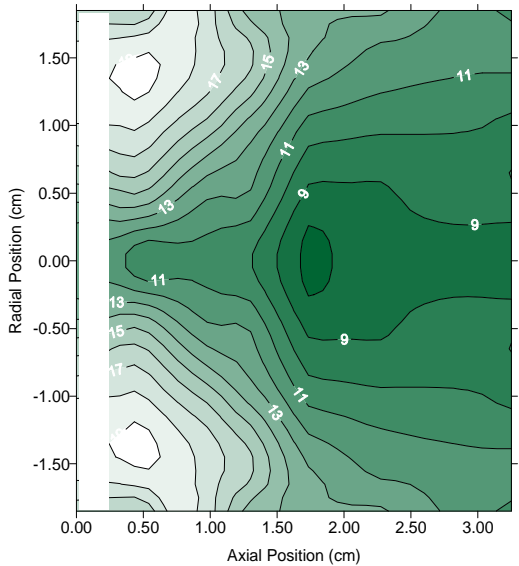


**Figure 56:  $n_e$  contour plot for SCP2 ( $\times 10^9 \text{ cm}^{-3}$ ).** **Figure 57:  $n_e$  contour plot for SCP3 ( $\times 10^9 \text{ cm}^{-3}$ ).**

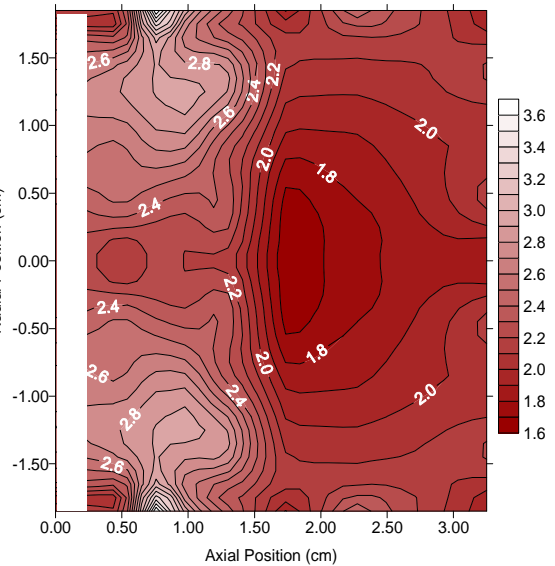
formation may either be pushed closer into the cathode or may not occur at all for this emission current level.

Figure 58 and Figure 59 show plasma potential and electron temperature contours for SCP3. By comparing Figure 58 to Figure 43, one can quickly see similarities. Each plot displays the characteristic “V” shaped valley falling away from the cathode and each contour plot ranges from around 20 V near the cathode to about 10 V in the center of the valley. Like before, ions created at  $r > 1.5 \text{ cm}$  and  $z < 0.5 \text{ cm}$  would tend to fall into this valley while electrons produced within the valley would tend to be accelerated away radially. Peak densities for each condition were measured at  $\sim 3 \times 10^{11} \text{ cm}^{-3}$ .

The electron temperature contours shown in Figure 58 follow the shape of the potential contours and the temperature ranges between 2 and 3 eV. However, it seems that the inclusion of the near-field plate anode has decreased the electron temperature in SCP3 by about 0.5 eV throughout the measurement region. In addition, a prominent “cliff” in electron temperature is observed at the start of the v-shaped potential valley structure. A cliff-like structure was present in Figure 45 as well, but it was not fully formed and it followed the V-shaped potential valley of Figure 43 rather than being



**Figure 58:  $V_p$  plot for Condition # SCP3 (V).**



**Figure 59:  $T_e$  contour plot for SCP3 (eV).**

freestanding like the feature in Figure 58. At the present time, we do not know why a steep electron temperature gradient aligns itself with the flat plate anode surface. As the discharge voltage was increased to 8 A, the plasma discharge became too unstable to be characterized, and a transition to full-plume mode was visually confirmed, which was similar to the SC4 (8 A, 1.5 sccm) test case.

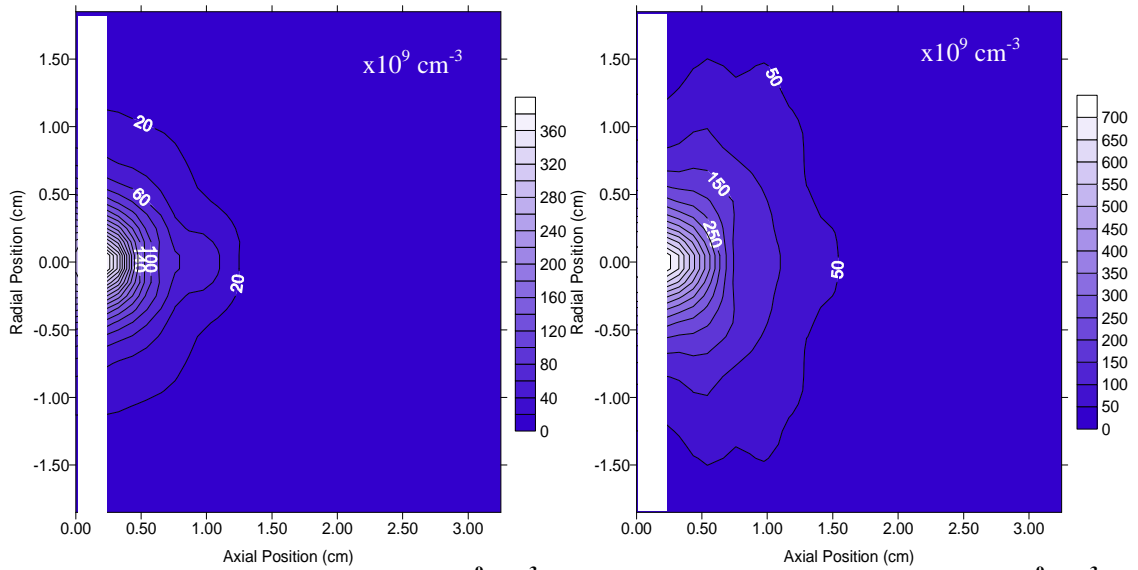


**Figure 60:**  $n_e$  contour plot for SCP4 ( $\times 10^9 \text{ cm}^{-3}$ ). **Figure 61:**  $n_e$  contour plot for SCP5 ( $\times 10^9 \text{ cm}^{-3}$ ).

Figure 60 through Figure 62 show the effect on plasma density as the discharge current was increased from 2 A to 6 A at 3 sccm of xenon. Figure 60 (SCP4, 2 A, 3 sccm) shows a standard expansion with peak densities of  $4 \times 10^{11} \text{ cm}^{-3}$ . Figure 61 (SCP5, 4 A, 3 sccm) shows again a standard expansion with peak densities reaching  $7.5 \times 10^{11} \text{ cm}^{-3}$ , roughly double that seen in Figure 60. A plasmoid is partially formed at 6 A, 3 sccm as shown in Figure 62 (SCP6) with peak densities around  $9 \times 10^{11} \text{ cm}^{-3}$  just in front of the

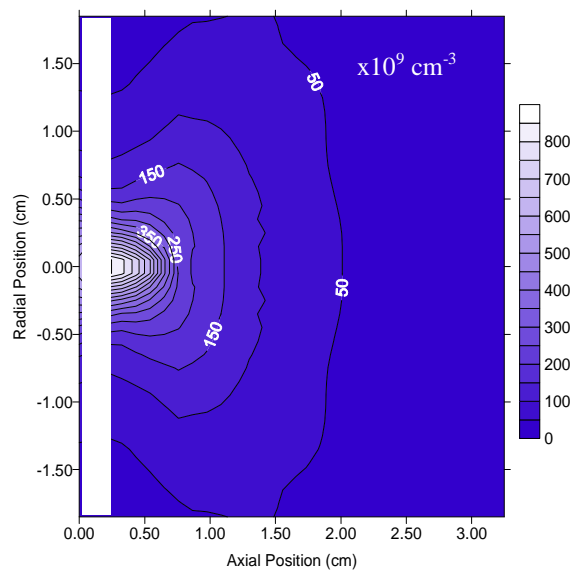


**Figure 62:**  $n_e$  contour plot for SCP6 ( $\times 10^9 \text{ cm}^{-3}$ ).

cathode.

The plasma potential and electron temperature plots for condition SCP6 (6 A, 3 sccm) can be seen in Figure 63 and Figure 64, respectively. The previously observed V-shaped valleys of Figure 43 and Figure 45 now contain cliff features (i.e., at 2-cm axially downstream from the cathode a quick drop in potential from 12 V to 9 V is present that corresponds to a 0.5 eV drop in electron temperature). In general, our study has found that areas of low plasma potential contain cooler electrons compared to areas of high

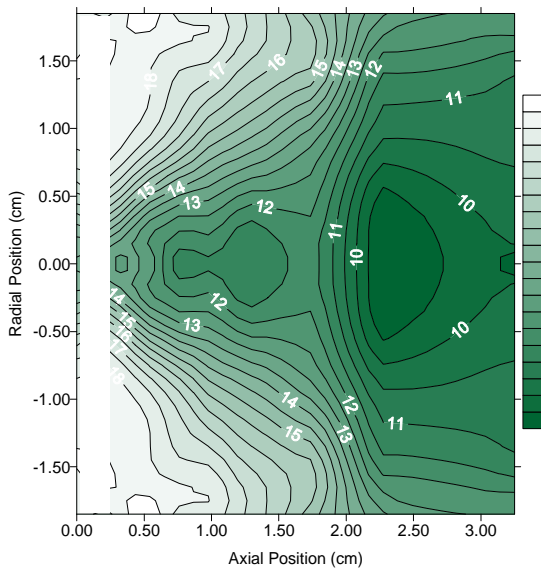


Figure 63:  $V_p$  contour plot for SCP6 (V).

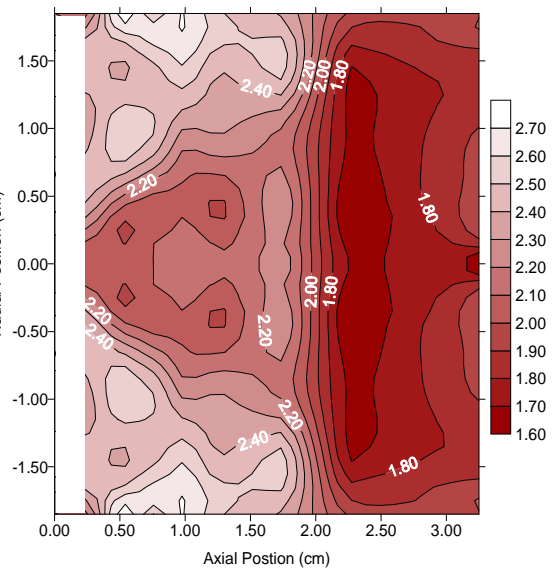
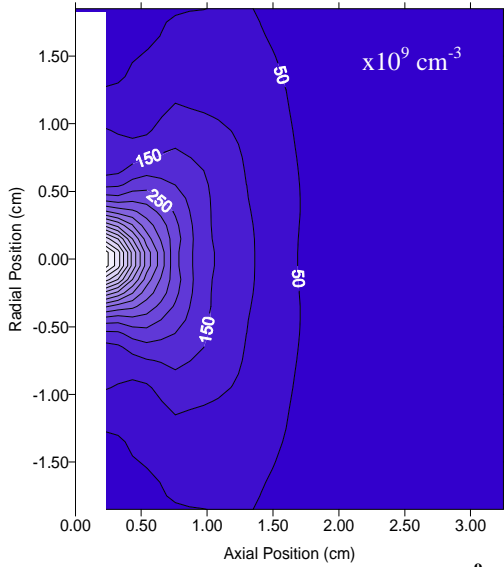
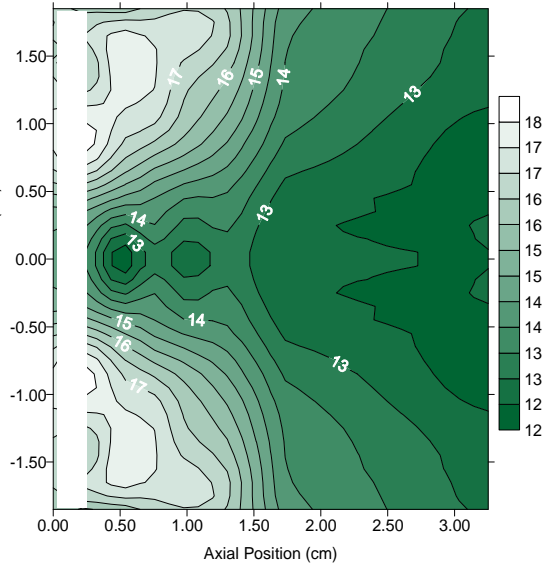


Figure 64:  $T_e$  contour plot for SCP6 (eV).

plasma potential.



**Figure 65:**  $n_e$  contour plot for SCP9 ( $\times 10^9 \text{ cm}^{-3}$ ).



**Figure 66:**  $V_p$  contour plot for SCP9 (V).

Figure 65, Figure 66, and Figure 67 contain plasma property contour plots obtained at test condition SCP9 (4 A, 4.5 sccm). In Figure 65 we again see a standard expansion that corresponds to a V-shaped potential map (Figure 66). A peak plasma density of  $10^{12} \text{ cm}^{-3}$  was measured. As in SCP6, a plasmoid is nearly formed at the higher flow rate condition of SCP9 (see Figure 65 and compare to Figure 40). At SCP9 (4 A, 4.5 sccm) the potential contour shows an interesting depression just in front of the cathode. This

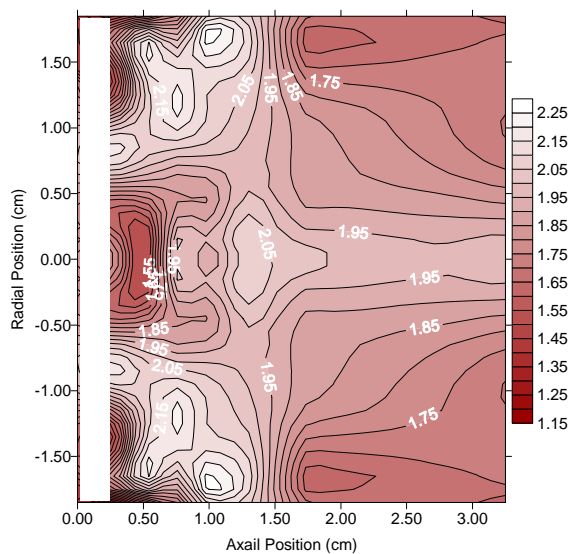


**Figure 67:**  $T_e$  contour plot for SCP9 (eV).

depression is also present in the temperature contour, dropping about 0.5 eV. While the V-shape seen previously is again present, the cliff of previous SCP configuration test cases is not. At higher flows, it may be that processes causing the cliff formation have moved closer to the cathode and are creating the temperature and potential depressions observed near the cathode. Table 5 contains a summary of contour structures seen in the SCP configuration tests.

Table 5: Contour plot shape comparison list for the simple cathode, near-plate anode test cases.

Operating Condition	$J_d$ (A)	$V_d$ (V)	$\dot{m}$ (sccm)	Pressure ( $\times 10^{-5}$ Torr)	$n_e$ Shape	$T_e$ Shape	$V_p$ Shape
SCP1	2	34.0	1.5	3.5	Standard Expansion	Cathode Depression	V Shaped Slight
SCP2	4	41.7	1.5	3.5	Std Exp. w/ Plasmoid	Constant	V Shaped Slight
SCP3	6	49.7	1.5	3.5	Plasmoid	Cliff	V Shaped
SCP4	2	31.1	3	5.9	Standard Expansion	Constant	Valley from Cath
SCP5	4	40.8	3	5.9	Standard Expansion	Constant	V Shaped
SCP6	6	44.9	3	5.9	Standard Exp. w/ Plasmoid	V Shaped w/ Cliff	V Shaped w/ Cliff
SCP7	8	55.1	3	5.9	Standard Expansion	Cathode Depression	V Shaped, Steep near Cath. Radially
SCP8	2	32.2	4.5	8.0	Standard Expansion	Cathode Depression	V Shaped
SCP9	4	34.0	4.5	8.0	Plasmoid	Valley from Cath w/ Cliff	V Shaped

### 5.3 Keeper Orifice Diameter = 2.7 mm (SK)

Tests of enclosed keeper configurations were performed with three different keeper orifice diameters using the near plate anode. For all tests, the keeper-to-cathode spacing

was set to 1.3 mm. Table 6 contains a list of operating conditions studied using the 2.7 mm diameter keeper orifice configuration.

Table 6: Operating conditions for the cathode configuration with an enclosed keeper (orifice dia. = 2.7 mm).

Operating Condition	$J_d$ (A)	$V_d$ (V)	$\dot{m}$ (sccm)	Pressure ( $\times 10^{-5}$ Torr)
*NA	2	36.5	1.5	3.8
SK1	4	41.5	1.5	3.8
		40.4		3.4
*NA	6	78.0	1.5	3.8
<hr/>				
*NA	2	29.5	3	5.6
SK2	4	37.8	3	5.6
		40.1		5.6
SK3	6	47.0	3	5.6
SK4	8	56.0	3	5.6
<hr/>				
SK5	2	32.6	4.5	8.0
SK6	4	39.5	4.5	8.0
SK7	6	47.5	4.5	8.0
SK8	8	55.7	4.5	8.0

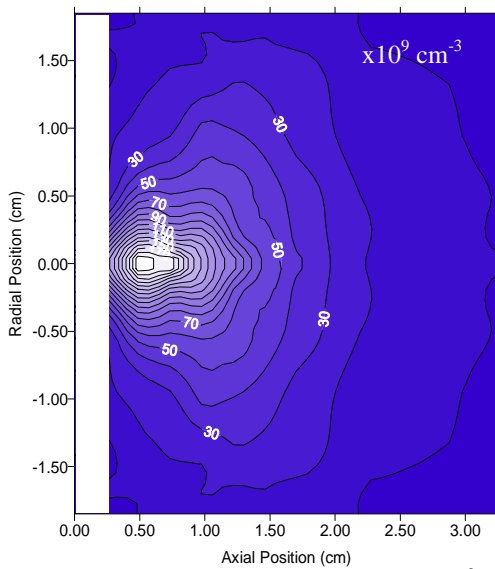


Figure 68:  $n_e$  contour plot for SK1 ( $\times 10^9 \text{ cm}^{-3}$ ).

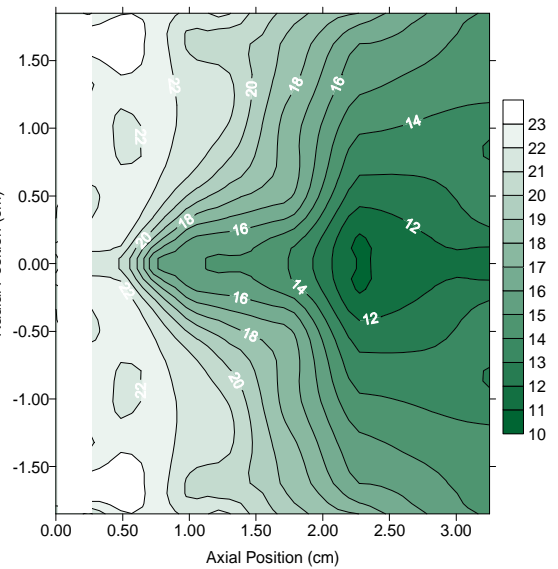
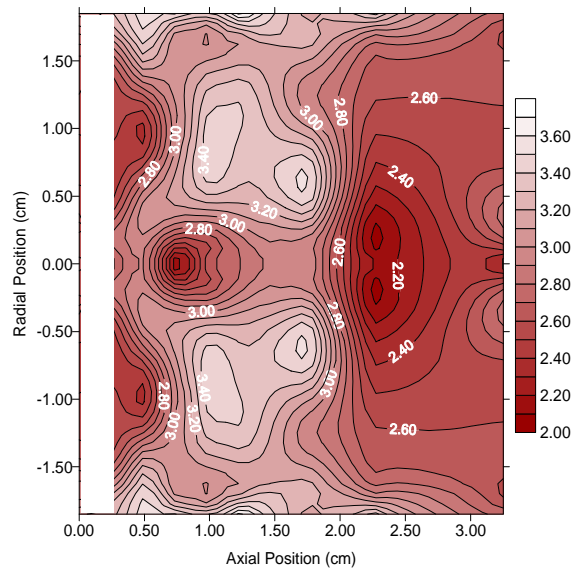


Figure 69:  $V_p$  contour plot for SK1 (V).

The plasma property contours shown in Figure 68 to Figure 70 were constructed for the only condition at 1.5 sccm that resulted in a stable plasma discharge. This was the 4 A case (the 2 A case was unstable and the 6 and 8 A cases corresponded to full-plume mode operation where the discharge voltage fluctuated  $\pm 5V$ ). In Figure 68 a fully developed plasmoid can be seen. Peak density in the plasmoid is roughly  $2 \times 10^{11} \text{cm}^{-3}$ . The unusual elongated shape of the plasmoid may be caused by the keeper orifice hole being small enough to enhance the neutral density along the cathode axis. Figure 69



**Figure 70:  $T_e$  contour plot for SK1 (eV).**

plasma potential contours show a v-shaped valley in the regions downstream of the cathode. Figure 70 electron temperature contours show peaks developing off axis and a cliff at  $z = 2$  cm.

Figure 71 through Figure 73 contain plasma density contours for test conditions where the current was increased from 4 to 8 A at a higher flow rate of 3 sccm. One can see that as the current doubles, the peak plasma density roughly doubles as well (from  $3 \times 10^{11} \text{cm}^{-3}$

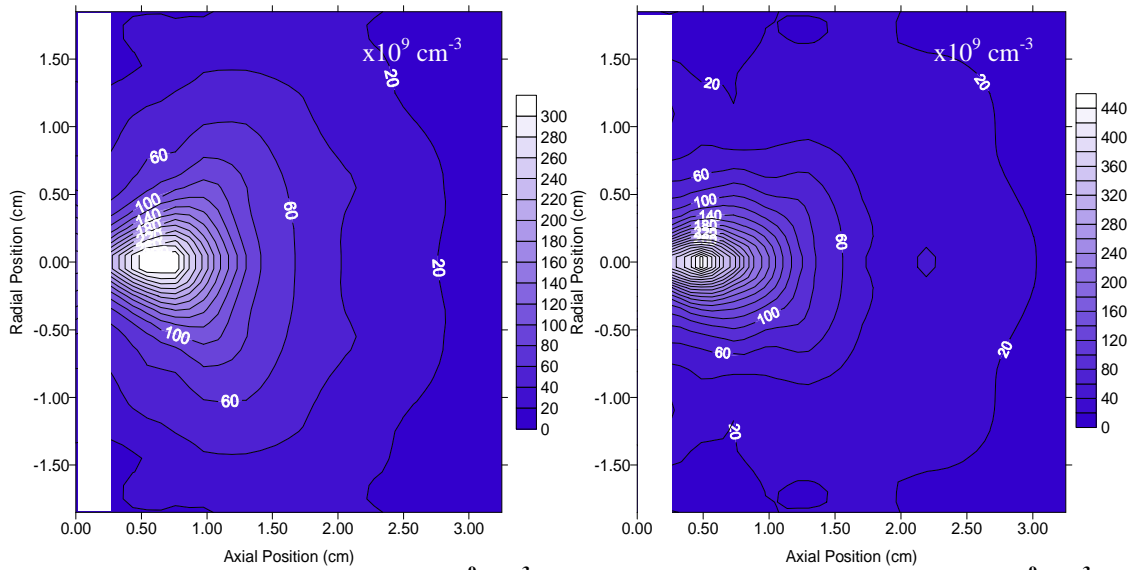


**Figure 71:  $n_e$  contour plot for SK2 ( $\times 10^9 \text{ cm}^{-3}$ ).** **Figure 72:  $n_e$  contour plot for SK3 ( $\times 10^9 \text{ cm}^{-3}$ ).**

to  $6 \times 10^{11} \text{ cm}^{-3}$ ). All three test conditions show the presence of well developed plasmoid structures.

Figure 74 and Figure 75 compare plasma potential for 4 and 8 A (3 sccm) where no significant differences are observed. Both contour plots range from about 20 to 10 V and both display v-shaped structures with about a 5 V drop. In addition no significant cliff structure was observed anywhere in either contour. In both cases, the base of the v-shape

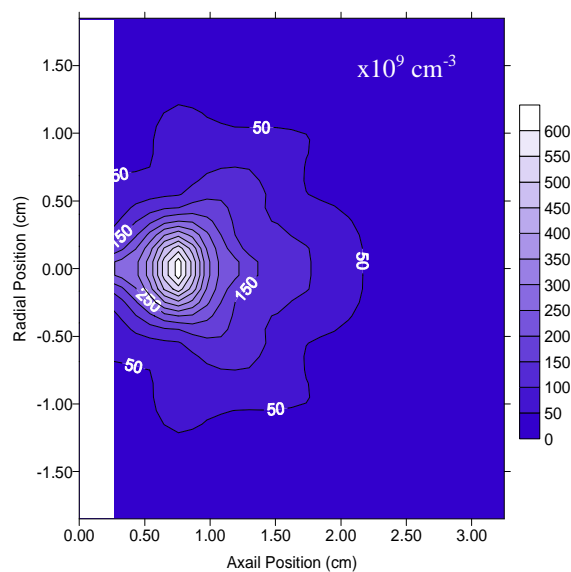


**Figure 73:  $n_e$  contour plot for SK4 ( $\times 10^9 \text{ cm}^{-3}$ ).**

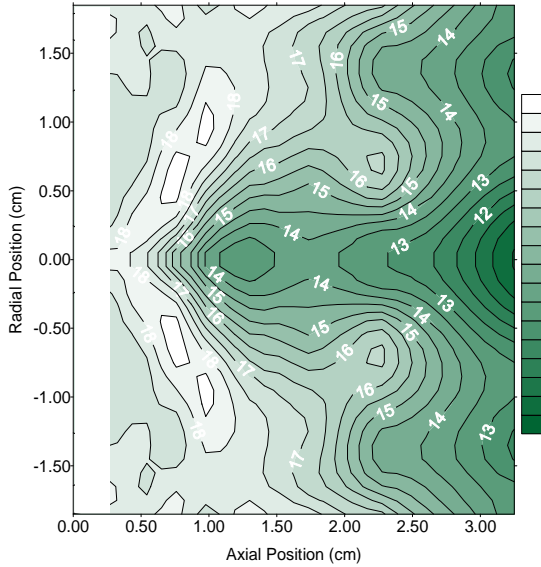


**Figure 74:  $V_p$  contour plot for SK2 (V).**

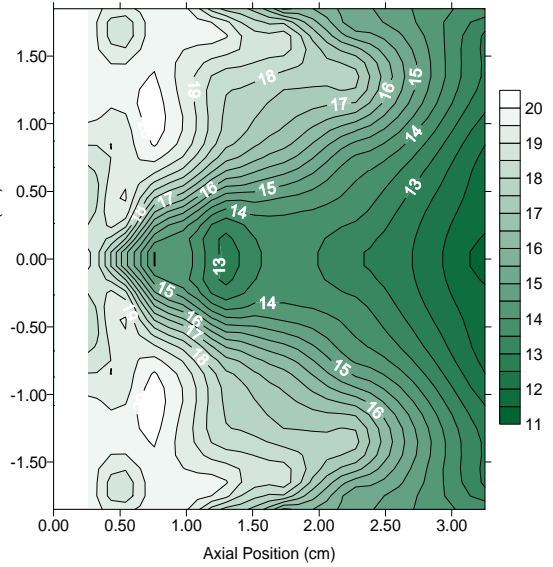


**Figure 75:  $V_p$  contour plot for SK4 (V).**

potential field lies under the center of the plasmoid.

Figure 76 and Figure 77 are electron temperature contours for both 4 and 8 A at 3 sccm. These temperature maps are similar to SK1 (Figure 70, 4 A, 1.5 sccm), but are quite different to those presented before. Here, no cliff was observed, but instead a hollow is seen directly in front of the cathode where the temperature drops about 1 eV. This hollow structure surrounded by peak formations may suggest the keeper is enhancing the neutral density along the axis of the cathode. Figure 77 suggests that areas directly under the plasmoid have slightly lower electron temperatures. Interestingly, in both Figure 76 and Figure 77 two peaks are present roughly at  $z=2.25$  cm and  $r=1$  cm. Assuming azimuthal symmetry, this contour suggests that a toroid or doughnut structure of high temperature electrons exists. The peaks in electron temperature lay directly on top of high voltage “peninsulas” seen in plasma potential plots in Figure 74 and Figure 75.

It was first thought that the electron temperature plots may be erroneous and the entire set of electron temperature contour plots was re-constructed for the SK case. It was found that all conditions with flow rates above 1.5 sccm exhibited electron temperature plots similar to those shown in Figure 76 and Figure 77. In fact Figure 70, an electron temperature plot for a condition at 1.5 sccm, does possess many of the features observed in Figure 76 and Figure 77, but with the addition of a cliff structure at a large axial location.

At 4.5 sccm very similar results to those above were found. Graphs for the final condition in this test (SK8, 8 A, 4.5 sccm) can be seen in Figure 78, Figure 79, and Figure 80. When compared to SK4 one can see that the plasmoid has grown in size slightly while dropping in temperature, maintaining the total random thermal current over a closed surface to around 8 A. Table 7 presents a summary of contour structures observed in the SK configuration.

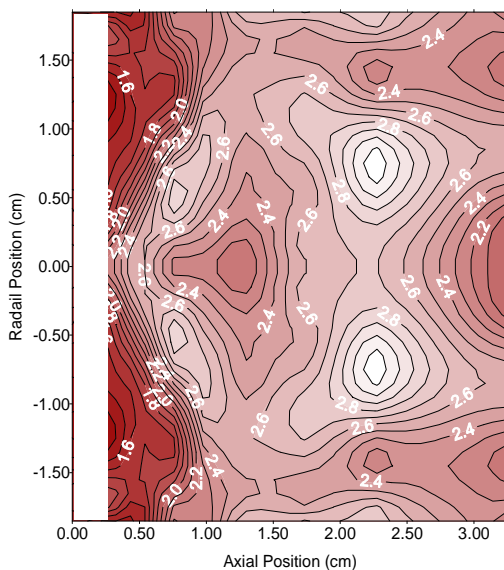


**Figure 76:  $T_e$  contour plot for SK2 (eV).**

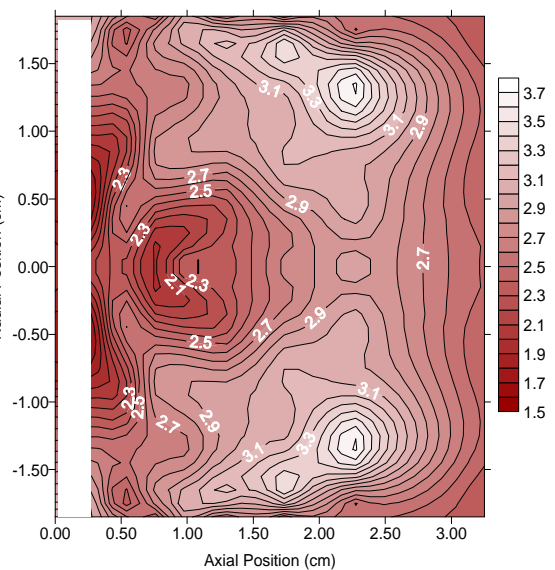


**Figure 77:  $T_e$  contour plot for SK4 (eV).**

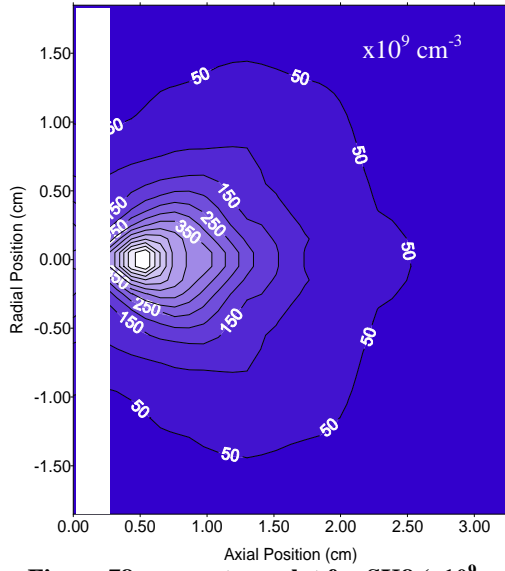


Figure 78:  $n_e$  contour plot for SK8 ( $\times 10^9 \text{ cm}^{-3}$ ).

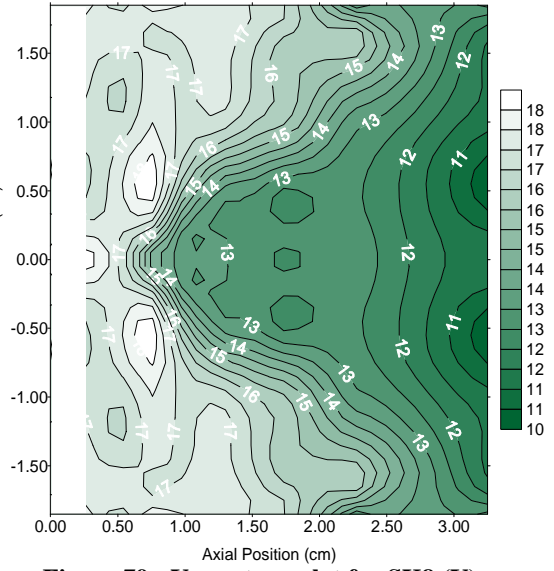


Figure 79:  $V_p$  contour plot for SK8 (V).

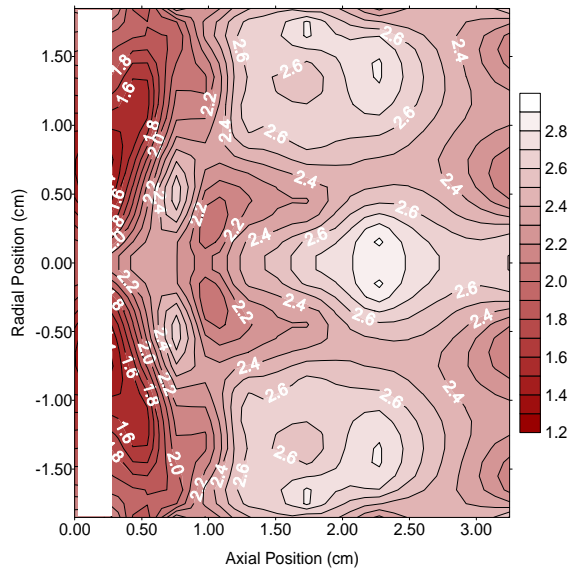


Figure 80:  $T_e$  contour plot for SK8 (eV).

Table 7: Contour plot shape comparison table for small orifice enclosed keeper case.

Operating Condition	J <sub>d</sub> (A)	V <sub>d</sub> (V)	$\dot{m}$ (sccm)	Pressure (x10 <sup>-5</sup> Torr)	n <sub>e</sub> Shape	T <sub>e</sub> Shape	V <sub>p</sub> Shape
SK1	4	41.5 40.4	1.5	3.8 3.4	Plasmoid	V Shaped w/ Cliff	V Shaped
SK2	4	37.8 40.1	3	5.6 5.6	Plasmoid	Cathode Depression	V Shaped w/ Plasmoid Depression
SK3	6	47.0	3	5.6	Plasmoid	Cathode Depression	V Shaped
SK4	8	56.0	3	5.6	Plasmoid	Cathode Depression	V Shaped w/ Plasmoid Depression
SK5	2	32.6	4.5	8.0	Plasmoid	Constant	V Shaped
SK6	4	39.5	4.5	8.0	Plasmoid	Cathode Depression	V Shaped
SK7	6	47.5	4.5	8.0	Plasmoid	Cathode Depression	V Shaped w/ Plasmoid Depression
SK8	8	55.7	4.5	8.0	Plasmoid	Cathode Depression	V Shaped

## 5.4 Keeper Orifice Diameter = 3.8 mm (MK)

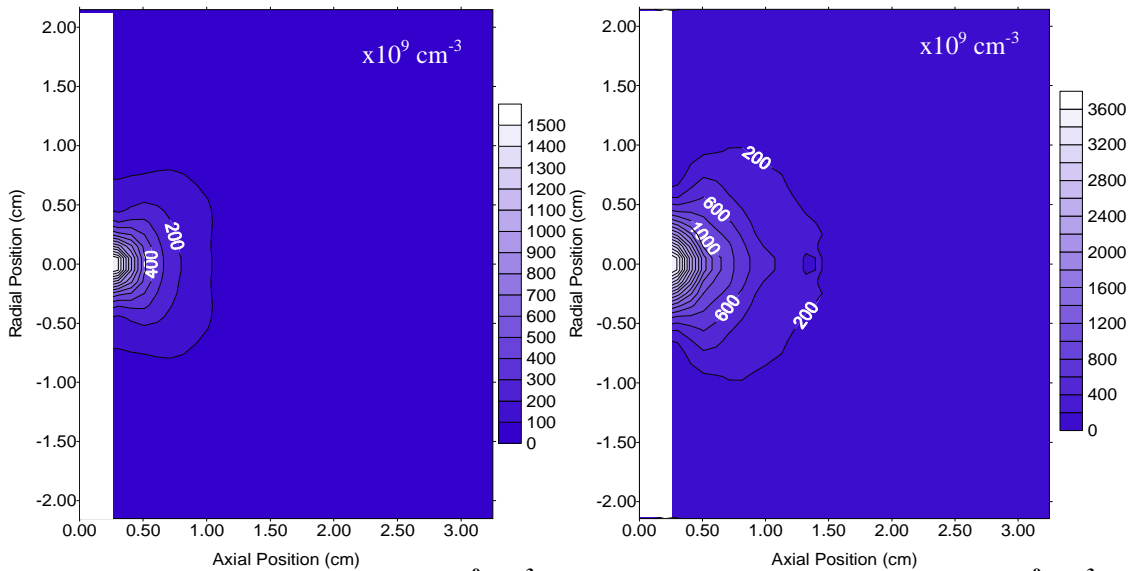
A diameter of 3.8 mm was selected for the second keeper orifice diameter. The keeper face plate was removed from the keeper and drilled to size. It was then re-spot welded to the keeper body. Conditions tested during this specific study are shown in Table 8.

Table 8: Cathode with Enclosed keeper of 3.8mm in diameter operating conditions

Operating Condition	J <sub>d</sub> (A)	V <sub>d</sub> (V)	$\dot{m}$ (sccm)	Pressure (x10 <sup>-5</sup> Torr)
MK1	2	36.7	1.5	4.2
MK2	4	42.4	1.5	4.2
MK3	6	50.2	1.5	4.2
MK4	8	56.9	1.5	4.2
MK5	2	34.1	3	5.9
MK6	4	41.8	3	5.9
MK7	6	46.2	3	5.9
MK8	8	53.8	3	5.9

MK9	2	33.8	4.5	7.3
MK10	4	32.5	4.5	7.3
MK11	6	43.7	4.5	7.3
MK12	8	52.7	4.5	7.3

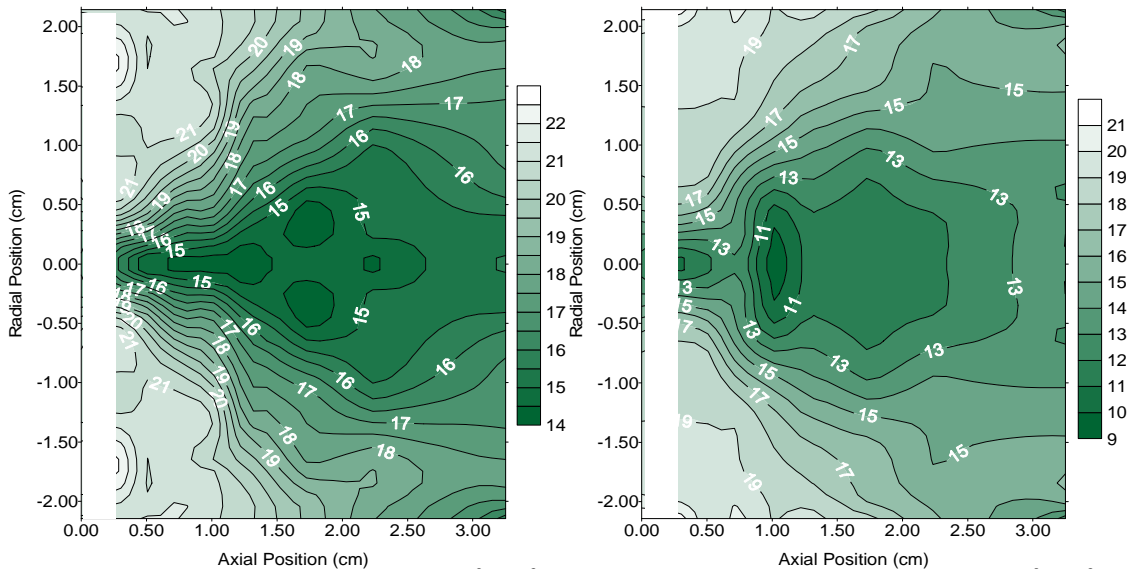
A definite change was noticed immediately when contour maps for this case (MK) were compared to those in the previous section (SK). Where previously every condition resulted in a plasmoid expansion structure, here every condition resulted in a monotonic



**Figure 81:**  $n_e$  contour plot for MK1 ( $\times 10^9 \text{ cm}^{-3}$ ). **Figure 82:**  $n_e$  contour plot for MK4 ( $\times 10^9 \text{ cm}^{-3}$ ).

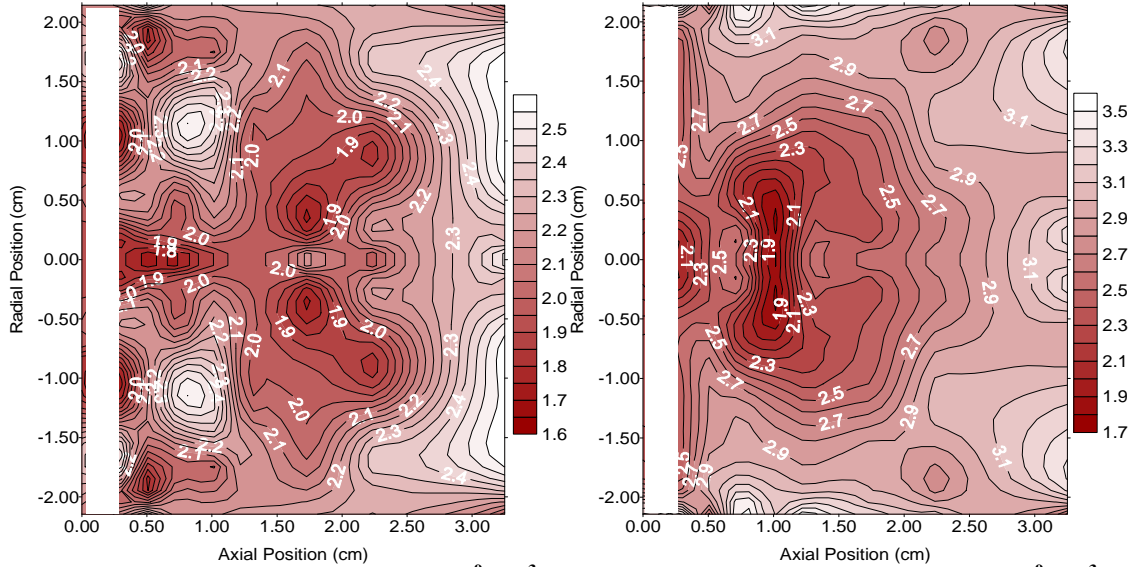
expansion. The small keeper orifice may offer significantly more surface area where plasma ions can re-combine and reduce plasma conductivity. To adjust, the small keeper orifice cathode apparently forms free-standing plasmoid structures to produce the plasma necessary to conduct the current being demanded of it. At this time, we do not know the conditions when a cathode is forced to create different plasma-bridge flow fields or the processes by which the cathode accomplishes this feat.

Figure 81 and Figure 82 display plasma density plots for the MK1 and MK4 cases, respectively. They correspond to a change in current from 2 to 8 A at a constant flow rate of 1.5 sccm. Both cases show standard expansion behavior. This is characteristic of all plasma density maps for the MK configuration. In Figure 81, the peak plasma density was  $1.6 \times 10^{12} \text{cm}^{-3}$ . Figure 82 (the 8 A, 1.5 sccm case) peaks at double the density of Figure 81, at about  $3.5 \times 10^{12} \text{cm}^{-3}$ . The random thermal current passing through the  $600 \times 10^9 \text{cm}^{-3}$  contour line was found to be 7.8 A, which is in good agreement with the



**Figure 83:  $V_p$  contour plot for MK1 ( $\times 10^9 \text{cm}^{-3}$ ).** **Figure 84:  $V_p$  contour plot for MK4 ( $\times 10^9 \text{cm}^{-3}$ ).**  
discharge current setting of 8 A.

Figure 83 and Figure 84 contain plasma potential maps for the above density contours. Figure 83 shows a v-shaped potential valley falling away from the cathode. The v-shaped ridgelines in this case blend into the base of the valley a little better than most reported previously. Figure 84, the potential plot for MK4 (8 A, 1.5 sccm), reveals an even smoother v-shaped valley. No cliff structure nearby the anode was observed during this test. The last two figures presented for 1.5 sccm are electron temperature plots for



**Figure 85:  $T_e$  contour plot for MK1 ( $\times 10^9 \text{ cm}^{-3}$ ).** **Figure 86:  $T_e$  contour plot for MK4 ( $\times 10^9 \text{ cm}^{-3}$ ).**

MK1 and MK4, respectively, in Figure 85 and Figure 85. Each displays a hollow structure corresponding to the broadening of the v-shape valley in the potential, again low temperatures at low potentials were observed.

Almost identical results were observed at 3 sccm where MK5 (2A), MK7 (6A), and MK8 (8A) all exhibit monotonic expansions. In addition, each test condition resulted in a v-shaped plasma potential structure valley and each exhibits nearly constant electron temperature with slight hollow structures forming at the base of the potential valleys. The only condition that differs from these is MK6 (4A, 3 sccm). Figure 87 and Figure 88 compare plasma density contours for MK5 (2A) and MK6 (4 A). Figure 88 displays a plasmoid expansion for the 4 A case, MK6. The peak plasma density in the plasmoid is significantly lower than the peak plasma density of the lower current, MK5 (2 A) monotonic expansion, as was common with most plasmoids when compared to monotonic expansions that occurred at nearby conditions.

Potential plots for each case above are shown in Figure 89 and Figure 90. Figure 89 again shows a common v-shaped valley for the standard expansion of MK5. In contrast, Figure 90 reveals a central tightening of the “V” into a near column and a slight hollow. Electron temperatures for both cases were mostly constant at about 2.2 eV. The peak plasma density at 8 A for the 3 sccm condition was around  $5 \times 10^{12} \text{cm}^{-3}$ . This is about a factor of 10 higher than the peak density seen in all of 8 A test conditions with the smaller keeper (SK) orifice configuration, where plasmoids were the only form of expansion that was observed. Increasing the orifice area seems to have the effect of increasing the plasma density immediately downstream of the cathode. This is not to say that higher densities did not exist in the small orifice configuration, they may have been simply confined to within the cathode-keeper spacing or nearby the keeper orifice.

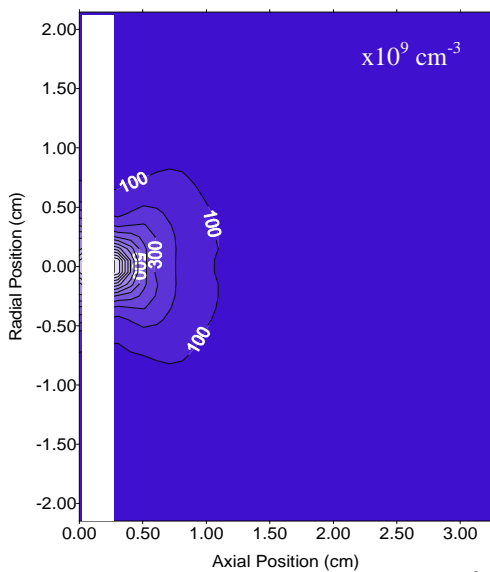


Figure 87:  $n_e$  contour plot for MK5 ( $\times 10^9 \text{cm}^{-3}$ ).

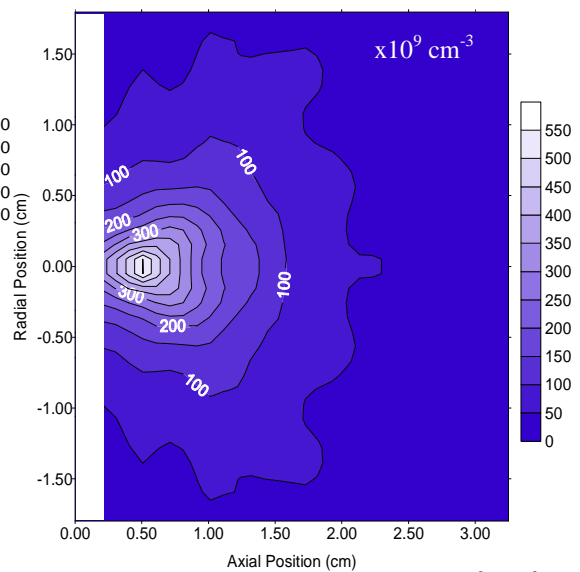
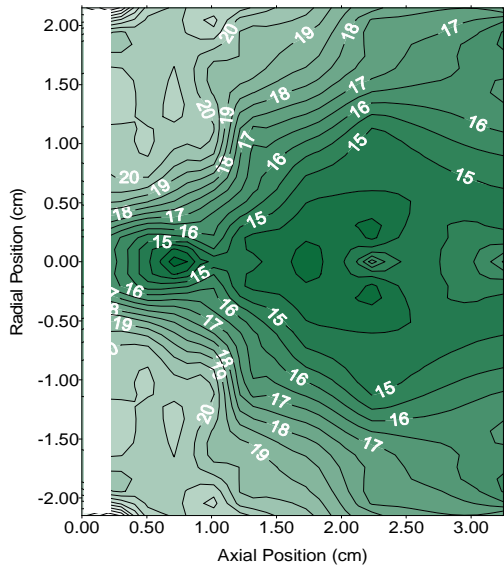
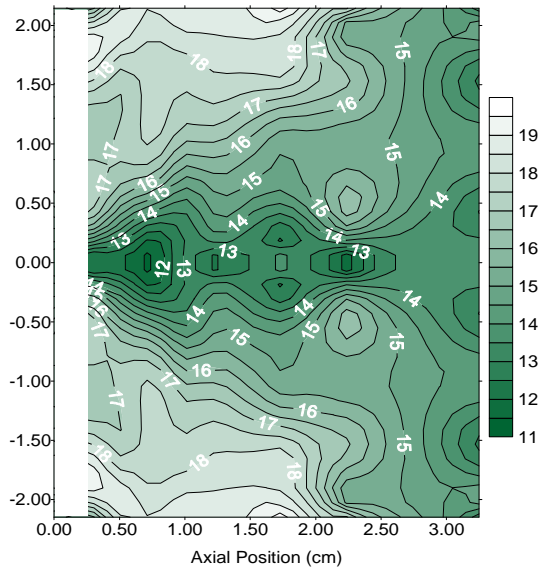


Figure 88:  $n_e$  contour plot for MK6 ( $\times 10^9 \text{cm}^{-3}$ ).



**Figure 89:  $V_p$  contour plot for MK5 (V).**



**Figure 90:  $V_p$  contour plot for MK6 (V).**

The higher flow rate condition of 4.5 sccm resulted in contour plots that were similar to the 3 sccm test condition. For this case we only plot data for the final condition, MK12 (8 A). Figure 91 and Figure 92 are plots of the plasma density and plasma potential, respectively. In Figure 91 we see a standard density expansion peaking just under  $5 \times 10^{12} \text{cm}^{-3}$ . As mentioned above, this expansion is similar to others observed at lower flow rate for the MK configuration. The density increases quickly near the cathode and dominates the contour plot to the point where features in the surrounding area are hard to discern. A radial sweep taken at  $z = 0.25 \text{ cm}$  for MK12 is shown in Figure 93. Here an increase of three orders of magnitude in density can be seen near the cathode center line ( $r = 0 \text{ cm}$ ). The plasma potential plot of Figure 92 again reveals a v-shaped valley falling away from the cathode. At this condition, the bottom of the valley structure is broader and flatter than those seen previously. Table 9 contains a summary of structures observed during the MK study.

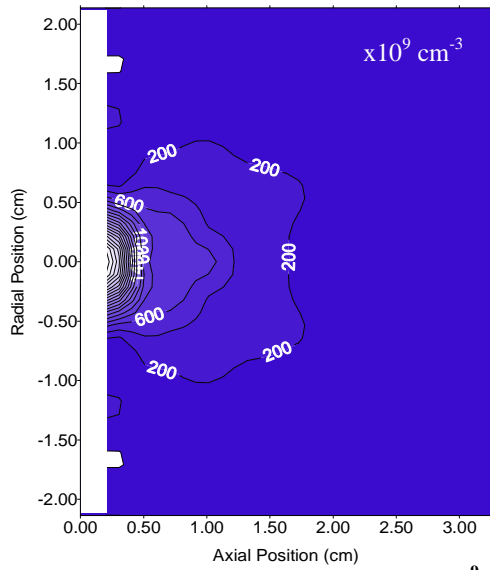


Figure 91:  $n_e$  contour plot for MK12 ( $\times 10^9 \text{ cm}^{-3}$ ).

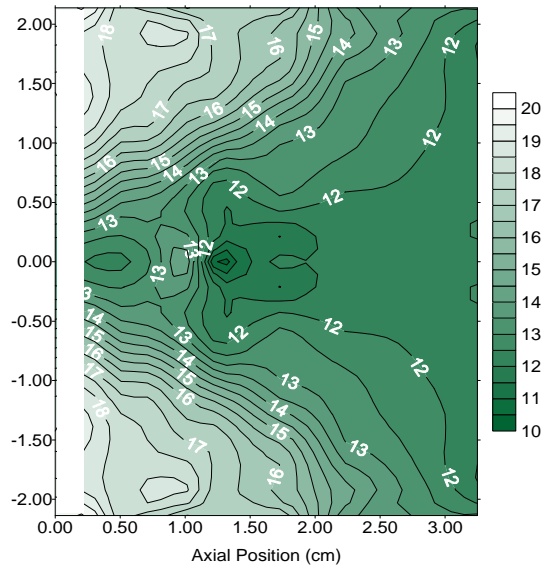


Figure 92:  $V_p$  contour plot for MK12 (V).

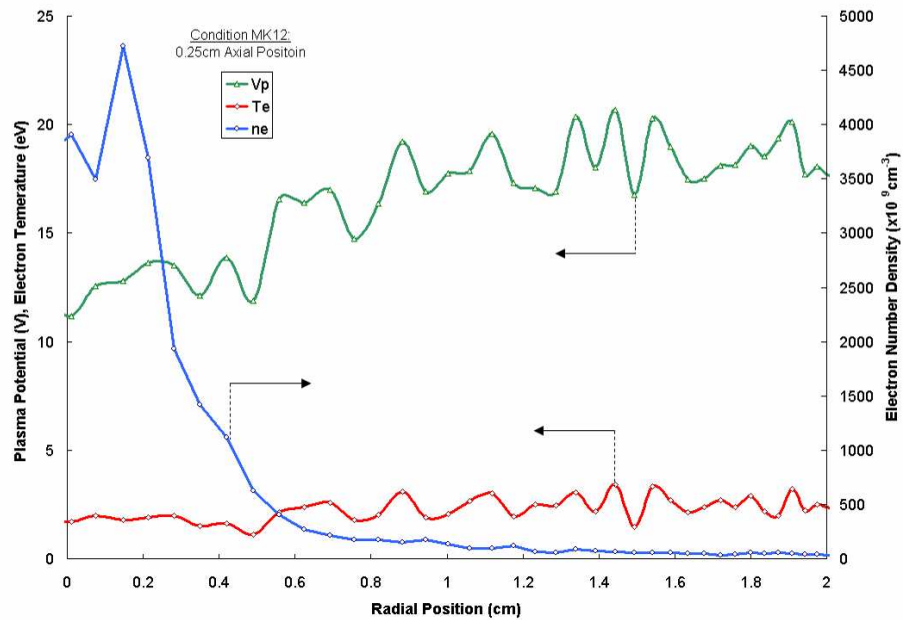


Figure 93: Single radial sweep at 0.25 cm axial position for MK12. Showing three orders of magnitude increase in density close to the cathode. Also displayed are the plasma potential and electron temperature profiles.

Table 9: Contour plot shape comparison table for medium orifice, enclosed keeper configuration.

Operating Condition	$J_d$ (A)	$V_d$ (V)	$\dot{m}$ (sccm)	Pressure ( $\times 10^{-5}$ Torr)	$n_e$ Shape	$T_e$ Shape	$V_p$ Shape
MK1	2	36.7	1.5	4.2	Standard Expansion	Central Depression	V Shaped
MK2	4	42.4	1.5	4.2	Standard Expansion	Constant	V Shaped
MK3	6	50.2	1.5	4.2	Standard Exp. w/ Plasmoid	Constant	V Shaped
MK4	8	56.9	1.5	4.2	Standard Exp. w/ Plasmoid	Cathode Depression	V Shaped
MK5	2	34.1	3	5.9	Standard Expansion	Constant	V Shaped
MK6	4	41.8	3	5.9	Plasmoid	Cathode Depression	V Shaped
MK7	6	46.2	3	5.9	Standard Expansion	Cathode Depression	V Shaped
MK8	8	53.8	3	5.9	Standard Expansion	Cathode Depression	V Shaped
MK9	2	33.8	4.5	7.3	Standard Expansion	Constant	V Shaped Slight
MK10	4	32.5	4.5	7.3	Standard Expansion	Constant	V Shaped
MK11	6	43.7	4.5	7.3	Standard Expansion	Constant	V Shaped
MK12	8	52.7	4.5	7.3	Standard Expansion	Constant w/ Central Depression	V Shaped

## 5.5 Keeper Orifice Diameter = 4.75mm (LK)

The largest keeper orifice diameter studied was 4.75 mm, equaling that of the NSTAR discharge cathode. A list of test conditions for this configuration is shown in Table 10.

Table 10: Operating conditions for a keeper orifice diameter of 4.7 mm.

Operating Condition	$J_d$ (A)	$V_d$ (V)	$\dot{m}$ (sccm)	Pressure ( $\times 10^{-5}$ Torr)
LK1	2	36.4	1.5	3.4
LK2	4	42.3	1.5	3.4
LK3	6	51.1	1.5	3.4
LK4	8	57.0	1.5	3.4
LK5	2	34.6	3	5.2
LK6	4	42.2	3	5.2
LK7	6	45.7	3	5.2
LK8	8	54.5	3	5.2
LK9	2	34.5	4.5	6.6
LK10	4	34.5	4.5	6.6
LK11	6	44.5	4.5	6.6
LK12	8	53.5	4.5	6.6

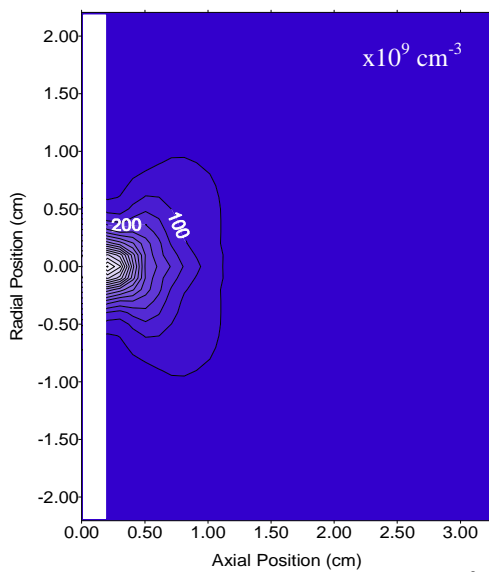


Figure 94:  $n_e$  contour plot for LK1 ( $\times 10^9 \text{ cm}^{-3}$ ).

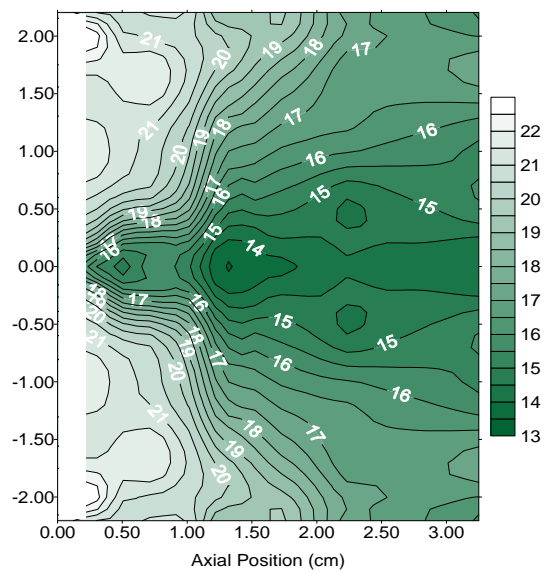
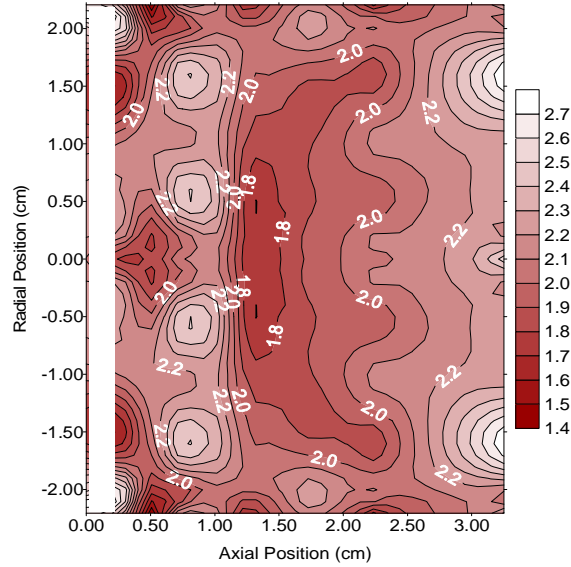
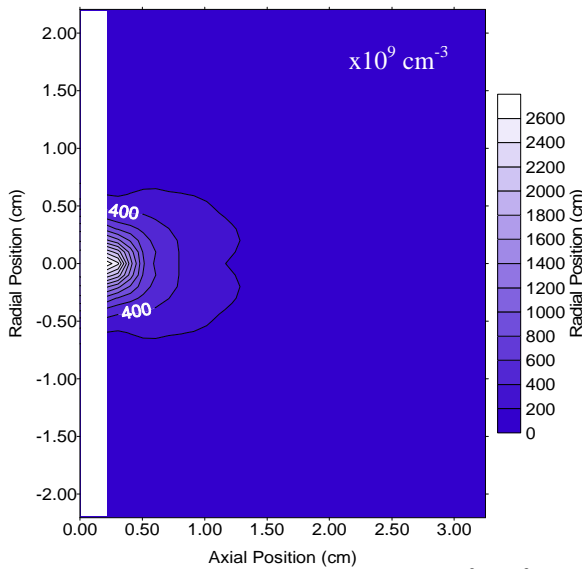


Figure 95:  $V_p$  contour plot for LK1 (V).



**Figure 96:  $T_e$  contour plot for LK1 (eV).**

Results similar to those observed with the MK configuration were obtained. Figure 94, Figure 95, and Figure 96 are contour plots taken from the condition of 2 A at 1.5sccm (LK1). Figure 94 plasma density contours reveal a standard expansion with a peak density just under  $10^{12}\text{cm}^{-3}$ . Figure 95 plasma potential contours reveal the common v-shaped valley. However, a slight cliff structure is shown at  $z = 1$  cm. This cliff in plasma potential corresponds to a  $\sim 1$  eV drop in electron temperature, as shown in Figure 96. It



**Figure 97:  $n_e$  contour plot for LK4 ( $\times 10^9 \text{ cm}^{-3}$ ).**

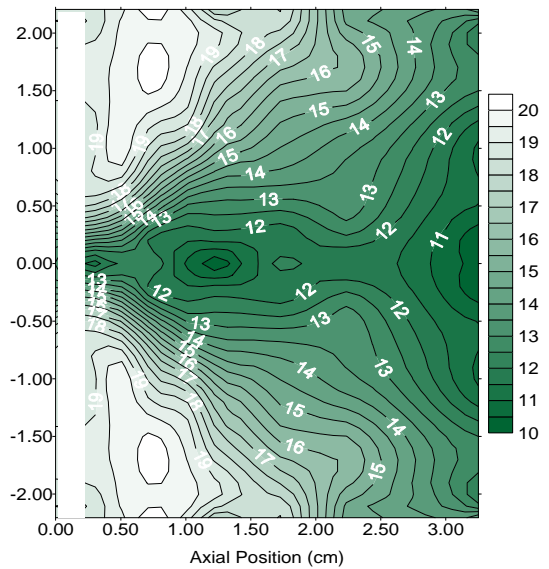


**Figure 98:  $V_p$  contour plot for LK4 (V).**

is odd to see this cliff reappear from the SK case. Although the cliff was present at LK1 (2 A, 1.5 sccm), it is not as strong as those seen with the SK configuration and the cliff in plasma potential is not present in any LK test conditions.

Figure 97, Figure 98, and Figure 99 contain contours taken at LK4 (8 A, 1.5 sccm). Here again we see a monotonic expansion in Figure 97 and a v-shaped valley falling away from the cathode in Figure 98, however, no cliff structure is present. An electron temperature rise is observed to occur in regions corresponding to the walls of the v-shaped potential valley.

As the flow is increased from 1.5 sccm to 3 sccm we again see similar trends. Figure 100, Figure 101, and Figure 102 are contours of density, potential, and temperature taken from condition LK5 (2A, 3 sccm). A monotonic density expansion is observed with a peak just under  $10^{12} \text{ cm}^{-3}$  and a v-shaped potential valley falling away from the cathode. Also again, at 2 A, some evidence of a slight cliff structure is observed. At  $z=1.25 \text{ cm}$  the potential drops to around 14 V (at  $r=0 \text{ cm}$ ) from about 19 V (at  $r=0.6 \text{ cm}$ ). This

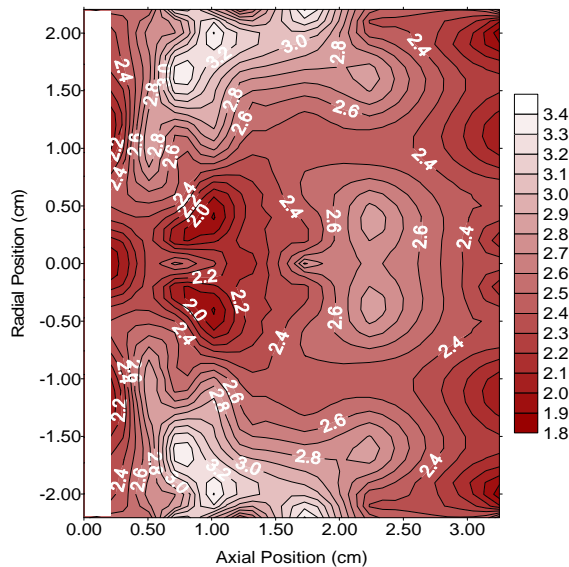


**Figure 99:  $T_e$  contour plot for LK4 (eV).**

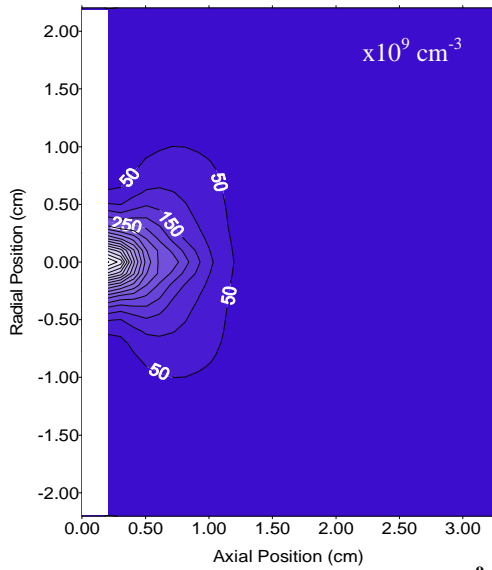


Figure 100:  $n_e$  contour plot for LK5 ( $\times 10^9 \text{ cm}^{-3}$ ).

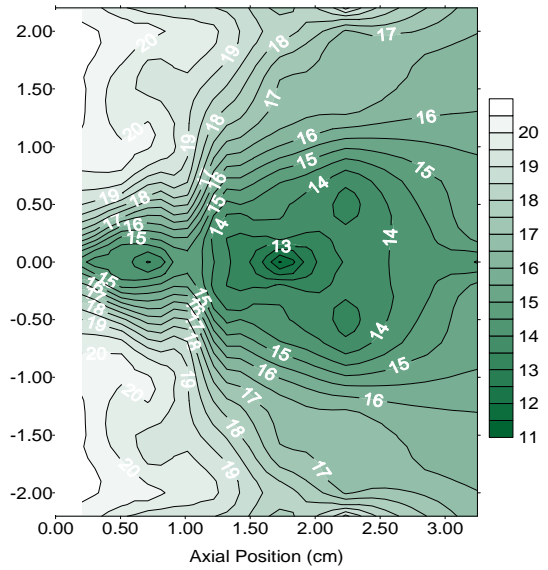


Figure 101:  $V_p$  contour plot for LK5 (V).

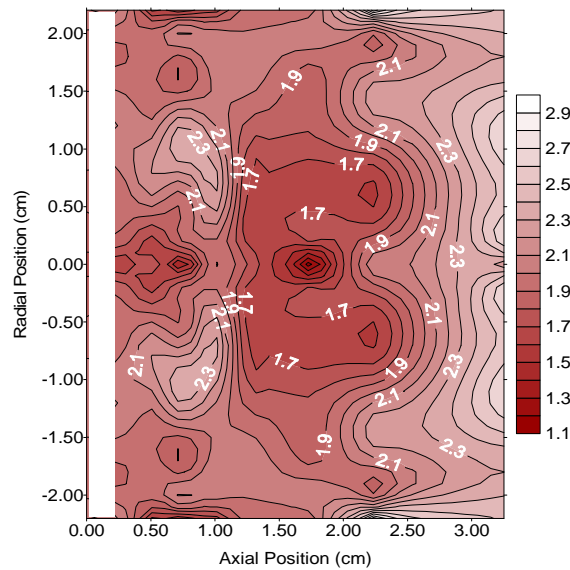


Figure 102:  $T_e$  contour plot for LK5 (eV).

potential structure corresponds to a drop in temperature of about 0.5 eV, as shown in Figure 102. As before, the cliff is rather weak.

As the current was increased to 8 A, conditions changed much as they did for the 1.5 sccm case. Density, still in a monotonic expansion, increased to a peak value above  $2 \times 10^{12} \text{ cm}^{-3}$  and the potential “V” was formed. Again at 8A no valley was observed in

temperature, however, a slight increase in temperature nearby the regions on the plasma potential “V” walls was observed.

For 4.5 sccm, as in both the 1.5 and 3 sccm tests, all conditions displayed a monotonic density expansion with a v-shaped potential valley structure. Slight temperature changes were observed at low current, slowly flattening out as the current was increased. Figure 103, Figure 104, and Figure 105 show density, potential, and temperature plots for condition LK12. Peak density in this case rose to about  $5 \times 10^{12} \text{cm}^{-3}$  and the potential “V” was broadened a bit. Also, a slight temperature decrease was observed near the cathode surrounded by a region of constant temperature of 2.4 eV. Table 11 is a summary of contour structures observed in the LK configuration tests.

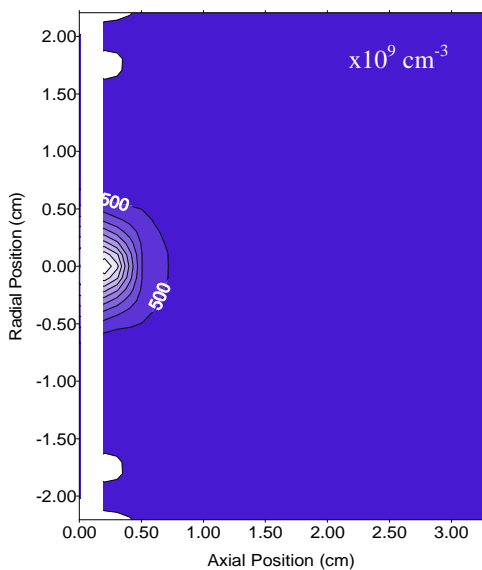


Figure 103:  $n_e$  contour plot for LK12 ( $\times 10^9 \text{cm}^{-3}$ ).

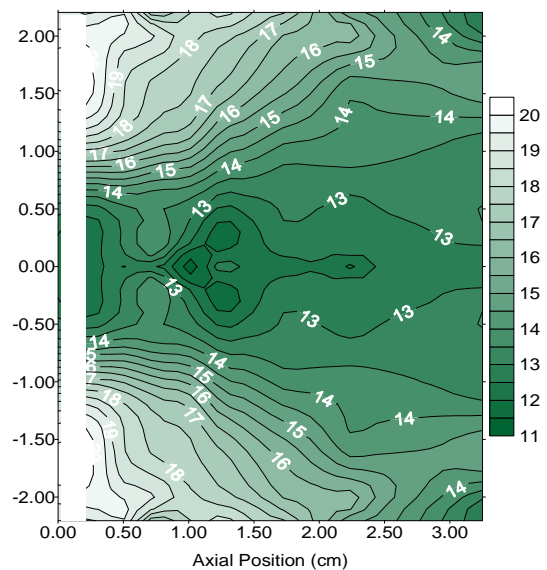


Figure 104:  $V_p$  contour plot for LK12 (V).

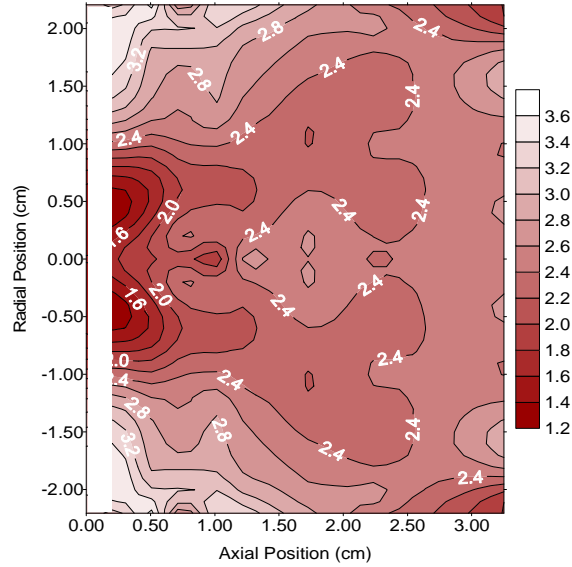


Figure 105:  $T_e$  contour plot for LK12 (eV).

Table 11: Contour plot shape comparison table for NSTAR orifice enclosed keeper case.

Operating Condition	$J_d$ (A)	$V_d$ (V)	$\dot{m}$ (sccm)	Pressure ( $\times 10^{-5}$ Torr)	$n_e$ Shape	$T_e$ Shape	$V_p$ Shape
LK1	2	36.7	1.5	4.2	Standard Exp. w/ Plasmoid	Constant w/ Cliff	V Shaped w/ Cliff
LK2	4	42.4	1.5	4.2	Standard Expansion	Const w/ Cath Depression	V Shaped
LK3	6	50.2	1.5	4.2	Standard Expansion	Constant	V Shaped
LK4	8	56.9	1.5	4.2	Standard Expansion	Const w/ Cath Depression	V Shaped
LK5	2	34.1	3	5.9	Standard Expansion	Constant	V Shaped
LK6	4	41.8	3	5.9	Standard Expansion	Constant	V Shaped
LK7	6	46.2	3	5.9	Standard Expansion	Constant	V Shaped
LK8	8	53.8	3	5.9	Standard Expansion	Constant	V Shaped
LK9	2	33.8	4.5	7.3	Standard Expansion	Constant	V Shaped
LK10	4	32.5	4.5	7.3	Standard Expansion	Constant	V Shaped
LK11	6	43.7	4.5	7.3	Standard Expansion	Constant	V Shaped
LK12	8	52.7	4.5	7.3	Standard Expansion	Constant	V Shaped

## 5.6 Cathode in a Magnetic Field with a Plate Anode (MP)

The effect of an axial magnetic field on the discharge plasma of our hollow cathode is presented next. The same enclosed keeper and cathode used in previous tests was utilized in this configuration. For the first case examined under the presence of a magnetic field, the near-field, flat-plate anode was left in place. It was observed in early testing that the discharge of the cathode was highly collimated and the discharge current was collected on a relatively small area of the anode located on the axis of the cathode. This caused the anode to glow red hot at the plasma attachment point. For fear of melting the anode, only measurements at 2 A and 4 A emission currents at 1.5 sccm were performed. Table 12 lists the details of these two operating conditions that are designated MP1 and MP2.

Table 12: Cathode in axial magnetic field with plate anode

Operating Condition	$J_d$ (A)	$V_d$ (V)	$\dot{m}$ (sccm)	Pressure ( $\times 10^{-5}$ Torr)
MP1	2	26.6	1.5	4.2
MP2	4	25.9	1.5	4.2

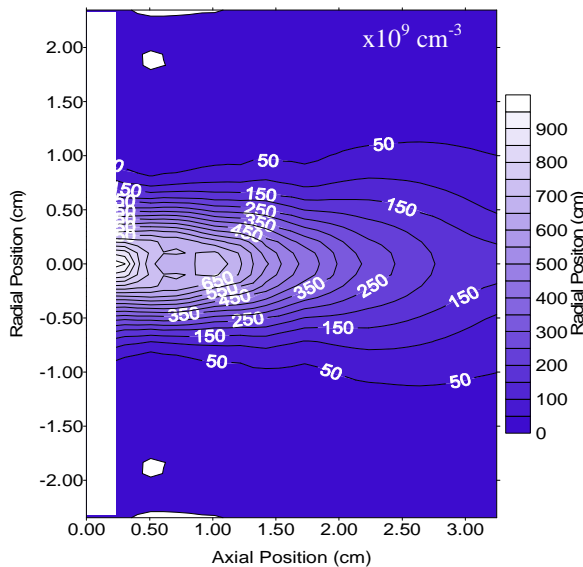


Figure 106:  $n_e$  contour plot for MP1 ( $\times 10^9 \text{ cm}^{-3}$ ).

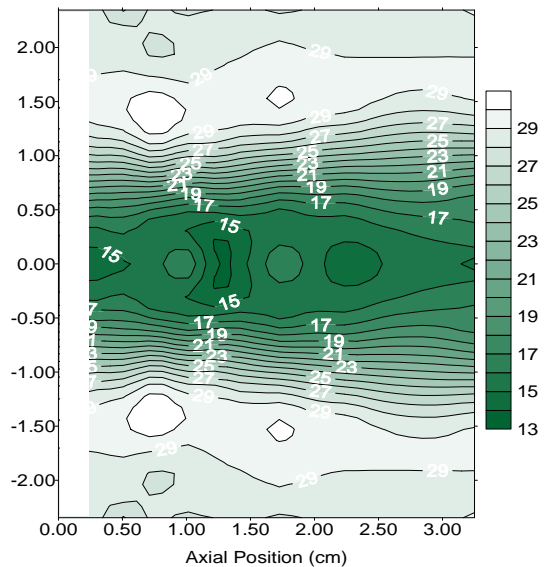
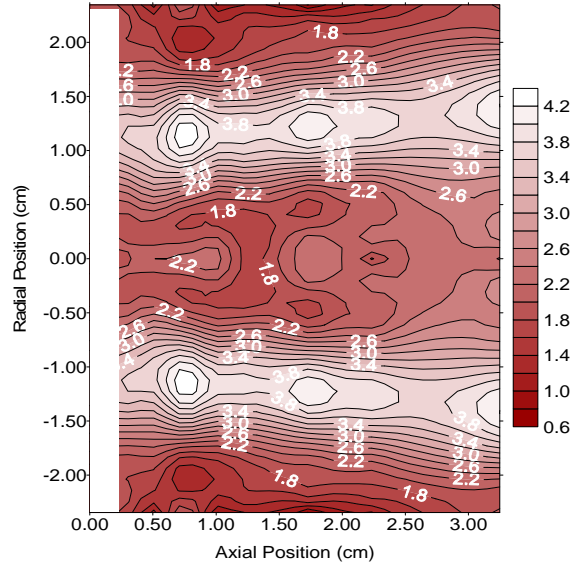


Figure 107:  $V_p$  contour plot for MP1 (V).



**Figure 108:  $T_e$  contour plot for MP1 (eV).**

As mentioned above, the inclusion of an axial magnetic field was expected to confine the discharge plasma along the cathode axis. Figure 106, Figure 107, and Figure 108 show contour plots created from the MP1 operating condition (2 A, 1.5 sccm), and, as expected, a drastic change was observed between these contour plots and ones constructed from measurements made without a magnetic field. Specifically, a completely new plasma density expansion is shown in Figure 106. This expansion is very collimated and extends further into the measurement field than other expansions shown above. We will refer to this expansion type as a plasma “jet” in the text to follow. The plasma jet observed in Figure 106 displays a peak density of  $1 \times 10^{12} \text{cm}^{-3}$ . However, densities just below the peak extend almost ten times farther into the measurement field compared to expansions measured without a magnetic field. The magnetic field strength nearby the cathode is about 100 gauss, giving the electrons a gyro radius of about 0.3 mm at 2 eV. Xenon ions at an assumed (low energy) of 0.2 eV on the other hand have a gyro radius of several centimeters at this field strength.

It is noted that the  $250 \times 10^9 \text{ cm}^{-3}$  contour in Figure 106 has an area of about  $7.8 \text{ cm}^2$ . The random thermal current of electrons across this surface is  $\sim 7.6 \text{ A}$ , which is quite a bit larger than the  $2 \text{ A}$  emission current condition for MP1. However, when one integrates the random thermal current density across a plane oriented perpendicular to the cathode axis, a value closer to the expected  $2 \text{ A}$  is obtained. Obviously the electrons along a particular contour oriented parallel to the applied magnetic field are being contained. Although electrons along axially oriented contour lines are being confined in the radial direction, it is noted that there is a gradient of potential in the radial direction that is perpendicular to the applied magnetic field (see Figure 107). The rate of electrons being supplied to the radial boundary of the potential gradient is difficult to determine, but, if the core of the plasma jet is sufficiently turbulent, this rate could be non trivial. It is noted in this case that a significant level of azimuthal (Hall) current is very likely to develop in the region where the potential gradient exists.

The plasma potential contour shown in Figure 107 displays a canyon or trench structure, following the plasma jet of Figure 106. The walls of this canyon are relatively steep, increasing almost  $15 \text{ V}$  over a radial distance of  $0.5 \text{ cm}$ , with a base voltage around  $13 \text{ V}$ . This canyon has the effect of collecting and trapping low energy ions on the cathode centerline, and the anode end of the trench should reflect ions back toward the cathode. Data presented by Jameson et al. show similar potential structure result when an axial magnetic field is present<sup>36</sup>, although an even greater potential increase on axis was seen in their study, which was performed at a higher discharge current.

Electron temperature contours are shown in Figure 108 for MP1 ( $2 \text{ A}$ ,  $1.5 \text{ sccm}$ ). Here we have a rather interesting feature of symmetric high temperature ridgelines lying

directly over the walls of the plasma potential structure. Another interesting result to note is that, at radial positions past the ridge, the electron temperature falls back to the value measured on the cathode centerline. Electron heating is occurring on the potential canyon walls causing this 3 eV rise in temperature, and this result supports our supposition that a significant azimuthal current may have developed. The processes causing the dramatic rise in electron temperature may also tie into observations of high energy ions made with remotely located probes that were sighted at zenith angles just off centerline and at 90° from centerline of an NSTAR discharge chamber.<sup>23,26</sup>

As alluded to above, with an applied magnetic field, some azimuthal current may be present. Ohm's Law is written as:

$$\mathbf{j} = \sigma_c \cdot \mathbf{E} \quad 5.1$$

Where  $\sigma_c$  is the conductivity, being in this case a tensor. Equation 5.1 can be expanded and converted into cylindrical coordinates as the following:

$$\begin{pmatrix} j_r \\ j_\theta \\ j_z \end{pmatrix} = \frac{q^2 \cdot n_e}{m_e} \cdot \begin{pmatrix} \frac{v_e}{v_e^2 + \omega_e^2} \cdot \cos(\theta) & \frac{-\omega_e}{v_e^2 + \omega_e^2} \cdot \sin(\theta) & 0 \\ -\frac{\omega_e}{v_e^2 + \omega_e^2} \cdot \sin(\theta) & \frac{v_e}{v_e^2 + \omega_e^2} \cdot \cos(\theta) & 0 \\ 0 & 0 & \frac{1}{v_e} \end{pmatrix} \cdot \begin{pmatrix} E_x \\ E_y \\ E_z \end{pmatrix} \quad 5.2$$

The equation above assumes that a magnetic field is applied only in the axial (z) direction. Also, the neutral density near the cathode may be enhanced above the background density due to flow from the cathode, but will drop to lower values as a

function of distance from the cathode. Therefore the electron-neutral collision frequency can be written as:

$$v_e = \sqrt{\frac{8 \cdot k_b \cdot T_e}{\pi \cdot m_e}} \cdot \sigma_{en} \cdot \left( n_o + \frac{n' \cdot \cos(\theta)}{\pi \cdot r^2 \cdot v_o} \right) \quad 5.3$$

By applying the measured values for plasma density, potential, and temperature to the above Equation (Eq. 5.2), an estimate for the azimuthal current ( $j_\theta$ ) can be made for MP1. Figure 109 shows the azimuthal current density in A/m<sup>2</sup> as a function of radial and axial position. As can be seen, the most intense azimuthal current density is found where the plasma density is greatest, just at the start of the potential trench observed in Figure 106. By integrating over all positive radial positions (the dotted area show in Figure 109), we calculate that the total azimuthal current in this region to be 0.657A, some 30% of the discharge current (2A). While this does not account for the 7.6A of assumed random thermal current, it does point to the fact that with an applied magnetic field, plasma expansion is not strictly axial to the anode and may be much more complex. It is also noted that the 0.657A azimuthal current value is the net current, and, in fact, the peak (local) azimuthal current coming out of the r-z plane may be greater due to the two regions shown in blue near the centerline that flow into the r-z plane (in the opposite direction of the red colored zones). The regions of positive and negative azimuthal current density suggest the presence of a complex counter flow system.

Lastly, as a check on our azimuthal current density calculations, we can measure the current carried by the drift velocity induced between the electric and magnetic field. This current can be written as:

$$j_d = q \frac{E_{\perp}}{|B|} n_e \quad 5.4$$

The integrated drift current in the upper half of Figure 109 was again calculated to be

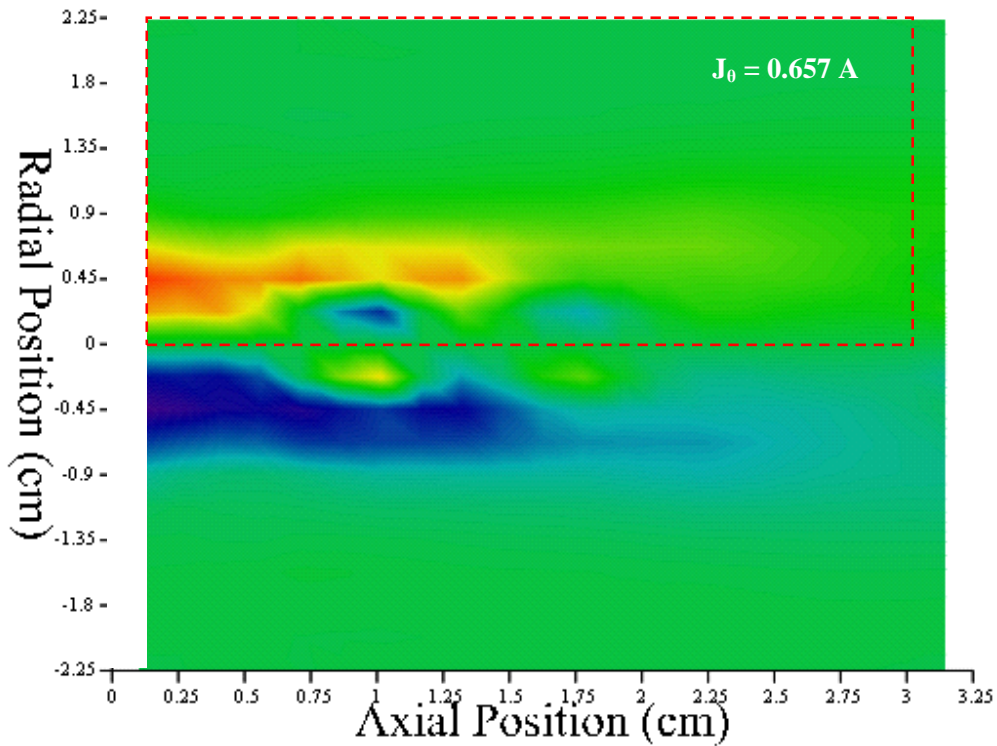


**Figure 109: Azimuthal Current Density for MP1 ( $J_D = 2A$ ,  $m = 1.5\text{sccm}$ ).**

0.657 A, suggesting that the predicted azimuthal current is nearly collisionless and equal to the drift current. In our case the electric field in the y-direction is unknown and assumed to be zero, which effectively eliminates the  $v_e$  term in equation 5.2. While this is most likely a reasonable assumption, further measurements (performed in three

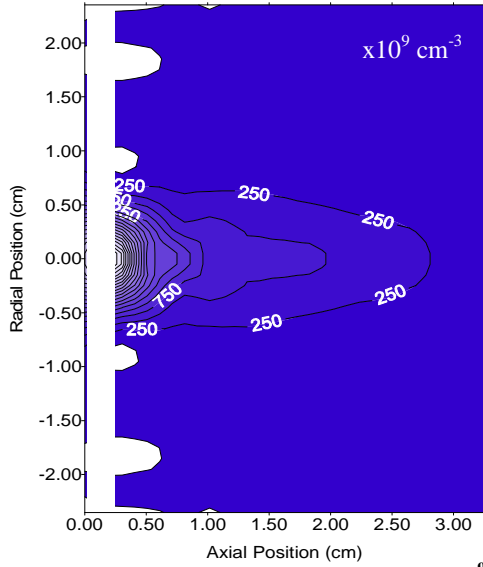


Figure 110:  $n_e$  contour plot for MP2 ( $\times 10^9 \text{ cm}^{-3}$ ).

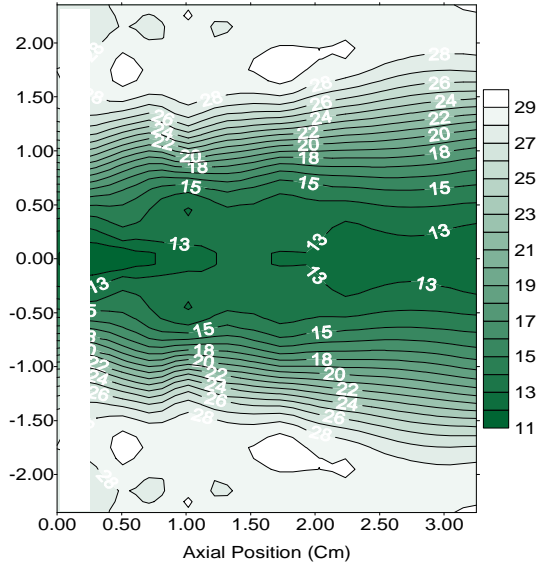


Figure 111:  $V_p$  contour plot for MP2 (V).

dimensions) would be required to quantify the current density flow structure of our plasma.

Figure 110, Figure 110, and Figure 112 are contour maps created from the MP2 (4 A, 1.5 sccm) condition. Here we see a nearly identical situation to MP1. The peak density in Figure 110 is about five times greater than the peak density of Figure 106 (i.e.,  $5 \times 10^{12} \text{ cm}^{-3}$ ). Figure 113 contains a contour plot of the calculated azimuthal current

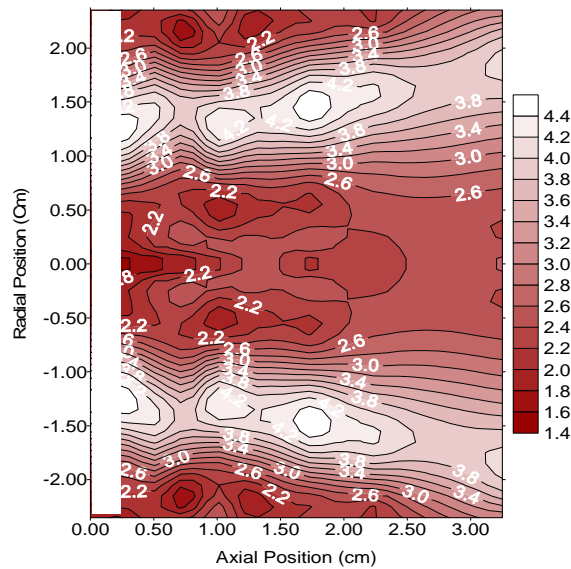


Figure 112:  $T_e$  contour plot for MP2 (eV).

density for MP2. Here the peak current density is observed much closer to the cathode, as the plasma density drops quickly with distance from the cathode (see Figure 110). The calculated Hall (azimuthal) current in the top half of Figure 113 was calculated to be 1.28A, about 30% of the discharge current. Table 13 presents a brief summary of the contour structures for the MP configuration.

Table 13: Contour plot shape comparison table for a cathode in an axial magnetic field with a plate anode.

Operating Condition	$J_a$ (A)	$V_d$ (V)	$\dot{m}$ (sccm)	Pressure ( $\times 10^{-5}$ Torr)	$n_e$ Shape	$T_e$ Shape	$V_p$ Shape
MP1	2	26.6	1.5	4.2	Plasma Jet	Ridgeline over $V_p$ Trench	Central Trench
MP2	4	25.9	1.5	4.2	Plasma Jet	Ridgeline over $V_p$ Trench	Central Trench

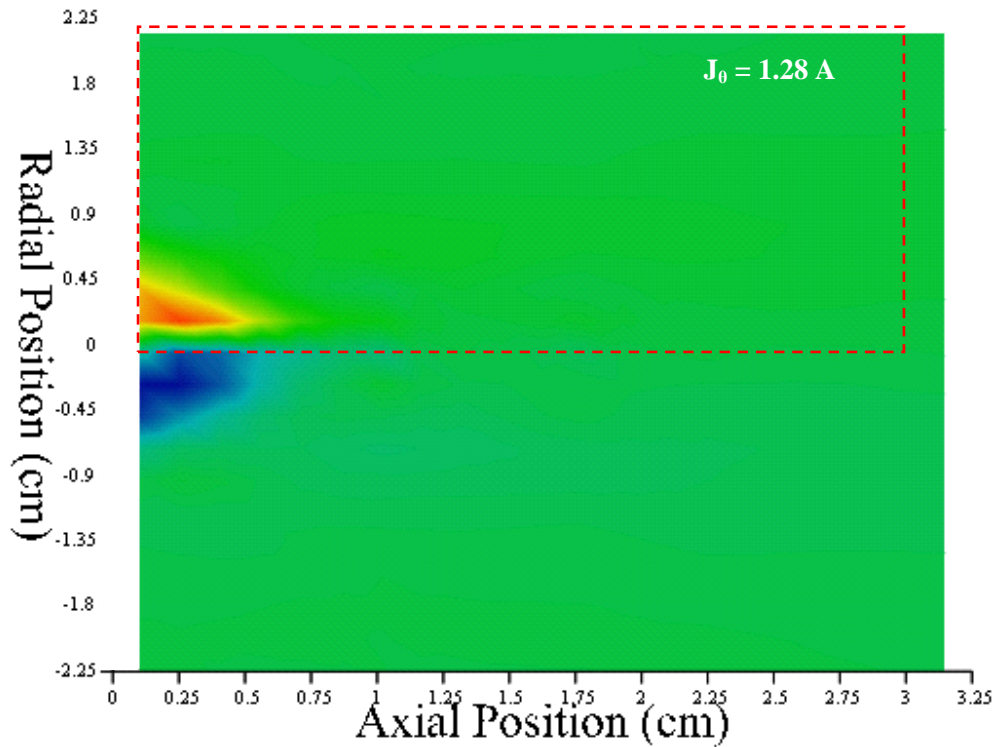


Figure 113: Azimuthal Current Density for MP2 ( $J_D = 4A$ ,  $m = 1.5\text{sccm}$ ).

## 5.7 Cathode in a Magnetic Field with a Ring Anode (MR)

Another ring anode was constructed that was similar to the one used in the SC case, but wider and placed closer to the cathode (see Figure 27). With this anode, a full set of operating conditions was achievable with the magnetic field, and the conditions that were evaluated are listed in Table 14.

Table 14: Cathode in axial magnetic field with ring anode

Operating Condition	$J_a$ (A)	$V_a$ (V)	$\dot{m}$ (sccm)	Pressure ( $\times 10^{-5}$ Torr)
MR1	2	34.8	1.5	4.2
MR2	4	32.6	1.5	4.2
MR3	6	31.7	1.5	4.2
MR4	8	25.6	1.5	4.2
MR5	2	32.1	3	6.6
MR6	4	29.0	3	6.6
MR7	6	28.0	3	6.6
MR8	8	25.9	3	6.6
MR9	2	30.0	4.5	9.1
MR10	4	26.5	4.5	9.1
MR11	6	26.8	4.5	9.1
MR12	8	25.0	4.5	9.1

Figure 114, Figure 115, and Figure 116 contain contour plots for condition MR1 (2A, 1.5 sccm). These plots are similar to ones obtained for MP1 (2A, 1.5 sccm) except the plasma potential measured within the trench was higher than MP1 and the plasma potential at large radial positions was lower than MP1. The plasma density contours shown in Figure 114 are very similar to those observed in Figure 106. A plasma jet has formed, extending some distance downstream, with a peak density near  $10^{12}\text{cm}^{-3}$ , again showing the confining effect of the magnetic field. Figure 115 contains the plasma

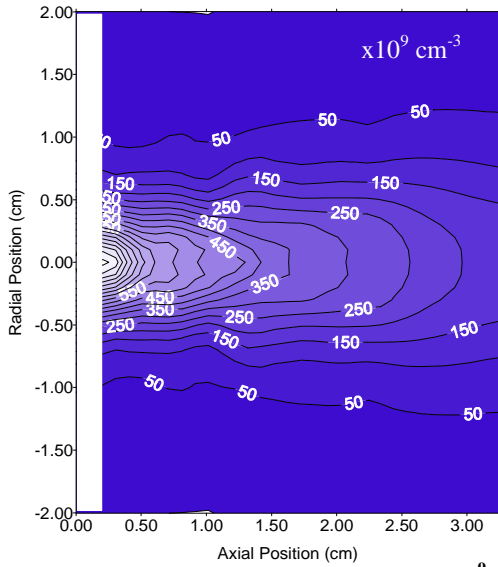


**Figure 114:**  $n_e$  contour plot for MR1 ( $\times 10^9 \text{ cm}^{-3}$ ).

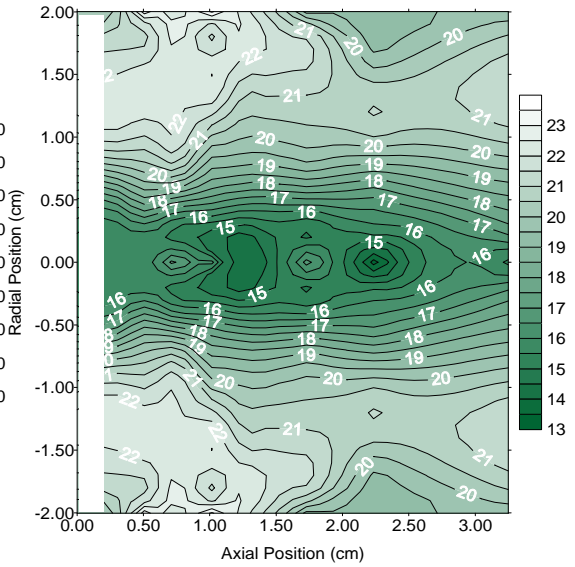


**Figure 115:**  $V_p$  contour plot for MR1 (V).

potential map for this condition. A potential canyon structure is observed, as in Figure 107, but with less voltage drop across the ridgeline (8 V for MR1 compared to 15 V for MP1). The electron temperature is the only big difference between the ring (MR1) and plate anode (MP1) conditions. Where before a strong temperature ridgeline (3 eV) occurred directly over the potential canyon walls, now only a slight rise in temperature of about 1 eV is observed. It is also noted that an anode voltage increase of about 12 V was required to establish a 2 A discharge to the ring anode (over what was required with the flat plate anode).

Plasma property contours were similar in structure throughout the 1.5 sccm testing. Below we show the final three contour maps constructed at 1.5 sccm, condition MP4 (8 A). Note again that a plasma jet has formed (Figure 117) with a peak density of around  $3 \times 10^{12} \text{ cm}^{-3}$ , although this jet is beginning to transition into a standard expansion structure nearby the cathode.

Plasma potential contours for MR4 (8 A, 1.5 sccm) display a canyon structure on the cathode centerline. The canyon walls near the cathode are steeper for this case, and, as a

result, a temperature canyon structure is also observed in Figure 119. Temperature rise across the canyon wall is about 2 eV. Further downstream a temperature increase of 1 eV was also observed in regions far from the cathode centerline.

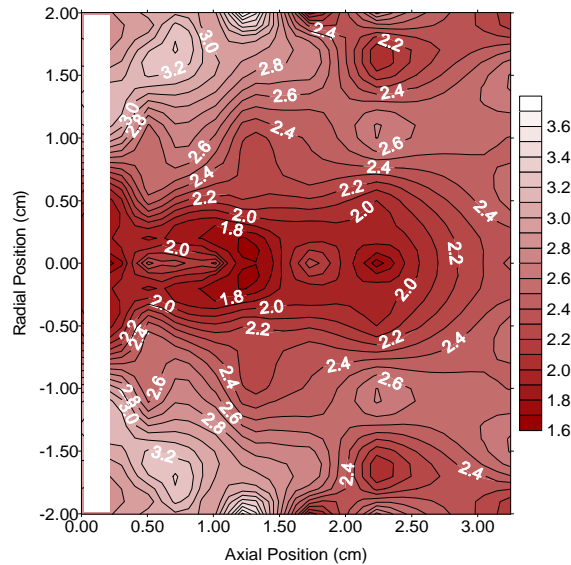


**Figure 116:  $T_e$  contour plot for MR1 (eV).**

At 3 sccm, all four discharge current conditions display plasma jets ranging in density from  $1$  to  $7 \times 10^{12} \text{cm}^{-3}$ . Potential canyons were seen in all cases as well, with voltage changes across the walls of  $\sim 8$  V. Electron temperature plots for the 3 sccm case were relatively flat with a slight rise in temperature radially from centerline as shown in Figure 119 and Figure 120. The 4.5 sccm tests displayed plasma jet expansions as well, with some evidence of standard plasma expansion nearby the cathode (e.g., see Figure 121, MR11, 6 A). When the discharge current was increased to 8A, the standard expansion features were more pronounced. Peak density in this case is more than double that of the 6A case at  $1.7 \times 10^{13} \text{cm}^{-3}$ .

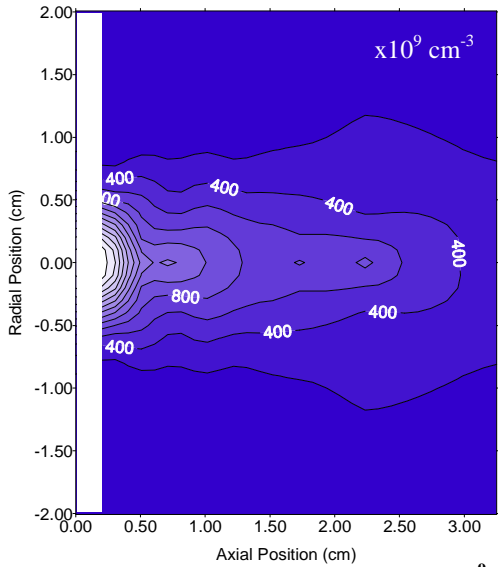


Figure 117:  $n_e$  contour plot for MR4 ( $\times 10^9 \text{ cm}^{-3}$ ).

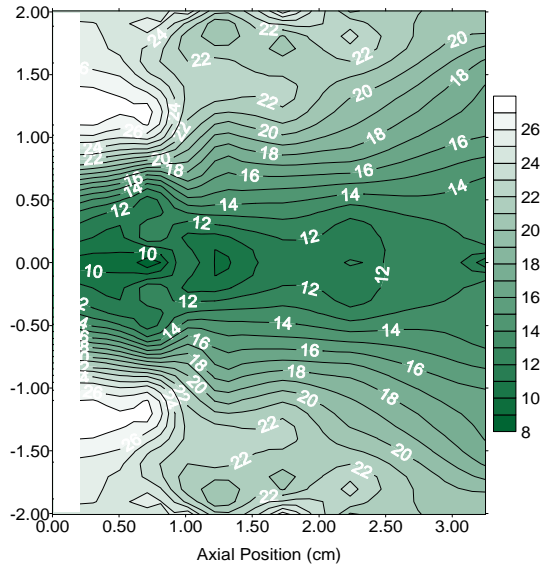


Figure 118:  $V_p$  contour plot for MR4 (V).

Plasma potential and electron temperature contour maps for MR12 (8 A, 4.5 sccm) are shown in Figure 123 and Figure 124. Here again a potential canyon is shown along with the plasma jet, although this time we begin to see the end of the canyon, as the plasma jet is smaller than most. This hints that other potential canyons like this one may have a termination point at some point downstream of the cathode after which they slowly rise to higher potential. This is to be expected as the plasma jet is expected to eventually

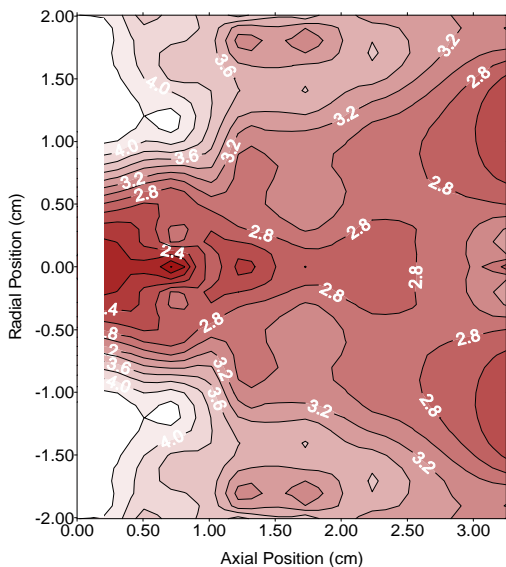


Figure 119:  $T_e$  contour plot for MR4 (eV).

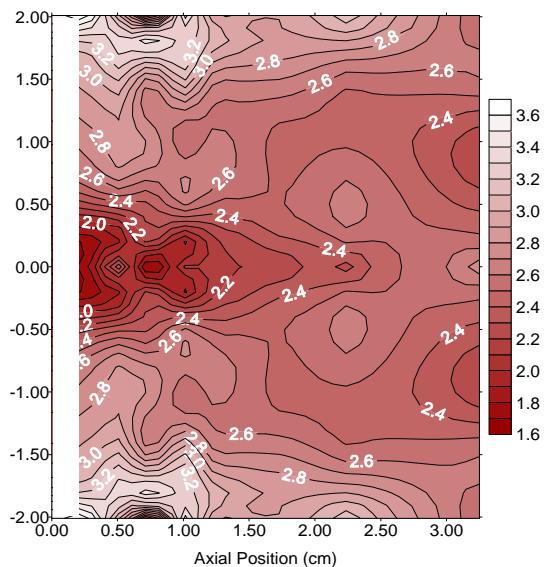


Figure 120:  $T_e$  contour plot for MR7 (eV).

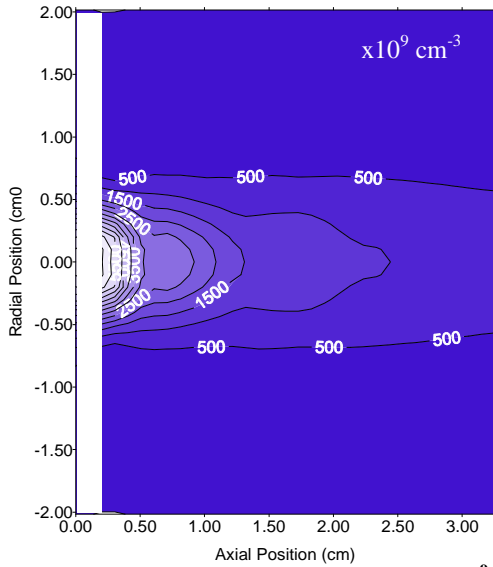


Figure 121  $n_e$  contour plot for MR11 ( $\times 10^9 \text{ cm}^{-3}$ ).

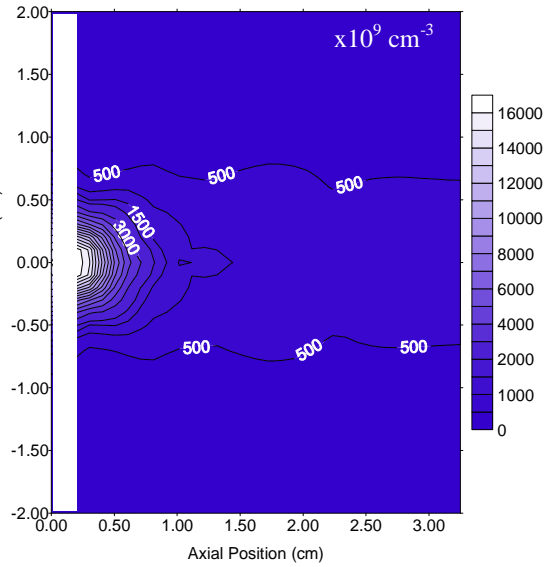


Figure 122:  $n_e$  contour plot for MR12 (V).

equilibrate with the boundary conditions being imposed by the anode. A dip in potential directly under the intense monotonic expansion is shown in Figure 123. The electron temperature in Figure 124 is relatively constant, but there is a noticeable drop in temperature under the density expansion as there was in Figure 120. In addition, a slight rise in temperature was observed at high radial positions of about 1 eV.

Lastly, the calculated azimuthal current density for MR11 is shown in Figure 125.

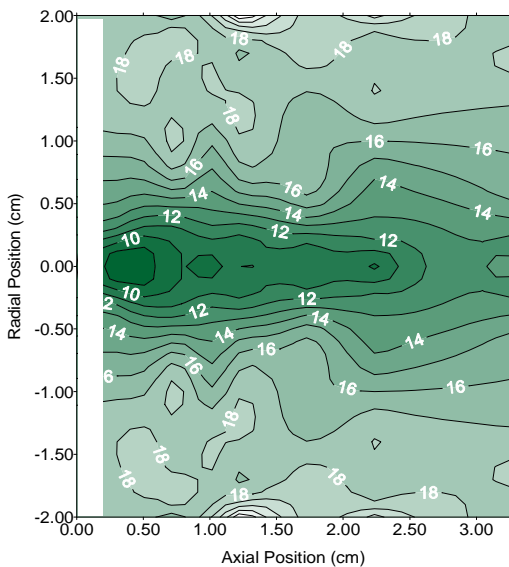


Figure 123:  $V_p$  contour plot for MR12 (V).

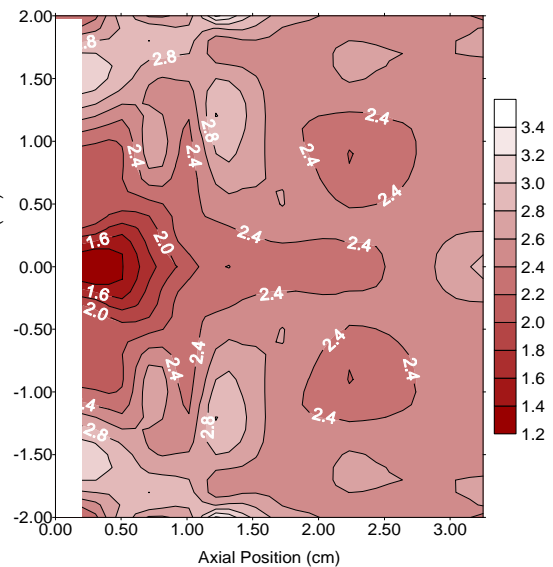


Figure 124:  $T_e$  contour plot for MR12 (eV).

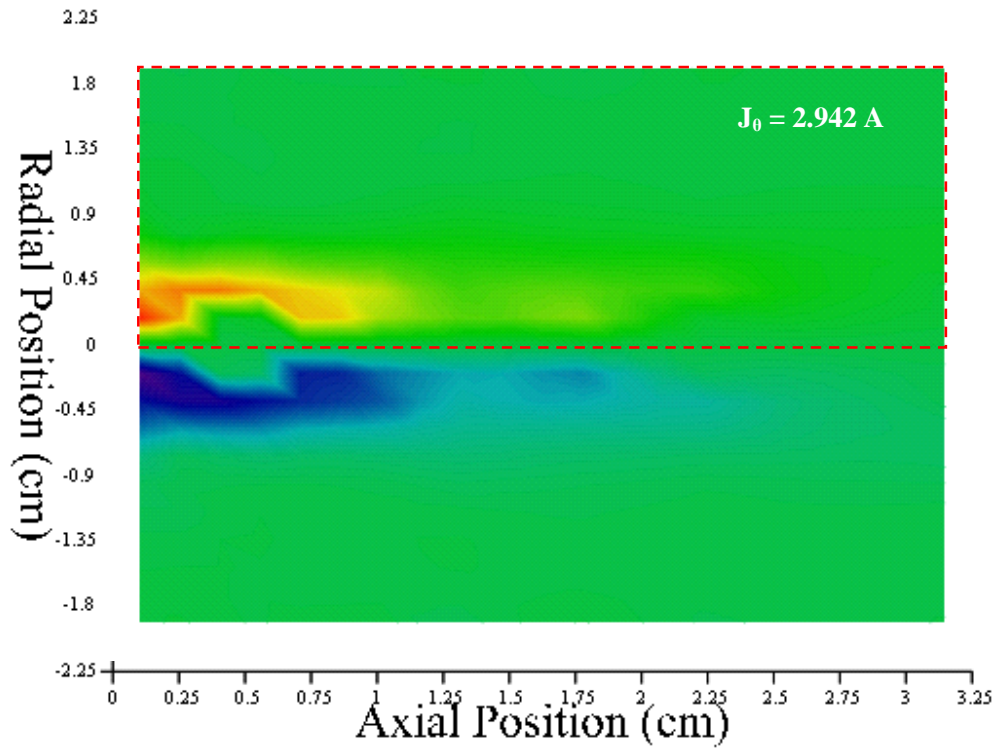


Figure 125: Azimuthal Current Density for MR11 ( $J_D = 6A$ ,  $m = 4.5\text{sccm}$ ).

Temperature and potential data used for this calculation come from contour plots shown in Appendix A. Here the Hall (azimuthal) current is roughly 50% the discharge current, at 2.9 A. Table 15 presents a brief summary of the contour structures described above.

Table 15: Contour plot shape comparison table for cathode in axial magnetic field with ring anode.

Operating Condition	$J_d$ (A)	$V_d$ (V)	$\dot{m}$ (sccm)	Pressure ( $\times 10^{-5}$ Torr)	$n_e$ Shape	$T_e$ Shape	$V_p$ Shape
MR1	2	34.8	1.5	4.2	Plasma Jet	Central Depression	Central Trench
MR2	4	32.6	1.5	4.2	Plasma Jet	Ridgeline over $V_p$ Trench	Central Trench
MR3	6	31.7	1.5	4.2	Plasma Jet	Central Depression	Central Trench
MR4	8	25.6	1.5	4.2	Plasma Jet w/ Stnd. Exp.	Central Depression	Central Trench
MR5	2	32.1	3	6.6	Plasma Jet	Central Depression	Central Trench

MR6	4	29.0	3	6.6	Plasma Jet	Central Depression	Central Trench
MR7	6	28.0	3	6.6	Plasma Jet	Central Depression	Central Trench
MR8	8	25.9	3	6.6	Plasma Jet	Central Depression	Central Trench
MR9	2	30.0	4.5	9.1	Plasma Jet	Central Depression	Central Trench
MR10	4	26.5	4.5	9.1	Plasma Jet	Central Depression	Central Trench
MR11	6	26.8	4.5	9.1	Plasma Jet w/ Std. Exp.	Central Depression	Central Trench
MR12	8	25.0	4.5	9.1	Plasma Jet w/ Std. Exp.	Const w/ Cathode Depression	Central Trench

## 5.8 Cathode in a Magnetic Field with a Ring Anode at High Discharge Currents (MRH)

Several tests were conducted at high discharge currents, and the results are described below. The same large ring anode used in the MR configuration was utilized for the high current tests. Table 16 contains a list of the operating conditions that were investigated.

Table 16: Cathode in axial magnetic field with ring anode and at high power.

Operating Condition	$J_d$ (A)	$V_d$ (V)	$\dot{m}$ (sccm)	Pressure ( $\times 10^{-5}$ Torr)
MRH1	10	35.2	1.5	3.8
MRH2	10	25.2	3	4.2
MRH3	15	27.7	3	4.2
MRH4	20	29.8	3	4.2
MRH5	10	26.7	4.5	7.7
MRH6	15	26.9	4.5	7.7
MRH7	20	28.0	4.5	7.7

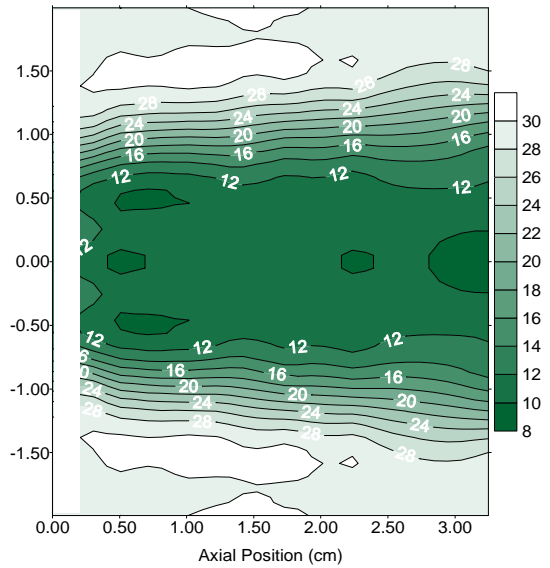
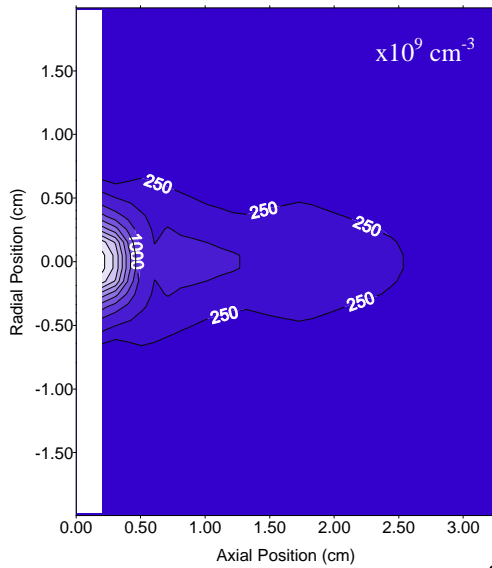


**Figure 126:  $n_e$  contour plot for MRH1 ( $\times 10^9 \text{ cm}^{-3}$ ).** **Figure 127:  $V_p$  contour plot for MRH1 (V).**

The only condition tested at 1.5 sccm corresponded to 10 A. As one can see from Table 16, the anode voltage for this was close to 40 V, the maximum voltage output of the high current power supply. For this reason, currents higher than 10 A, which required larger output voltage at 1.5 sccm, were not possible. Figure 126, Figure 127, and Figure 128 contain plasma property contour plots for MRH1 condition. In Figure 126, a dual plasma jet/monotonic expansion mode was observed. The peak plasma density was

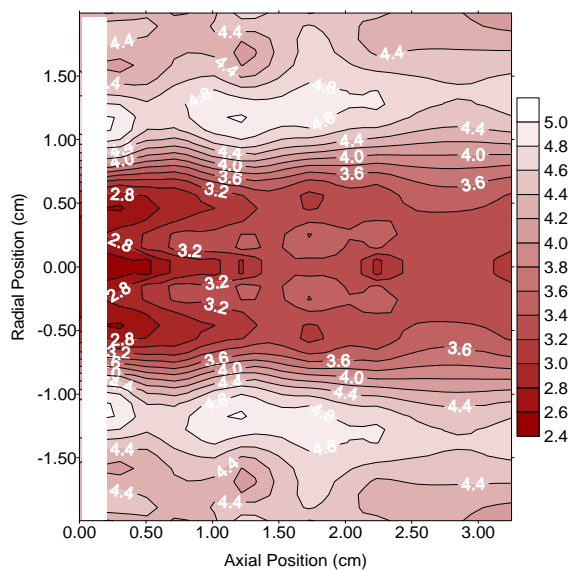


**Figure 128:  $T_e$  contour plot for MRH1 (eV).**

$5 \times 10^{12} \text{ cm}^{-3}$ .

The plasma density contour is less interesting than the potential and temperature contours. For MRH1, we observed one of the deepest and widest potential canyons detected in our study. The walls of this canyon jump some 20 V from the cathode centerline potential of about 9 V. The increased width of this canyon was anticipated from earlier studies showing how discharge current widens the valley floor. The electron temperature map is likewise very interesting. Specifically, an increase of  $\sim 2$  eV was observed across the potential canyon walls and three separate structures can be seen. Directly under the monotonic density expansion, a temperature depression of 0.5 eV is seen (as is common throughout this study). This depression rises slightly axially through the canyon following the plasma jet. The walls of the temperature canyon rise some 2 eV and then fall slightly back to 4.5 eV in the surrounding plasma.

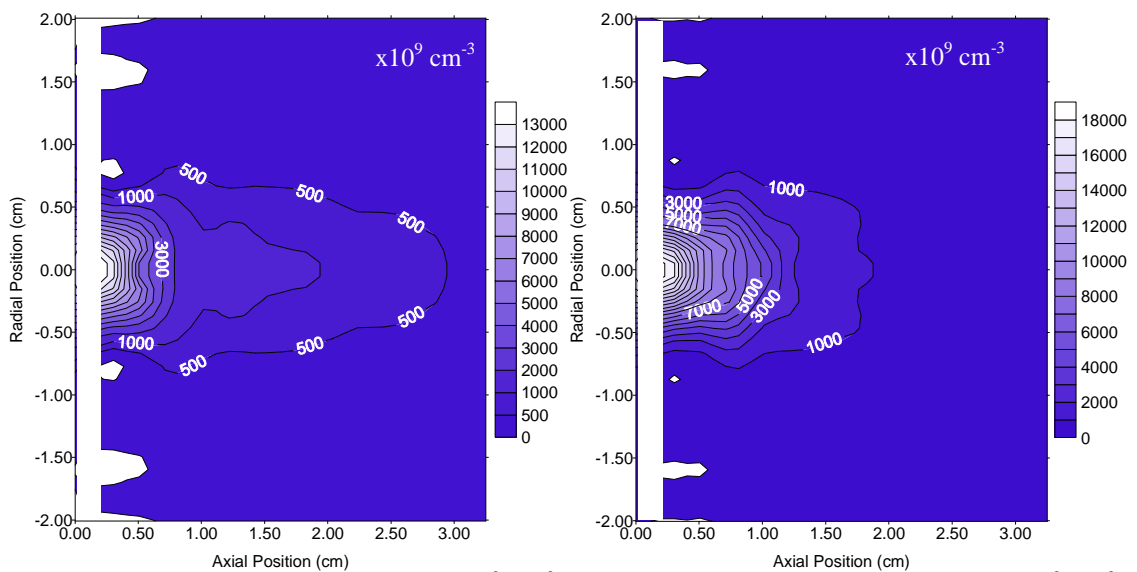
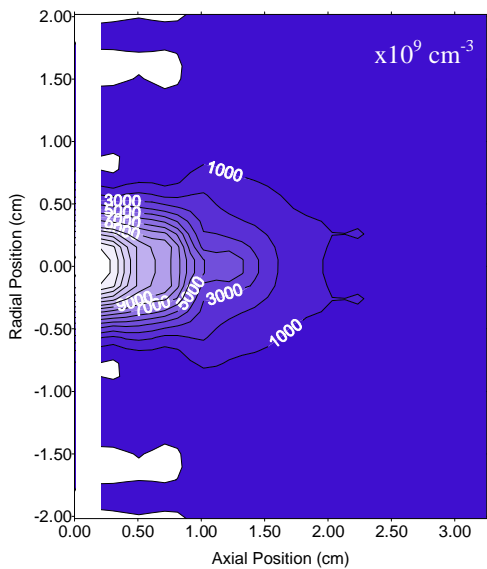
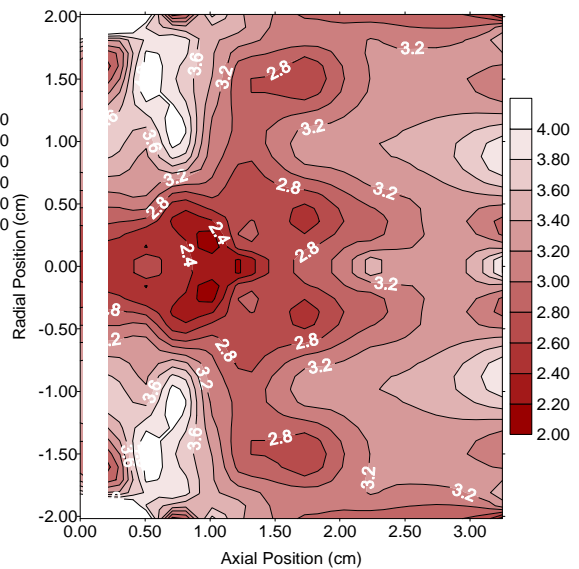


Figure 129:  $n_e$  contour plot for MRH2 ( $\times 10^9 \text{ cm}^{-3}$ ) Figure 130:  $n_e$  contour plot for MRH3 ( $\times 10^9 \text{ cm}^{-3}$ )

Data were collected at 10, 15, and 20 A of discharge current for the 4.5 sccm flow condition. Plasma density plots for all three cases are shown in Figure 129, Figure 130, and Figure 131. Between the three we see the effect of the plasma jet diminishing, while the effect of a monotonic expansion region seems to increase as the discharge current is increased. Peak densities for all three are in the low  $10^{13}\text{cm}^{-3}$  range, with increasing density-area products as the current is increased. Potential maps for all three conditions were virtually unchanged and featured a canyon with a base potential of about 10 V and a



**Figure 131:**  $n_e$  contour plot for MRH4 ( $\times 10^9 \text{ cm}^{-3}$ ).



**Figure 132:**  $T_e$  contour plot for MRH4 (eV).

15 V potential rise across the canyon walls.

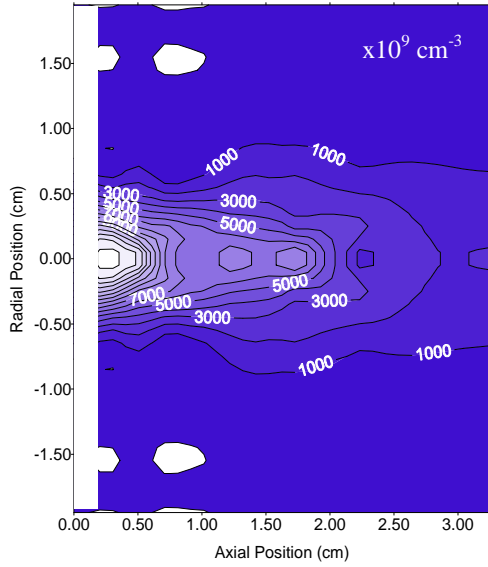


Figure 133:  $n_e$  contour plot for MRH7 ( $\times 10^9 \text{ cm}^{-3}$ )

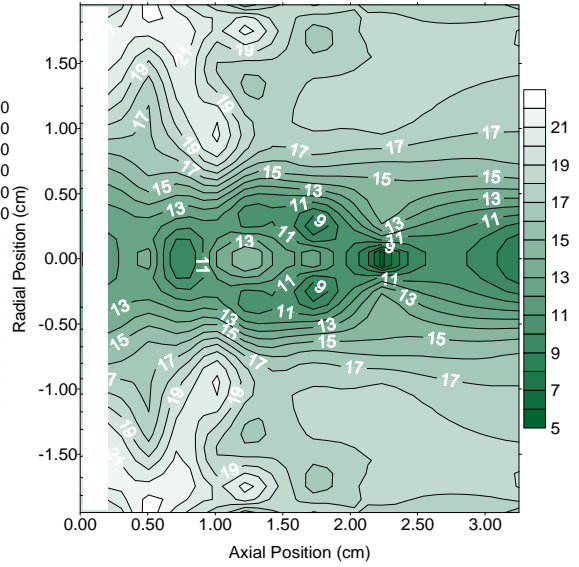


Figure 134:  $V_p$  contour plot for MRH7 (V).

Electron temperature maps remained fairly constant as well, all taking on a shape similar to Figure 132. We see in Figure 132 that as the density drops off rapidly in the monotonic density expansion, the temperature rises inversely. This is much like the temperature canyon shown in Figure 128, although for some reason this canyon now falls back into the discharge plasma past the monotonic expansion.

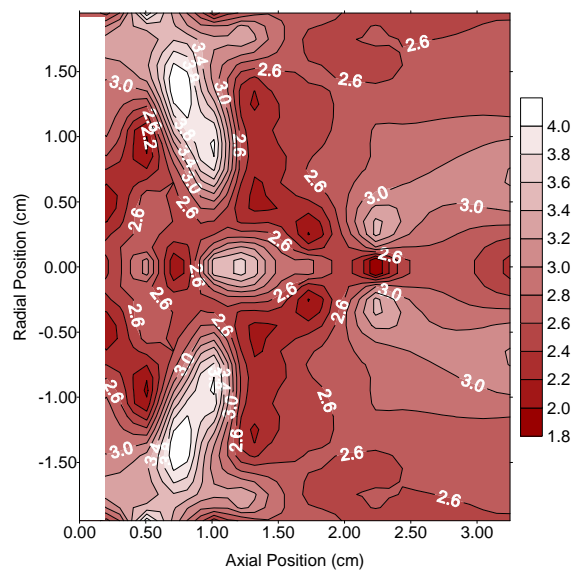


Figure 135:  $T_e$  contour plot for MRH7 (eV).

Finally, we come to the high discharge current conditions for the 4.5 sccm case. A combination of the first two high discharge current test structures was seen here. Maps for the final condition, 4.5 sccm and 20 A, are shown in Figure 133, Figure 134, and Figure 135. Here we see a plasma jet density expansion with a peak above  $10^{13}\text{cm}^{-3}$ , as was the case earlier at 3 sccm. A monotonic expansion section near the cathode was again seen for this condition, although it was not as prominent as previous, lower flow test conditions. Again a potential valley is seen here with somewhat smaller walls of only 8 V. A slight rise in potential forming a peninsula is observed as well that is positioned under an electron temperature peak structure shown Figure 135. This peak structure is the strongest of its kind seen in this study, possessing an electron temperature increase of  $>2$  eV. The azimuthal current calculated for MRH7 is shown in Figure 136.

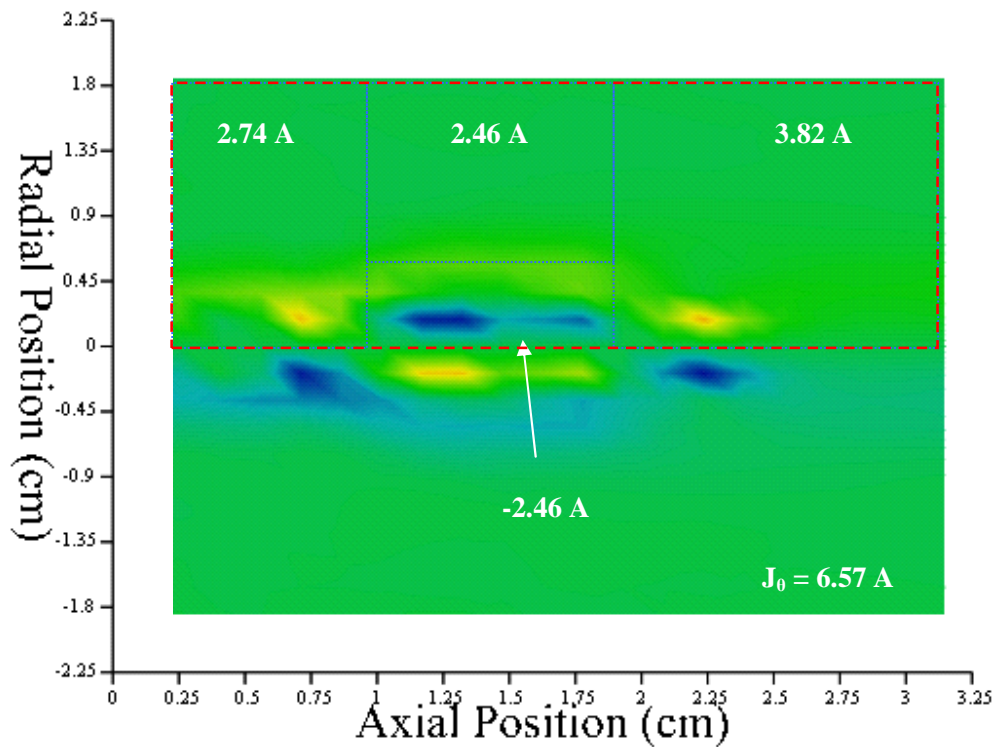


Figure 136: Azimuthal Current Density for MRH7 ( $J_D = 20\text{A}$ ,  $m = 4.5\text{sccm}$ ).

Here several counter-rotating Hall current structures are observed. The Hall current carried in several regions is shown on the figure. It is interesting to note that the center counter-rotating region seems to exactly cancel its surrounding counter part. The total Hall current was calculated to be 6.57 A, or again about 30% of the discharge current. Table 17 presents a brief summary of the contour structures described above.

*Table 17: Contour plot shape comparison table for cathode in axial magnetic field with ring anode and at high power.*

Operating Condition	$J_a$ (A)	$V_d$ (V)	$\dot{m}$ (sccm)	Pressure ( $\times 10^{-5}$ Torr)	$n_e$ Shape	$T_e$ Shape	$V_p$ Shape
MRH1	10	35.2	1.5	3.8	Plasma Jet w/ Stnd. Exp.	Ridgeline over $V_p$ Trench	Central Trench
MRH2	10	25.2	3	4.2	Plasma Jet w/ Stnd. Exp.	Central Depression	Central Trench
MRH3	15	27.7	3	4.2	Standard Expansion	Central Depression w/ Toroid	Central Trench
MRH4	20	29.8	3	4.2	Standard Expansion w/ Jet	Central Depression w/ Toroid	Central Trench
MRH5	10	26.7	4.5	7.7	Plasma Jet w/ Stnd. Exp.	Central Depression	Central Trench
MRH6	15	26.9	4.5	7.7	Plasma Jet w/ Stnd. Exp.	Central Depression w/ Toroid	Central Trench
MRH7	20	28.0	4.5	7.7	Plasma Jet	Toroid	Central Trench

## 5.9 FFT Analysis

As Goebel et al.<sup>23</sup> have suggested, moderate frequency oscillations in plasma potential (50 kHz to 500 kHz) observed at the edge of ball structures, herein referred to as plasmoid structures, may allow for the creation of high energy ions that could bombard the cathode and keeper and other nearby surfaces. In several instances we have observed strong oscillations in probe current for groups of individual Langmuir traces. One such

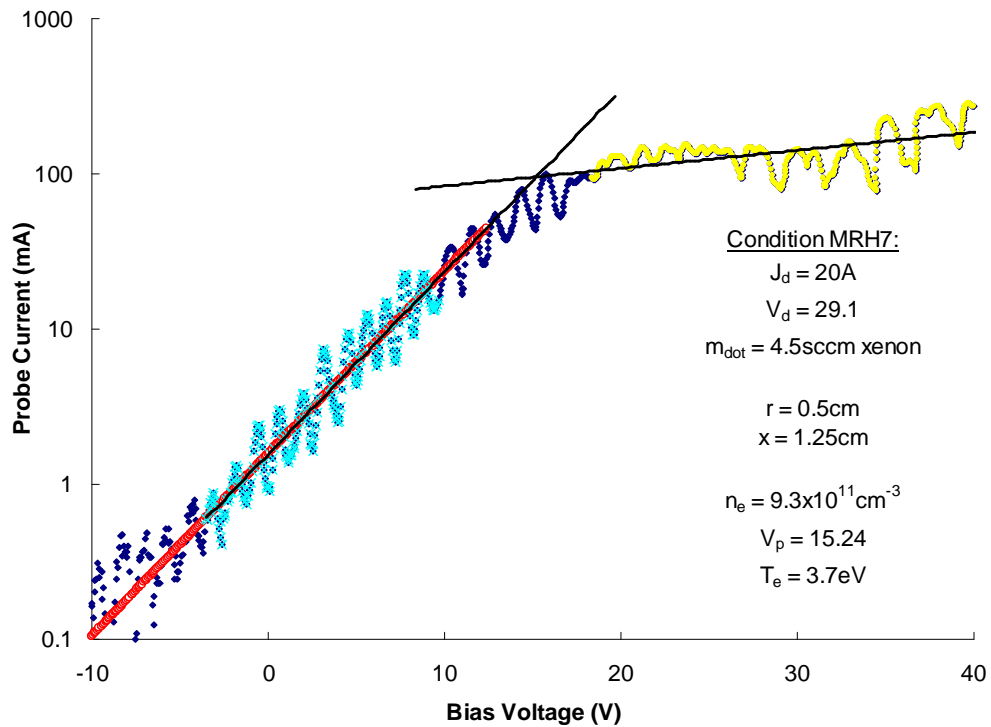


**Figure 137: Periodic oscillation seen in Langmuir trace at conditions listed.**

trace is shown in Figure 137, where both the electron retardation region and the electron saturation regions show oscillations occurring in the Langmuir probe current. Note that the entire trace was obtained in about 0.25 ms.

A Fast Fourier Transform (FFT) was applied to the probe current signal to obtain the frequency spectrum of the oscillations. This was done for data contained in the three different particle collection regions of the Langmuir probe trace (i.e., one in the ion saturation region, one in the electron retardation region, and one in the electron saturation region). Frequency spectrum results are shown in Figure 138. Although the spectrum is noisy, several peaks appear between 40 and 120 kHz. Note that frequency information above 120 kHz is strongly attenuated by the low pass filter action of the current sense circuit. Higher frequency content was observed in the electron retardation and ion saturation regions, while lower frequency content was observed in the electron saturation

region. Throughout this study there were several cases where oscillations were observed in Langmuir traces at about 60 kHz, possibly corresponding to the predator-prey mode described in Ref. 23. Information at frequencies less than 10 kHz (due to the length of typical data intervals) and greater than 120 kHz (due to the current sense circuitry) is not available from existing data sets. Further work is required to fully characterize the frequency spectrum of the probe current signal.

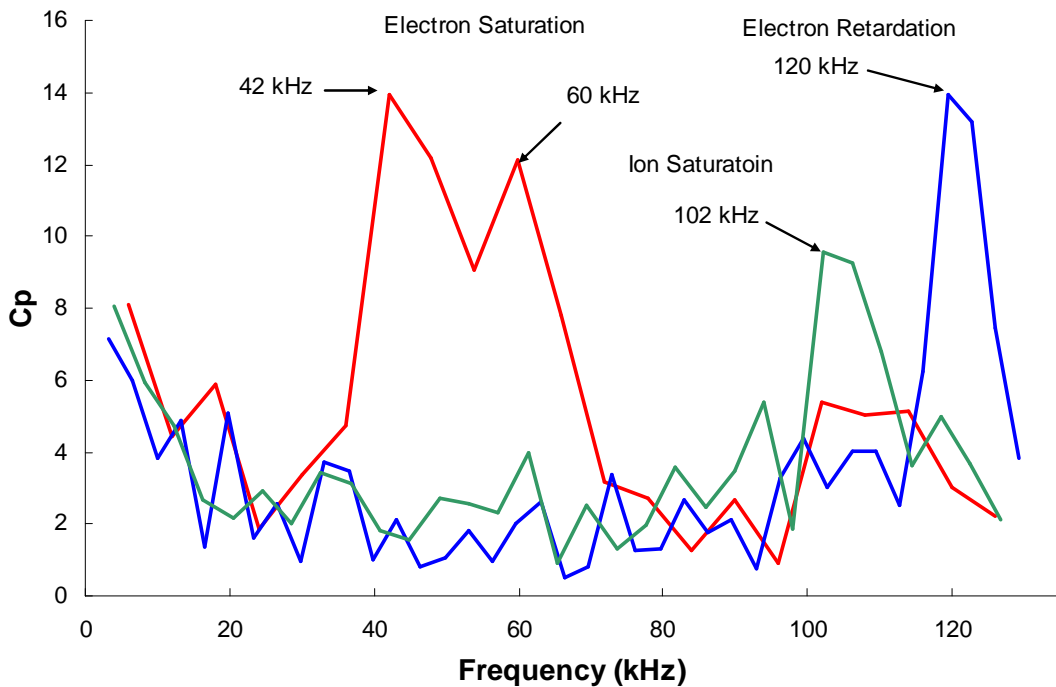
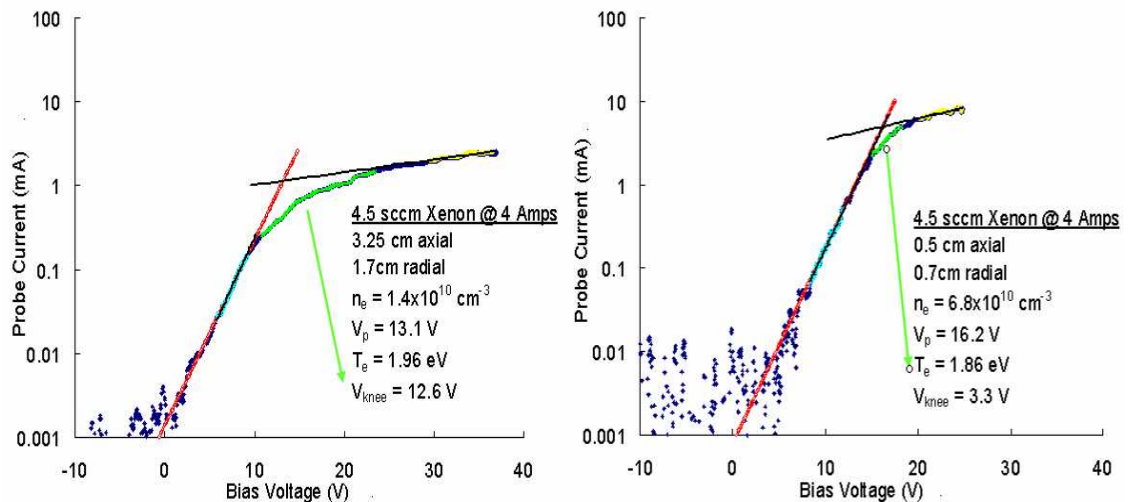


Figure 138: FFT analysis for MRH7.

## 5.10 Knee Analysis

A possible qualitative method to judge relative plasma noise level is through examination of the “knee” region of a Langmuir trace.<sup>68</sup> The knee of a Langmuir trace is defined as the region in which the transition from the electron retardation to the electron saturation occurs. As shown in Figure 139, this transition can occur over a small or large voltage range and the magnitude of the voltage range in which this transition occurs can be used as a measure for detecting regions where the plasma is relatively unstable<sup>68,69</sup>.



**Figure 139: Knee region of two different Langmuir traces showing a small and large voltage range.** Comparing the two different Langmuir traces taken at the same operating condition shown in Figure 139, we see that the one on the left has a large knee voltage, spanning over about 12 V while the one on the right has a small knee, spanning only about 3V.

As explained in Section 3.1, electrons in an ideal IV curve are assumed to be Maxwellian, giving rise to the shape of both the ideal curve seen in Figure 17 and most traces taken during this study. Non-Maxwellian electrons, be it primaries or other non-thermalized electrons, would tend to shift the shape of a Langmuir trace from ideal and might aid in the formation of the differences trace shape observed in Figure 139. To

check for this effect, the Electron Energy Distribution Functions (EEDFs) corresponding to different knee shapes were constructed using the Druyvesteyn method.<sup>3,68,69,71</sup> Druyvesteyn showed that an EEDF can be obtained from Langmuir probe traces by taking the second derivative of electron current with respect to probe potential if the velocity distribution is isotropic. This is shown in Equation 5.5.

For  $V < V_p$ :

$$f_e(E) = \frac{-2}{q^2 A_{probe}} \sqrt{\frac{2m_e(V_p - V)}{q}} \frac{d^2 I_e(V)}{dV^2}$$

5.5

Also, the second derivative can be determined numerically by<sup>69</sup>:

$$\frac{d^2 I_e(V)}{dV^2} = \frac{I_e(V + \Delta V) + I_e(V - \Delta V) - 2I_e(V)}{\Delta V^2} + \Sigma$$

5.6

Where  $\Delta V$  is an incremental step in voltage during the Langmuir trace and  $\Sigma$  is the residual error defined by Equation 5.7.

$$\Sigma = \frac{2}{\Delta V^2} (I^{(4)} \Delta V^4 + I^{(6)} \Delta V^6 + \dots)$$

5.7

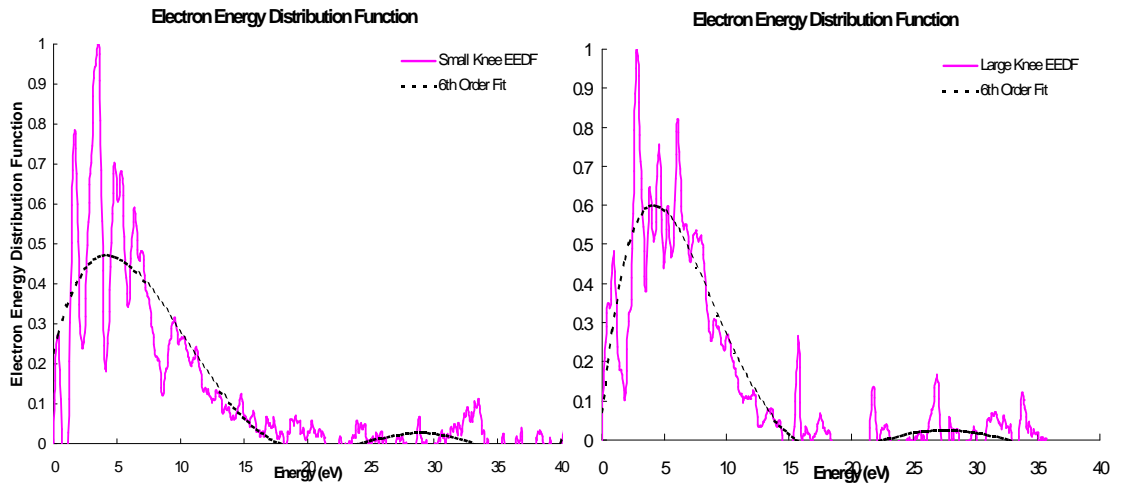


Figure 140: EEDF plots for traces possessing a 2.3 V and 9.6V knee.

As long as  $\Delta V$  is kept small (in our case about 5 mV),  $\Sigma$  can be neglected. By applying this technique, along with some smoothing and data modifications, EEDF plots for traces with different knee shapes were constructed. These plots are shown in Figure 140, normalized to peak distribution, for traces taken at the Simple Cathode condition 3 (SC3) along the 0.75cm inward radial sweep. They correspond to a knee span of 2.3 V

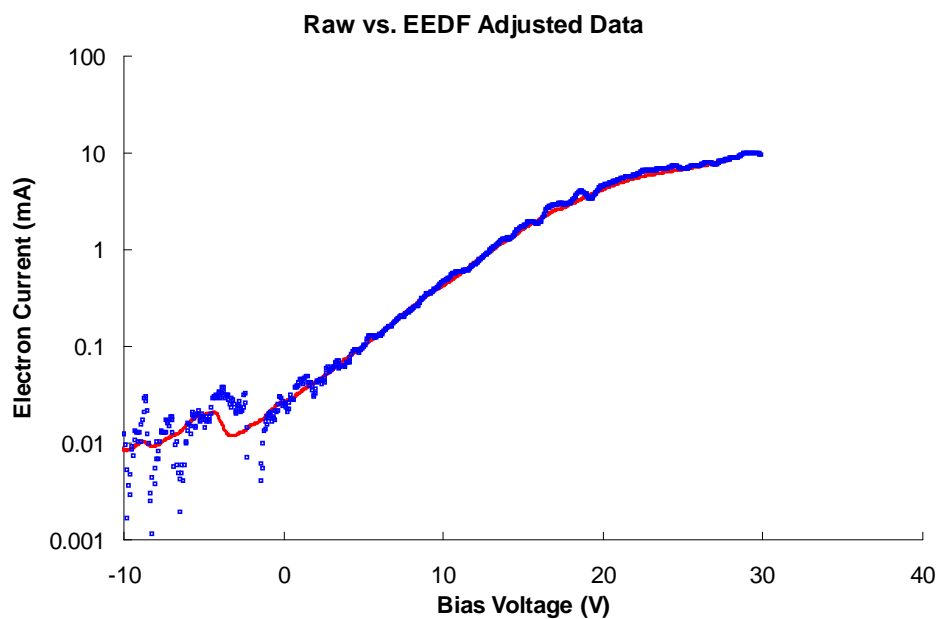


Figure 141: Sample modified trace for the SC3 condition possessing a knee voltage of 2.3V.

and 9.6 V respectively. Also, a sample modified Langmuir trace from the process is shown in Figure 141, possessing the 2.3 V knee. Although noisy, both plots in Figure 140 appear Maxwellian in nature, showing little signs of non-thermalized electrons. This was true for all traces constructed for the SC3 condition. Also, through the use of a simple analytical model containing both Maxwellian and primary electrons as well as background noise, it was shown that evidence of independent energy groups was difficult to find unless the lesser of the two groups possessed an amplitude no less than  $\sim 1\%$  of the main group. This then became the minimum value at which separate energy groups can be found, where values below this threshold are unknown and not believed to be a major contributor in the total electron current. Through this and plots similar to the one shown in Figure 140, it appears that the electron energy distribution is most likely Maxwellian and not the driving mechanism in formation of different knee shapes seen in Figure 139 and elsewhere in the study.

During this study attempts were made to construct EEDFs for the conditions presented earlier (Sections 5.1 through 5.8). Unfortunately, taking the second derivative of the electron current proved very difficult and was only achieved through extensive smoothing and data modification, making it impractical for the full study.

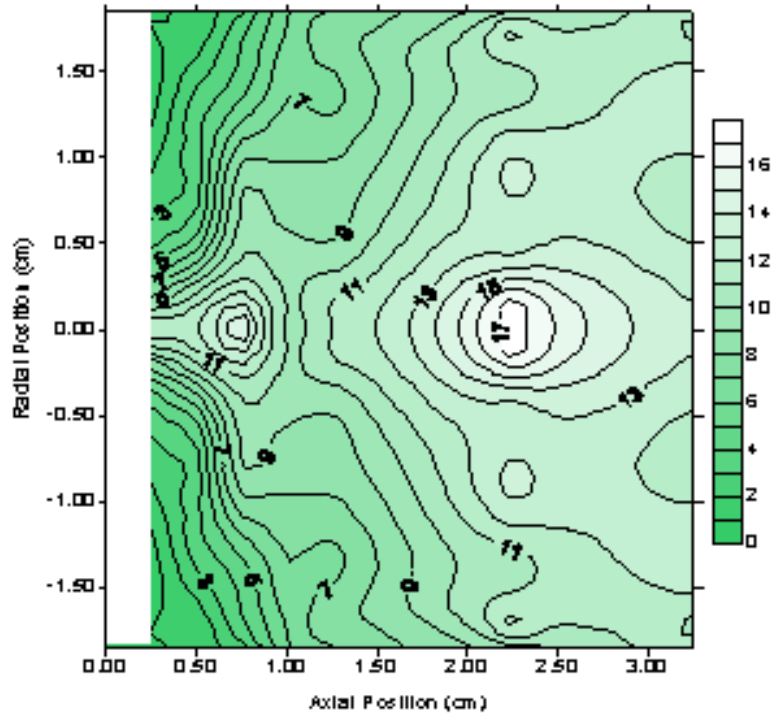


Figure 142: Knee contour plot for Condition # SC3.

The knee voltage spans of many Langmuir probe traces recorded for test condition SC3 (6 A, 1.5 sccm) were measured and assembled into a knee contour map in Figure 142. Also shown are both the plasma density and plasma potential contours for this test condition. Two distinct regions of peaked knee voltage are present in Figure 142. The

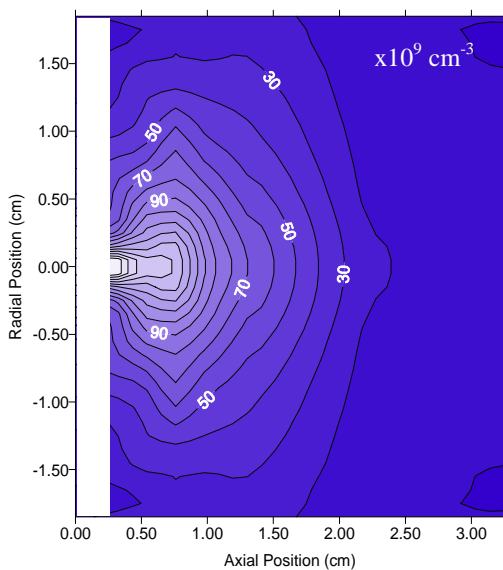


Figure 143:  $n_e$  contour plot for MRH7 ( $\times 10^9 \text{ cm}^{-3}$ ).

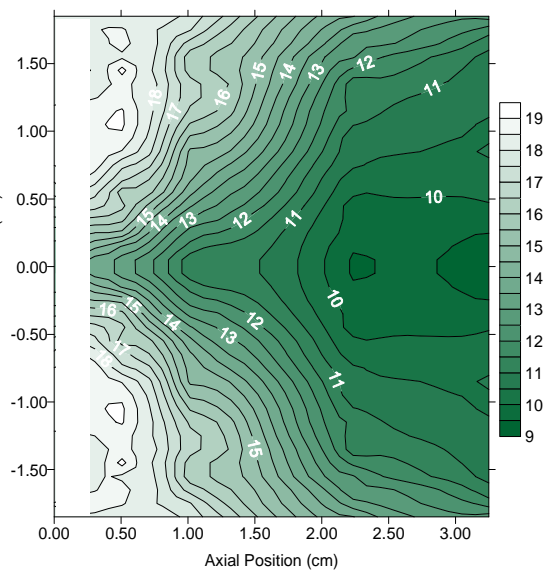


Figure 144  $V_p$  contour plot for MRH7 (V).

first is directly underneath the plasmoid evident in the plasma density contour in Figure 143. Here the knee voltage is 14 V. The second peak in knee voltage (of magnitude of 17 V) is located directly over the potential valley floor (see Figure 143). Most knee contour plots resembled Figure 142 and possessed peaks over density and potential structures, revealing possible plasma instability at these points.

## 5.11 Discharge Characteristics

Of notable interest is the effect of the Langmuir probe on the cathode discharge. To minimize perturbation of the plasma from the probe and melting of the probe by the plasma, the RAPID system employed (1) high speed motion, (2) small probe construction, and (3) probe segmentation. These steps do not completely eliminate plasma perturbation by the probe, however, and a quick check was performed to

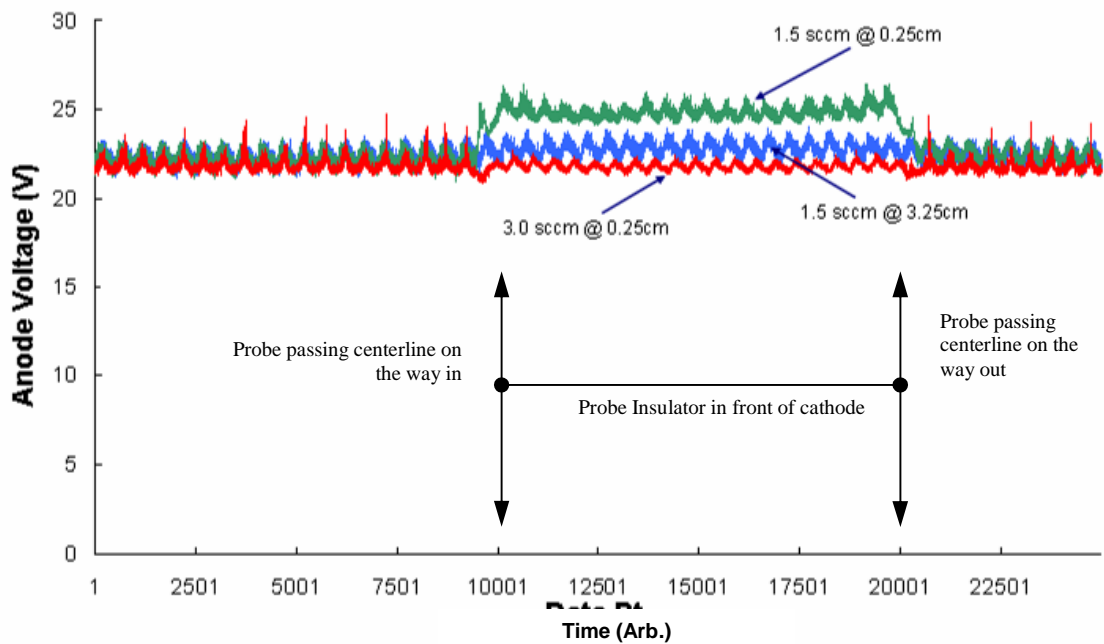


Figure 145: Discharge fluctuations due to probe sweep through cathode plume.

determine if excessive probe-induced perturbations were occurring. To do this a system was devised to monitor the anode voltage as the probe passed through the cathode plume at different axial locations and test conditions.

Figure 145 is a plot of the anode voltage versus time for three different axial locations where radial sweeps were performed. The one shown in blue, is the effect on anode voltage as the probe passes through the plume at a large axial distance (3.25 cm). Only a tiny rise in anode voltage was observed when the probe structure was directly in front of the cathode. The green curve was obtained at the same operating condition with the probe axis positioned at  $z=0.25$  cm. Here we see a larger anode voltage rise as the probe passes through the centerline of the cathode. This voltage increase is less than 10% of the anode voltage. The last curve, shown in red, was also a close probe sweep ( $z=0.25$  cm), but at a higher flow rate. Here it is noted that no change in mean anode voltage was

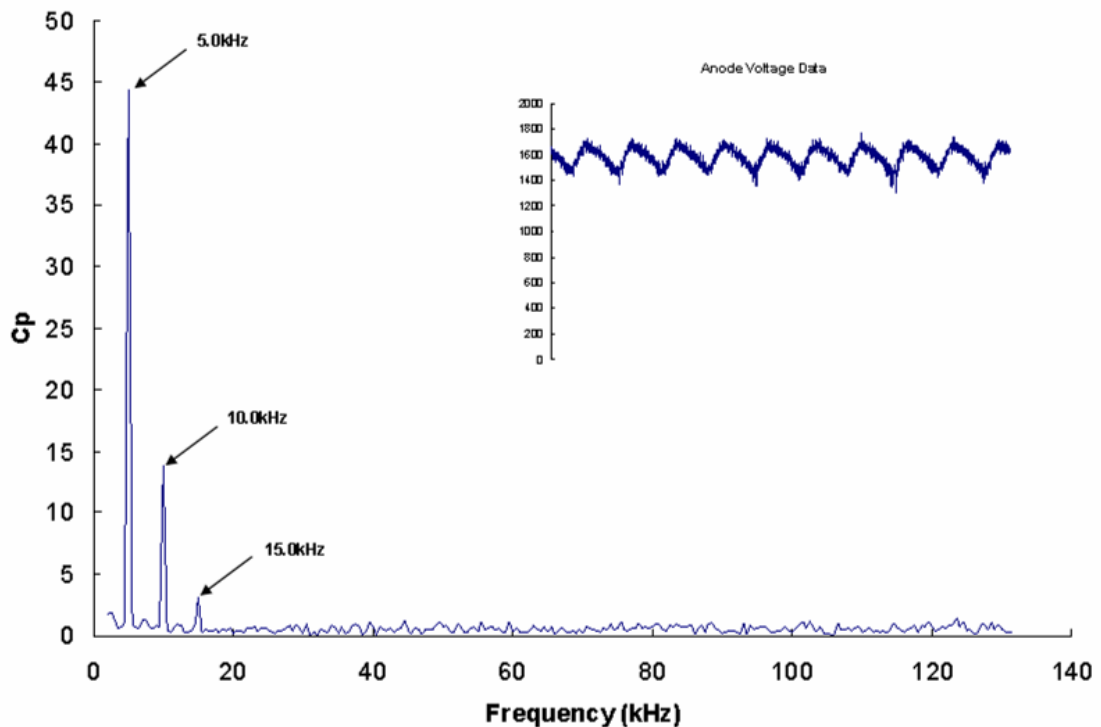


Figure 146: FFT analysis of anode voltage, revealing three harmonics of the anode oscillation.

observed, but rather a filter effect of some sort has occurred. Without the probe, the anode voltage is noted to display oscillations with a magnitude of about 5% the steady state value. During times when the probe structure is in front of the cathode, the magnitude of this oscillation drops to around 1%, quieting the discharge voltage slightly. Although the probe is observed to perturb the discharge voltage, it is noted that the perturbation only occurs after the probe has flown past the cathode centerline, when Langmuir probe data are still acquired, but are not used in constructing plasma property maps. The anode voltage oscillation evident in Figure 145 was determined to be at 5 kHz from FFT analysis (see Figure 146). Several harmonics are also present in the anode voltage signal. The 5-kHz oscillation was not observed in FFT analysis of individual probe traces due to the limited data interval periods (i.e., most Langmuir probe traces were obtained in about 0.25 ms, which corresponds to a minimum frequency bin of ~10 kHz).

## CHAPTER 6: CONCLUSIONS

Plasma density, plasma potential, and electron temperature measurements were made in the near field of a hollow cathode using a fast-actuating Langmuir probe system (RAPID). Contour plots of these properties display a wide variety of behavior as the hollow cathode operating condition and configuration were changed. Specifically, evidence of plasmoids (localized dense plasma regions) were observed at several operating conditions. For most operating conditions, however, point-source-like plasma density expansion was observed from the hollow cathode, corresponding to V-shaped valleys in plasma potential leading away from the cathode. This was not the case with the inclusion of an axial magnetic field, where a plasma potential trench was observed along the cathode axis along with a collimated plasma-jet density expansion structure. Electron temperature contours often displayed similar trends to those of the potential contours. Macroscopic trends include: (1) Plasma density increased everywhere when flow rate and/or discharge current was increased. (2) When plasmoid or large plasma jet structures were seen, peak densities within such structures were lower than that of monotonic expansion structures. However, the overall area of plasmoid structures was noticeably larger than that of monotonic expansions (i.e. the random thermal current on a convex surface of constant density is constant and approximately equal to the discharge current when no applied magnetic field was present). (3) With an applied magnetic field, azimuthal current structures were often observed following potential gradients. (4) Electron temperature was seen to increase with the presence of a plasmoidal density expansion structure. (4) Plasma potential is highly a function of density structure, while it

is only mildly dependent on flow rate and current for most cases. (5) Plasma potential drops where density increases. (6) Potential and temperature profiles often formed V-shaped valleys where no applied magnetic field was present and trench structures when an axial magnetic field was applied. (7) Electron temperature seems to be a function of both potential and density structures, decreasing somewhat with high density and more so with low potential. (8) Lastly, electron temperature increased slightly as discharge current increased, but was largely in-sensitive to flow rate variations used in this study. Along with the above macroscopic trends, many key observations were made specific to operation condition and cathode complexity. These observations are summarized below.

## **6.1 Simple Cathode Plasma Parameters**

To start we provide a baseline summary of our simplest case, the cathode without a keeper or magnetic field (SC case). This will be useful for comparisons as cathode complexity is increased. It was noticed during the SC study that as the discharge current was increased a transition occurred from a monotonic density expansion to a plasmoidal one and finally to a full plume expansion. This can be explained by the requirements placed on the plasma to conduct more and more current to the anode. At low current, the plasma created inside the cathode orifice and close to the cathode is sufficient to carry the current being demanded. As the power requirements to the anode are increased (i.e., the discharge current is increased), this is no longer true and additional ionization must occur to achieve adequate conductivity. This extended expansion is small at first, the plasmoid, but expands rapidly into a full-plume mode as current requirements increase. Interestingly, when plasmoid density expansions were seen, overall peak plasma densities dropped, but the area corresponding to a particular plasma density contour increased.

Full plume mode occurred only at the lowest flow rates and at the highest current condition (i.e., 8 A). Discharge voltages at low flow rates increase rapidly with current and at a certain point no further current can be collected, indicating a possible conduction limit at that condition.

As is the common case throughout this study, without the inclusion of an applied magnetic field, potential contours often formed V-shaped depressions leading away from the cathode. Likewise, electron temperature contours were observed to follow the potential contours, but were more uniform, typically remaining within 2 to 2.5 eV. In most instances, electron temperature was at or near a minimum in regions of dense plasma near the cathode orifice.

#### **Near Plate Anode vs. Distant Ring Anode**

With the addition of the plate anode, density expansions were observed to move toward the cathode. A double layer was also seen in some cases positioned parallel to the near plate anode between the anode and the plasma flow field created downstream of the cathode. This feature suggests that an anode plasma could be forming downstream of the anode layer. It's possible that similar anode sheaths formed on the distant ring anode, but these regions were far outside of the measurement zone of the RAPID system. Plasma density maximums were not affected greatly by the anode sheath, nor was electron temperature. Lastly, inclusion of the near plate anode qualitatively increased the stability of the plasma, as is evident by higher definition and smoother potential and density contours and nearly noise-free I-V curves.

## **6.2 Enclosed Keeper Effects**

With the inclusion of an enclosed keeper, several changes in the plasma flow field were observed. Two things that were not noticed to change, however, were the discharge voltage and the types of plasma potential structures that formed.

### **Small Keeper Case (Diameter = 2.7mm)**

During the small keeper diameter study all density expansion structures were plasmoidal in structure. This is believed to be a result of restricted gas flow from the cathode caused by the small keeper orifice (which results in a less diffuse jet of neutrals along the cathode-keeper centerline), and by plasma recombination on the keeper structure (which can reduce plasma conductivity and force the formation of a plasmoid region to enhance ion production rates). As is the common case, all plasma potential structures were observed to be V-shaped. The “V”, however, was a good deal more defined compared to measurements made without an enclosed keeper, again presumably resulting from flow enhancement along the cathode-keeper centerline. It was also noted that at lower flow rates a slight double layer was observed near the anode. This disappeared (or moved out of our measurement region toward the anode) as flow was increased.

Electron temperature increased slightly on average for the small keeper condition, increasing to ~2.5 eV. The increase in electron temperature corresponded to both the appearance of plasmoid structures and a corresponding decrease in peak density. As plasmoids are believed to form to help conduct the current being demanded of the cathode, it is interesting to note that when plasmoids occur electron temperatures increase slightly, and higher electron temperatures will result in higher ion production rates under a given neutral density flow field condition.

### **Medium Keeper Case (Diameter = 3.8mm)**

For this configuration almost all expansion structures were observed to be monotonic. The keeper orifice was no longer restricting cathode flow as much. As a result, the V-shaped potential contours extended closer to the cathode orifice, following the densest plasma regions. It is noted that the gradients within the potential V structure were stronger than the SC and SCP cases, but not as strong as the small keeper orifice configuration condition.

A slight drop in electron temperature on average was observed as the keeper orifice was expanded (from 2.5eV to 2.2 eV). This is expected as the plasma and neutral flow fields are more similar to the simple cathode configuration. Also, at this point in our study no full plume modes were observed. That is not to say that this mode was not possible to achieve, but rather the current required to cause a transition may just be greater than those studied (i.e., greater than 8 A).

### **NSTAR Keeper Case (Diameter = 4.75mm)**

Monotonic density expansion structures were observed for the large keeper orifice configuration. For both the MK and LK configurations, peak plasma densities on a whole increased slightly.

The large keeper orifice resulted in plasma potential “V” expansions that formed a tighter valley leading away from the cathode. In addition, the base of the potential structures no longer decreased beyond a fixed distance from the cathode. In fact, in some cases it actually increased and a bowl (or depression) was formed, as was seen with the inclusion of an axial magnetic field in this study and by several other investigations<sup>3, 31,</sup>

<sup>36</sup>.

A slight anode double layer was observed at low flow rates, showing evidence of an anode plasma formation. The anode layer dis-appeared from our measurement zone as before when flow or discharge power was increased. The electron temperature was relatively uniform throughout our measurement region at  $\sim 2.2$  eV similar to the SC and SCP configurations.

### **6.3 Magnetic Field Effects**

At this point the NSTAR keeper equipped cathode was placed within an axial magnetic field similar to that of the NSTAR discharge chamber. Three different anode setups were tested with the presence of the magnetic field, both the earlier near plate anode and a near ring anode. These tests were followed by ones conducted at high discharge currents with the near ring anode configuration. With the inclusion of the magnetic field, the centerline plasma potential decreased closer to the cathode. This was unlike most previous cases where the potential was either constant or increasing as cathode was approached. Also, discharge voltages decreased dramatically. The discharge voltage dropped as a result of the enhanced conductivity of the plasma flow field caused by the confinement of electrons in a magnetic field and the subsequent increase in the volumetric ion production rate.

#### **Near Plate Anode w/ Axial Magnetic Field**

A new density expansion structure occurred with the inclusion of an axial magnetic field where the plasma was found to expand in a “Jet” fashion, somewhat similar to a plasmoid that has been stretched out from the cathode along the cathode centerline. This feature has also been observed in several previous studies<sup>3, 6, 33,61</sup>. Plasma potential structures have also changed from the previously observed V-shape to a deep, axially

oriented trench that follows the plasma jet. The peak potential outside of the trench was much higher compared to the ridge regions of the V-shaped valleys observed in all other test conditions without a magnetic field. The plasma potential along the trench was often higher than the discharge potential by a few volts, suggesting that a potential drop occurred near the anode to reduce the electron current to the value being demanded, as has been reported elsewhere<sup>33</sup>. The walls of the potential trench represent a very strong double layer ( $\Delta V/T_e \sim 5$ ), with a voltage increase ( $\Delta V$ ) of nearly 15 V in some cases. A correspondingly large increase in electron temperature was seen on and nearby the trench walls (from 2 eV to 4 eV). At the base of the trench and in the surrounding plasma, electron temperatures were near 2 eV, which was similar to temperatures measured without magnetic fields. The electron heating and good electron confinement by the magnetic field could lead to an increase in the creation of energetic and multiply charged ions off the cathode centerline as observed by both CSU and JPL research groups<sup>26, 31</sup>.

Peak plasma densities within the plasma jet region near the cathode were about an order of magnitude greater than other conditions measured without a magnetic field.

### **Near Ring with Axial Magnetic Field**

With a near ring anode configuration, the plasma jet from above displays a small region of monotonic (point-source like) plasma expansion near the cathode. This is more apparent as current and flow rate were increased. Also, a less defined potential trench develops. This occurs because electrons must now diffuse across the magnetic field to reach the anode. In general, plasma density was observed to be slightly lower everywhere compared to when a flat plate anode is used (i.e., the plasma became more

spread out). Lastly higher discharge voltages were required to pull current through the axial magnetic field to the anode.

### **Near Ring Anode at High Power**

A higher current power supply was used to continue testing of the near ring anode configuration. With this power supply, currents up to 20 A were tested. It was noted that density expansions flipped from plasma jets with some evidence of a monotonic expansion near the cathode to a much more pronounced monotonic expansion with some evidence of a plasma jet. With this change, the strong potential trench structure of the flat plate anode reappeared. Electron temperature also increased everywhere to just under 3 eV and temperature ridgelines seen earlier condensed into single peak structures some distance downstream of the cathode and off axis of the cathode. In three dimensions one could imagine that a toroid structure haloing the cathode was formed. This could again lead to an increase in multiply charged and energetic ions that have been observed to form off axis of high current hollow cathodes operated in strong magnetic fields.

## **6.4 Plasma Oscillations**

Previous studies<sup>3,31</sup> have suggested that strong oscillations occur in hollow cathode discharges in both the load presented to the discharge power supply and in the plasma flow field properties. In the current study, individual Langmuir probe traces display periodic fluctuations in the probe current as a function of time and applied voltage. No precise frequency of oscillation was determined, but rather a wide range of oscillations was noted from ~10 kHz to ~120 kHz. At the macroscopic level (power supply load) a

definite 5 kHz discharge oscillation was observed, suggesting that a predator-prey type of driving mechanism is at play as described by Goebel<sup>31</sup>. In the current study, contour plots were constructed of the qualitative noise level (using measurements of the knee voltage) and two regions of high noise intensity were found to occur on the cathode centerline, one near the cathode and one further away in the bowl region of the plasma potential structure. It is suggested that future research be performed to correlate oscillations to plasma flow field structure and test configuration. The goal being to find optimal conditions and device configurations where the formation of multiply charged and energetic ions is minimized.

## 6.5 Final Statements

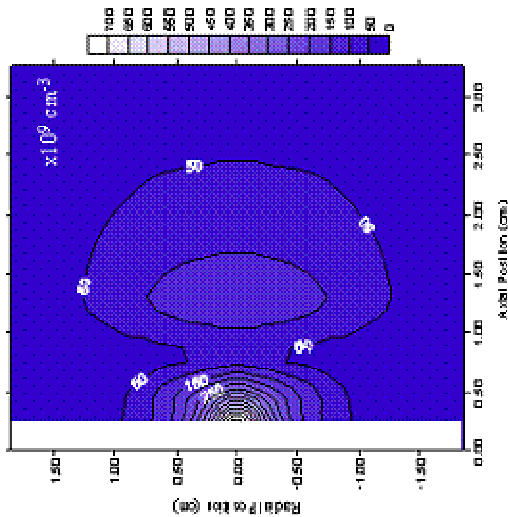
The mapping of discharge structure for various complex cathode configurations in the current work agrees with other researchers work, and these measurements along with ones of simpler test configurations will play an important role in validating models of hollow cathode discharges that are currently and soon to be available. While the exact cause of cathode erosion has not been pin-pointed, it appears that a stationary potential hill structure is not formed in the test configurations and conditions studied herein. However, that doesn't eliminate the possibility of the presence of an oscillating (in both position and plasma potential) hill, which would explain oscillations observed in some individual Langmuir probe traces, as well as the development of significant "knee" regions of Langmuir probe traces taken at higher densities and within regions of strong potential gradients. Evidence of strong double layers ( $\Delta V/T_e \sim 15 \text{ V}/3 \text{ eV} \sim 5$ ) and plasma structures that may assist in the creation of energetic, multi-charged particle flow back to the cathode has been uncovered. Also the conditions at which specific discharge

structures occur has been tabulated, enabling future work to both study each condition specifically and avoid those that may prove harmful to cathode/thruster operation. The discharge plasma property maps provided herein may also be of use in erosion models as measured inputs for various conditions. Understanding the discharge effects caused by cathode/keeper components were also presented and may assist in the design and improvement of future cathodes.

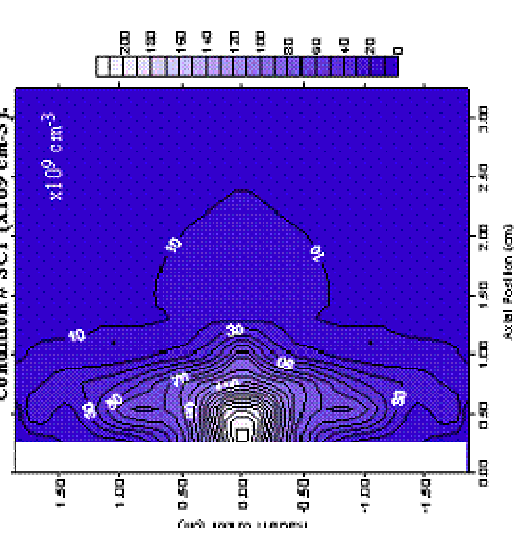
# APPENDIX A

## Simple Cathode (SC091405)

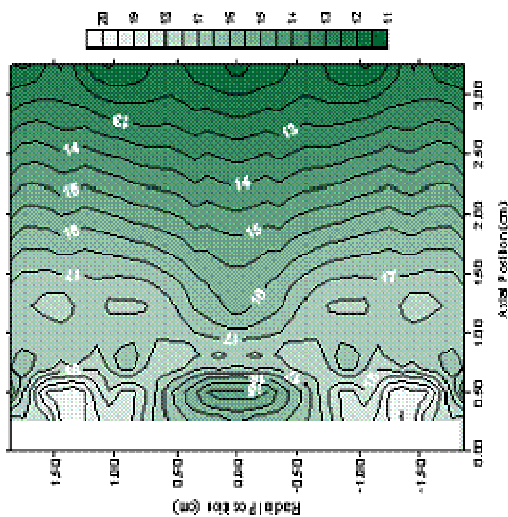
Operating Condition	(A)	$V_d$ (V)	$z$ (sccm)	Pressure ( $\times 10^{-5}$ Torr)
SC1	2	37.4	1.5	3.5
SC2	4	48.7	1.5	3.5
SC3	6	56.7	1.5	3.5
SC4	8	86.4	1.5	3.5
SC5	2	36.4	3	6.4
SC6	4	42.1	3	6.5
SC7	6	52.9	3	6.5
SC8	8	59.3	3	6.6
SC9	2	35.5	4.5	8.6
SC10	4	42.1	4.5	8.6
SC11	6	53.4	4.5	8.6
SC12	8	57.6	4.5	8.6



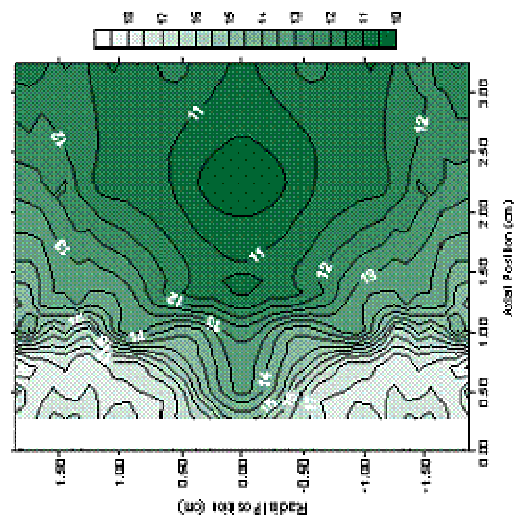
Electron number density contour plot for Condition # SC1 ( $\times 10^9 \text{ cm}^{-3}$ ).



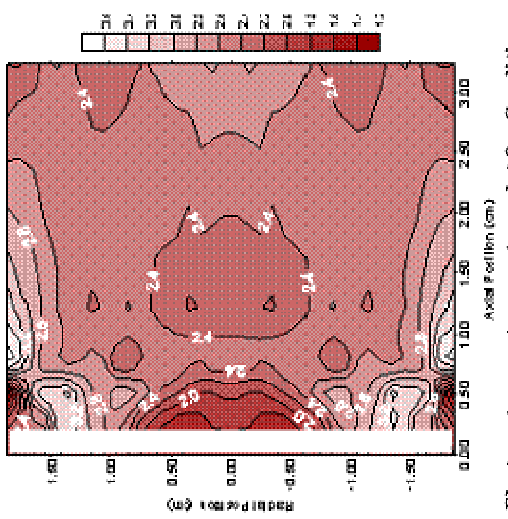
Electron number density contour plot for Condition # SC2 ( $\times 10^9 \text{ cm}^{-3}$ ).



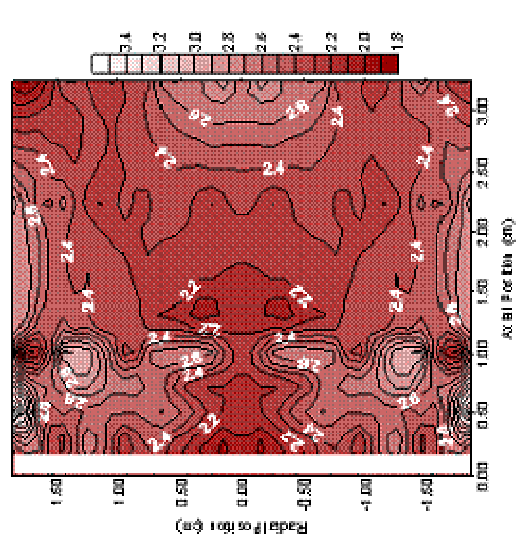
Plasma potential contour plot for Condition # SC1 (V).



Plasma potential contour plot for Condition # SC2 (V).

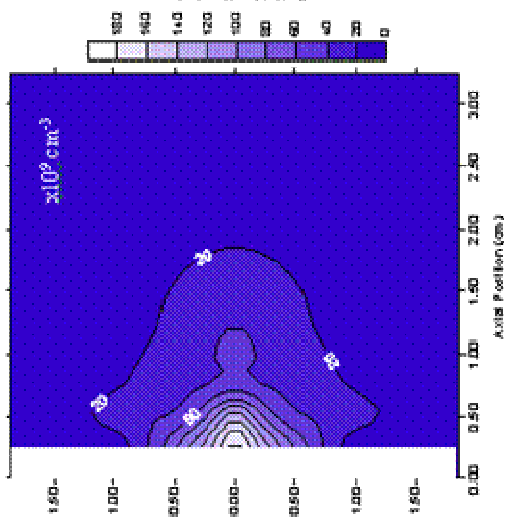


Electron temperature contour plot for Condition # SC1 (eV).

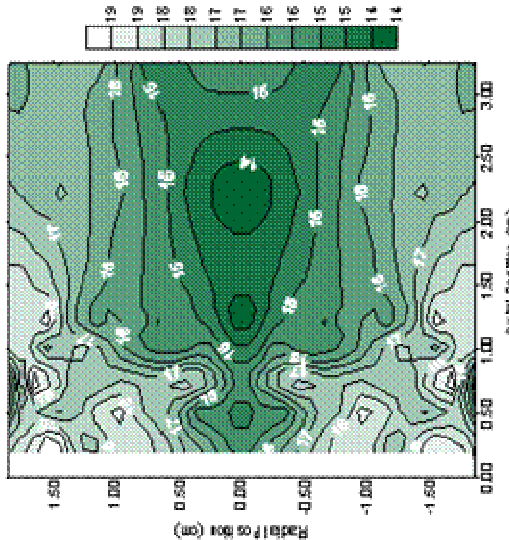


Electron temperature contour plot for Condition # SC2 (eV).

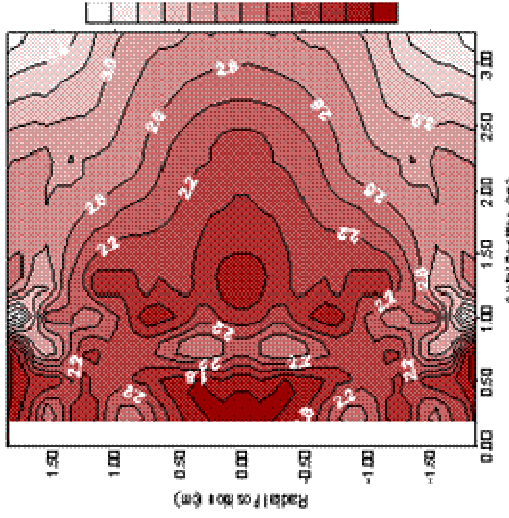




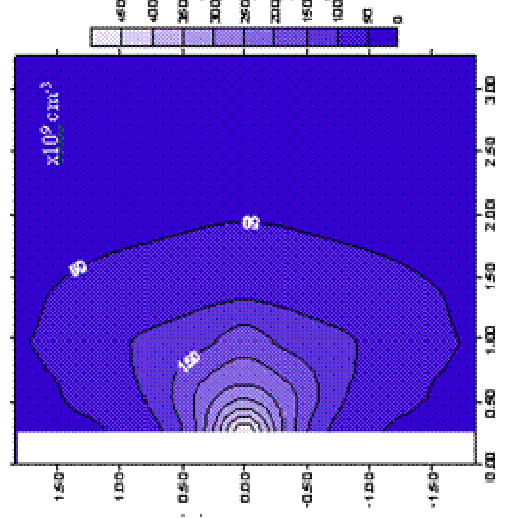
Electron number density contour plot for Condition # SC5 ( $\times 10^{20} \text{ cm}^{-3}$ ).



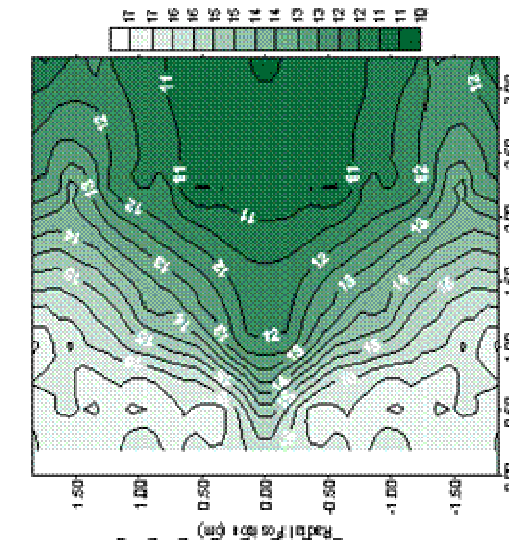
Plasma potential contour plot for Condition # SC5 (V).



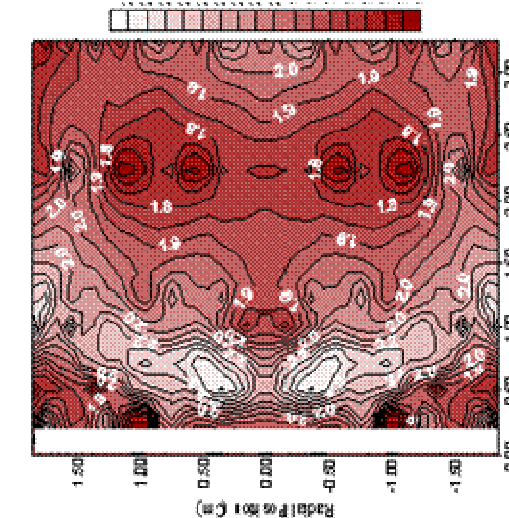
Electron temperature contour plot for Condition # SC5 (eV).



Electron number density contour plot for Condition # SC6 ( $\times 10^{20} \text{ cm}^{-3}$ ).

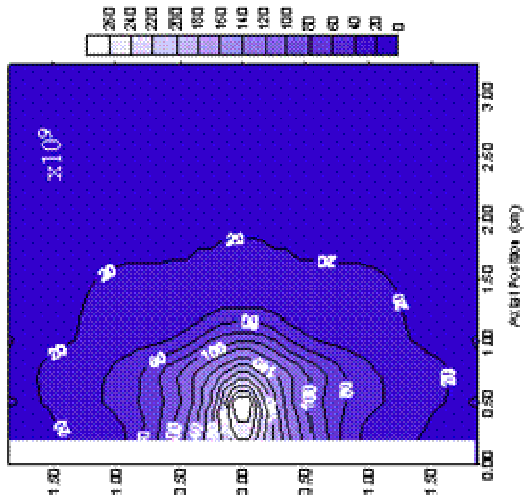


Plasma potential contour plot for Condition # SC6 (V).

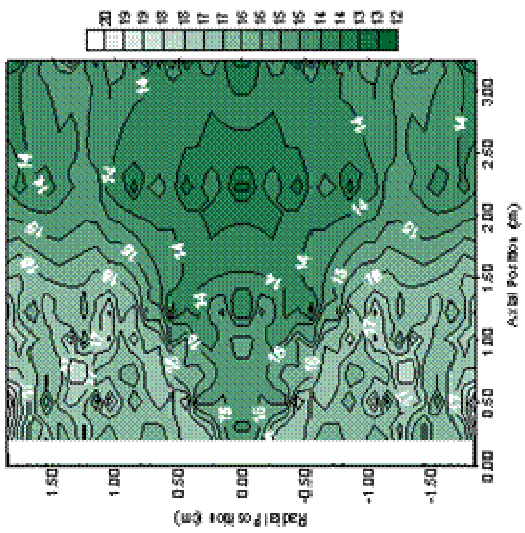


Electron temperature contour plot for Condition # SC6 (eV).

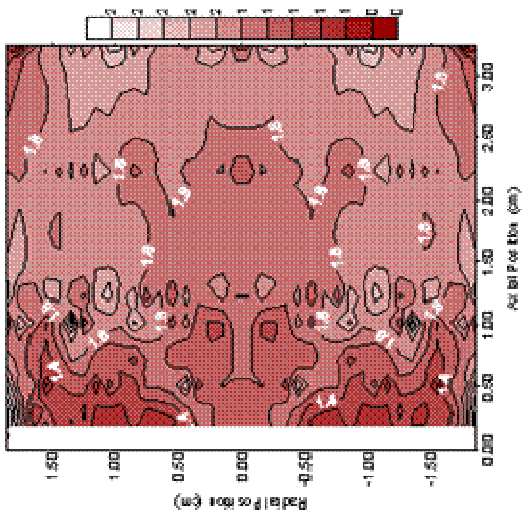




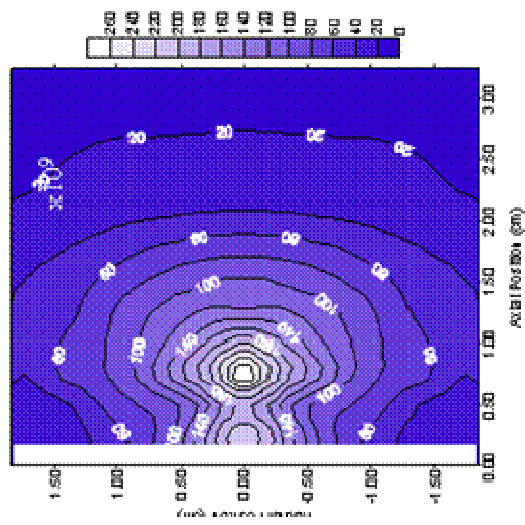
Electron number density contour plot for Condition # SC9 ( $\times 10^9 \text{ cm}^{-3}$ ).



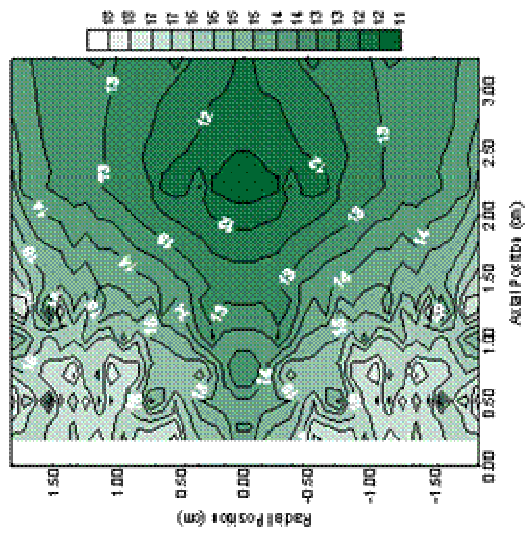
Plasma potential contour plot for Condition # SC9 (V).



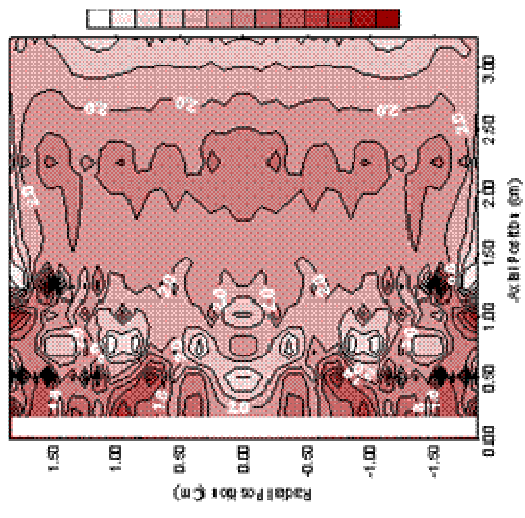
Electron temperature contour plot for Condition # SC9 (eV).



Electron number density contour plot for Condition # SC10 ( $\times 10^9 \text{ cm}^{-3}$ ).



Plasma potential contour plot for Condition # SC10 (V).

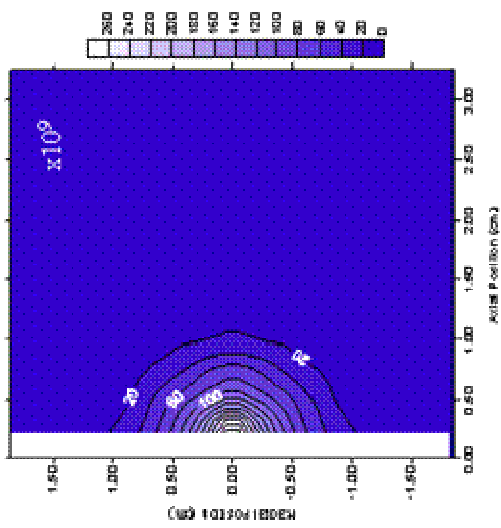


Electron temperature contour plot for Condition # SC10 (eV).

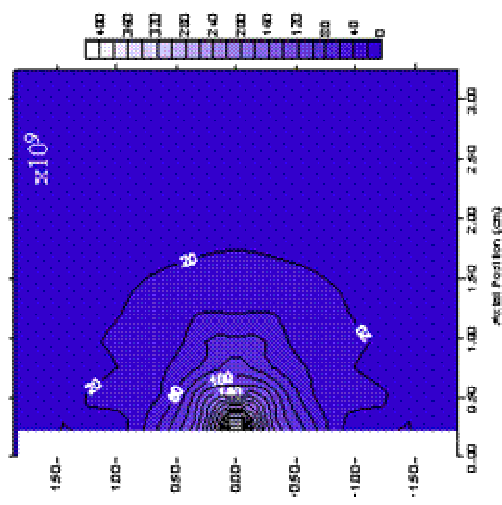


### Simple Cathode with Near Plate Anode (SCP 100505)

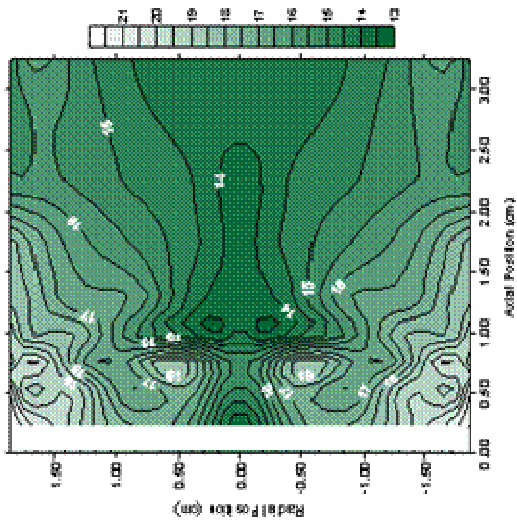
Operating Condition	(A)	$V_a$ (V)	$I_a$ (scem)	Pressure ( $\times 10^{-5}$ Torr)
SCP1	2	34.0	1.5	3.5
SCP2	4	41.7	1.5	3.5
SCP3	6	49.7	1.5	3.5
NA	8	75.6	1.5	3.5
SCP4	2	31.1	3	5.9
SCP5	4	40.8	3	5.9
SCP6	6	44.9	3	5.9
SCP7	8	55.1	3	5.9
SCP8	2	32.2	4.5	8.0
SCP9	4	34.0	4.5	8.0
NA	6	44.1	4.5	8.0
NA	8	56.7	4.5	8.0



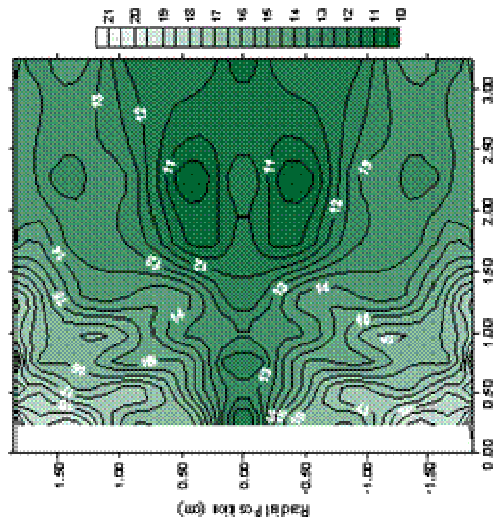
Electron number density contour plot for Condition # SCP1 ( $\times 10^9 \text{ cm}^{-3}$ ).



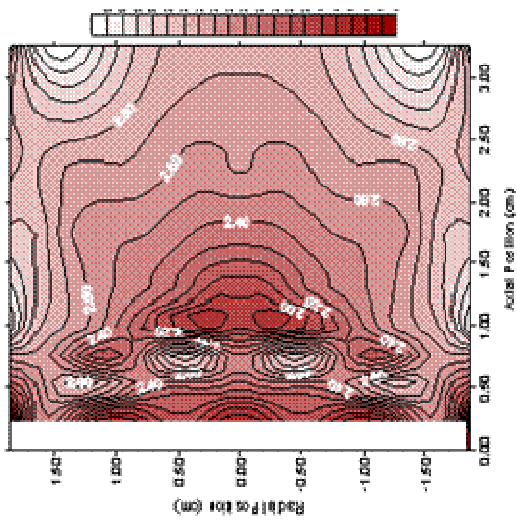
Electron number density contour plot for Condition # SCP2 ( $\times 10^9 \text{ cm}^{-3}$ ).



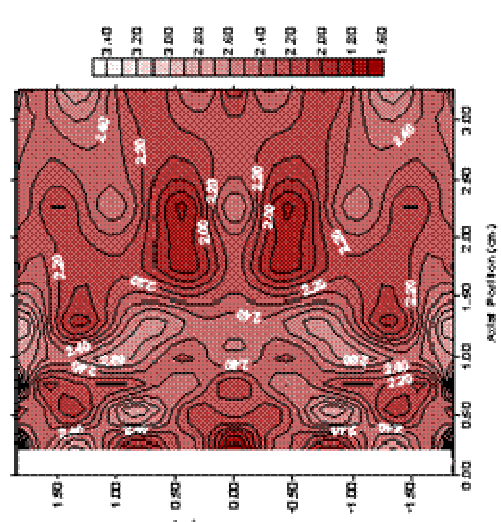
Plasma potential contour plot for Condition # SCP1 (V).



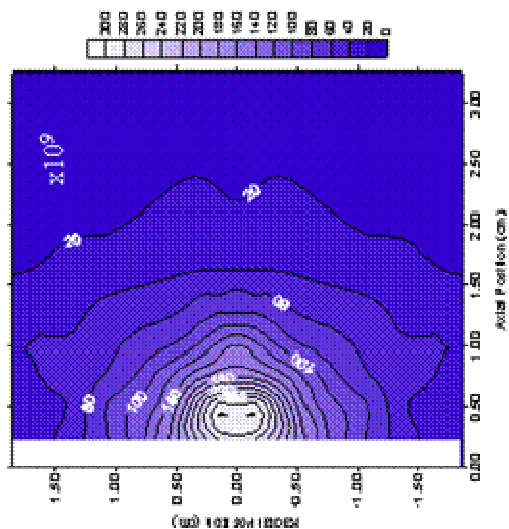
Plasma potential contour plot for Condition # SCP2 (V).



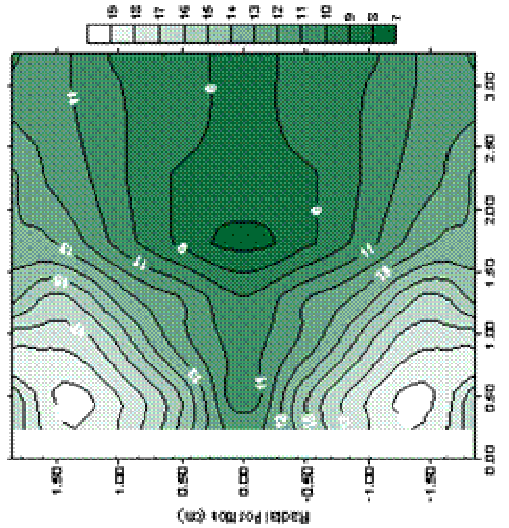
Electron temperature contour plot for Condition # SCP1 (eV).



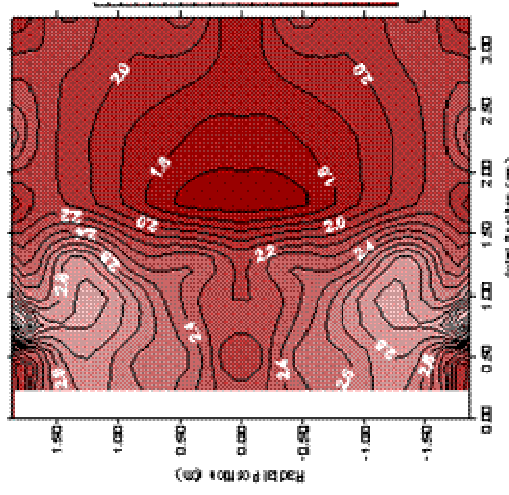
Electron temperature contour plot for Condition # SCP2 (eV).



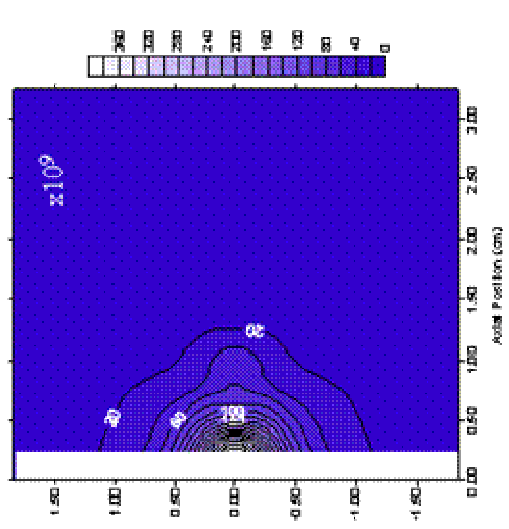
Electron number density contour plot for Condition # SCP3 ( $\times 10^9 \text{ cm}^{-3}$ ).



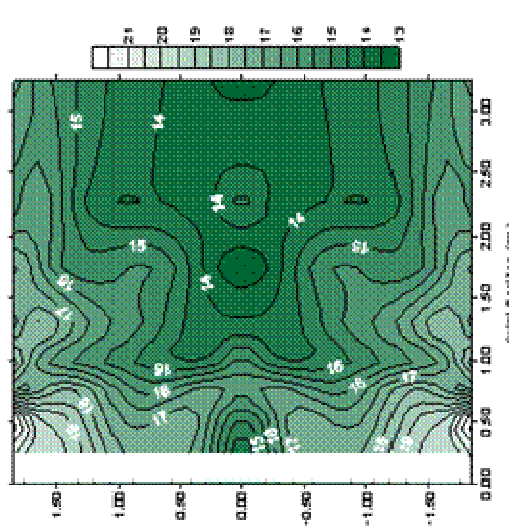
Plasma potential contour plot for Condition # SCP3 (V).



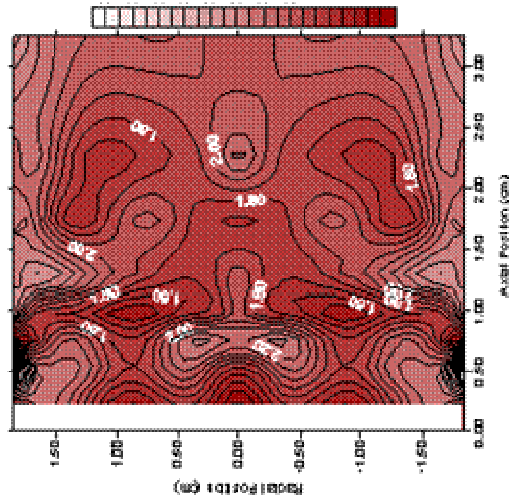
Electron temperature contour plot for Condition # SCP3 (eV).



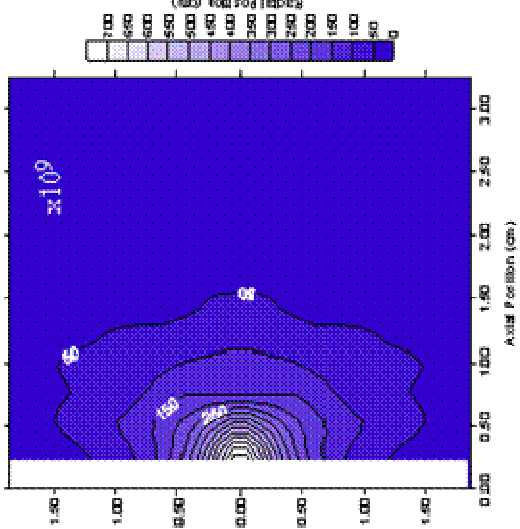
Electron number density contour plot for Condition # SCP4 ( $\times 10^9 \text{ cm}^{-3}$ ).



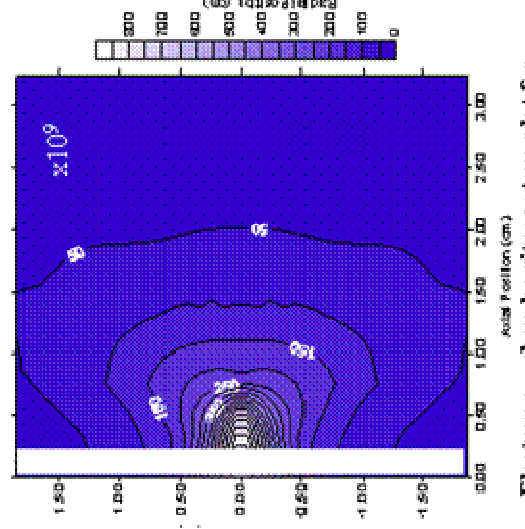
Plasma potential contour plot for Condition # SCP4 (V).



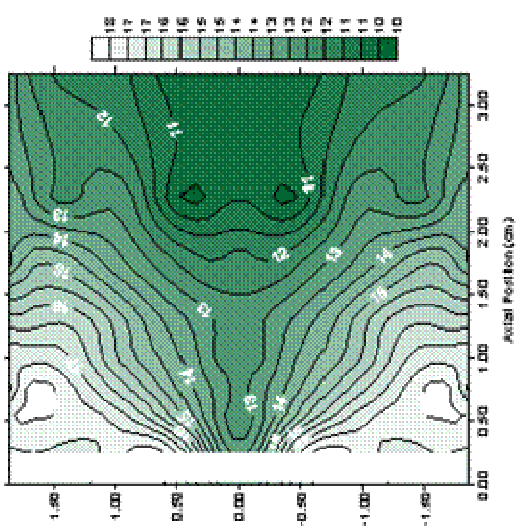
Electron temperature contour plot for Condition # SCP4 (eV).



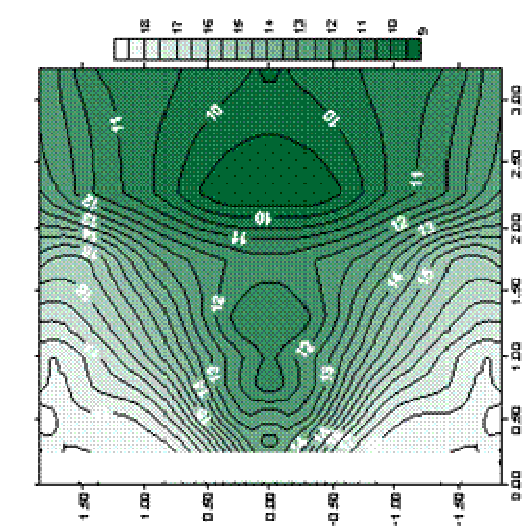
Electron number density contour plot for Condition # SCP5 ( $\times 10^9 \text{ cm}^{-3}$ ).



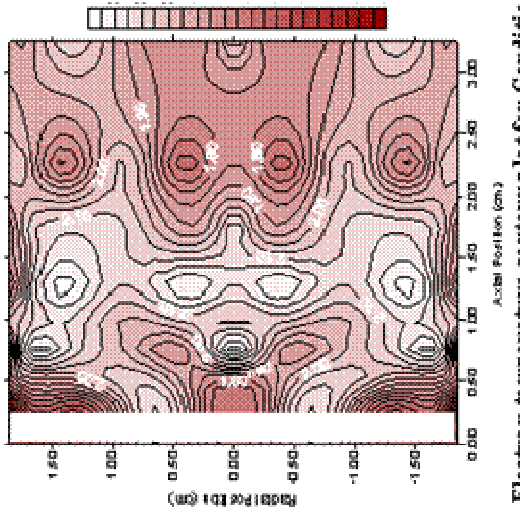
Electron number density contour plot for Condition # SCP6 ( $\times 10^9 \text{ cm}^{-3}$ ).



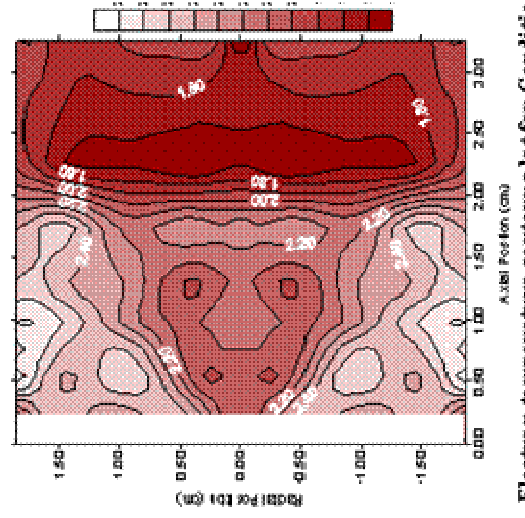
Plasma potential contour plot for Condition # SCP5 (V).



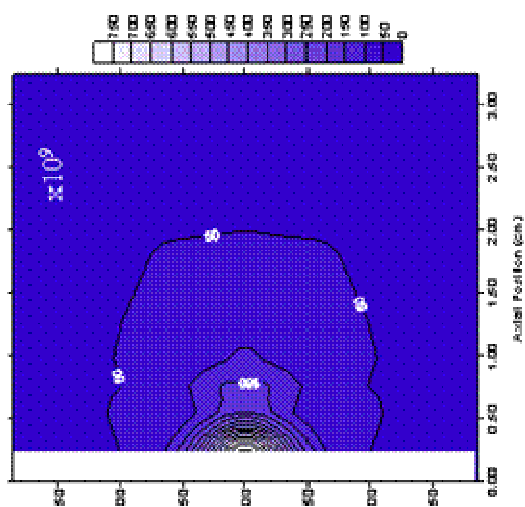
Plasma potential contour plot for Condition # SCP6 (V).



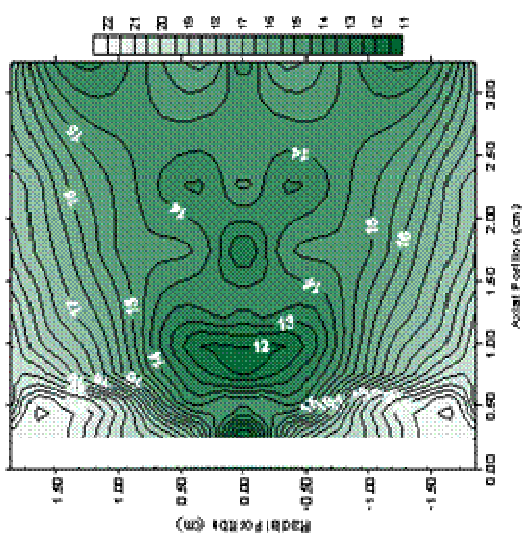
Electron temperature contour plot for Condition # SCP5 (eV).



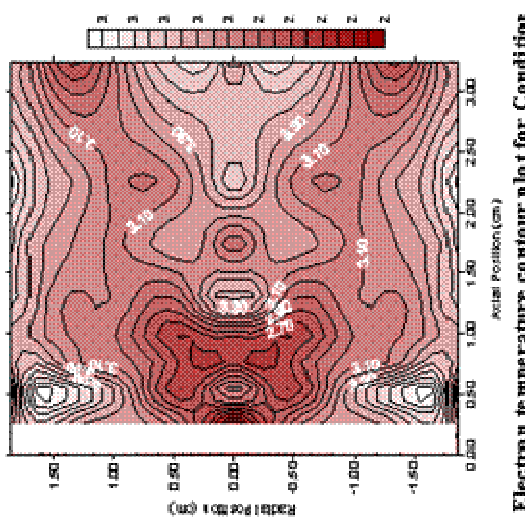
Electron temperature contour plot for Condition # SCP6 (eV).



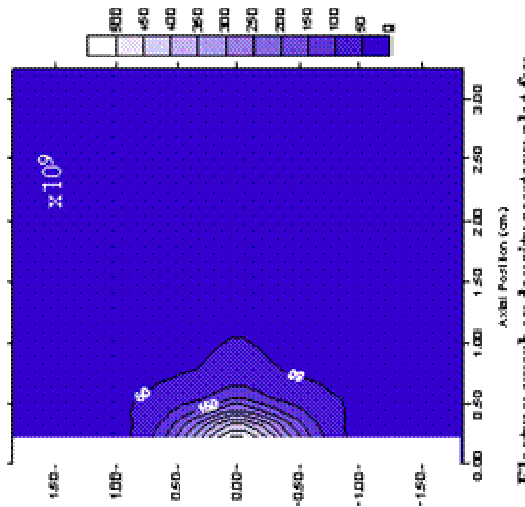
Electron number density contour plot for Condition # SCP7 ( $\times 10^9 \text{ cm}^{-3}$ ).



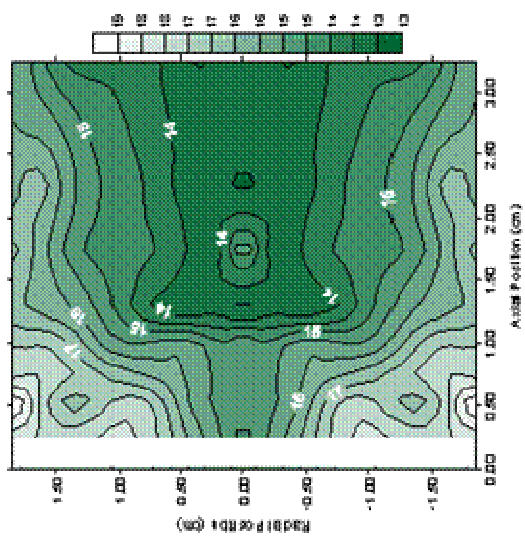
Plasma potential contour plot for Condition # SCP7 (V).



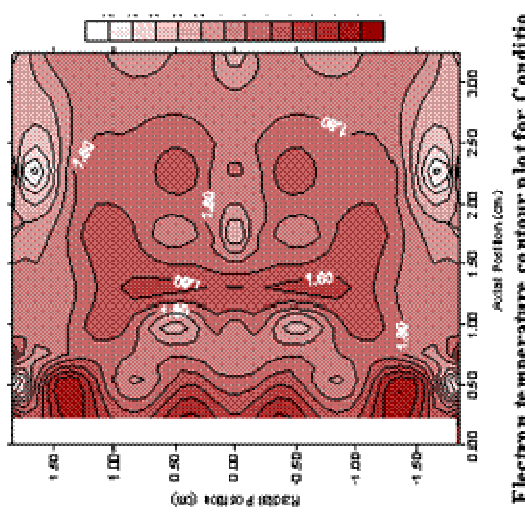
Electron temperature contour plot for Condition # SCP7 (eV).



Electron number density contour plot for Condition # SCP8 ( $\times 10^9 \text{ cm}^{-3}$ ).



Plasma potential contour plot for Condition # SCP8 (V).

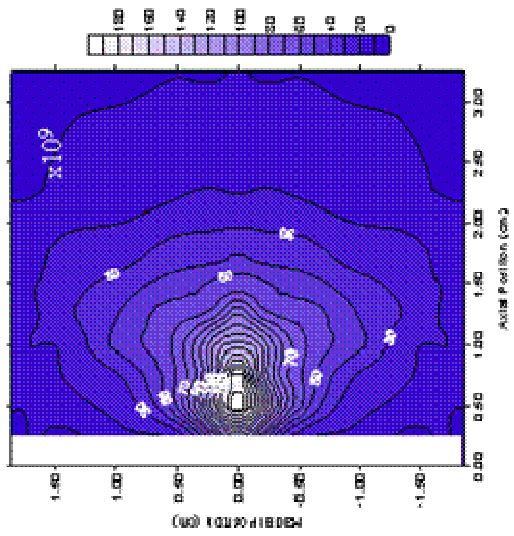


Electron temperature contour plot for Condition # SCP8 (eV).

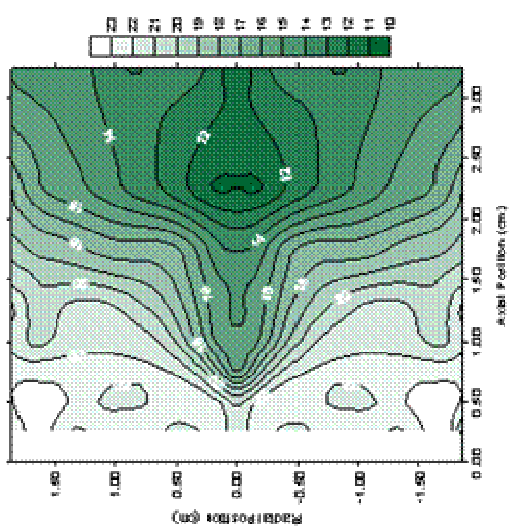


### Small Orifice Keeper (SK 101805, 102405)

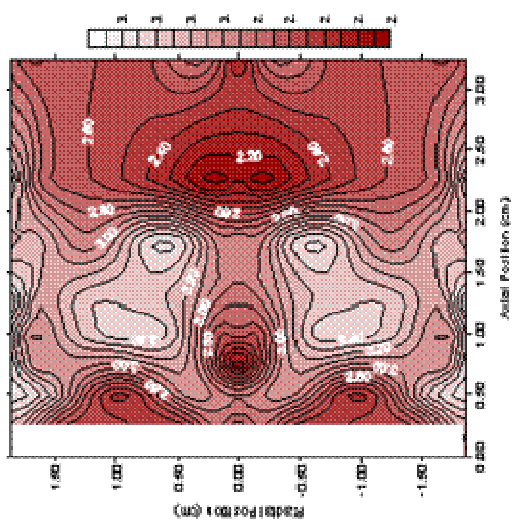
Operating Condition	(A)	$V_d$ (V)	$z$ (sccm)	Pressure ( $\times 10^{-5}$ Torr)
NA	2	36.5	1.5	3.8
SK1	4	41.5	1.5	3.8
		40.4		3.4
NA	6	78.0	1.5	3.8
NA	2	29.5	3	5.6
SK2	4	37.8	3	5.6
		40.1		5.6
SK3	6	47.0	3	5.6
SK4	8	56.0	3	5.6
SK5	2	32.6	4.5	8.0
SK6	4	39.5	4.5	8.0
SK7	6	47.5	4.5	8.0
SK8	8	55.7	4.5	8.0



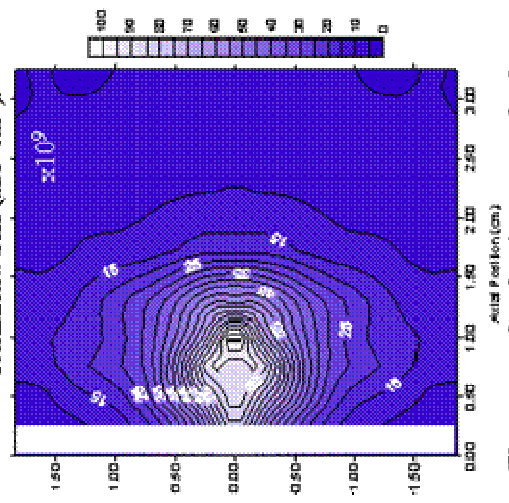
Electron number density contour plot for Condition # SK1 ( $\times 10^9 \text{ cm}^{-3}$ ).



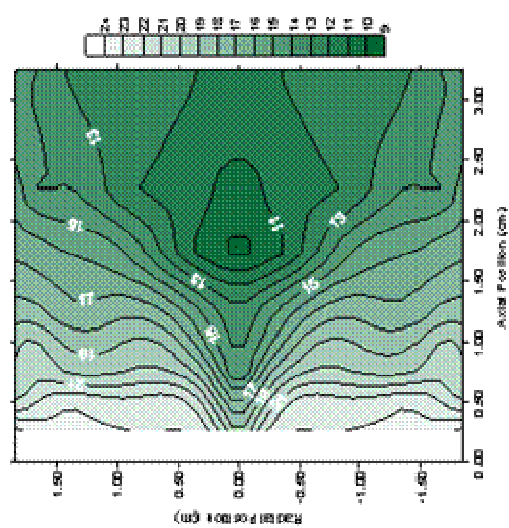
Plasma potential contour plot for Condition # SK1 (V).



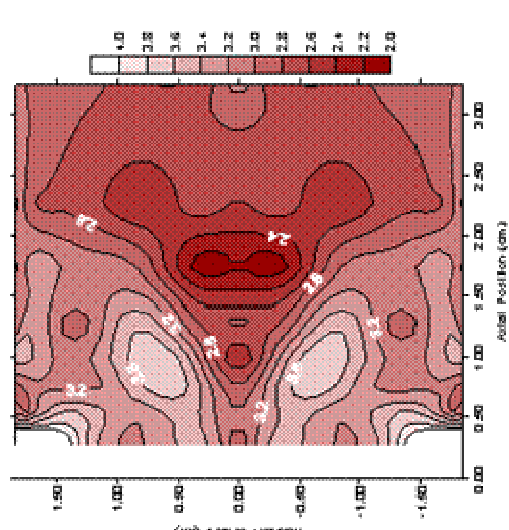
Electron temperature contour plot for Condition # SK1 (eV).



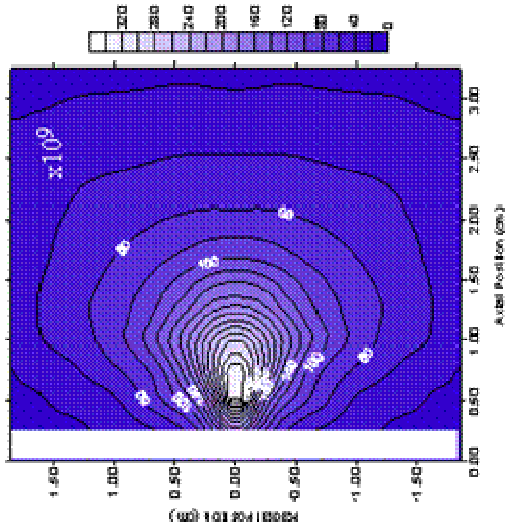
Electron number density contour plot for Condition # SK1 ( $\times 10^9 \text{ cm}^{-3}$ ).



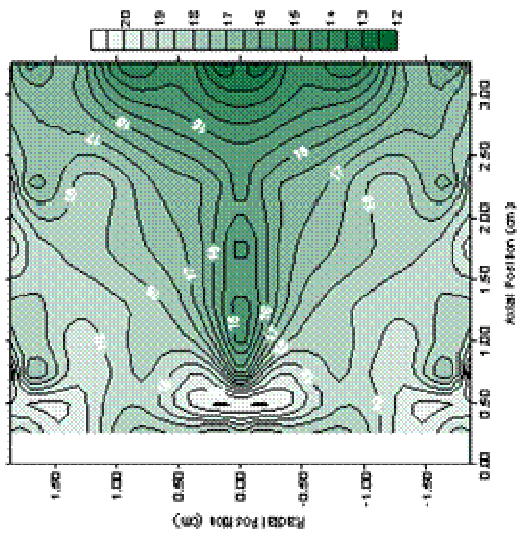
Plasma potential contour plot for Condition # SK1 (V).



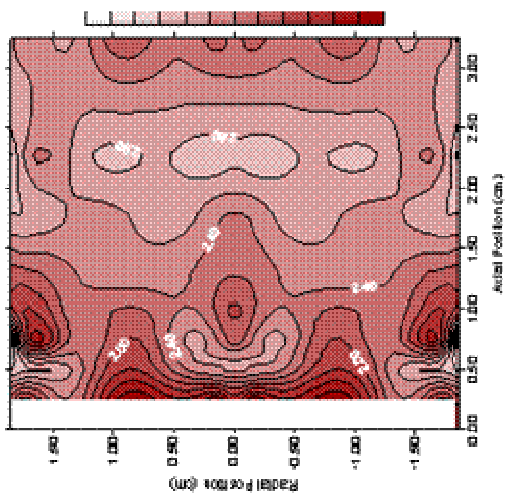
Electron temperature contour plot for Condition # SK1 (eV).



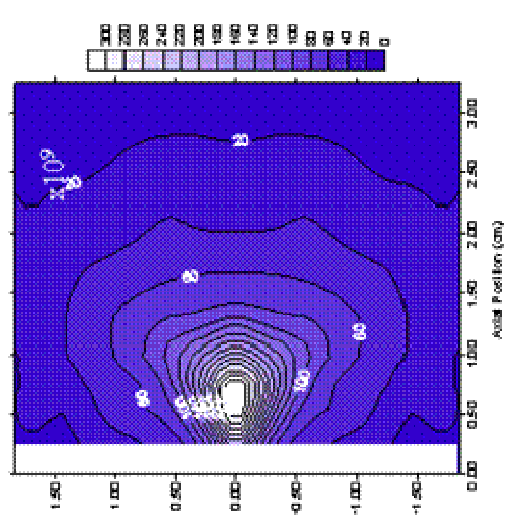
Electron number density contour plot for Condition # SK2 ( $\times 10^9 \text{ cm}^{-3}$ ).



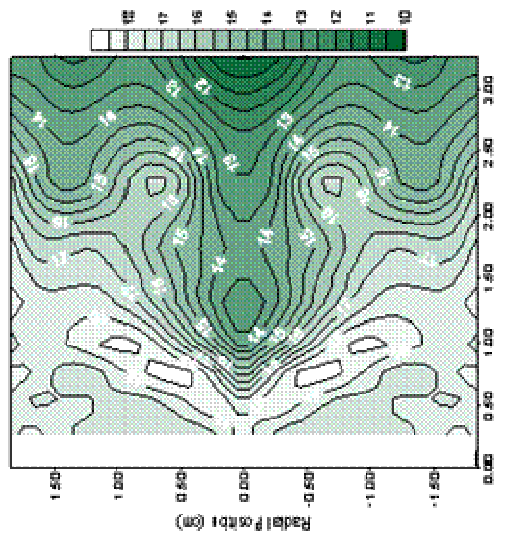
Plasma potential contour plot for Condition # SK2 (V).



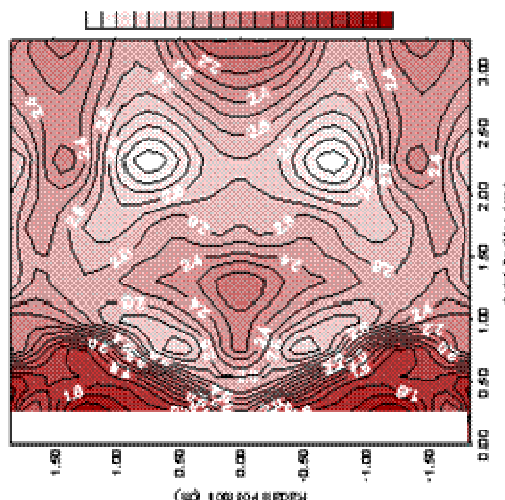
Electron temperature contour plot for Condition # SK2 (eV).



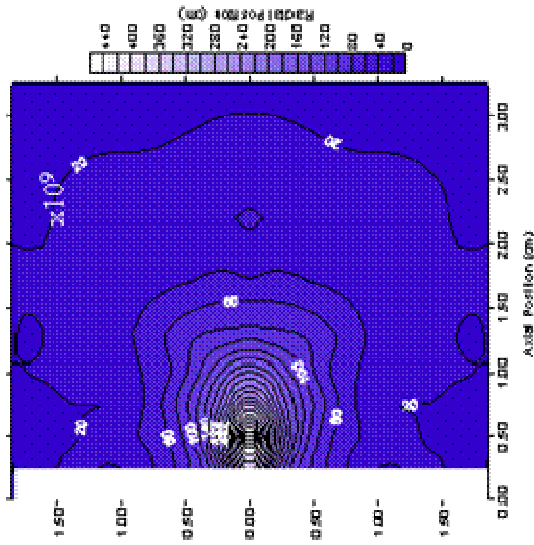
Electron number density contour plot for Condition # SK2 ( $\times 10^9 \text{ cm}^{-3}$ ).



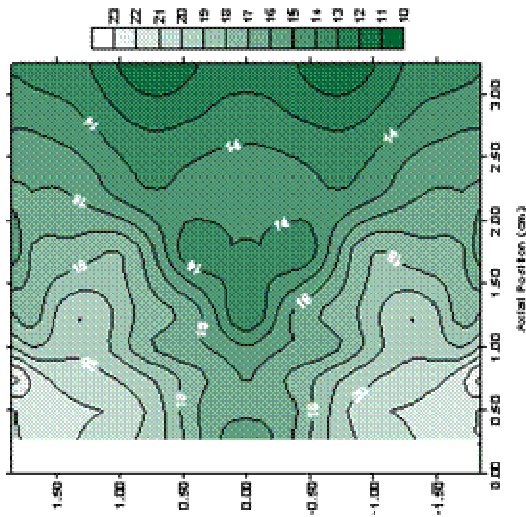
Plasma potential contour plot for Condition # SK2 (V).



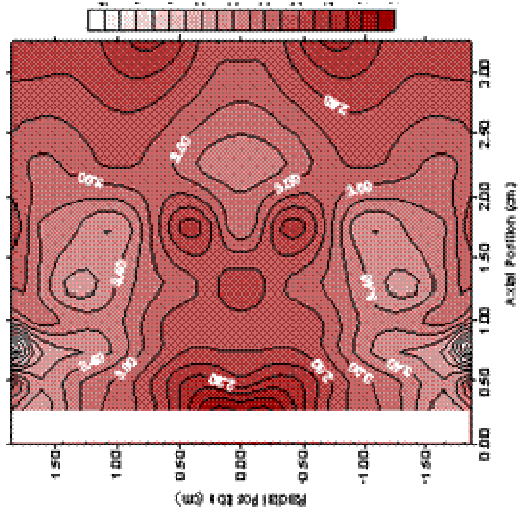
Electron temperature contour plot for Condition # SK2 (eV).



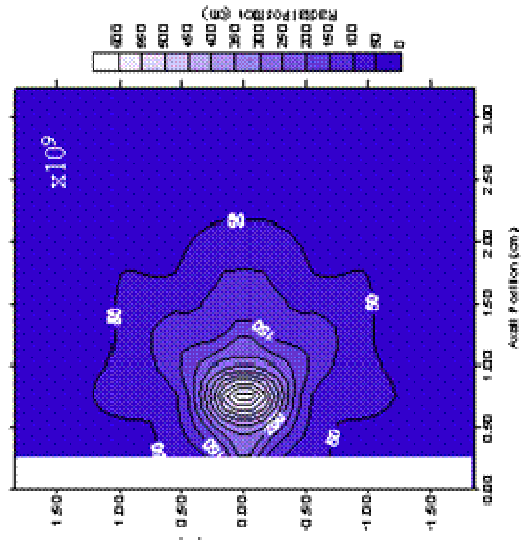
Electron number density contour plot for Condition # SK3 ( $\times 10^9 \text{ cm}^{-3}$ ).



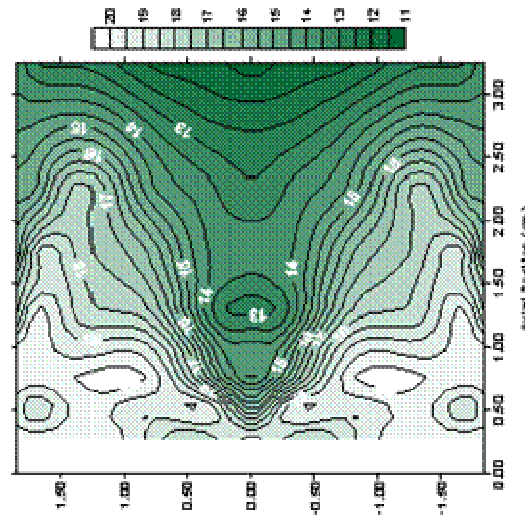
Plasma potential contour plot for Condition # SK3 (V).



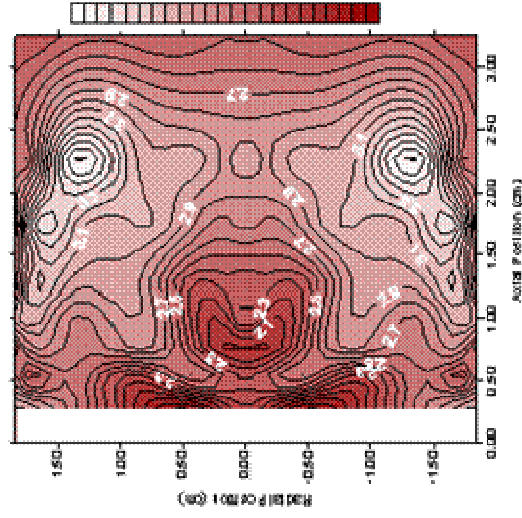
Electron temperature contour plot for Condition # SK3 (eV).



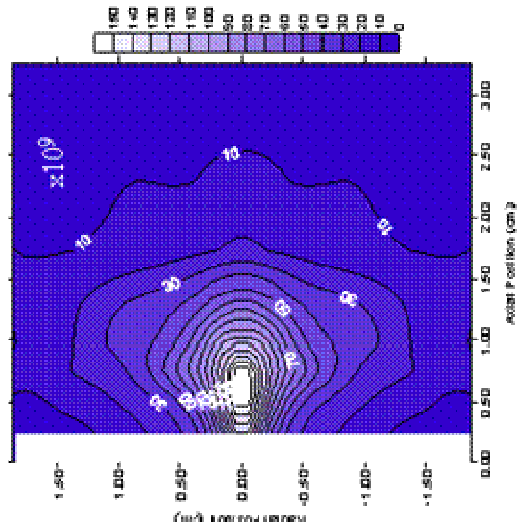
Electron number density contour plot for Condition # SK4 ( $\times 10^9 \text{ cm}^{-3}$ ).



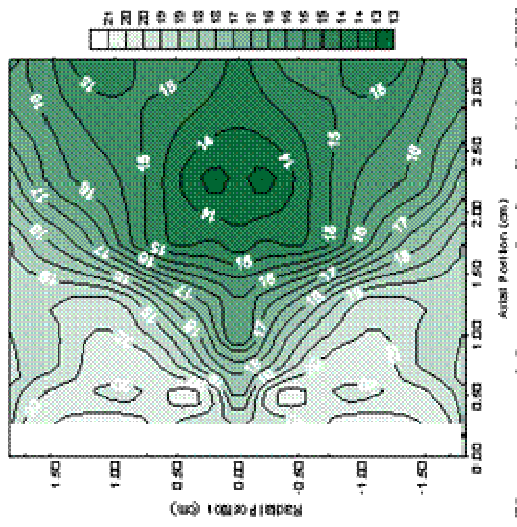
Plasma potential contour plot for Condition # SK4 (V).



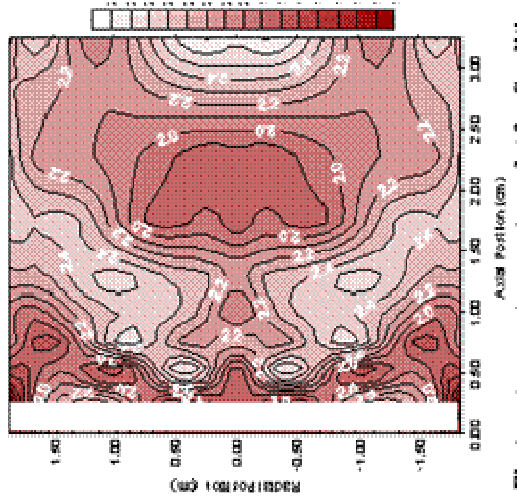
Electron temperature contour plot for Condition # SK4 (eV).



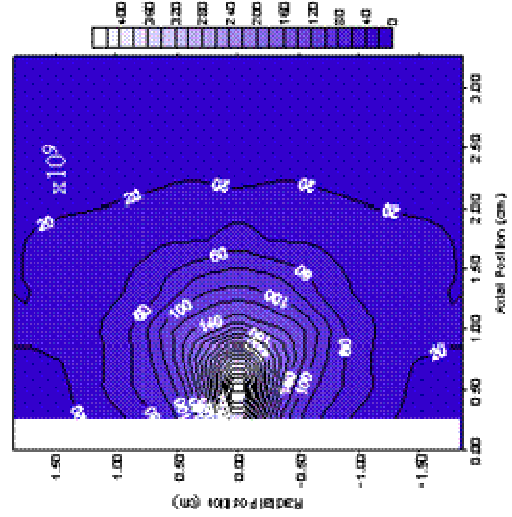
Electron number density contour plot for Condition # SK5 ( $\times 10^9 \text{ cm}^{-3}$ ).



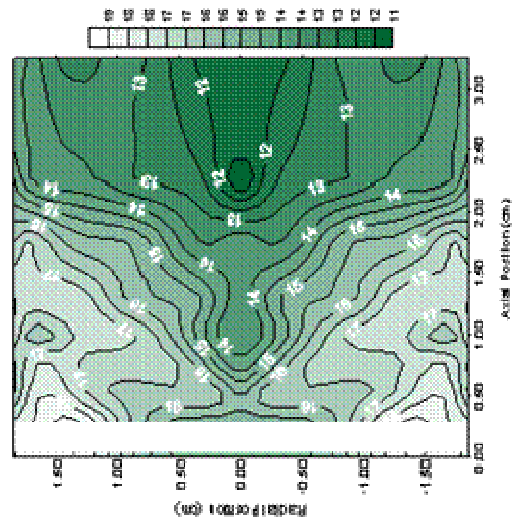
Plasma potential contour plot for Condition # SK5 (V).



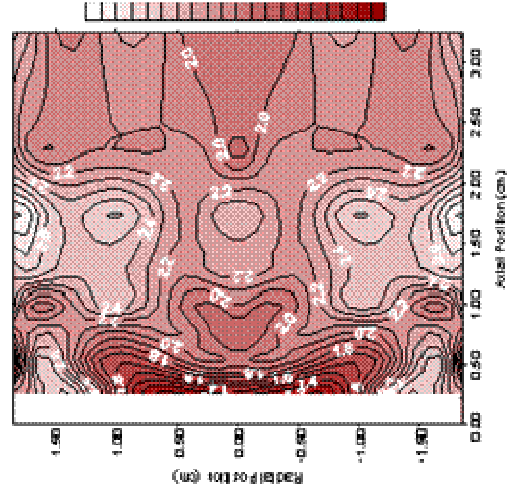
Electron temperature contour plot for Condition SK5 (eV).



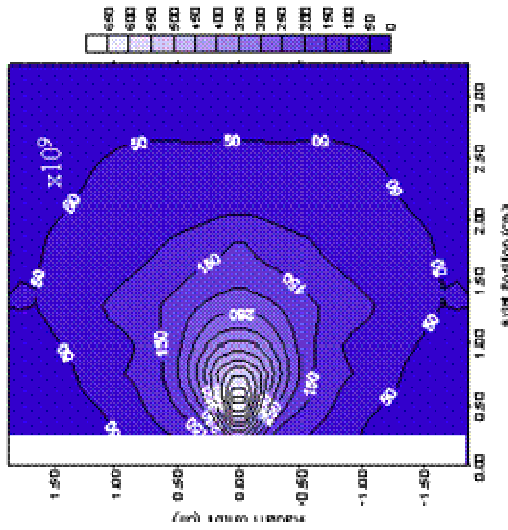
Electron number density contour plot for Condition # SK6 ( $\times 10^9 \text{ cm}^{-3}$ ).



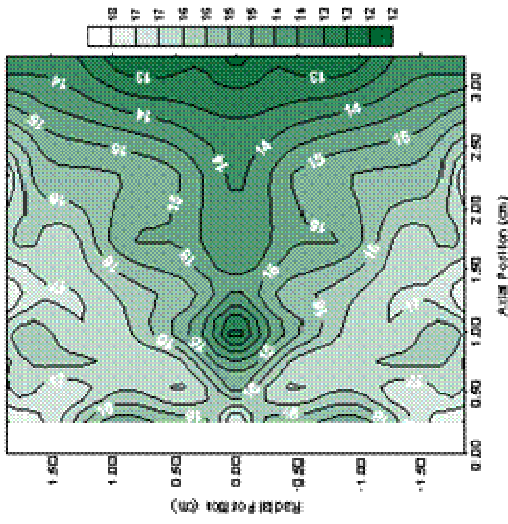
Plasma potential contour plot for Condition # SK6 (V).



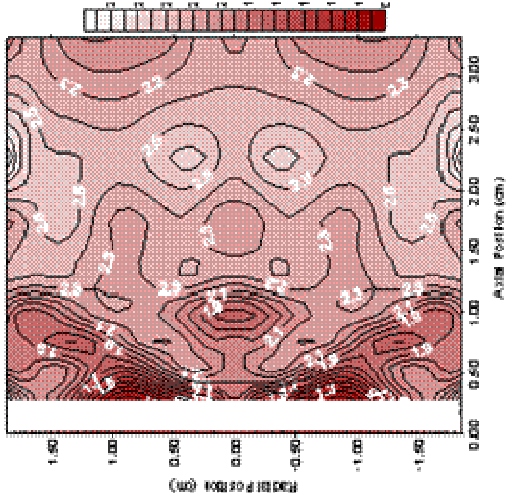
Electron temperature contour plot for Condition SK6 (eV).



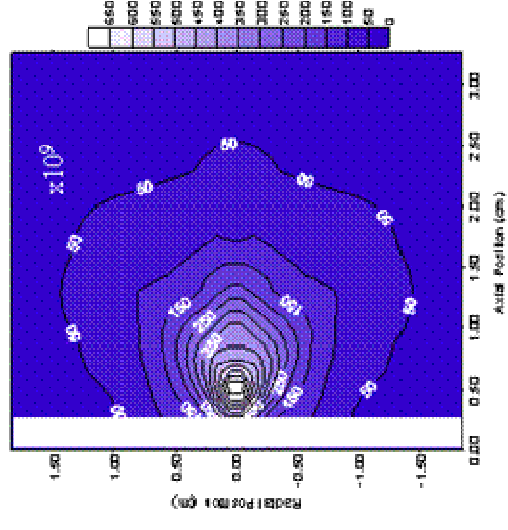
Electron number density contour plot for Condition # SK7 ( $\times 10^9 \text{ cm}^{-3}$ ).



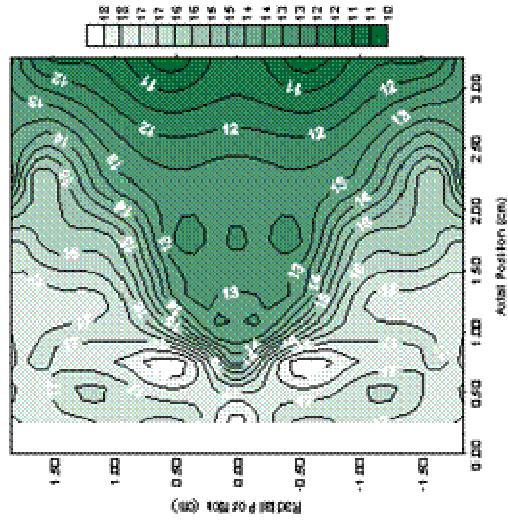
Plasma potential contour plot for Condition # SK7 (V).



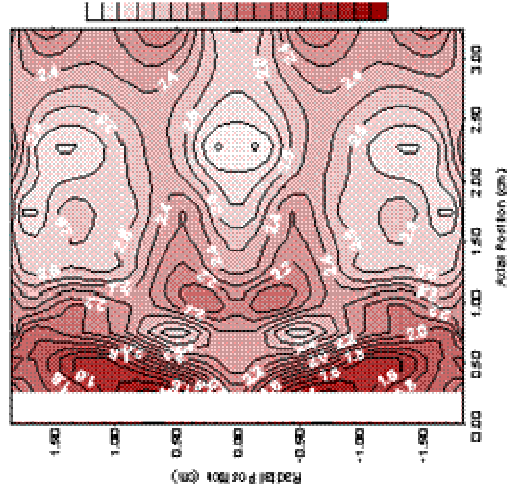
Electron temperature contour plot for Condition SK7 (eV).



Electron number density contour plot for Condition # SK8 ( $\times 10^9 \text{ cm}^{-3}$ ).



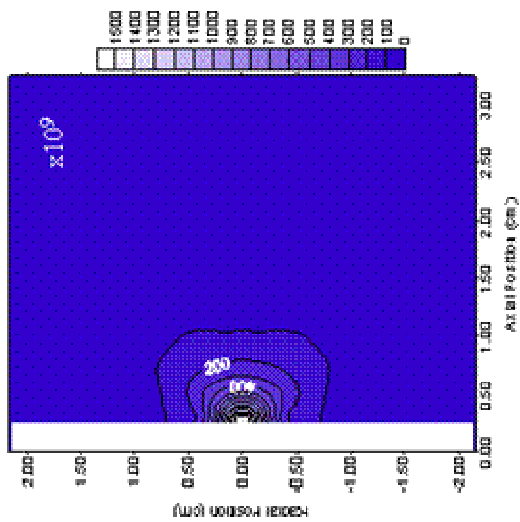
Plasma potential contour plot for Condition # SK8 (V).



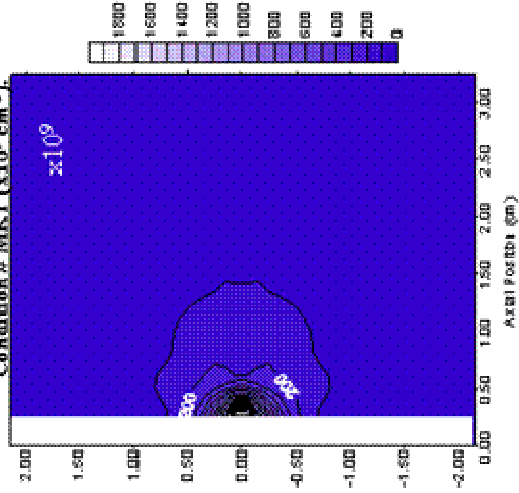
Electron temperature contour plot for Condition SK8 (eV).

### Medium Orifice Keeper (MK 101805, 102405)

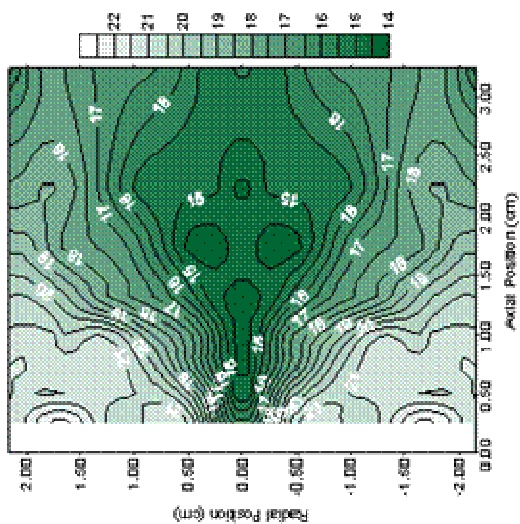
Operating Condition	(A)	$f_d$ (V)	$z$ (sccm)	Pressure ( $\times 10^{-5}$ Torr)
MK1	2	36.7	1.5	4.2
MK2	4	42.4	1.5	4.2
MK3	6	50.2	1.5	4.2
MK4	8	56.9	1.5	4.2
MK5	2	34.1	3	5.9
MK6	4	41.8	3	5.9
MK7	6	46.2	3	5.9
MK8	8	53.8	3	5.9
MK9	2	33.8	4.5	7.3
MK10	4	32.5	4.5	7.3
MK11	6	43.7	4.5	7.3
MK12	8	52.7	4.5	7.3



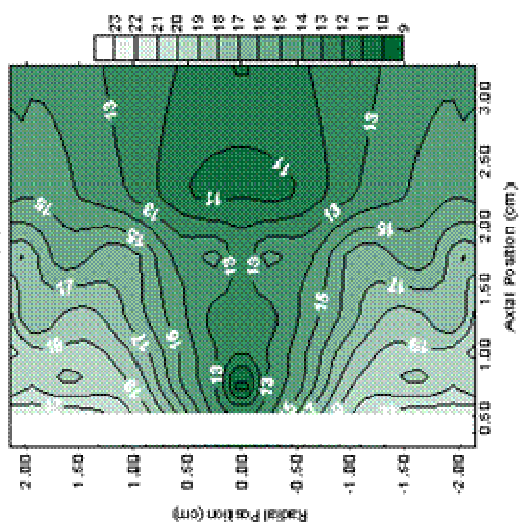
Electron number density contour plot for Condition # MK1 ( $\times 10^9 \text{ cm}^{-3}$ ).



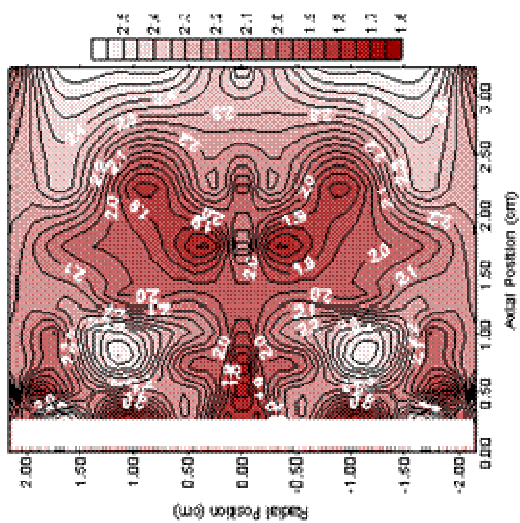
Electron number density contour plot for Condition # MK2 ( $\times 10^9 \text{ cm}^{-3}$ ).



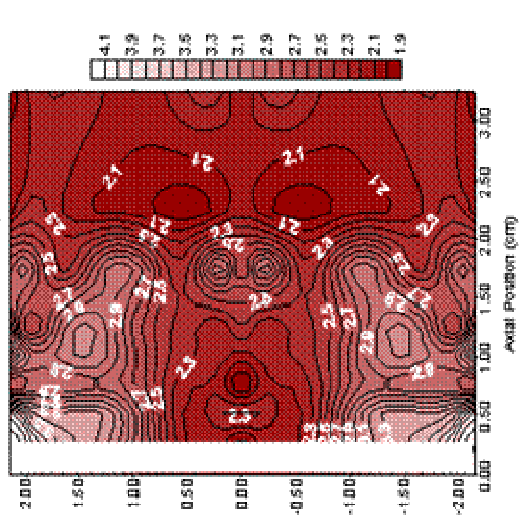
Plasma potential contour plot for Condition # MK1 (V).



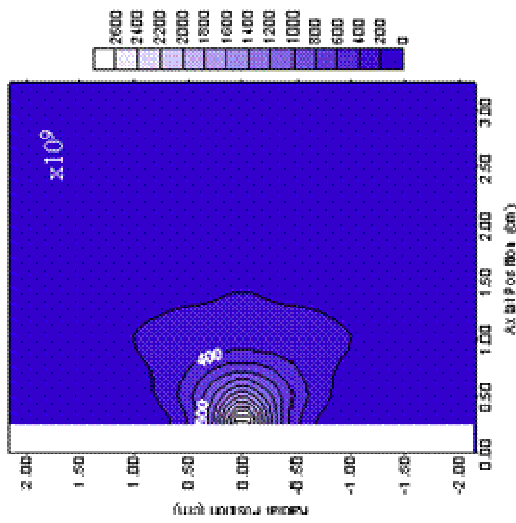
Plasma potential contour plot for Condition # MK2 (V).



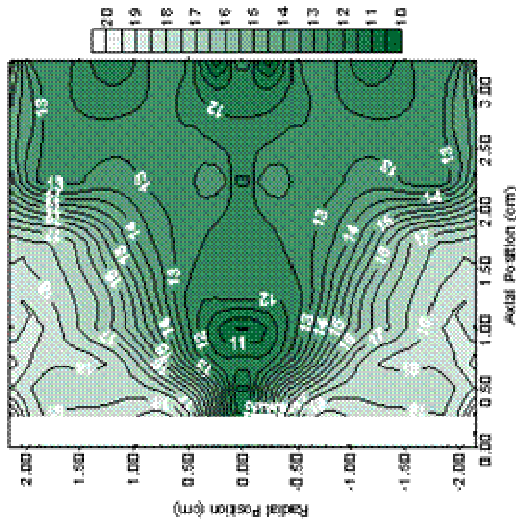
Electron temperature contour plot for Condition # MK1 (eV).



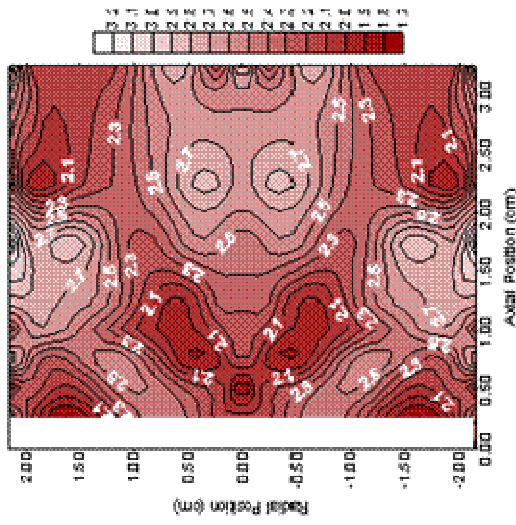
Electron temperature contour plot for Condition # MK2 (eV).



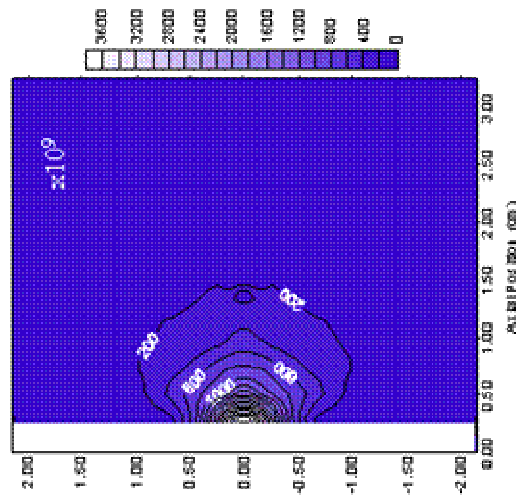
Electron number density contour plot for Condition # MK3 ( $\times 10^9 \text{ cm}^{-3}$ ).



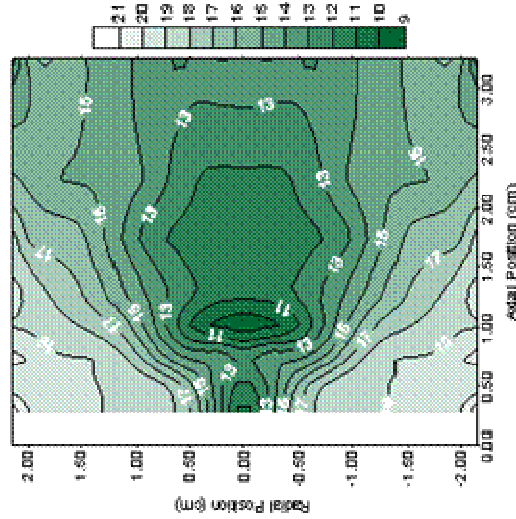
Plasma potential contour plot for Condition # MK3 (V).



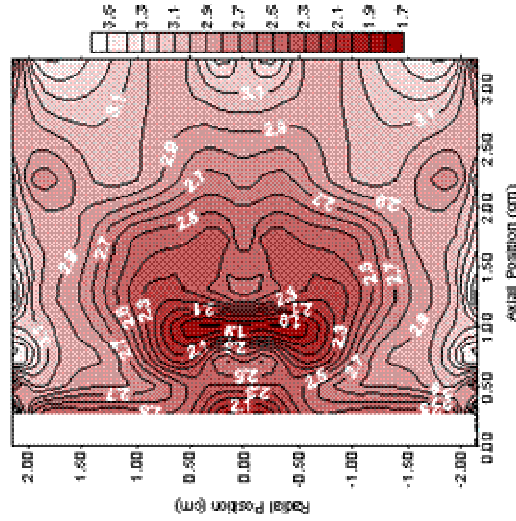
Electron temperature contour plot for Condition # MK3 (eV).



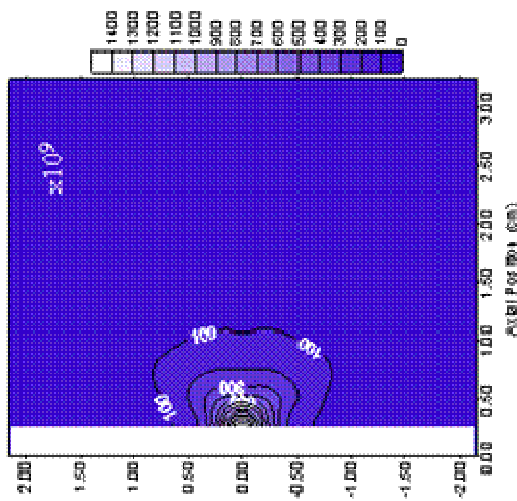
Electron number density contour plot for Condition # MK4 ( $\times 10^9 \text{ cm}^{-3}$ ).



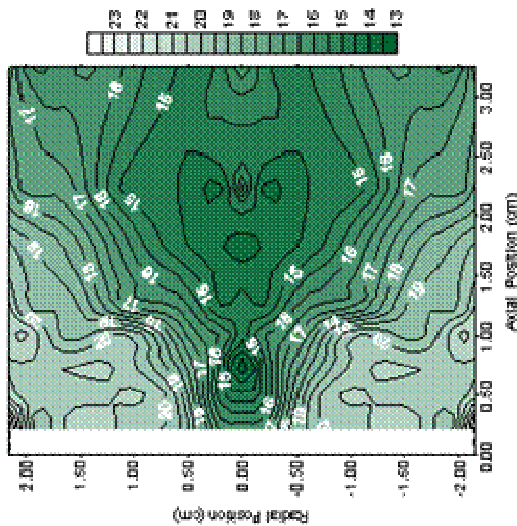
Plasma potential contour plot for Condition # MK4 (V).



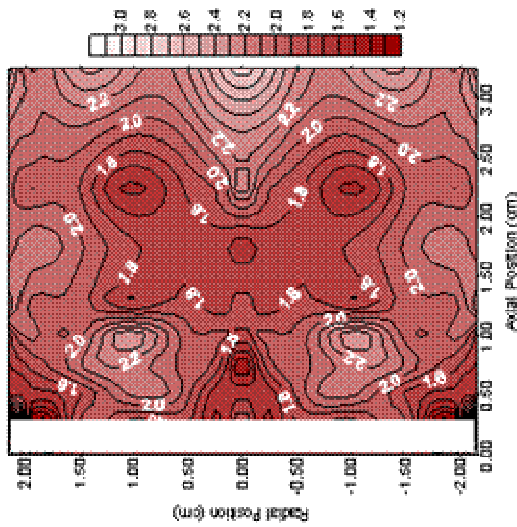
Electron temperature contour plot for Condition # MK4 (eV).



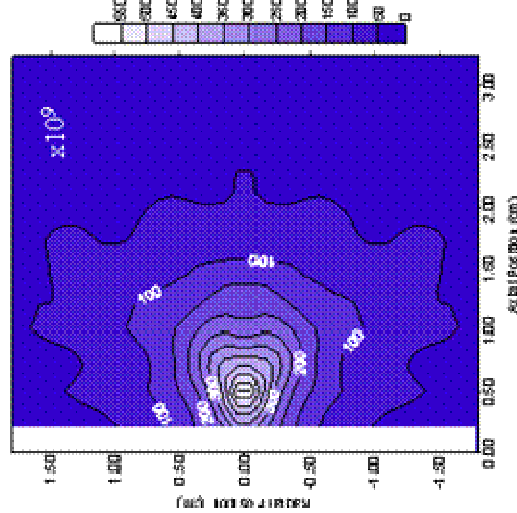
Electron number density contour plot for Condition # MK5 ( $\times 10^9 \text{ cm}^{-3}$ ).



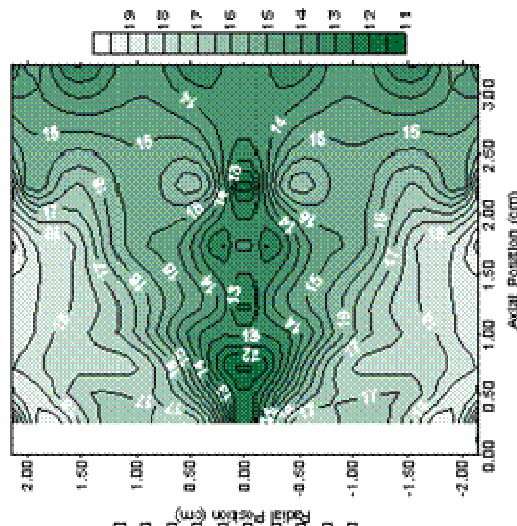
Plasma potential contour plot for Condition # MK5 (V).



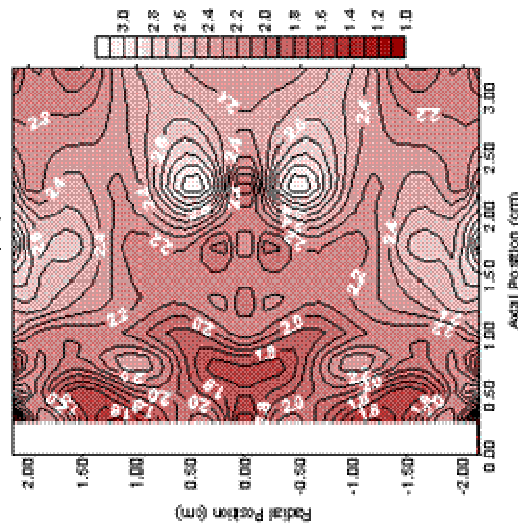
Electron temperature contour plot for Condition # MK5 (eV).



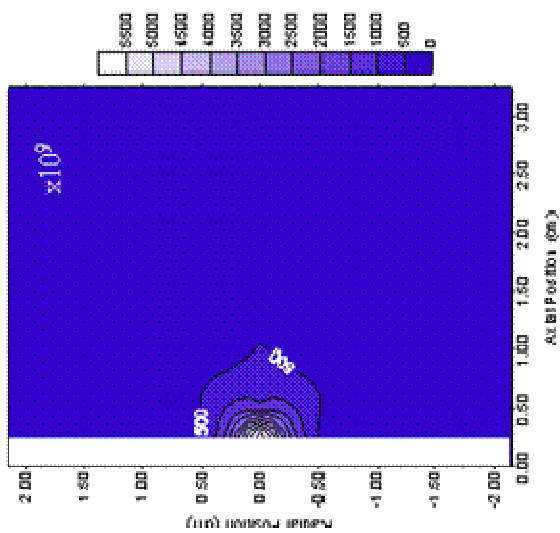
Electron number density contour plot for Condition # MK6 ( $\times 10^9 \text{ cm}^{-3}$ ).



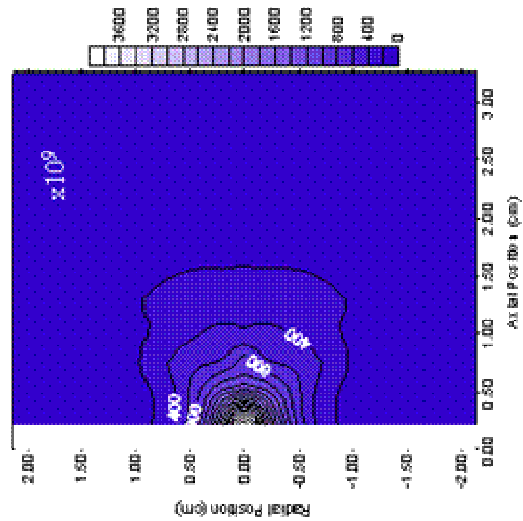
Plasma potential contour plot for Condition # MK6 (V).



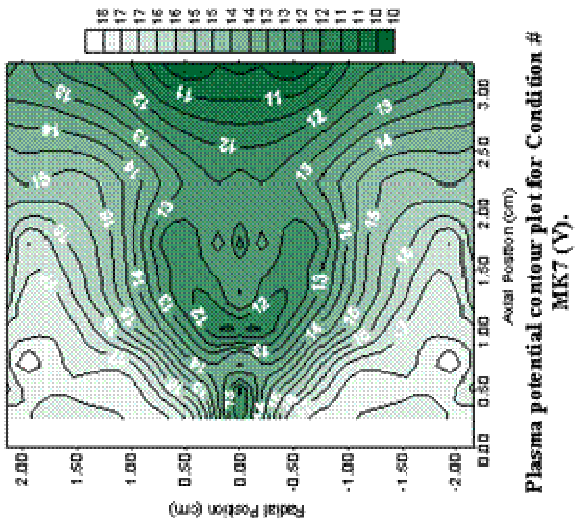
Electron temperature contour plot for Condition # MK6 (eV).



Electron number density contour plot for

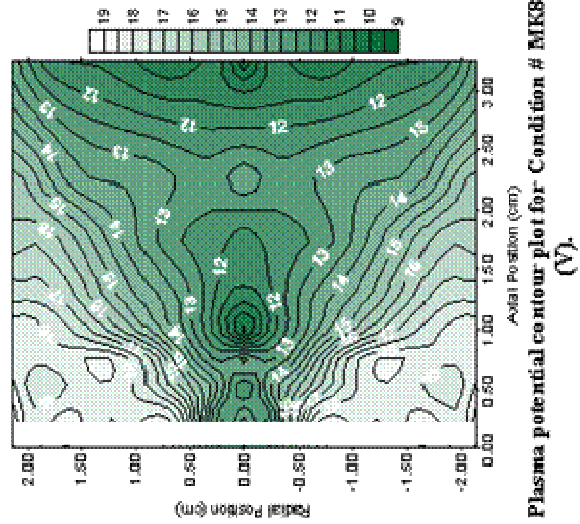


Electron number density contour plot for  
Condition # MK8 ( $\times 10^9 \text{ cm}^{-3}$ ).

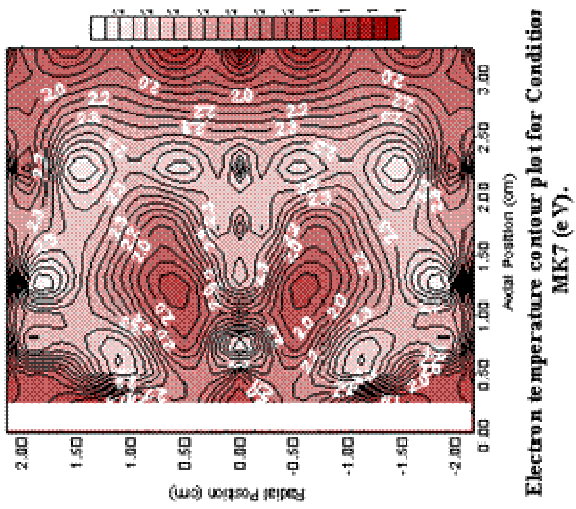


Plasma potential contour plot for Condition #

MK7 (V).

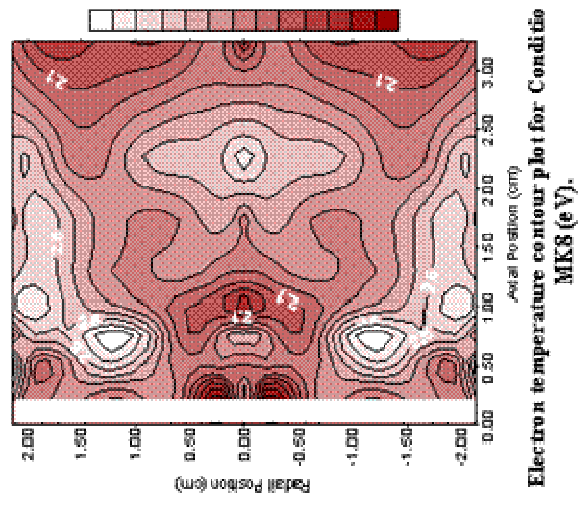


Plasma potential contour plot for Condition # MK8  
(V).

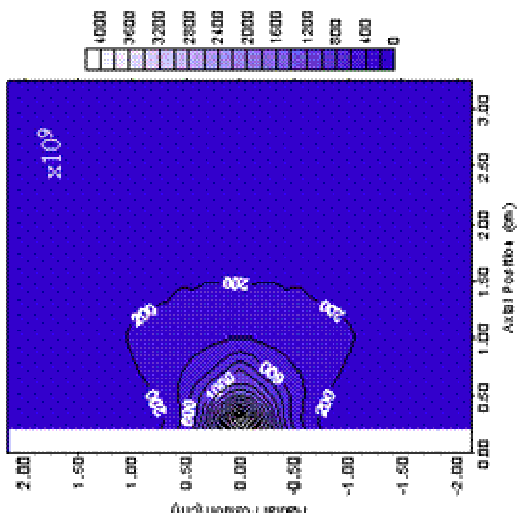


Electron temperature contour plot for Condition

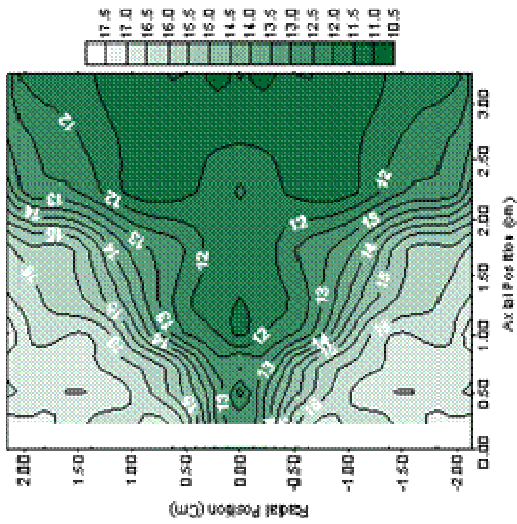
MK7 (eV).



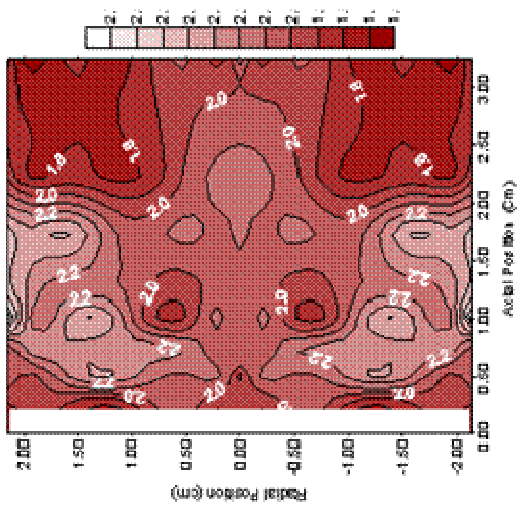
Electron temperature contour plot for Condition  
MK8 (eV).



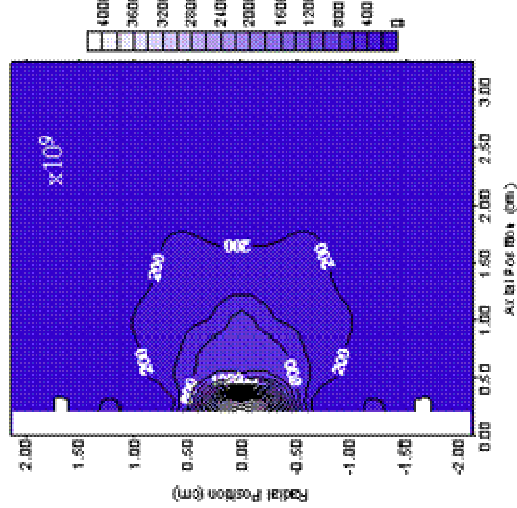
Electron number density contour plot for Condition # MK11 ( $\times 10^9 \text{ cm}^{-3}$ ).



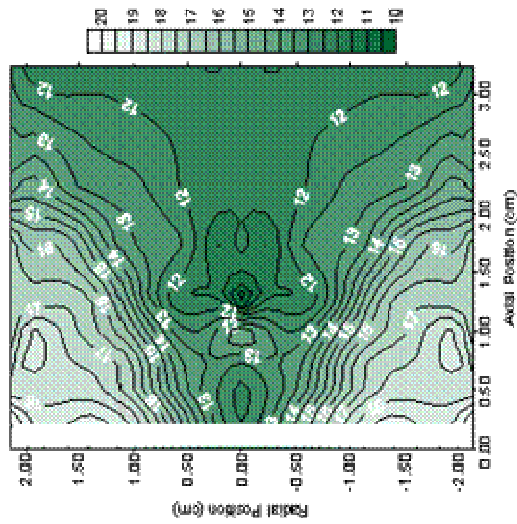
Plasma potential contour plot for Condition # MK11 (V).



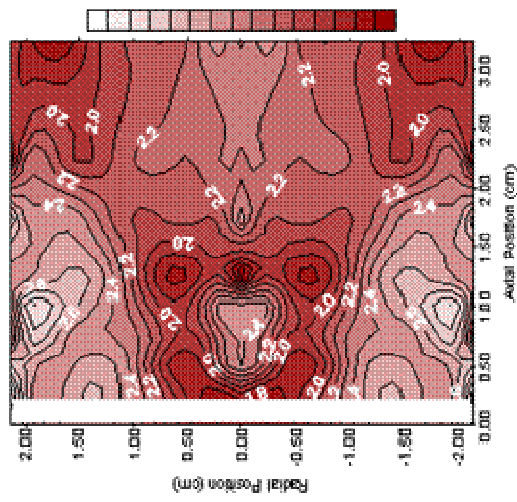
Electron temperature contour plot for Condition # MK11 (eV).



Electron number density contour plot for Condition # MK12 ( $\times 10^9 \text{ cm}^{-3}$ ).



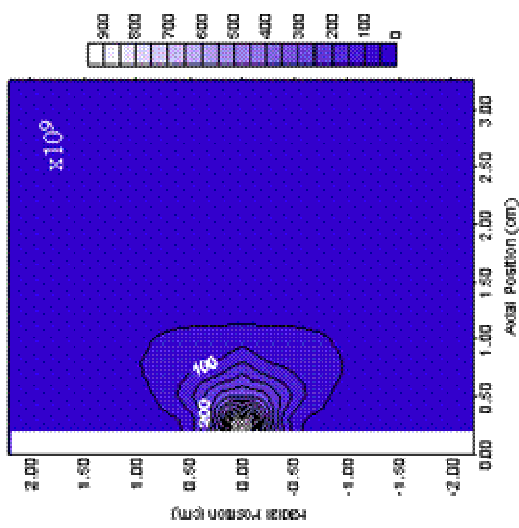
Plasma potential contour plot for Condition # MK12 (V).



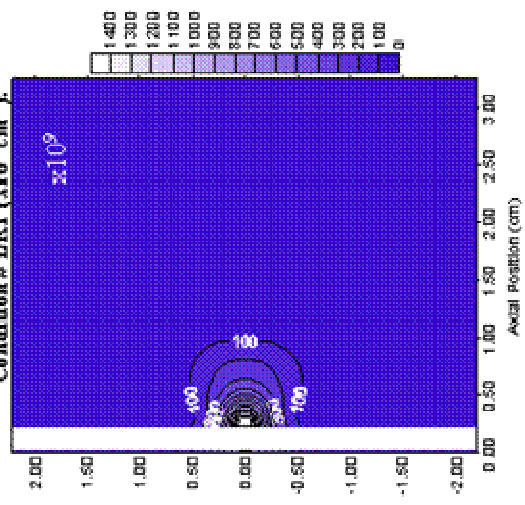
Electron temperature contour plot for Condition # MK12 (eV).

### NSTAR Orifice Keeper (LK 121305)

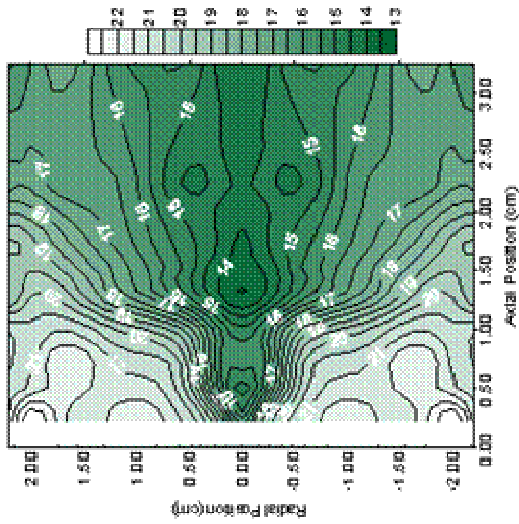
Operating Condition	(A)	$V_a$ (V)	$I_a$ (scm)	Pressure ( $\times 10^{-5}$ Torr)
LK1	2	36.4	1.5	3.4
LK2	4	42.3	1.5	3.4
LK3	6	51.1	1.5	3.4
LK4	8	57.0	1.5	3.4
LK5	2	34.6	3	5.2
LK6	4	42.2	3	5.2
LK7	6	45.7	3	5.2
LK8	8	54.5	3	5.2
LK9	2	34.5	4.5	6.6
LK10	4	34.5	4.5	6.6
LK11	6	44.5	4.5	6.6
LK12	8	53.5	4.5	6.6



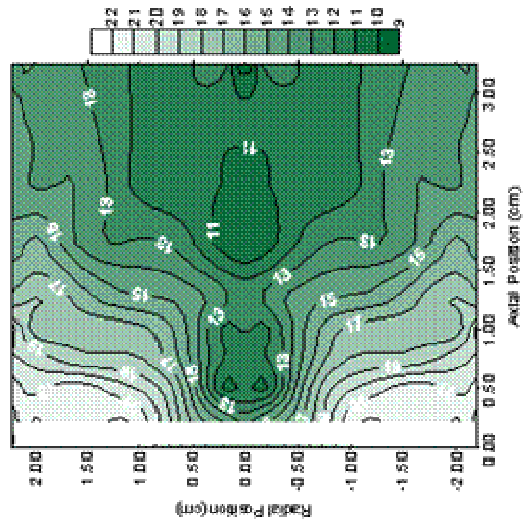
Electron number density contour plot for Condition # LK1 ( $\times 10^9 \text{ cm}^{-3}$ ).



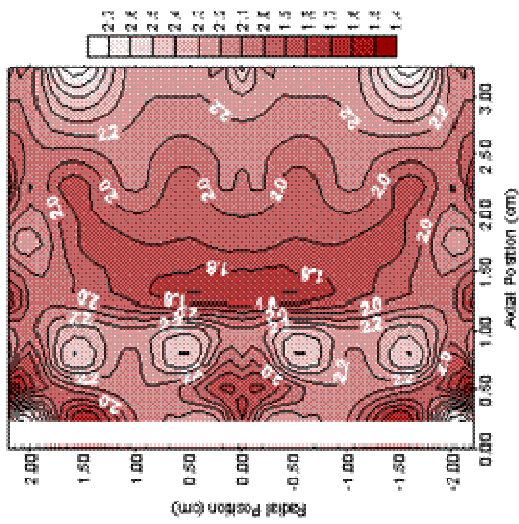
Electron number density contour plot for Condition # LK2 ( $\times 10^9 \text{ cm}^{-3}$ ).



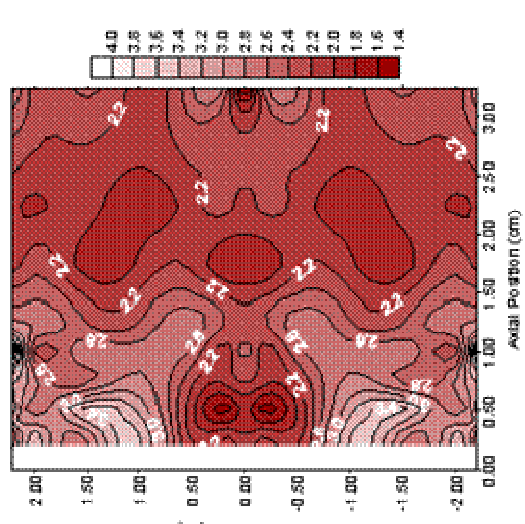
Plasma potential contour plot for Condition # LK1 (V).



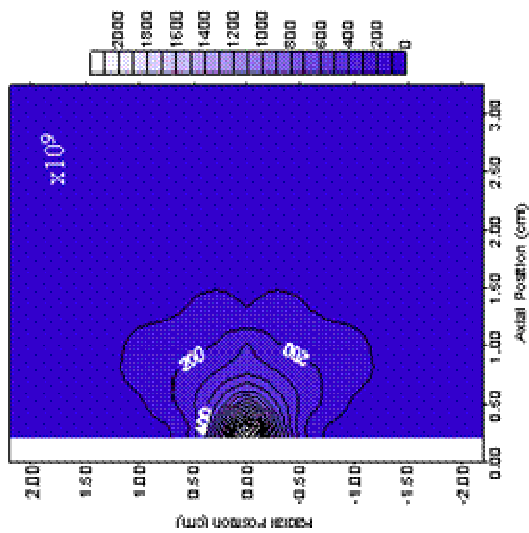
Plasma potential contour plot for Condition # LK2 (V).



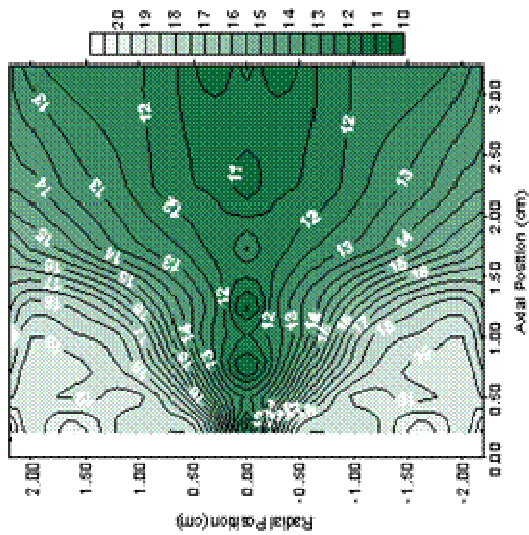
Electron temperature contour plot for Condition # LK1 (eV).



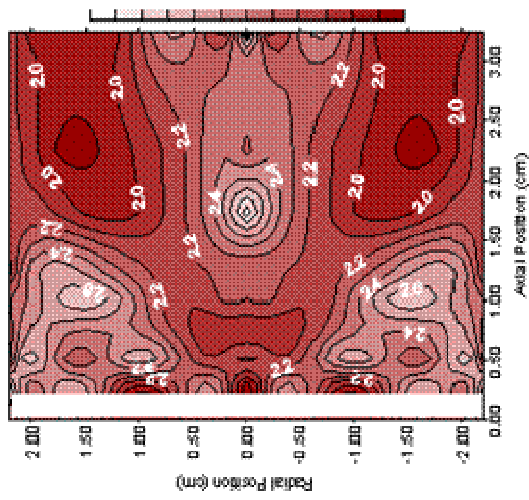
Electron temperature contour plot for Condition # LK2 (eV).



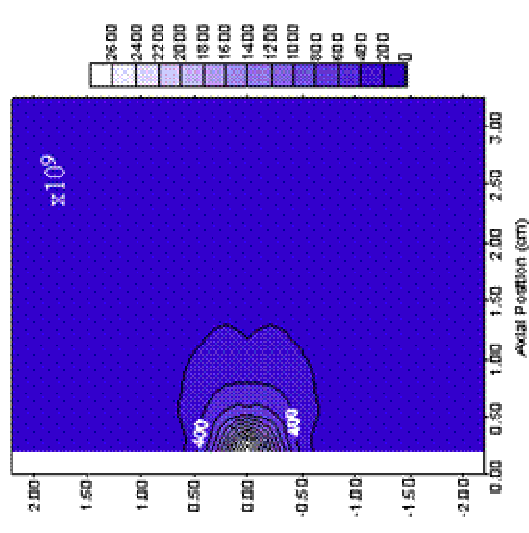
Electron number density contour plot for Condition # LK3 ( $\times 10^9 \text{ cm}^{-3}$ ).



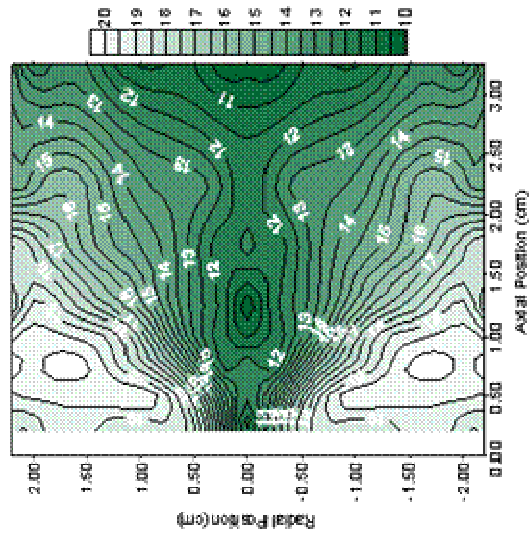
Plasma potential contour plot for Condition # LK3 (V).



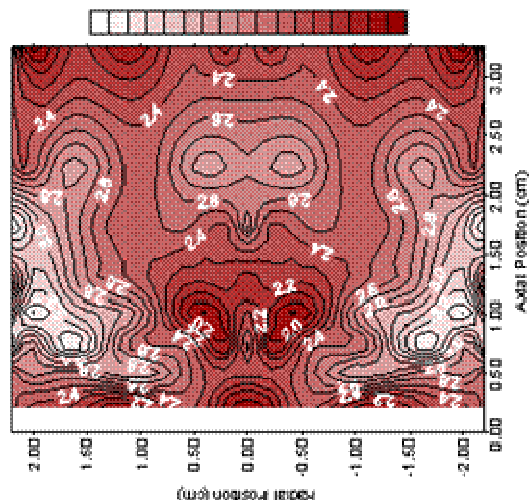
Electron temperature contour plot for Condition # LK3 (eV).



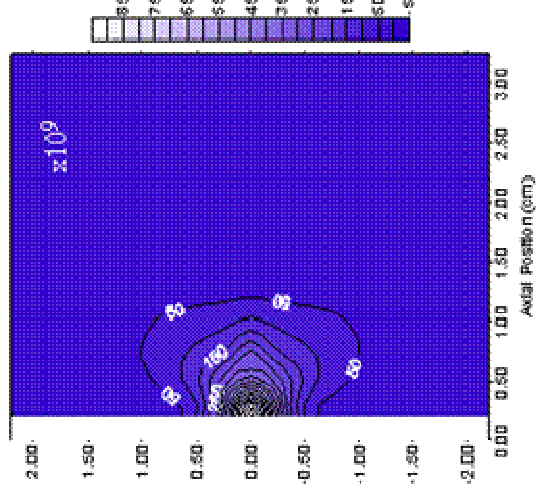
Electron number density contour plot for Condition # LK4 ( $\times 10^9 \text{ cm}^{-3}$ ).



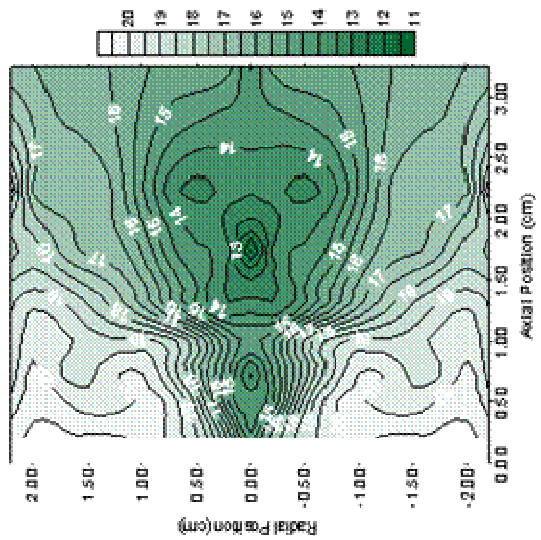
Plasma potential contour plot for Condition # LK4 (V).



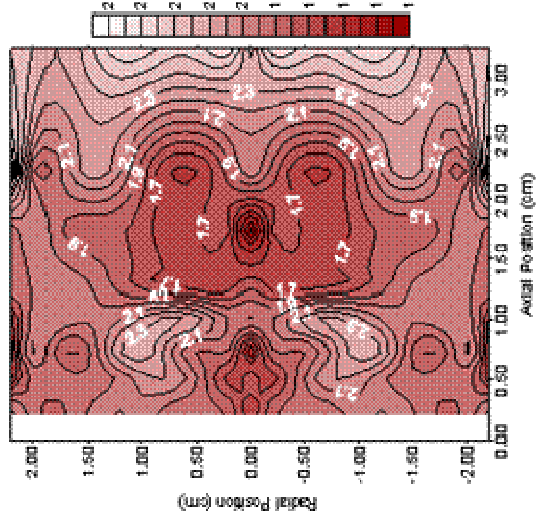
Electron temperature contour plot for Condition # LK4 (eV).



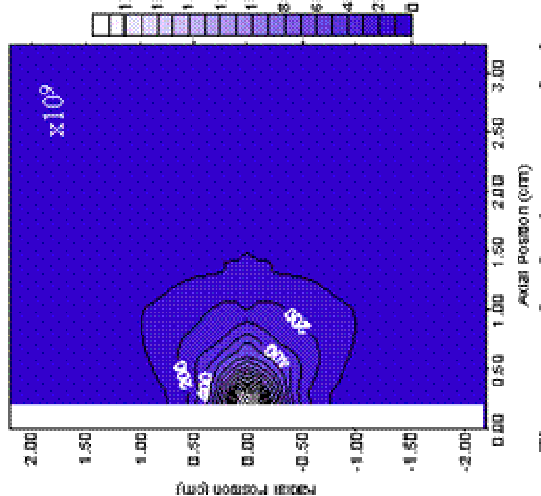
Electron number density contour plot for Condition # LK5 ( $\times 10^9 \text{ cm}^{-3}$ ).



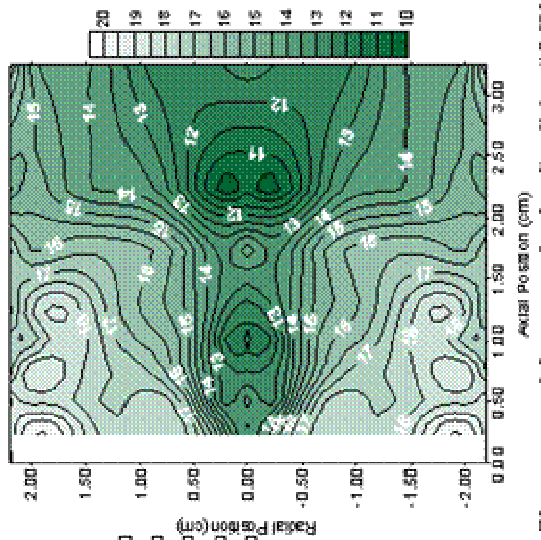
Plasma potential contour plot for Condition # LK5 (V).



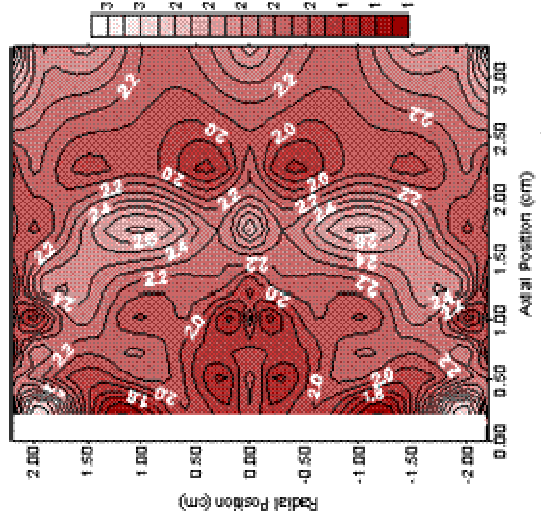
Electron temperature contour plot for Condition LK5 (eV).



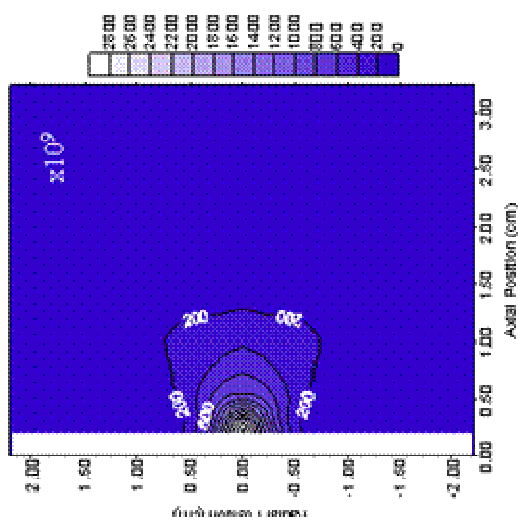
Electron number density contour plot for Condition # LK6 ( $\times 10^9 \text{ cm}^{-3}$ ).



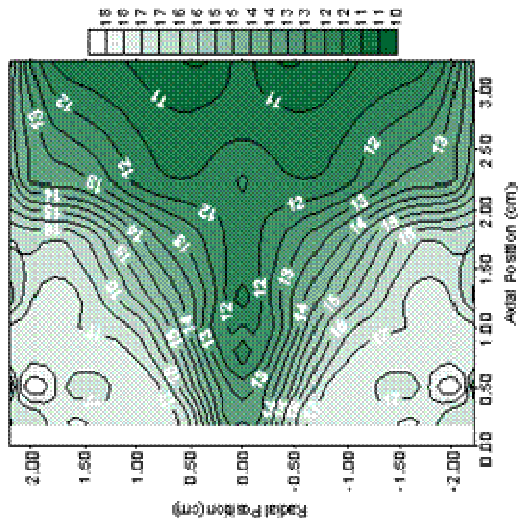
Plasma potential contour plot for Condition # LK6 (V).



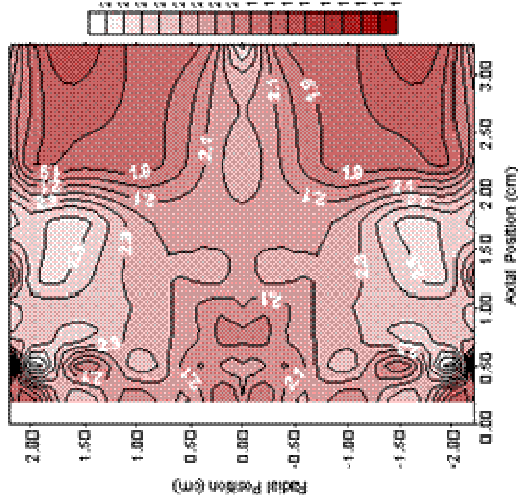
Electron temperature contour plot for Condition LK6 (eV).



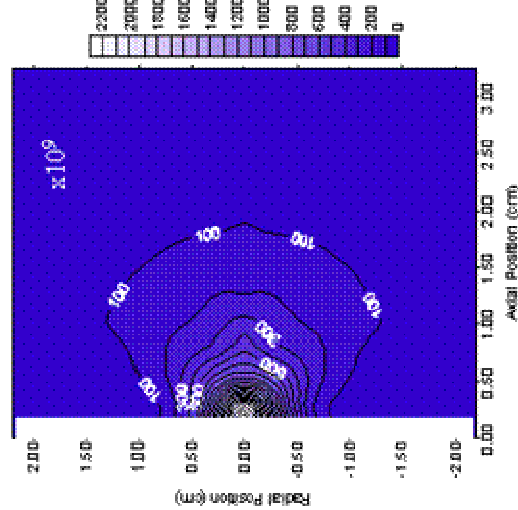
Electron number density contour plot for Condition # LK7 ( $\times 10^9 \text{ cm}^{-3}$ ).



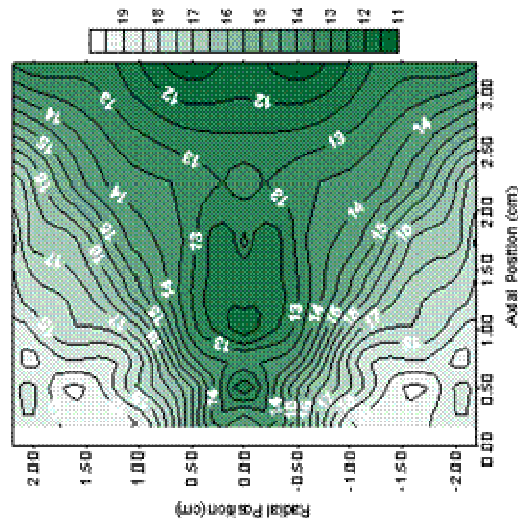
Plasma potential contour plot for Condition # LK7 (V).



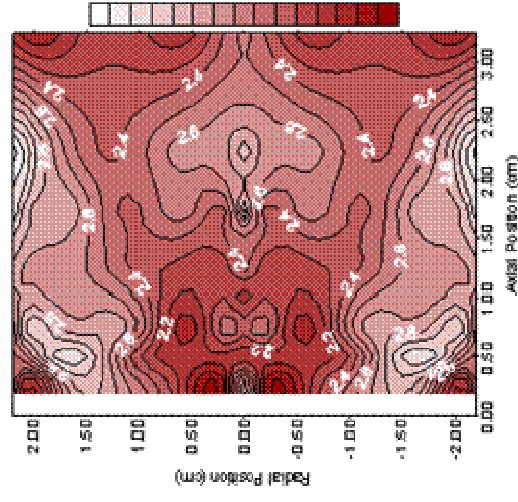
Electron temperature contour plot for Condition LK7 (eV).



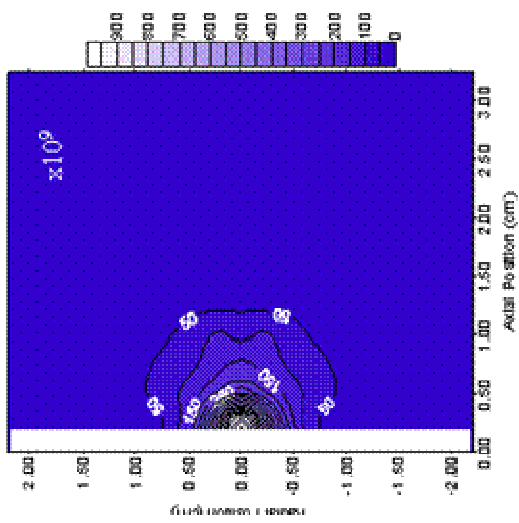
Electron number density contour plot for Condition # LK8 ( $\times 10^9 \text{ cm}^{-3}$ ).



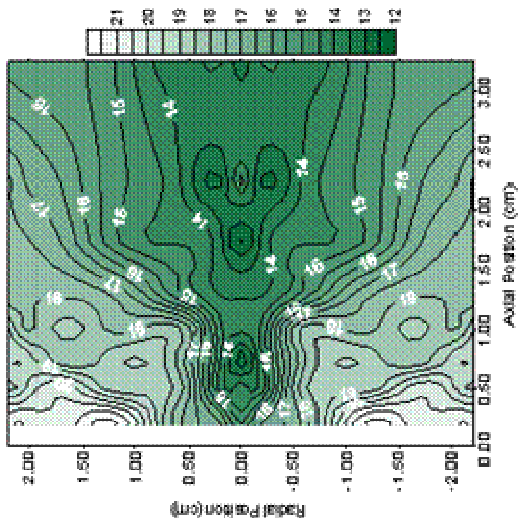
Plasma potential contour plot for Condition # LK8 (V).



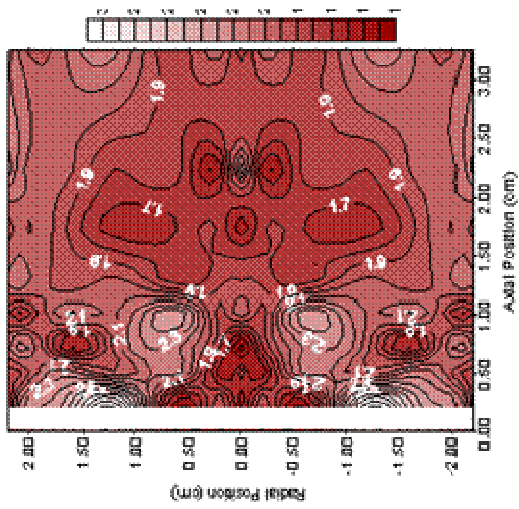
Electron temperature contour plot for Condition LK8 (eV).



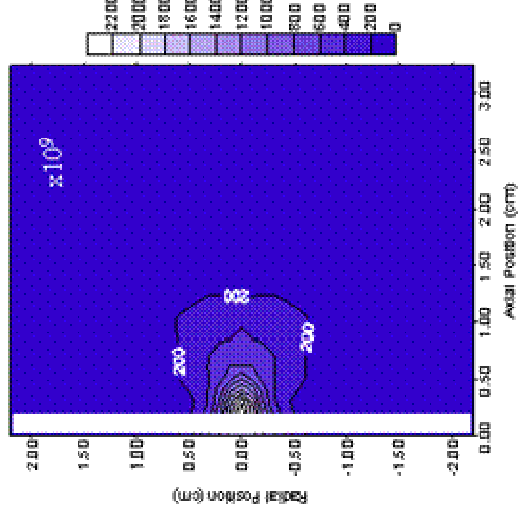
Electron number density contour plot for Condition # LK9 ( $\times 10^9 \text{ cm}^{-3}$ ).



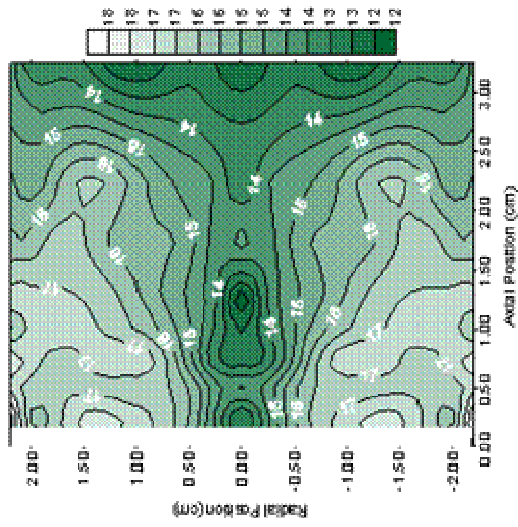
Plasma potential contour plot for Condition # LK9 (V).



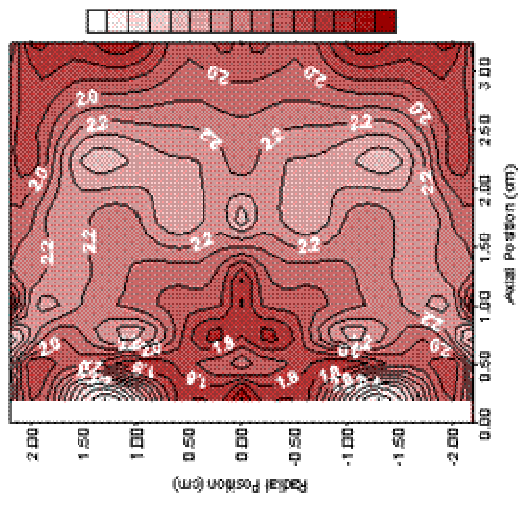
Electron temperature contour plot for Condition LK9 (eV).



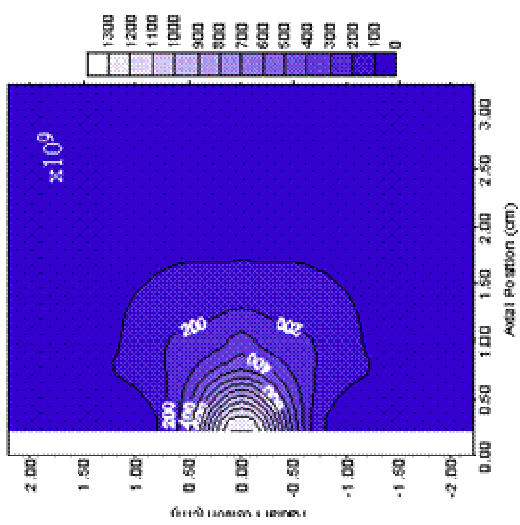
Electron number density contour plot for Condition # LK10 ( $\times 10^9 \text{ cm}^{-3}$ ).



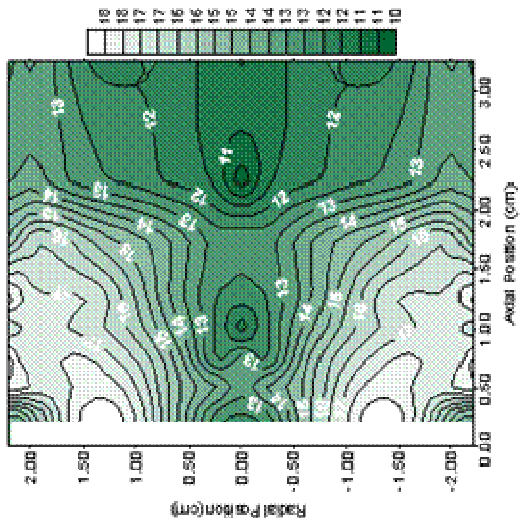
Plasma potential contour plot for Condition # LK10 (V).



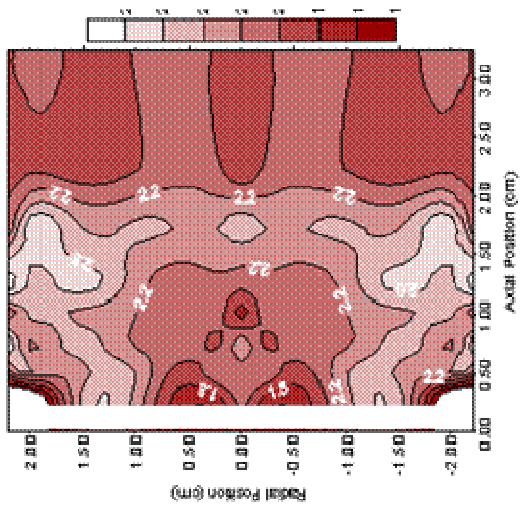
Electron temperature contour plot for Condition LK10 (eV).



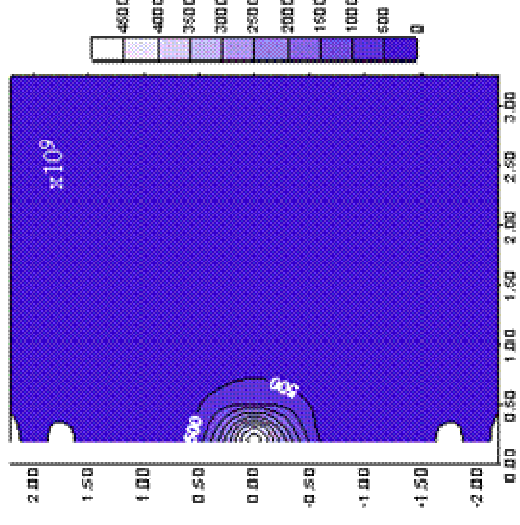
Electron number density contour plot for Condition # LK11 ( $\times 10^9 \text{ cm}^{-3}$ ).



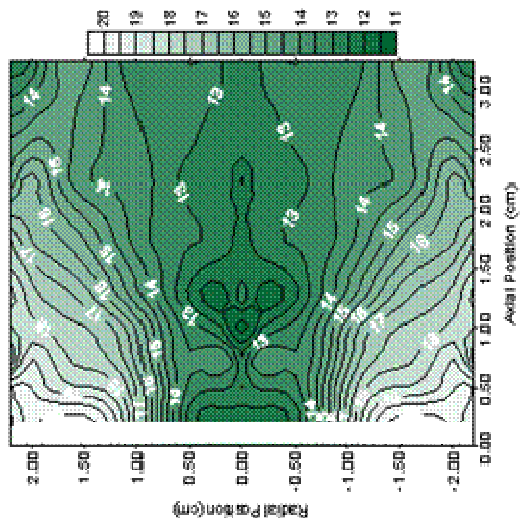
Plasma potential contour plot for Condition # LK11 (V).



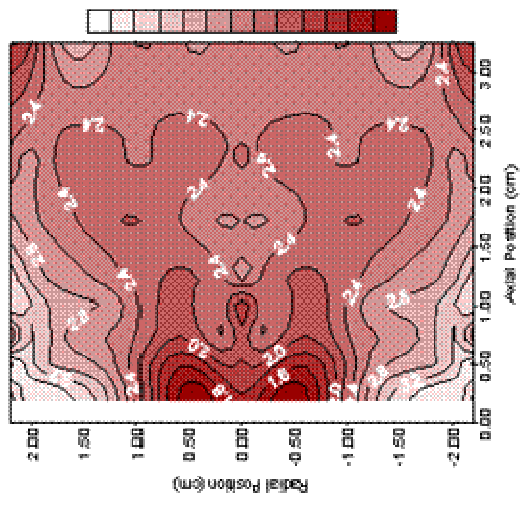
Electron temperature contour plot for Condition LK11 (eV).



Electron number density contour plot for Condition # LK12 ( $\times 10^9 \text{ cm}^{-3}$ ).



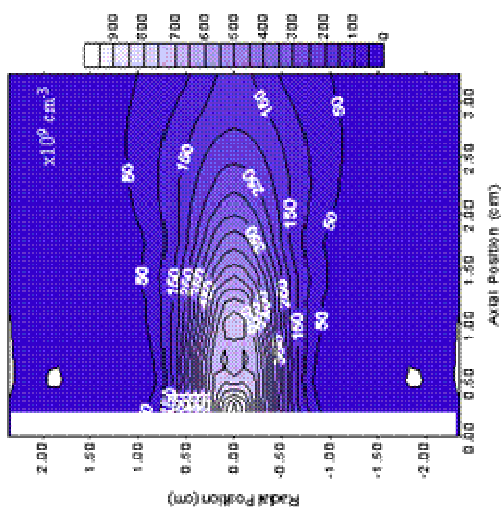
Plasma potential contour plot for Condition # LK12 (V).



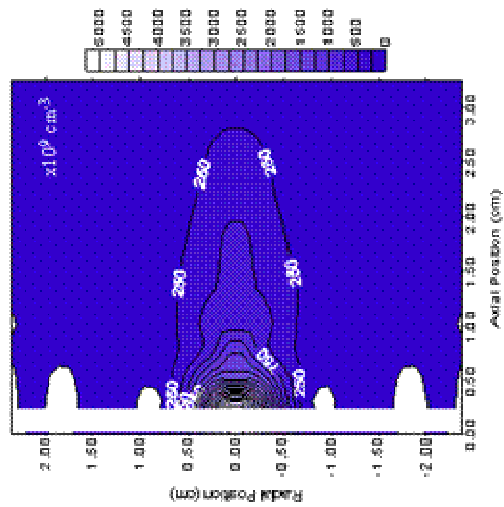
Electron temperature contour plot for Condition LK12 (eV).

### Cathode in Magnetic Field with Plate Anode (MP 012706)

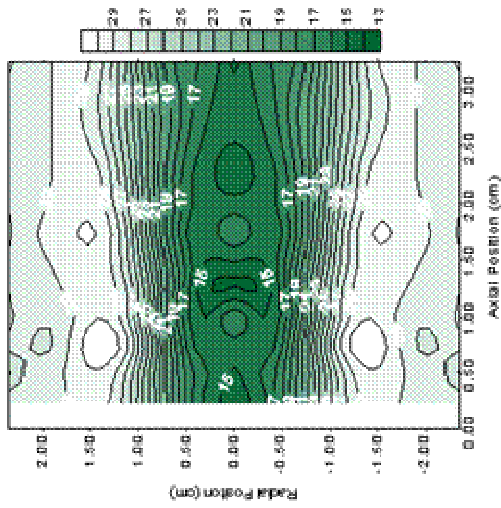
Operating Condition	(A)	$V_d$ (V)	$i$ (scem)	Pressure ( $\times 10^{-5}$ Torr)
MP1	2	26.6	1.5	4.2
MP2	4	25.9	1.5	4.2



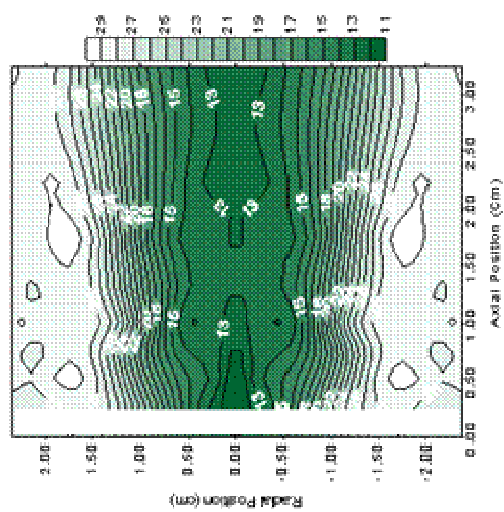
Electron number density contour plot for Condition # MPI ( $\times 10^{19} \text{ cm}^{-3}$ ).



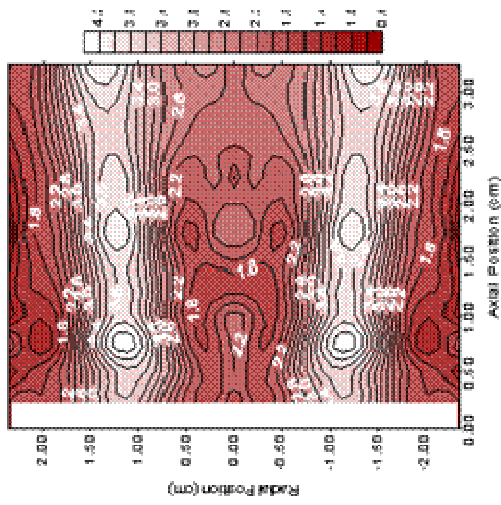
Electron number density contour plot for Condition # MP2 ( $\times 10^{19} \text{ cm}^{-3}$ ).



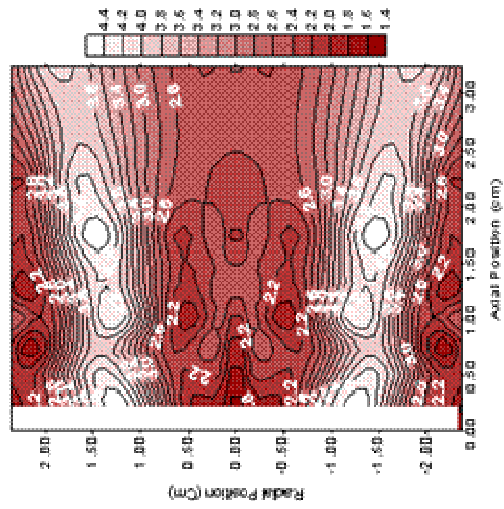
Plasma potential contour plot for Condition # MPI (V).



Plasma potential contour plot for Condition # MP2 (V).



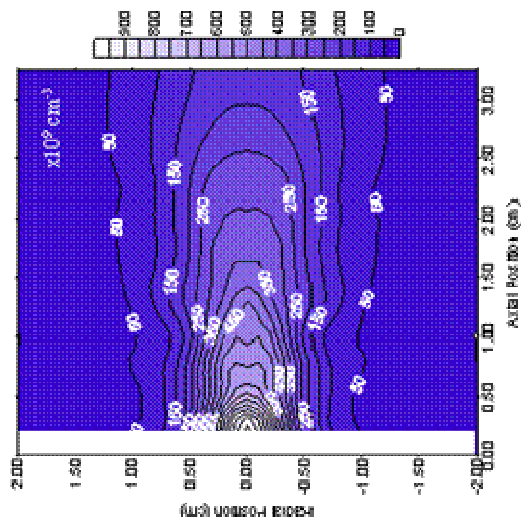
Electron temperature contour plot for Condition # MPI (eV).



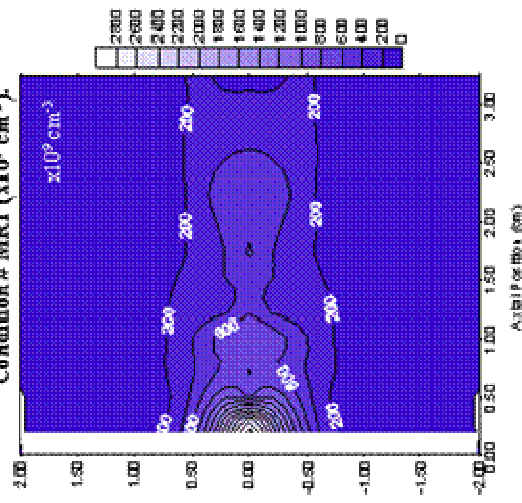
Electron temperature contour plot for Condition # MP2 (eV).

**Cathode in Magnetic Field with Ring Anode (MP 013106)**

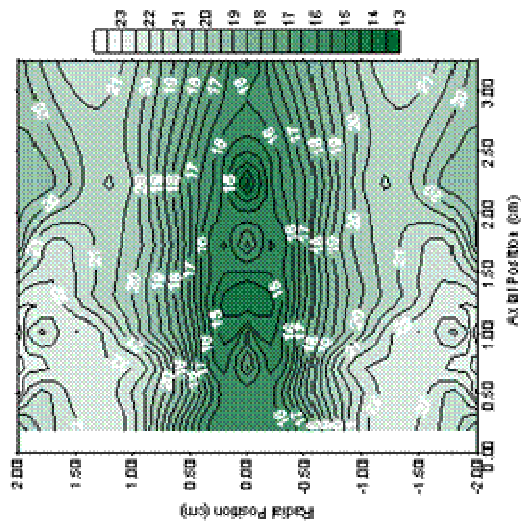
<b>Operating Condition</b>	<b>(A)</b>	<b><math>V_a</math> (V)</b>	<b><math>i_c</math> (sccm)</b>	<b>Pressure (<math>\times 10^{-5}</math> Torr)</b>
MR1	2	34.8	1.5	4.2
MR2	4	32.6	1.5	4.2
MR3	6	31.7	1.5	4.2
MR4	8	25.6	1.5	4.2
MR5	2	32.1	3	6.6
MR6	4	29.0	3	6.6
MR7	6	28.0	3	6.6
MR8	8	25.9	3	6.6
MR9	2	30.0	4.5	9.1
MR10	4	26.5	4.5	9.1
MR11	6	26.8	4.5	9.1
MR12	8	25.0	4.5	9.1



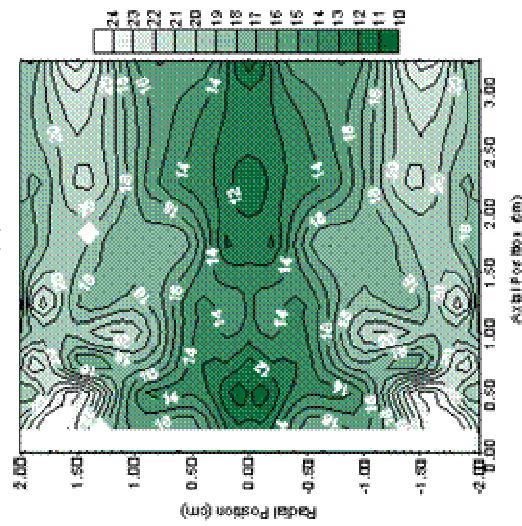
Electron number density contour plot for Condition # MRI1 ( $\times 10^{20} \text{ cm}^{-3}$ ).



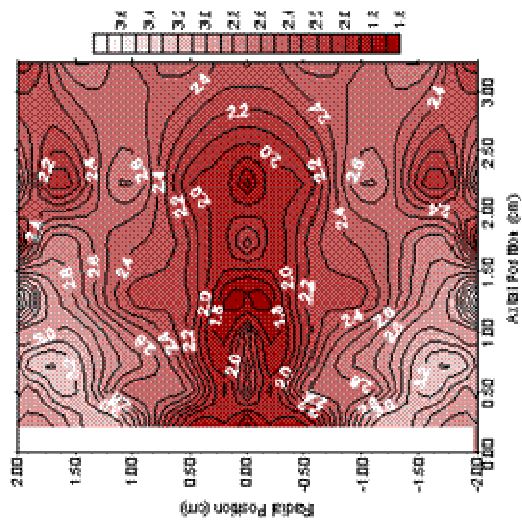
Electron number density contour plot for Condition # MRI2 ( $\times 10^{20} \text{ cm}^{-3}$ ).



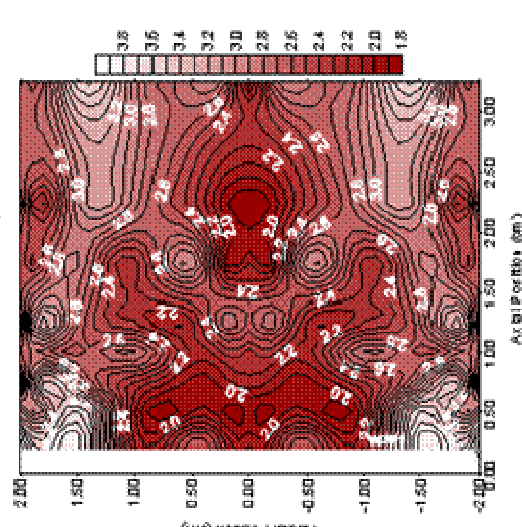
Plasma potential contour plot for Condition # MRI1 (V).



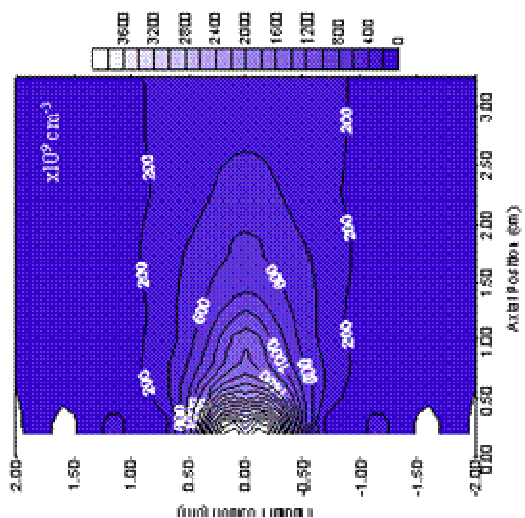
Plasma potential contour plot for Condition # MRI2 (V).



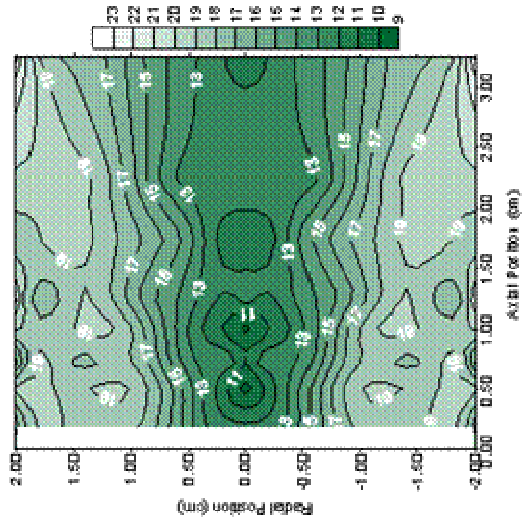
Electron temperature contour plot for Condition # MRI1 (eV).



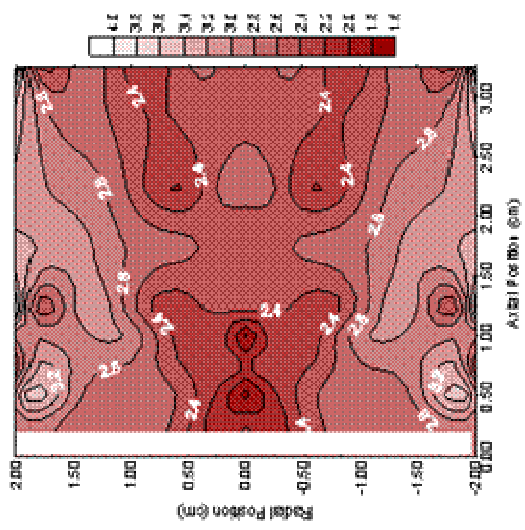
Electron temperature contour plot for Condition # MRI2 (eV).



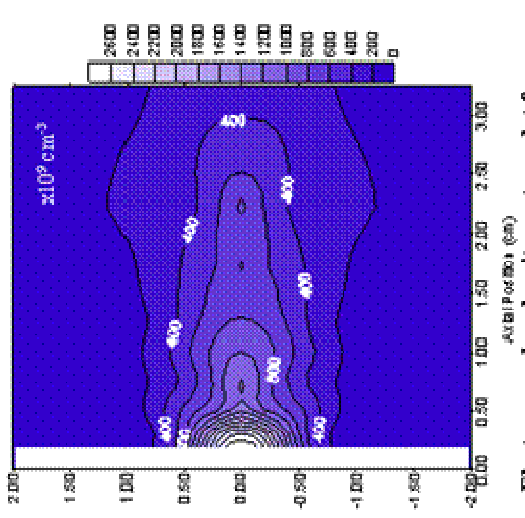
Electron number density contour plot for Condition # MR3 ( $\times 10^9 \text{ cm}^{-3}$ ).



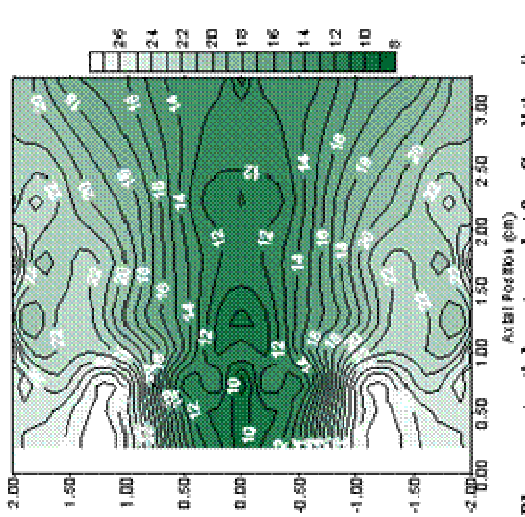
Plasma potential contour plot for Condition # MR3 (V).



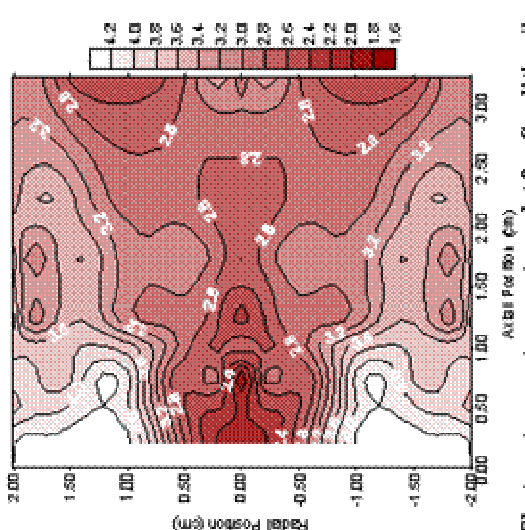
Electron temperature contour plot for Condition # MR3 (eV).



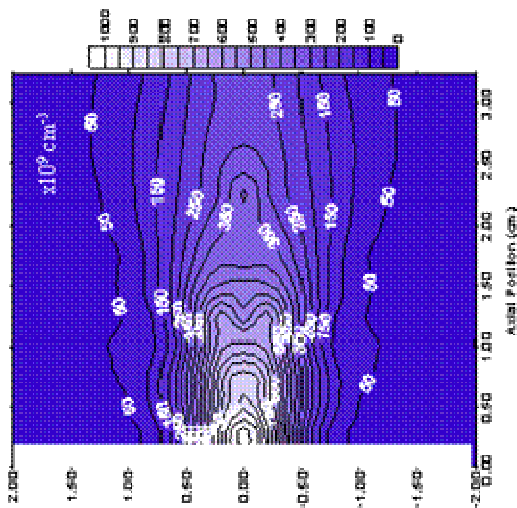
Electron number density contour plot for Condition # MR4 ( $\times 10^9 \text{ cm}^{-3}$ ).



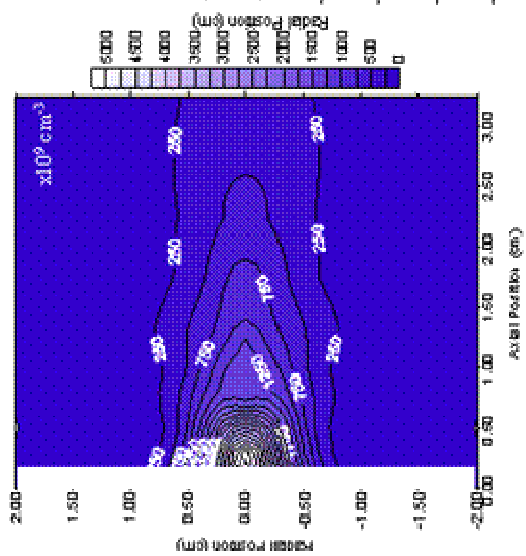
Plasma potential contour plot for Condition # MR4 (V).



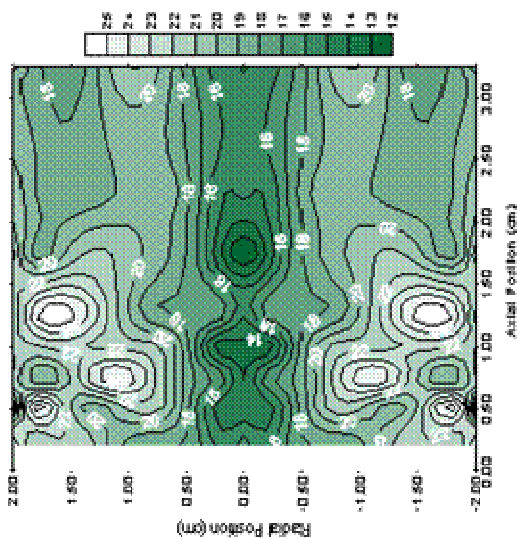
Electron temperature contour plot for Condition # MR4 (eV).



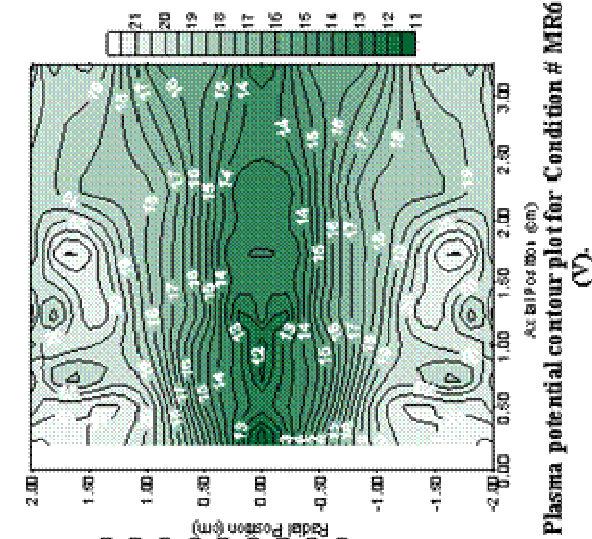
Electron number density contour plot for Condition # MR5 ( $\times 10^9 \text{ cm}^{-3}$ ).



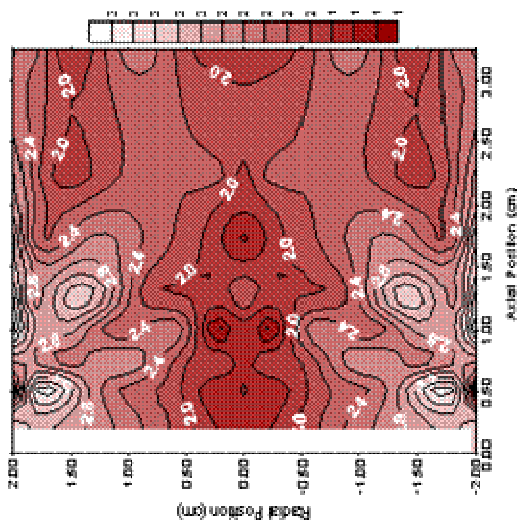
Electron number density contour plot for Condition # MR6 ( $\times 10^9 \text{ cm}^{-3}$ ).



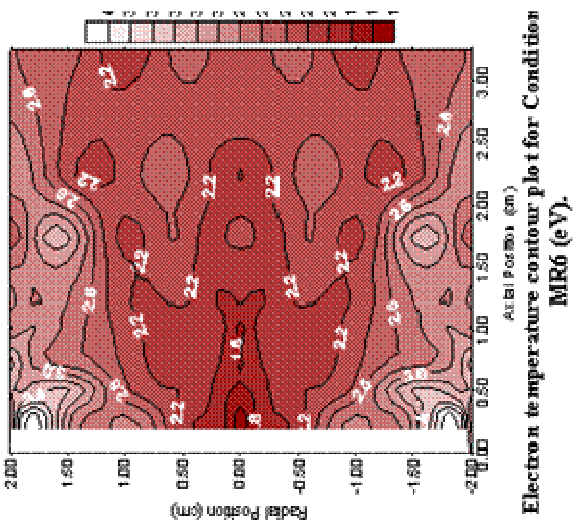
Plasma potential contour plot for Condition # MR5 (V).



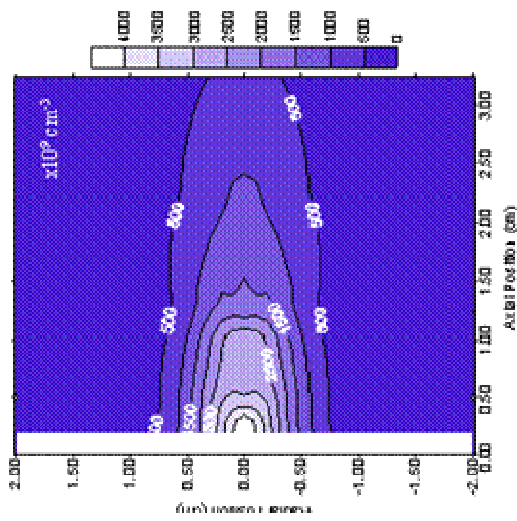
Plasma potential contour plot for Condition # MR6 (V).



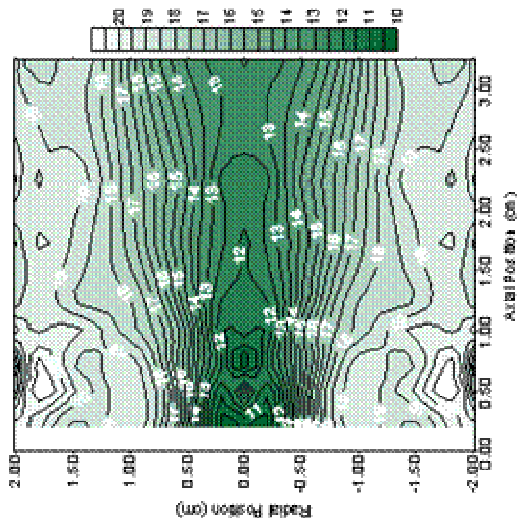
Electron temperature contour plot for Condition # MRS (eV).



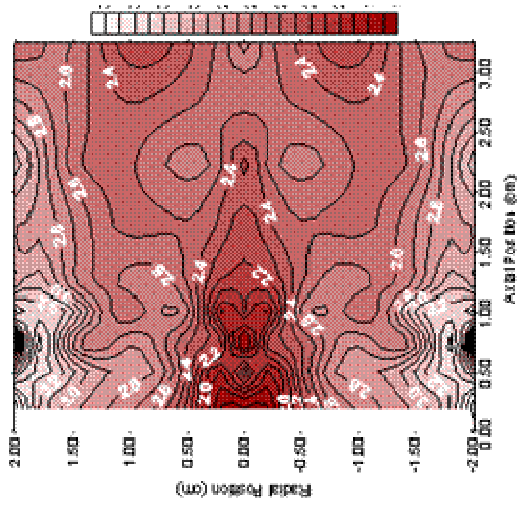
Electron temperature contour plot for Condition # MR6 (eV).



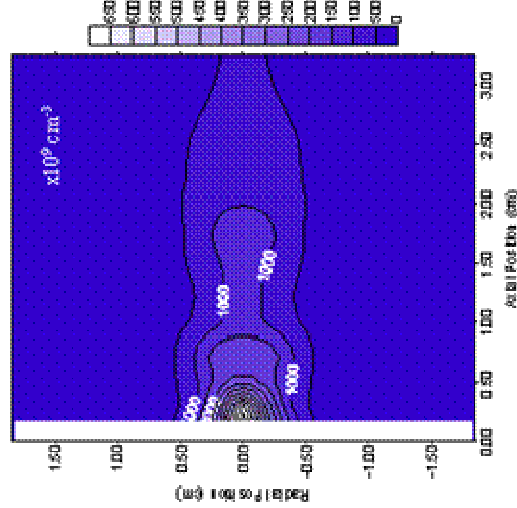
Electron number density contour plot for Condition # MR7 ( $\times 10^9 \text{ cm}^{-3}$ ).



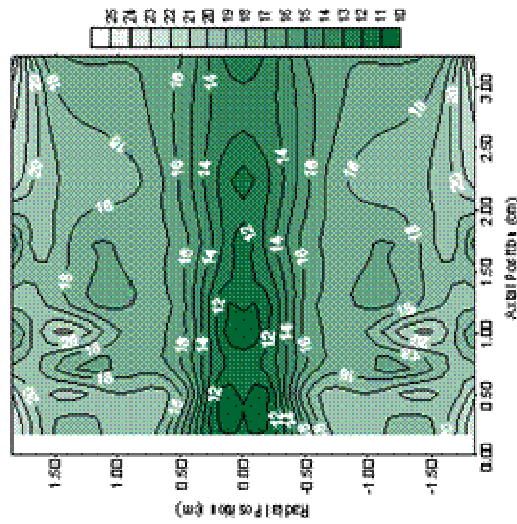
Plasma potential contour plot for Condition # MR7 (V).



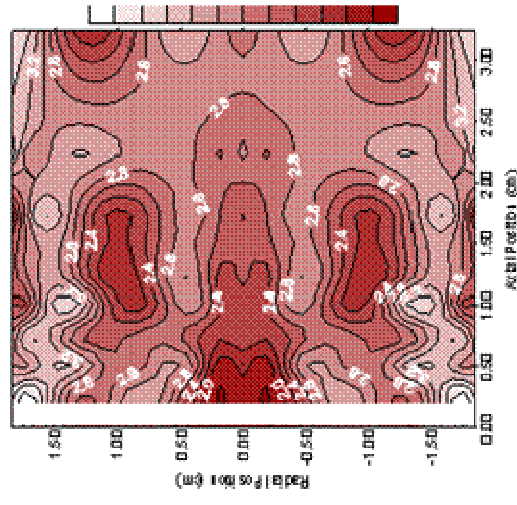
Electron temperature contour plot for Condition MR7 (eV).



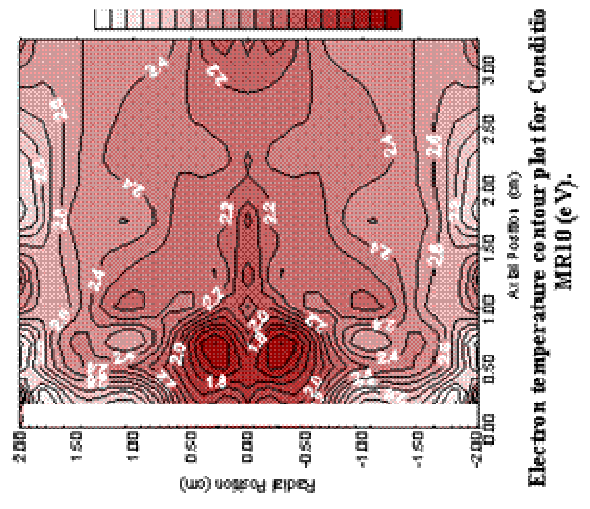
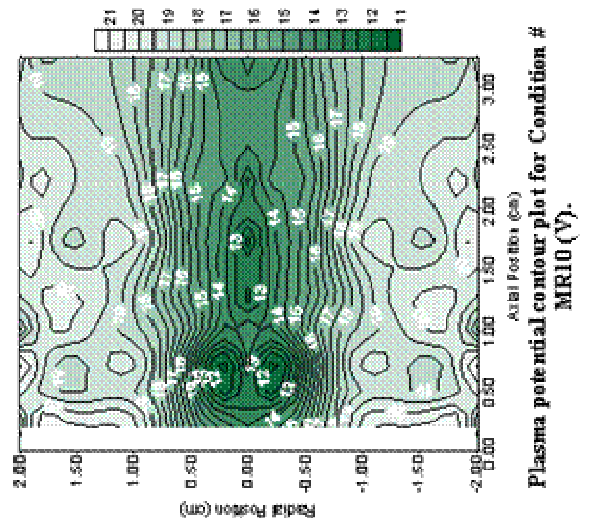
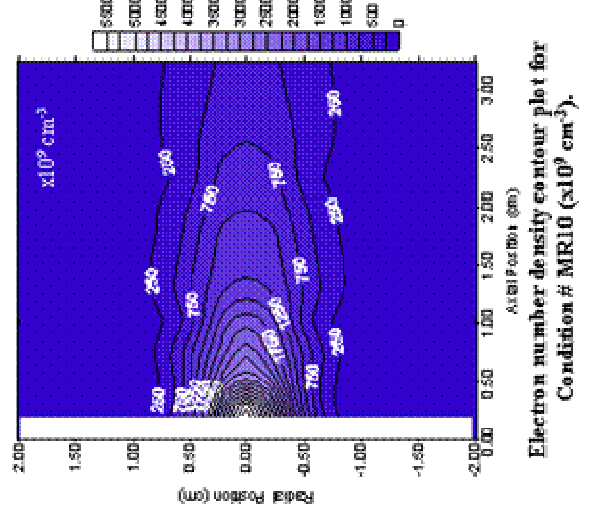
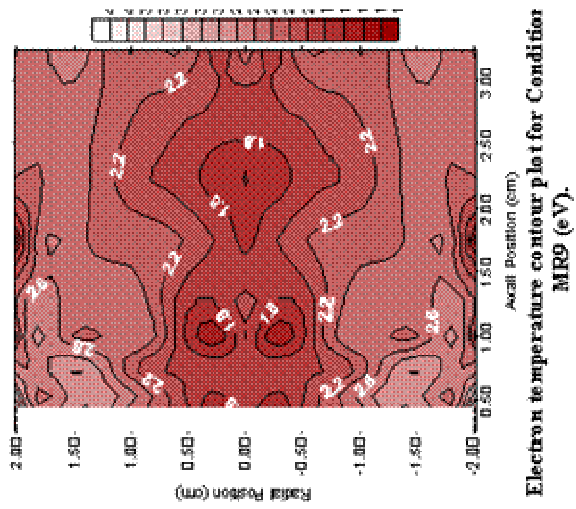
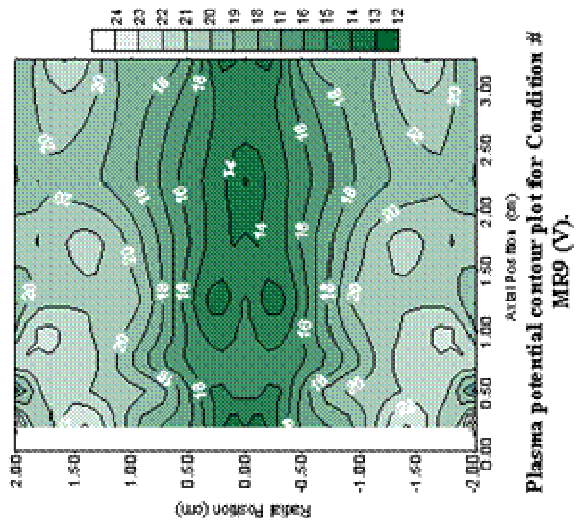
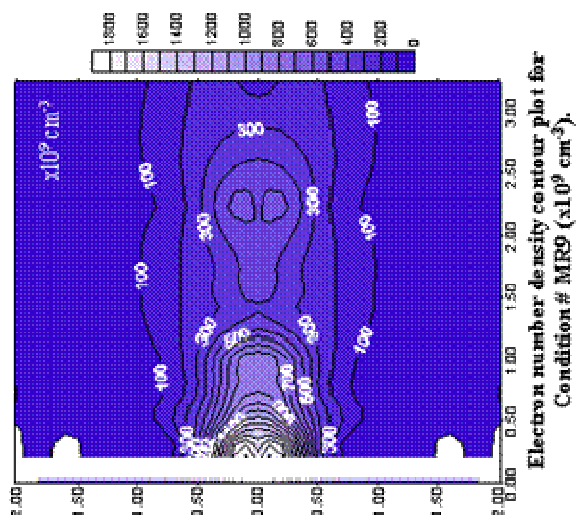
Electron number density contour plot for Condition # MR8 ( $\times 10^9 \text{ cm}^{-3}$ ).

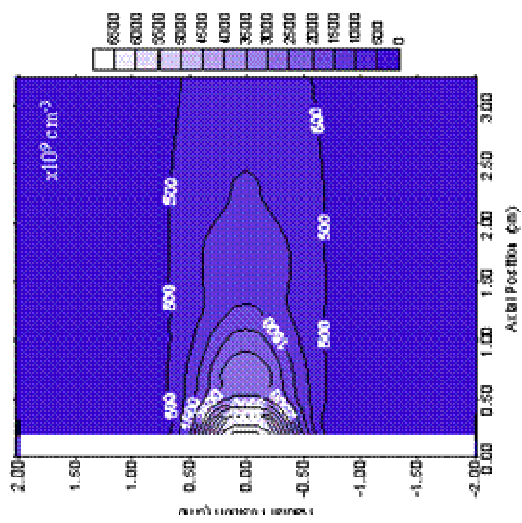


Plasma potential contour plot for Condition # MR8 (V).

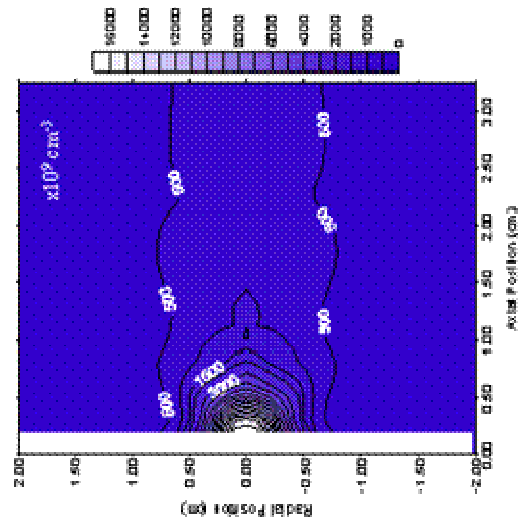


Electron temperature contour plot for Condition MR8 (eV).

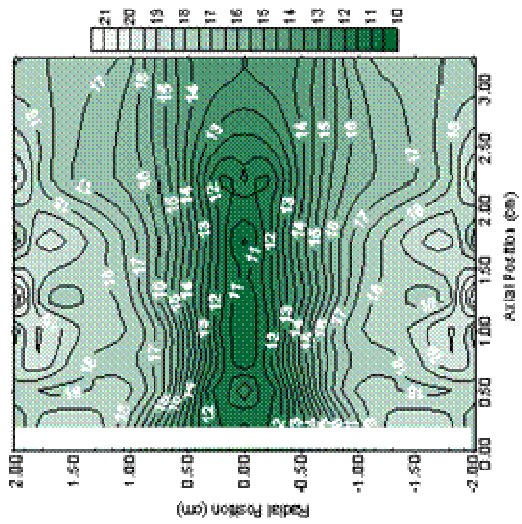




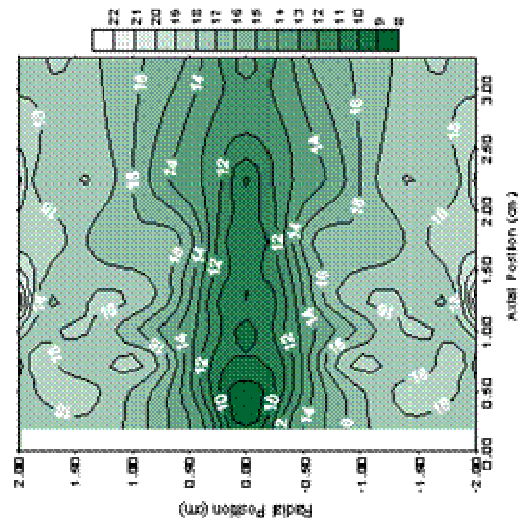
Electron number density contour plot for Condition # MR11 ( $\times 10^9 \text{ cm}^{-3}$ ).



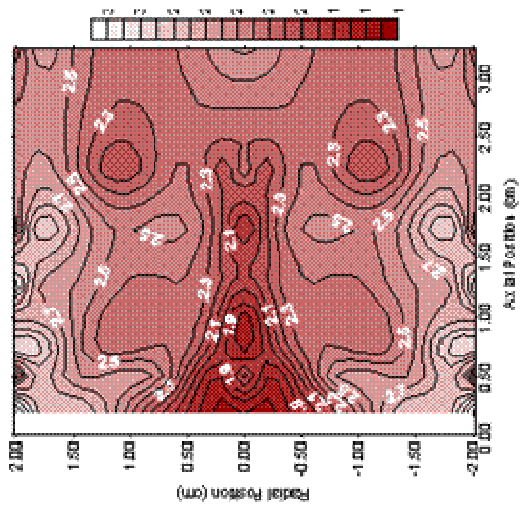
Electron number density contour plot for Condition # MR12 ( $\times 10^9 \text{ cm}^{-3}$ ).



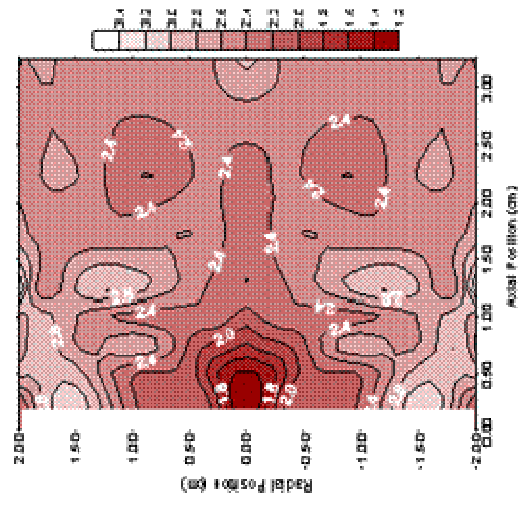
Plasma potential contour plot for Condition # MR11 (V).



Plasma potential contour plot for Condition # MR12 (V).



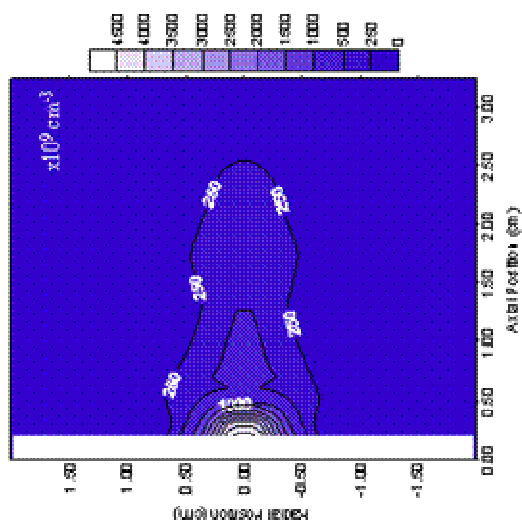
Electron temperature contour plot for Condition # MR11 (eV).



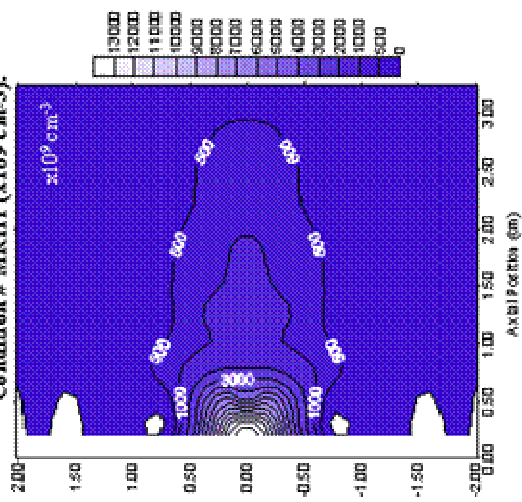
Electron temperature contour plot for Condition # MR12 (eV).

### Cathode in Magnetic Field with Ring Anode at High Power (MPH 021506)

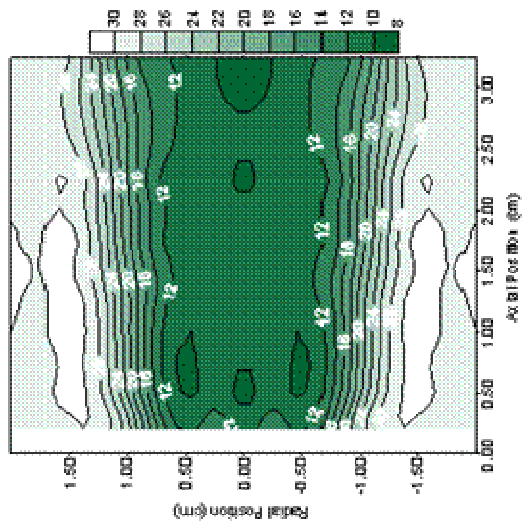
Operating Condition	(A)	$V_a$ (V)	$I_a$ (sccm)	Pressure ( $\times 10^{-5}$ Torr)
MRH1	10	35.2	1.5	3.8
MRH2	10	25.2	3	4.2
MRH3	15	27.7	3	4.2
MRH4	20	29.8	3	4.2
MRH5	10	26.7	4.5	7.7
MRH6	15	26.9	4.5	7.7
MRH7	20	28.0	4.5	7.7



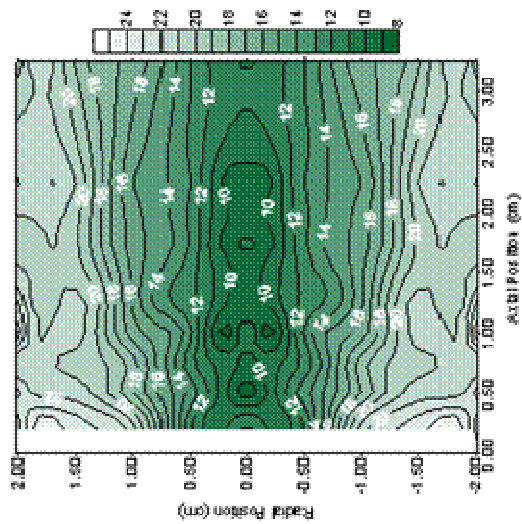
Electron number density contour plot for Condition # MRH1 ( $\times 10^9 \text{ cm}^{-3}$ ).



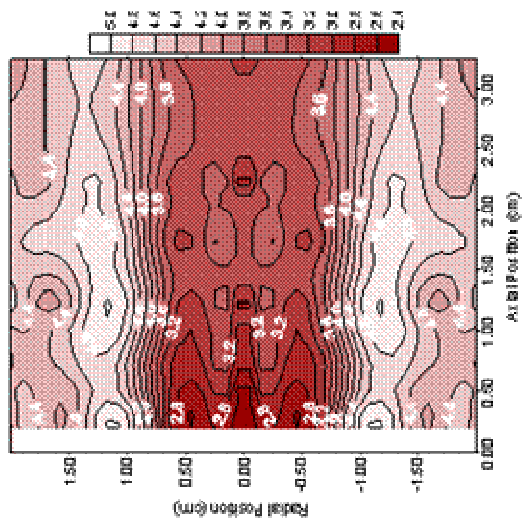
Electron number density contour plot for Condition # MRH2 ( $\times 10^9 \text{ cm}^{-3}$ ).



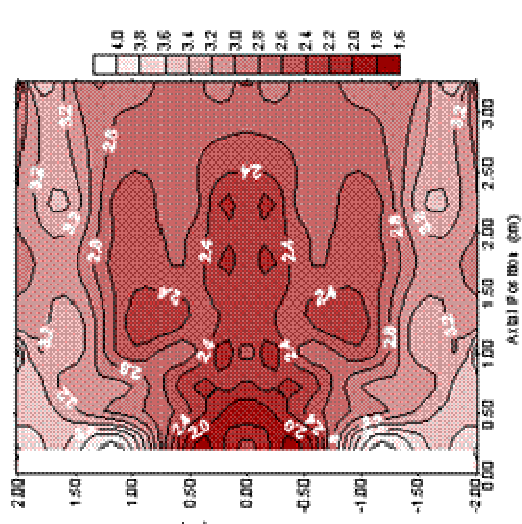
Plasma potential contour plot for Condition # MRH1 (V).



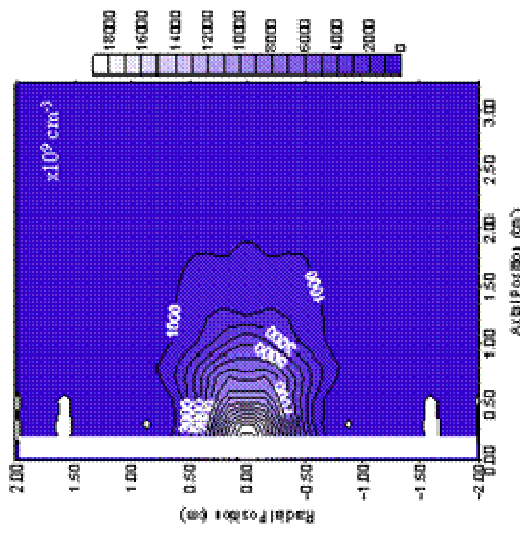
Plasma potential contour plot for Condition # MRH2 (V).



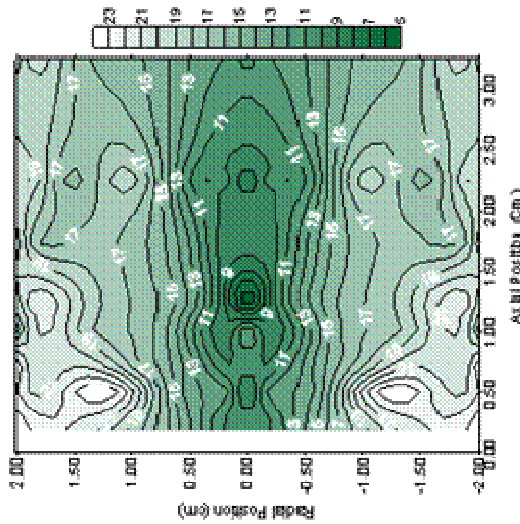
Electron temperature contour plot for Condition # MRH1 (eV).



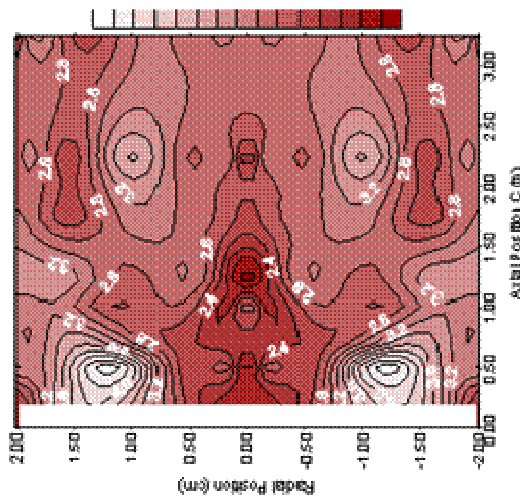
Electron temperature contour plot for Condition # MRH2 (eV).



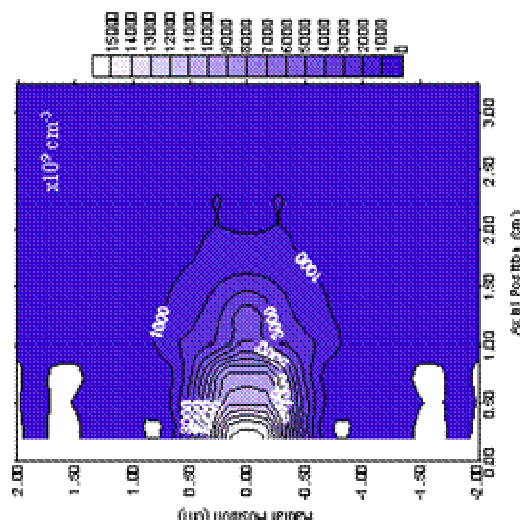
Electron number density contour plot for Condition # MRH3 ( $\times 10^9 \text{ cm}^{-3}$ ).



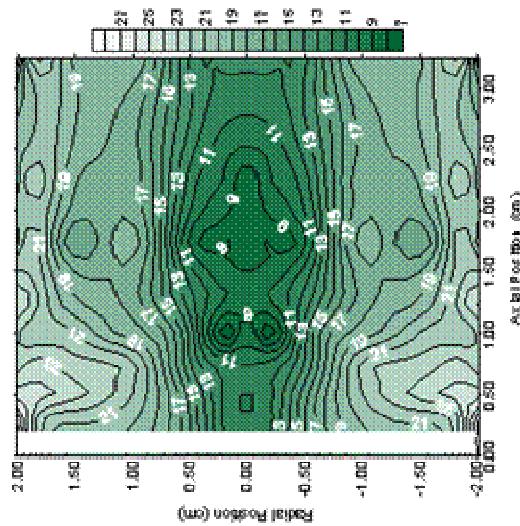
Plasma potential contour plot for Condition # MRH3 (V).



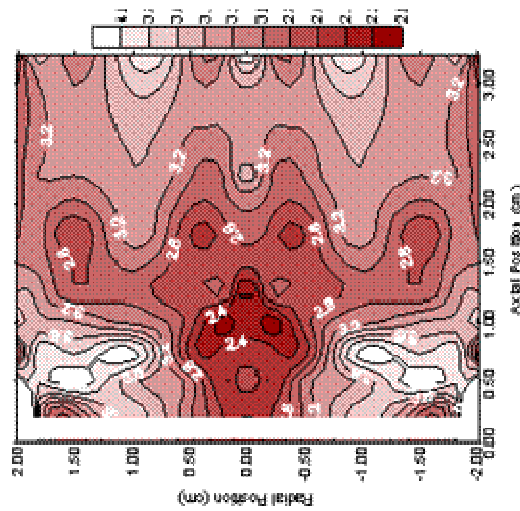
Electron temperature contour plot for Condition # MRH3 (eV).



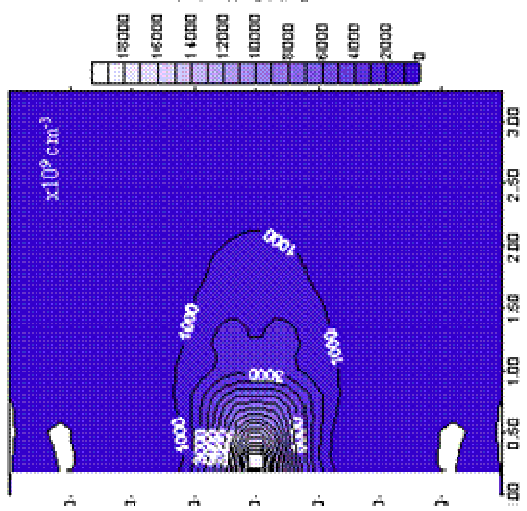
Electron number density contour plot for Condition # MRH4 ( $\times 10^9 \text{ cm}^{-3}$ ).



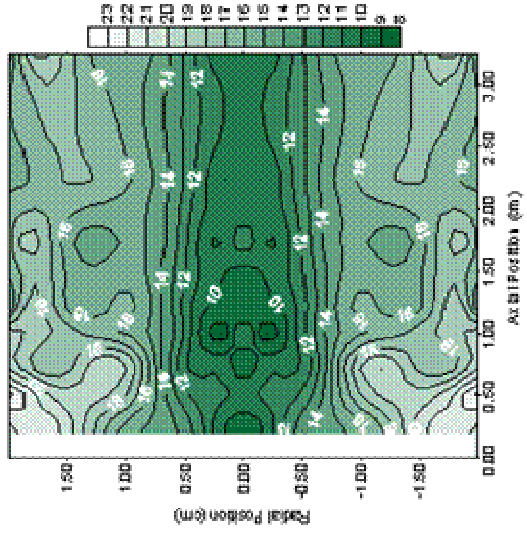
Plasma potential contour plot for Condition # MRH4 (V).



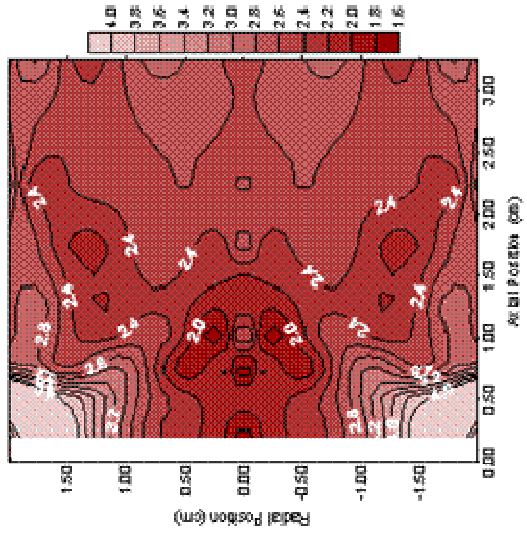
Electron temperature contour plot for Condition # MRH4 (eV).



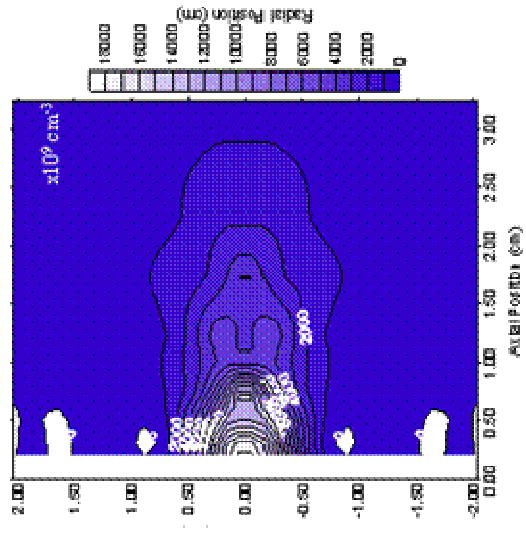
Electron number density contour plot for Condition # MRH5 ( $\times 10^9 \text{ cm}^{-3}$ ).



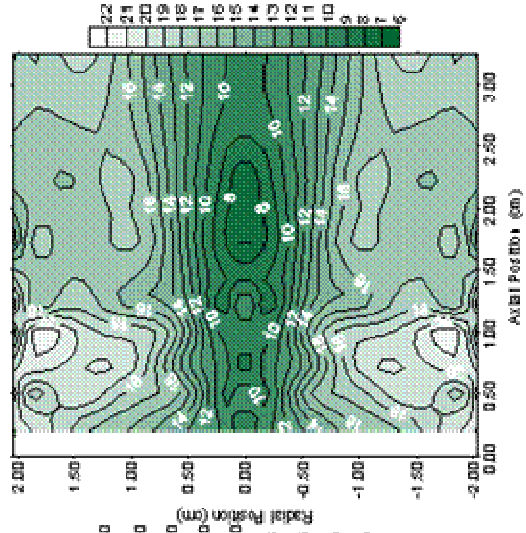
Plasma potential contour plot for Condition # MRH5 (V).



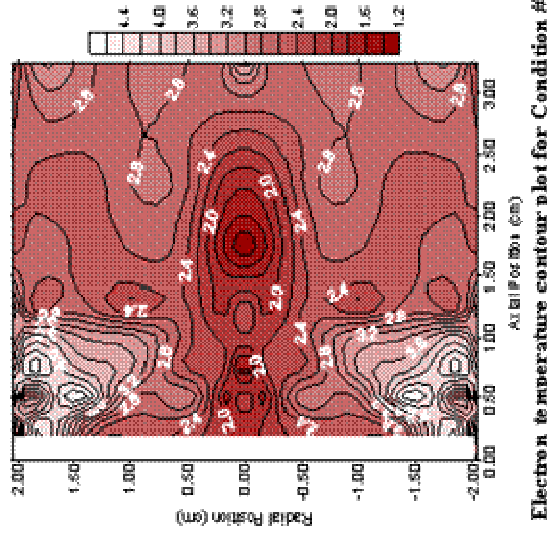
Electron temperature contour plot for Condition # MRH5 (eV).



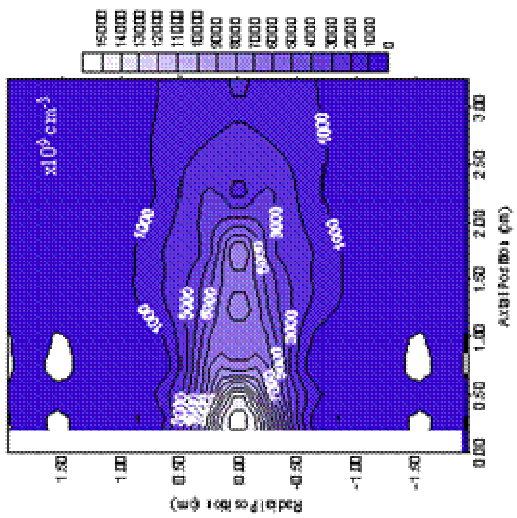
Electron number density contour plot for Condition # MRH6 ( $\times 10^9 \text{ cm}^{-3}$ ).



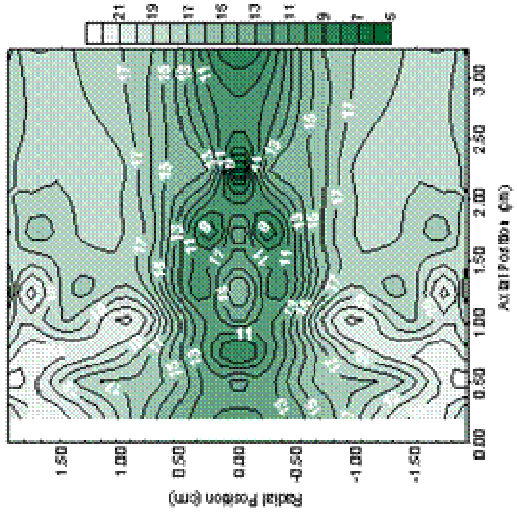
Plasma potential contour plot for Condition # MRH6 (V).



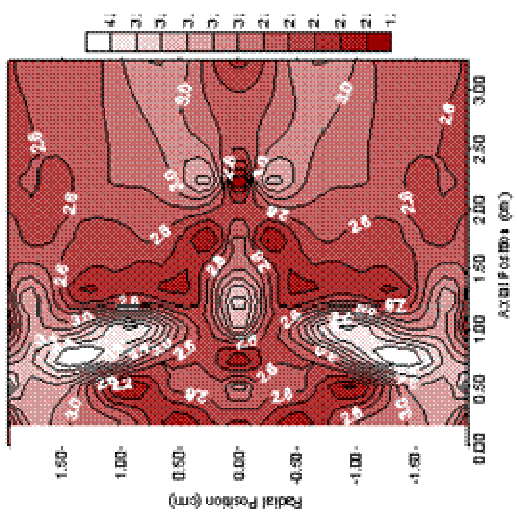
Electron temperature contour plot for Condition # MRH6 (eV).



Electron number density contour plot for Condition # MRH7 ( $\times 10^9 \text{ cm}^{-3}$ ).



Plasma potential contour plot for Condition # MRH7 (V).



Electron temperature contour plot for Condition # MRH7 (eV).

## REFERENCES

- <sup>1</sup> Choueiri, E. "Electric propulsion," Aerospace America, V. 37, Issue 12, (1999), pages 68-69.
- <sup>2</sup> Darling, David, "Electric Space Propulsion," The Encyclopedia of Astrobiology, Astronomy, and Spaceflight, <http://www.daviddarling.info/encyclopedia/E/electricprop.html>, [cited March 31<sup>st</sup> 2006].
- <sup>3</sup> Hermann, Daniel. "The Use of Electrostatic Probes to Characterize the Discharge Plasma Structure and Identify Discharge Cathode Erosion Mechanisms in Ring-Cusp Ion Thrusters," Ph. D. Dissertation, Aerospace Engineering Dept., University of Michigan, 2005.
- <sup>4</sup> Choueiri, E. "A Critical History of Electric Propulsion: The First 50 Years (1996 – 1956)," Journal of Propulsion and Power, V. 20, Issue 2, pages 193-203. March – April 2004.
- <sup>5</sup> Haas, James, "Low-Perturbation Interrogation of the Internal and Near-Field Plasma Structure of a Hall Thruster using a High-Speed Probe Positioning System," Ph. D. Dissertation, Aerospace Engineering Dept., University of Michigan, 2001.
- <sup>6</sup> Sengupta, A., "Experimental Investigation of Discharge Plasma Magnetic Confinement in an NSTAR Ion Thruster," AIAA-2005-4069.
- <sup>7</sup> R. R. Robson and W. S. Williamson, "Flight Model Discharge System Scientific Report No. 4," Air Force Geophys. Lab., Hanscomb AFB, MA, AFGL-TR-88-0150, 1988.
- <sup>8</sup> E. G. Mullen, A. R. Frederickson, G. P. Murphy, K. P. Ray, E. G. Holeman, D. E. Delorey, R. Robson, and M. Farar, "An Autonomous Charge Control System at Geosynchronous Altitude: Flight Results for Spacecraft Design Consideration," IEEE Trans. Nucl. Sci., V. 44, pp. 2174–2187, Dec. 1997.
- <sup>9</sup> L.H. Krause, D.L. Cooke, C.L. Enloe, G.I. Font, M.G. McHarg, V. Putz, K.P. Ray, and M.J. Toth Jr., "Survey of DSCS-III B-7 Differential Surface Charging," IEEE Trans. Nucl. Sci., V. 51, No. 6, pp. 3399-3407, Dec. 2004.
- <sup>10</sup> R.H. Comfort, T.E. Moore, P.D. Craven, C.J. Pollock, F.S. Mozer, and W.S. Williamson, "Spacecraft Potential Control by the Plasma Source Instrument on the POLAR Satellite," J. of Spacecraft and Rockets, V. 35, No. 6, pp. 845-849, Nov-Dec 1998.
- <sup>11</sup> L. Johnson, R.D. Estes, E. Lorenzini, M. Martinez-Sanchez, and J. Sanmartin, "Propulsive Small Expendable Deployer System Experiment," J. Spacecraft and Rockets, V. 37, No. 2, pp. 173-176 Mar-Apr 2000. See also: L. Johnson, B. Gilchrist, E. Lorenzini, N. Stone, and K. Wright, "Propulsive Small Expendable Deployer System (ProSEDS) Experiment: Mission Overview & Status, AIAA-2003-5094, 39th Joint Propulsion Conference and Exhibit, Huntsville, AL, July 20-23, 2003.
- <sup>12</sup> J.A. Vaughn, L. Curtis, B. Gilchrist, S. Bilen, and E. Lorenzini, "Review of the ProSEDS Electrodynamic Tether Mission Development," AIAA-2004-3501, 40th Joint Propulsion Conference and Exhibit, Fort Lauderdale, Florida, July 11-14, 2004.
- <sup>13</sup> T.L. Wilson, D. Chlouber, and R.J. Jost, "Electrodynamic Tether Currents in the Day/Night Ionosphere: Correlations During the Plasma Motor Generator Mission," J. Geophys. Res.- Space Phys., V. 101, No. A10, pp. 21,657-21,688, Oct. 1, 1996. And references therein.
- <sup>14</sup> Wilbur PJ, Rawlin VK, Beattie JR, "Ion thruster development trends and status in the United States," J. of Propulsion and Power, V. 14, No. 5, pp. 708-715, Sep.-Oct. 1998.

- 
- <sup>15</sup> M.G. Marcucci and J.E. Polk, "NSTAR Xenon Ion Thruster on Deep Space 1: Ground and Flight Tests," Rev. Sci. Instrum., V. 71, No. 3, pp. 1389-1400, March 2000.
- <sup>16</sup> B.H. Foing, G.D. Racca, A. Marini, E. Evrard, L. Stagnaro, M. Almeida, D. Koschny, D. Frew, J. Zender, D. Heather, M. Grande, J. Huovelin, H.U. Keller, A. Nathues, J.L. Josset, A. Malkki, W. Schmidt, G. Noci, R. Birkl, L. Iess, Z. Sodnik, and P. McManamon, "SMART-1 After Lunar Capture: First Results and Perspectives," J. of Earth System Science, V. 114, No. 6, pp. 687-695, Dec. 2005. And references therein.
- <sup>17</sup> D. Lichtin, "An Overview of Electric Propulsion Activities in US Industry – 2005," AIAA-2005-3532, 41st Joint Propulsion Conference and Exhibit, Tucson, AZ, July 10-13, 2005.
- <sup>18</sup> A.D. White, "New Hollow Cathode Glow Discharge," J. Appl. Phys., V. 30, No. 5, pp. 711-719, 1959.
- <sup>19</sup> Cronin, J. L., "Modern Dispenser Cathodes," IEE PROC., Vol. 128, Pt. 1, No.1, pp. 19-32, February 1981.
- <sup>20</sup> Sengupta, A., Brophy, J.R., and Goodfellow, K.D., "Status of Extended Life Test of the Deep Space 1 Flight Spare Ion Engine After 30,352 Hours of Operation," AIAA-2003-4558, 39<sup>th</sup> Joint Propulsion Conference, Huntsville, AL, 2003.
- <sup>21</sup> Sengupta, A., "Destructive Physical Analysis of Hollow Cathodes from the Deep Space 1 Flight Spare Ion Engine 30,000 Hr Life Test," IEPC-2005-026, 29th International Electric Propulsion Conference, Princeton University, Oct. 31st to Nov. 4th 2005.
- <sup>22</sup> H.R. Kaufman and J. Kahn, "Hollow Cathode Without Low-Work-Function Insert," IEPC-2005-047, 29th International Electric Propulsion Conference, Princeton, NJ, Oct. 31 – Nov. 4, 2005.
- <sup>23</sup> Goebel, D. M., Jameson, K., Katz, I., and Mikellides, I. G., "Energetic Ion Production and Keeper Erosion in Hollow Cathode Discharges," IEPC-2005-266, 29th International Electric Propulsion Conference, Princeton University, Oct. 31st to Nov. 4th 2005.
- <sup>24</sup> Goebel, D. M., Jameson, K. K., Watkins, R. M., Katz, I., and Mikellides, I. G., "Hollow Cathode Theory and Experiment. I. Plasma Characterization using Fast Miniature Scanning Probes," Journal of Applied Physics 98, 113302 (2005).
- <sup>25</sup> Polk, J. E., Anderson, J. R., Brophy, J. R., Rawlin, V. K., Patterson, M. J., Sovey, J. S. and Hamley, J., "An overview of the results from an 8200 hour wear test of the NSTAR ion thruster," AIAA-1999-2446, 35th AIAA / ASME / SAE / ASEE Joint Propulsion Conference, Los Angeles, California, June 20-24, 1999.
- <sup>26</sup> Martin, R., Farnell, C, and Williams, J., "Direct and Remote Measurements of Plasma Properties nearby Hollow Cathodes," IEPC-2005-294, 29th International Electric Propulsion Conference, Princeton University, Oct. 31st to Nov. 4th 2005.
- <sup>27</sup> Boyd, I. D. and Crofton, M. W., "Modeling the Plasma of a Hollow Cathode," Journal of Applied Physics, Vol. 95, No. 7, April 2004, Pages 3285-3295.
- <sup>28</sup> Williams, J. D. and Wilbur, P. J., "Electron Emission from a Hollow Cathode-Based Plasma Contactor," Journal of Spacecraft and Rockets, Vol. 29, No. 6, Nov-Dec 1992, Pages 820-829.
- <sup>29</sup> Kameyama, I. and Wilbur, P.J. "Measurements of Ions from High-Current Hollow Cathodes using Electrostatic Energy Analyzer," J. of Propulsion and Power, V. 16, No. 3, May-June 2000, Pages 529-535.

- 
- <sup>30</sup> Rovey, J.L., Herman, D.A., and Gallimore, A.D., "Potential Structure and Propellant Flow Rate Theory for Ion Thruster Discharge Cathode Erosion," IEPC-2005-022, 29th International Electric Propulsion Conference, Princeton, NJ, Oct 31-Nov 4, 2005
- <sup>31</sup> Goebel, D. M., Jameson, K., Katz, I., and Mikellides, I. G., "Energetic Ion Production and Keeper Erosion in Hollow Cathode Discharges," IEPC-2005-266, 29th International Electric Propulsion Conference, Princeton University, Oct. 31-Nov. 4, 2005.
- <sup>32</sup> Sengupta, A., "Experimental Investigation of Discharge Plasma Magnetic Confinement in an NSTAR Ion Thruster," AIAA-2005-4069.
- <sup>33</sup> Herman, Daniel A. and Gallimore, Alec D., "Discharge Chamber Plasma Structure of a 40-cm NEXT-type Ion Engine," AIAA-2005-4250, 41<sup>st</sup> AIAA/ASMA/SAE/ASEE Joint Propulsion Conference, Tucson, AZ, July 10-13, 2005.
- <sup>34</sup> Herman, Daniel A., Mcfarlane, Daniel S., and Gallimore, Alec D., "Discharge Plasma Parameters of a 30 cm Ion Thruster Measured without Beam Extraction using a High-Speed Probe Positioning System," IEPC-03-0069, 28<sup>th</sup> International Electric Propulsion Conference, Toulouse, France, March 17-21 2003, Pub. By Electric Rocket Propulsion Society.
- <sup>35</sup> Goebel, Dan M., Jameson, Kristina K., Watkins, Ron M., and Katz, Ira, "Hollow Cathode and Keeper-Region Plasma Measurements Using Ultra-Fast Miniature Scanning Probes," AIAA-2004-3430, 40<sup>th</sup> Joint Propulsion Conference, For Lauderdale, Florida, July 11-14, 2004.
- <sup>36</sup> Jameson, K., Goebel, D. M., and Watkins, R. M., "Hollow Cathode and Thruster Discharge Chamber Plasma Measurements Using High-Speed Scanning Probes," IEPC-2005-269, 29th International Electric Propulsion Conference, Princeton University, Oct. 31-Nov. 4 2005.
- <sup>37</sup> Goebel, D. M., Jameson, K. K., Watkins, R. M., Katz, I., and Mikellides, I. G., "Hollow Cathode Theory and Experiment. I. Plasma Characterization using Fast Miniature Scanning Probes," Journal of Applied Physics 98, 113302 (2005).
- <sup>38</sup> Bell, S., Jones, M., Maraccini, B., Perkins, J., and Schmitt, D., "Rapidly Actuating Probe for Ion Diagnostics (RAPID)," ME486A,B final paper, Colorado State University, Fort Collins, CO, Ion Propulsion Research Page, <http://www.engr.colostate.edu/me/ipr/index.htm> [cited May, 2005].
- <sup>39</sup> Alciatore, David G. and Hstand, Michael B. Introduction to Mechatronics and Measurement Systems, 1<sup>st</sup> addition, Boston, MA, McGraw-Hill Higher Education, 2003.
- <sup>40</sup> Chapra, Steven C. and Canale, Raymond P., Numerical Methods for Engineers, 4<sup>th</sup> edition, Boston, MA, McGraw Hill 2003.
- <sup>41</sup> Beer, Ferdinand P., et al. Mechanics of Materials. 3<sup>rd</sup> edition, Boston, MA, McGraw Hill, 2002.
- <sup>42</sup> Norton, Robert L. Machine Design: An Integrated Approach. 2<sup>nd</sup> edition, New Jersey, Prentice Hall, 2000.
- <sup>43</sup> Staack, D., Raitses, Y. and Fisch, N.J., "Shielded electrostatic probe for non-perturbing plasma measurements in Hall thrusters," Review of Scientific Instruments, Vol. 75, No. 2, Feb. 2004, pp. 393-399.
- <sup>44</sup> Martin, Paul J., and Roger P. Netterfield. "Ion-Assisted Dielectric and Optical Coatings," Handbook of Ion Beam Processing Technology: Principles, Deposition, Film Modification and Synthesis. Eds. Jerome J. Como, Stephen M. Rossnagel, and Harold R. Kaufman. New Jersey, Noyes Publications, 373-414, 1989.

- 
- <sup>45</sup> Rossnagel, Stephen M. "Methods and Techniques of Ion Beam Processes," Handbook of Ion Beam Processing Technology: Principles, Deposition, Film Modification and Synthesis, Eds. Jerome J. Como, Stephen M. Rossnagel, and Harold R. Kaufman. New Jersey: Noyes Publications, 362-372, 1989.
- <sup>46</sup> Aufderheide, Brian E. "Sputtered Thin Film Coatings" Coatings Technology Handbook, Eds. D. Satas and Arthur A. Tracton. New York: Marcel Dekker, Inc., 243-254, 2001.
- <sup>47</sup> Forsythe, W.E., Smithsonian Physical Tables, 9th Revised Edition, Knovel Library 1954 (Forsythe); 2003 (Knovel), <http://www.knovel.com/knovel2/Toc.jsp?BookID=736>, [cited Feb 2006].
- <sup>48</sup> Longo, R. T., "Physics of Thermionic Dispenser Cathode Aging," Journal of Applied Physics, Vol. 94, No. 10, pp. 6966-6975, Nov. 15<sup>th</sup> 2003.
- <sup>49</sup> Yamamoto, Shigehiko, "Fundamental Physics of Vacuum Electron Sources," Rep. Prog. Phys. 69, pp. 191-232, 2006.
- <sup>50</sup> Goebel, D. and Watkins, R., "LaB6 Hollow Cathodes for Ion and Hall Thrusters," AIAA-2005-4239, 41<sup>st</sup> Joint Propulsion Conference, Tucson, Arizona, July 10<sup>th</sup>-13<sup>th</sup>, 2004.
- <sup>51</sup> Hershkowitz, Noah, "How Langmuir Probes Work," Plasma Diagnostics, Auciello, Orlando (ed), and Flamm, Daniel L. (ed), Vol. 1, Academic Press, Inc., San Diego, CA, 1989, pp.113-183.
- <sup>52</sup> Domonkos, Gallimore, and Patterson, "An Evaluation of Hollow Cathode Scaling to Very Low Power and Flow Rate," Electric Rocket Propulsion Society, 1997.
- <sup>53</sup> Kennedy, R.V., "Theory of the Arc Hollow Cathode," Journal of Physics D: Applied Physics, 34: 787-793, 2000.
- <sup>54</sup> Wronski, Sielanko, and Sullivan. "Studies of Light Emission From Cathode Material in the Plasma Phase of a Glow Discharge," Journal of Physics D: Applied Physics, 29: 1509-1514, 1996.
- <sup>55</sup> Domonkos, Gallimore, and Patterson, "Low-Current Hollow Cathode Evaluation," American Institute of Aeronautics and Astronautics, AIAA-99-2575, 1999.
- <sup>56</sup> Hobbs, Wesson, "Heat Flow Through a Langmuir Sheath in the Presence of Electron Emission", Plasma Physics, 9:85-87, 1966.
- <sup>57</sup> Sarver-Verhey, Timothy, "Life Test of a Xenon Hollow Cathode for a Space Plasma Contactor," National Aeronautics and Space Administration. Washington DC, NASA CR-195403, 1994.
- <sup>58</sup> Sarver-Verhey, Timothy, "Extended Testing of Xenon Ion Thruster Hollow Cathodes" National Aeronautics and Space Administration. Washington DC, NASA CR-189227, 1992.
- <sup>59</sup> Domonkos, M. T., Gallimore, A. D., Williams, G. J., Patterson, M. J., "Low-Current Hollow Cathode Evaluation," AIAA-99-2575, [http://www.engin.umich.edu/dept/aero/spacelab/pdf/AIAA-99-2575\\_hca.pdf](http://www.engin.umich.edu/dept/aero/spacelab/pdf/AIAA-99-2575_hca.pdf), [cited March 25<sup>th</sup> 2006].
- <sup>60</sup> Modest, Michael, Radiative Heat Transfer, 2<sup>nd</sup> edition, New York, NY, Academic Press, 2003.
- <sup>61</sup> Mikellides, I. G., Katz, I., Goebel, D. M., and Polk, J. E., "Hollow Cathode Theory and Experiment. II. A Two-dimensional Theoretical Model of the Emitter Region," Journal of Applied Physics 98, 113303 (2005).
- <sup>62</sup> Chen, F., "Lecture notes on Langmuir Probe Diagnostics," Mini-Course on Plasma Diagnostics, IEEE-ICOPS meeting, Jeju, Korea, June 5th, 2003.

- 
- <sup>63</sup> Sternovsky, Z., Robertson, S., and Lamoe, M., "*The contribution of charge exchange ions to Langmuir probe current.*" University of Colorado, Boulder, CO and Plasma Physics Division, Naval Research Lab., Washington, D.C.
- <sup>64</sup> Wilbur, Paul, "*Broad Beam Ion Propulsion,*" ME567 course lecture notes, Jan – May 2004.
- <sup>65</sup> Rocca, Jorge and Tomasel, Fernando, "*Plasma Physics and Applications,*" EE580 course lecture notes, Jan – May 2006.
- <sup>66</sup> Passoth, E., Kudrna, P., Csambal, C., Behnke, J. F., Tichy, M., And Helbig, V., "*An Experimental Study of Plasma Density Determination by a Cylindrical Langmuir Probe at Different Pressures and Magnetic Fields in a Cylindrical Magnetron Discharge in Heavy Rare Gases,*" Journal of Applied Physics, Vol. 30, 1997, pages 1763-1777.
- <sup>67</sup> Garner, C., Brophy, J., Depano, M., Bond, T., Williams, J., "*Dawn Flight Ion Thruster Data Review,*" July 26, 2005.
- <sup>68</sup> Hershkowitz, Noah, "*How Langmuir Probes Work,*" Plasma Diagnostics, Auciello, Orlando (ed), and Flamm, Daniel L. (ed), Vol. 1, Academic Press, Inc., San Diego, CA, 1989, pp.113-183.
- <sup>69</sup> Zhong, Guanwu and Zhang, Jiquan, "*Determination of the second derivative of a Langmuir probe characteristic by current continuity,*" Review of Scientific instruments, 65 (7), July 1994, 2291-2294.
- <sup>70</sup> Domonkos, M.T., Patterson, M. T., and Gallimore, A. D., "*Low-Current, Xenon Orificed Hollow Cathode Performance for In-Space Applications,*" NASA/TM-2002-211574.
- <sup>71</sup> Hayakawa, Y., Miyazaki, K., and Kitamura, S., "*Measurements of Electron Energy Distributions in an Ion Thruster,*" J. Propulsion, Vol. 8, No. 1, 1994, 118-126.